

Investigation of Residual Stress in Selective Laser Melting

by

Luke Alexander Parry

Thesis

Submitted to the University of Nottingham

for the degree of

Doctor of Philosophy

Department of Engineering

2017

Abstract

Selective laser melting is an attractive technology, enabling the manufacture of customised, complex metallic designs, with minimal wastage. However, uptake by industry is currently impeded by several technical barriers, such as the control of residual stress, which have a detrimental effect on the manufacturability and integrity of a component. Indirectly, these impose severe design restrictions and reduce the reliability of components, driving up costs.

This thesis documents work on investigating the generation of residual stresses created in the selective laser melting process by the use of a finite element thermo-mechanical model. The thermo-mechanical model incorporated an adaptive meshing strategy which was used in conjunction with the use of high performance computing facilities. These together significantly increased the computational throughput for simulating selective laser melting of a single layer. Additionally, a volumetric hatching method was created to generate the laser scan vectors used in the process, with the ability to both simulate and manufacture on selective laser melting machines.

A number of studies were performed to better understand the effect of laser scan strategy on the generation of residual stress in selective laser melting. Using this model, a series of investigations were performed to understand the effect of scan strategy and scan area size on the generation of residual stress in this process. Further studies were also performed to investigate the role of laser parameters, geometry, and support structures in selective laser melting and their effect on the generation of residual stress.

The studies showed a complex interaction between transient thermal history and the build-up of residual stress has been observed in two conventional laser scan strategies (unidirectional and alternating) investigated. The temperature gradient mechanism was discovered for the creation of residual stress and the scan area size had an effect on the temperature sustained within the region.

The parametric study of the laser parameters showed that an increase in laser scan speed increased the melt pool aspect ratio, and increase in laser power increased the melt pool width. The parametric thermo-mechanical analysis

revealed that the laser scan speed had the most influence on the magnitude and anisotropy of the residual stresses generated. Varying the hatch distance had little effect on the maximum magnitude of residual stresses generated, but decreasing the hatch distance significantly increased the level of yielding that occurred.

A study of the geometrical effect on scan strategy revealed the importance of the thermal history on the transverse stresses generated, influenced by the arrangement of scan vectors. The higher magnitude longitudinal stresses had predictable behaviour; only dependent on the scan vector length and not the thermal history generated by the choice of laser scan geometry. It was shown that the laser scan strategy becomes less important for scan vector length beyond the typical 5 mm island sizes.

From the study of the support structures, it was found the insulating properties of the metal powder used in selective laser melting provide a significant thermal resistance for the dissipation of heat, and caused uniform overheating across the scanned region. In particular, the analysis showed localised overheating using support structures, which affected the melt pool geometry, and the residual stresses generated due to resistance against dissipating heat. Additionally, lattice structures such as the double gyroid showed localised overheating occurs using repeated exposures of short scan vectors. Suitable scan strategies therefore need to be developed to account for support structures.

A multi-scale methodology was developed by combining information from the *meso*-scale obtained from the thermo-mechanical model. This model was used to predict the mechanical response of a *macro*-scale part. This approach used the assumption that *meso*-scale regions in island scan strategies behave independently from each other. This assumption was verified by comparing with a thermo-mechanical analysis. This multi-scale method was applied to a 3D structure and also to a complex 2D geometrical shape. Performing the multi-scale analyses has verified that the proposed technique of superposition of *meso*-scale stress fields at the *macro*-scale is a valid technique.

The main strengths of the proposed multi-scale method is the decoupling of the *meso* and *macro* scale analyses. This has the benefit of reducing computational cost of the *macro*-scale analysis because it is independent of the complexity of the *meso*-scale analysis, and only requires performing once. These strengths translate into large computational time savings and also great flexibility in the physics incorporated at each scale.

Acknowledgements

The pursuit of knowledge is an endeavour taken by those explorers who seek to understand the alluring mystery of the unknown. It is an arduous journey, fraught with challenges and obstacles along the way. Navigating this path requires self determination and patience to reach the destination. Yet, it is undeniable that without the guidance and support of people around me, the journey would have not been possible. Like all travelling, the greatest achievement is not reaching the destination, rather, the unspoken journey that lies before it.

I would like to thank my dearest parents and my brother who have supported me throughout the course of the PhD and everything that preceded it. They made the impossible become reality, and in times of hardship, their presence has been unwavering. Under many occasions I would be without a roof over my head, and their commitment to support me even leading into sharing the daunting journey of boat building just to give me a home. The value of their support and belief in me is intangible.

Throughout the course of the PhD, I am grateful for the patience and guidance from my two supervisors Prof. Ian Ashcroft and Prof. Ricky Wildman who have channelled my energy and challenged my work to better improve my understanding and knowledge of 3D Printing. Also, I am thankful for the opportunity to study in this exciting research area provided by the combined efforts of all the academics in our research group. I wish to offer my gratitude to present and past fellow colleagues at the University of Nottingham, in particular David Brackett, Ajit Panesar, Meisam Abdi, Adedeji Aremu, Ian Maskery who together provided a source of guidance, discussion and ideas contributing to my PhD. I wish to thank our esteemed lab technicians Mark Hardy and Mark East, who's experience working in AM and running the lab like clockwork is highly valued by us all. I also finally like to thank fellow PhD students who I worked along side, who together made the journey palatable and enjoyable.

Finally, I wish to thank Andrew Bell at MSC Software for always having rigorous and thoughtful answers to all my technical questions encountered during the PhD.

Publications

Journal Papers

Parry L, Ashcroft IA, Wildman RD. Understanding the effect of laser scan strategy on residual stress in selective laser melting through thermo-mechanical simulation. *Additive Manufacturing* 2016;12:1–15

Catchpole-Smith S, Aboulkhair N, Parry L, Tuck C, Ashcroft I. Fractal Scan Strategies for Selective Laser Melting of ‘Unweldable’ Nickel Superalloys. *Additive Manufacturing* 2016.

Hirsch M, Dryburgh P, Catchpole-Smith S, Patel R, Parry L, Sharples S, Ashcroft I, Adam C. Targeted Rework Strategies for Powder Bed. *Additive Manufacture* 2017.

Conference Papers

Parry L, Ashcroft I, Bracket, D, Wildman R. Investigation of Residual Stresses in Selective Laser Melting. *Key Engineering Materials*, 627, 129–132. 2014. <https://doi.org/10.4028/www.scientific.net/KEM.627.129>

Conferences Presented

International Conference on Fracture and Damage Mechanics - 23rd September 2014: Investigation of Residual Stresses in Selective Laser Melting

Solid Freeform Fabrication 2015: Investigation of Residual Stresses in Selective Laser Melting of Ti-6Al-4V

ECCOMAS 2016: June 6th 2016. A multi-scale approach for efficient simulation of selective laser melting (8641). <http://eccomas2016.org/proceedings/pdf/8641.pdf>

WCCM 2016: Prediction of Residual Stress in Selective Laser Melting Using a Multi-Scale Approach (150721).

Table of contents

Abbreviations	xxiii
1 Introduction	1
1.1 Background	1
1.2 Aim and objectives of the research	2
1.3 Significance and novelty of the research	2
1.4 Research methodology	3
1.5 Thesis layout	5
2 Literature Review Part I: The selective laser melting process	9
2.1 Overview of Additive Manufacturing techniques for the production of metal components	9
2.1.1 Drop on demand systems	10
2.1.2 Direct metal deposition	10
2.1.3 Powder-bed fusion techniques	10
2.2 Overview of selective laser melting	11
2.2.1 Laser scan strategy	13
2.3 Thermo-physical phenomena in the process	15
2.3.1 Laser interaction with the powder bed	15
2.3.2 Effective thermal heat transfer within powder mediums	20
2.3.3 Sintering kinetics of particles	23
2.3.4 Thermo-fluid physics	24
2.3.5 The effects of Marangoni flow	26
2.3.6 Vaporisation	27
2.3.7 Keyhole and spatter formation	29
2.3.8 Denudation of powder	30
2.3.9 Summary	31
2.4 Residual stress in selective laser melting	37
2.4.1 Mechanisms for the generation of residual stress	37
2.4.2 Consequences of residual stress in SLM	38

2.4.3	Influence of material properties	39
2.4.4	Influence of laser scan parameters	40
2.4.5	Influence of laser scan strategy	41
2.4.6	Effect of pre-heating	44
2.5	Other manufacturing issues present in selective laser melting . .	45
2.5.1	Surface roughness	46
2.5.2	Anisotropy of built components and fatigue performance .	47
2.6	Process optimisation	48
2.6.1	Identifying the process window	48
2.6.2	Pre-sintering and laser surface re-melting	50
2.6.3	Dimensional analysis	51
2.7	Summary of literature and identified gaps in the literature	53
3	Literature Review Part II: Numerical modelling of selective laser melting	55
3.1	Micro-scale modelling	56
3.2	Meso and macro-scale modelling	59
3.2.1	Development of continuum models in powder-bed fusion processes	60
3.2.2	Accounting for shrinkage	61
3.3	Analytical modelling methods for prediction of residual stress . .	64
3.4	Methods for improving simulation throughput	67
3.4.1	Alternate heat flux models	67
3.4.2	Adaptive meshing techniques (HP-FEM) and XFEM . .	69
3.4.3	Global-local analysis	71
3.4.4	Spectral methods	71
3.4.5	Multi-scale modelling	72
3.5	Summary of literature and identified gaps in the literature	73
4	Material properties used for simulation work	77
4.1	Powder properties	77
4.2	Temperature dependent thermal properties	78
4.2.1	Measurement of thermal conductivity using laser flash analysis	78
4.2.2	Measured thermal properties	80
4.2.3	Comparison of experimental measurements with analytical models	82
4.3	Temperature dependent mechanical properties	85
4.4	Summary	85

5	Method for generating and processing laser scan geometry	87
5.1	Volume hatching method	88
5.1.1	Slicing the voxel representation	88
5.1.2	The hatching process	90
5.2	Functionality for interpreting machine build files - <i>libSLM</i>	92
5.2.1	Machine build file formats used in SLM and SLS	93
5.2.2	Disassembling the Realizer .rea format	95
5.2.3	Structure of the <i>libSLM</i> library	95
5.3	Summary	97
6	Thermo-mechanical finite element modelling of selective laser melting	99
6.1	Finite element formulation	99
6.1.1	Solution to non-linear systems	100
6.1.2	Solutions to systems of linear equations	104
6.2	Details of the thermo-mechanical implementation	106
6.2.1	Thermal definition	107
6.2.2	Laser heat input	108
6.2.3	Mechanical definition	109
6.2.4	Finite element mesh	110
6.2.5	Simulation options	111
6.2.6	Post-processing the results	111
6.3	Extension of the thermo-mechanical model	112
6.3.1	Adaptive meshing technique for improving simulation performance	112
6.3.2	Octree mesh refinement	113
6.3.3	Implementation of adaptive meshing scheme	114
6.3.4	Extension of adaptive meshing scheme for custom geometry	118
6.3.5	Benchmarking of the adaptive meshing scheme	122
6.3.6	Improving scalability through high performance computing facilities	128
6.3.7	Shared memory parallel computation of finite element systems	129
6.3.8	Distributed memory parallel computation of finite element systems	130
6.3.9	Implementation of the thermo-mechanical model on the HPC system	131
7	Investigations using transient thermo-mechanical model	133
7.1	Methodology	133
7.2	Results obtained from the thermo-mechanical model	135
7.2.1	Validation of thermal analysis with experiment	135

7.2.2	Thermal analysis of single layer sections	135
7.2.3	Stress analysis of single layer regions	140
7.2.4	Comparison between laser scan strategies	143
7.3	Discussion	145
7.4	Conclusions and summary	148
8	Investigation of the effect of laser parameters	151
8.1	Introduction	151
8.2	Methodology	151
8.3	Results	154
8.3.1	Parametric study for the thermal analysis	154
8.3.2	Parametric study for the thermo-mechanical analysis . . .	155
8.4	Discussion	159
8.5	Conclusions and summary	161
9	Investigation of geometrical effects on scan strategy	163
9.1	Introduction	163
9.2	Methodology	164
9.3	Results	167
9.4	Discussion	174
9.5	Conclusions and summary	175
10	Investigation of effect of support structures and overhang regions	177
10.1	Introduction	177
10.2	Methodology	178
10.3	Results	180
10.3.1	Powder	180
10.3.2	Pseudo-powder	182
10.3.3	Thin-wall support structure	182
10.3.4	Double gyroid support structure	185
10.3.5	Scanning the geometry of a double gyroid lattice	186
10.3.6	Steady-state thermal analysis of support structure	189
10.4	Discussion	190
10.5	Conclusions and summary	194
11	Multi-scale method for the prediction of residual stresses and distortion	197
11.1	Details of the multi-scale methodology	198
11.1.1	Generation of input for macro-scale analysis	201
11.1.2	Macro-scale analysis procedure	202
11.1.3	Extension of the multi-scale method for complex geometries	204

11.2	Test cases for the multi-scale methodology	207
11.2.1	Sensitivity analysis of the pre-processing method	207
11.2.2	Direct comparison between the thermo-mechanical and multi-scale analyses	208
11.2.3	Analysis of 3D pillars using multi-scale method	209
11.2.4	Extension for modelling complex geometry	210
11.3	Results	210
11.3.1	Sensitivity analysis of the image processing	211
11.3.2	Comparison of the results obtained at the meso-scale between the multi-scale method and the thermo mechanical analysis	213
11.3.3	Analysis of 3D rectangular pillars	220
11.3.4	Extension for modelling complex geometry	224
11.4	Discussion	225
11.4.1	Sensitivity analysis of image processing	225
11.4.2	Comparison between thermo-mechanical and multi-scale analyses	226
11.4.3	Analysis of 3D Pillars	228
11.4.4	Extension for modelling complex geometry	230
11.5	Conclusions and summary	232
12	Conclusions and recommendations for future work	235
12.1	Recommendation for future work	237
	References	239

List of Figures

1.1	Diagram of the research modelling framework	4
2.1	Illustration of the configuration of a typical SLM machine such as the Realizer SLM 50	12
2.2	Illustration of the exposure mechanism along a scan track used by a) pulsed laser systems and b) continuous laser systems	13
2.3	Illustration representing the composition of an applied scan strategy within a slice of a part geometry	14
2.4	Illustration of common laser scan strategies used in SLM	15
2.5	Illustration showing the intensity of the laser irradiation at the surface scattered into the powder medium	16
2.6	Normalised energy deposited in the powder layer determined in a model roposed by Gusarov et al.	19
2.7	Profiles showing the effect of optical thickness	32
2.8	Illustration showing the coalescence of two particles undergoing sintering	32
2.9	Single track process map of Stainless Steel 316L with a layer thickness of 50 μm taken from a study performed by Yadroitsev and Gusarov [51]	33
2.10	Illustration showing the capillary stability of a cylinder track on a solid substrate and a graph plotting the theoretical and experiment track stabilities	33
2.11	Illustration showing the role of surface tension affecting the geometry of the consolidated track	33
2.12	Illustration showing the effect of the surface tension gradient on the shape of the melt pool	34
2.13	Microscopy image of spherical porosity observed in AlSi10Mg processed using SLM	34
2.14	SEM image of keyhole pore formation enclosing un-melted powders when processing AlSi10Mg	34
2.15	Illustration of the sky-writing technique using ghost vectors	35

2.16	Optical micrograph (top) and height map (bottom) showing the powder denudation zone surrounding a single scan track	35
2.17	High-speed imaging showing the track progression and movement of particles during scanning	35
2.18	Graph showing the width of the denudation zone as a function of the ambient argon pressure over the surface.	36
2.19	Illustration showing the effect of surface pressure on the movement of powder particles during processing	36
2.20	Illustration showing the temperature gradient mechanism for the generation of residual stresses	38
2.21	Photograph of failed component caused by the build-up of residual stress	39
2.22	Illustration showing the application of meander and spiral scan strategy to build a complex component	42
2.23	Illustration of Hilbert area filling curve fractal scan strategy . . .	43
2.24	Graph showing the yield strength for stainless steel 304	44
2.25	Process map showing the maximum residual stress generated with various pre-heat temperatures	45
2.26	Photograph of dross formation in a hole and ‘tear-drop’ mitigation strategy	46
2.27	Process map of a tool steel experiment	49
2.28	Process map performed showing melt pool formation and stability of a single tracks	49
2.29	Process window taken from experiments of iron powders	50
3.1	CFD simulation of selective laser melting	57
3.2	Micro-scale simulation of the melt pool formation	58
3.3	Micro-scale simulation of the melt pool formation	59
3.4	Illustration of the iterative scheme used for the shrinking and re-melting algorithm	63
3.5	Multi-layer thermo-mechanical simulation accounting for shrinkage	64
3.6	Graph of experimental measurements of strains on platform during SLM build	65
3.7	Illustration of the beam bending model	65
3.8	Graphs of residual stress profiles in built samples	66
3.9	Illustration of the uniform instantaneous heat flux layer approach	68
3.10	Illustration of multi-scale methodology proposed by Keller et al .	68
3.11	Illustration of equivalent heat source model proposed by Li et al.	69
3.12	Illustration of dynamic adaptive mesh proposed by Zeng et al. . .	70

4.1	Graph of measured particle size distribution for Ti-6Al-4V virgin powder stock	78
4.2	Illustration of the laser flash apparatus	79
4.3	Diagram showing the half-time signal obtained using LFA	79
4.4	Graph of compiled thermal conductivity values of Ti-6Al-4V	80
4.5	Graph showing effective thermal conductivity of Ti-6Al-4V powder	84
4.6	Measurements of the temperature dependent specific heat capacity	84
5.1	Volumetric model of a ring geometry	88
5.2	Illustration showing the effect of aliasing	89
5.3	Diagram of voxel slicing procedure	89
5.4	Identification of closed boundaries during slicing	90
5.5	Effect of line simplification on boundaries	91
5.6	Hatching strategies applied to ring model	91
5.7	Photograph of a ring geometry manufactured in Ti-6Al-4V using SLM with the volumetric hatching method	92
5.8	Illustration showing the generation and consumption of machine build files	93
5.9	Diagram showing the typical structure of a machine build file used in SLM	94
5.10	Photographs of commercial SLM systems	95
5.11	Illustration showing contents of a machine build file	96
5.12	Diagram showing internal structure in <i>libSLM</i>	97
6.1	Illustration showing FE formulation	100
6.2	Illustration showing piecewise functions	100
6.3	Illustration showing Newton-Raphson procedure	102
6.4	Illustration showing iterative displacement convergence tolerance	103
6.5	Illustration of the bandwidth in a sparse matrix	104
6.6	An overview of inputs required by the simulation and the inter-dependency of the processes	106
6.7	Diagram showing the interaction of subroutines between MSC Marc	107
6.8	Illustration showing the point overlap factor	109
6.9	Illustration of the fixed thermo-mechanical model mesh	111
6.10	Illustration showing element balanced refinement	114
6.11	Illustration of the un-refinement phase	114
6.12	Illustration showing the placement of the starting mesh in adaptive-mesh strategies	116
6.13	Flow diagram of adaptive-mesh scheme	116
6.14	Illustration showing calculation of element size and centroid	117

6.15	Illustration of the adaptive-mesh for the thermo-mechanical analysis	118
6.16	Illustration of adaptive analysis incorporating supporting geometry	119
6.17	Flow diagram of the adaptive meshing routine used for incorporating support geometry	120
6.18	Illustration showing refinement procedure using a sampling method	120
6.19	Profile view of temperature using the adaptive mesh scheme . . .	122
6.20	Time lapse showing the initial mesh refinement at the beginning of the analysis	123
6.21	Profile views showing the von Mises stress distribution of (3 x 3) mm islands using the adaptive meshing scheme	124
6.22	Probability stress distributions of stresses at different un-refinement levels using the adaptive mesh scheme	125
6.23	Cross-section view along the ZX plane showing the σ_{xx} stress distribution in the adaptive mesh scheme	126
6.24	Graph showing the total number of elements against time using the adaptive mesh scheme	127
6.25	Illustration of HPC Facilities	128
6.26	Illustration of HPC job scheduling	129
6.27	Illustration of the HPC job submission process	131
7.1	Illustration of laser scan strategies investigated	134
7.2	Surface profiles whilst scanning a single layer in the thermo-mechanical simulation	135
7.3	Comparison of the scan tracks between the experiment and the simulation	136
7.4	Graph showing average solidified element temperature over time	137
7.5	Graph showing temperature profile of a single node	137
7.6	Graph showing the total number of elements above 825 °C . . .	137
7.7	Surface profile views of temperature distribution during scanning in the thermo-mechanical simulation	138
7.8	Transient probability density distributions of temperature during scanning	139
7.9	Profile views of single scan track	140
7.10	Profile view of thermo-mechanical response	141
7.11	Profile view of von Mises stress in (3 x 3) mm test cases	142
7.12	Profile view of surface normal stresses using unidirectional and alternating scan strategies	142
7.13	Mirrored profile views of temperature, temperature gradient, and σ_{yy} stress	143

7.14	Profile view of temperature distribution at start and end of scan vectors	144
7.15	Profile views showing generation of σ_{xx} stress at the start of a scan vector using the alternating strategy	144
7.16	Profile views showing generation of σ_{xx} stress at the start of a scan vector using unidirectional strategy	145
7.17	Profile view of total equivalent plastic strain fields	145
8.1	Plot of Normalised enthalpies suitable for Realizer SLM 50	153
8.2	Illustration of the scan vectors used for thermal analysis in the parametric study	154
8.3	Process map showing the effect on melt pool geometry	155
8.5	Parameter map showing the melt pool aspect ratio	155
8.4	Parameter map showing interpolated average melt pool dimensions	156
8.6	Profiles of residual stresses taken in parametric study	157
8.7	Process maps of laser power and speed on residual stress generation	158
8.8	Graphs of the residual stresses generated when varying the hatch distance	159
9.1	Illustration showing the localised build-up of heat created when scanning towards the corners of geometries	163
9.2	Illustration showing the geometrical test cases for the geometrical study	165
9.3	The hatched geometrical primitives generated for the geometrical study	166
9.4	Graphs of the mean and variance of the scan vector lengths plotted against the hatch angle	166
9.5	Profile views showing the von Mises stress distribution of scanned primitives	167
9.6	Graphs comparing probability density functions of von Mises Stress in triangle geometries	168
9.7	Profile of the surface showing the temperature distribution in a (2 x 5) mm triangle	169
9.8	Profile of the surface showing a) the transverse and b) longitudinal stresses created in a (2 x 5) mm triangle	170
9.9	Graph showing the residual stresses plotted against the effective scan vector length for vertically hatched triangles	171
9.10	Graph showing the residual stresses plotted against the effective scan vector length for horizontally hatched triangles	171

9.11	Graph showing the residual stresses plotted against the effective scan vector length for vertically hatched rectangles	171
9.12	Graph of the absolute difference between the transverse and longitudinal stress components against the effective scan vector length	172
9.13	Graph of the mean temperature of consolidated elements against time for hatched primitives	173
10.1	Voxelised support structure and double gyroid lattice	179
10.2	Scan pattern generated at the top of the lattice structure	179
10.3	Temperature distribution when scanning upon a powder bed	181
10.4	Profile views of the surface showing residual stresses generated when scanning upon a powder bed	181
10.5	Graph of the total displacement of a layer scanned upon the powder bed	182
10.6	Surface profile view of the temperature distribution when scanning upon a pseudo-powder phase	183
10.7	Surface profile views of residual stresses generated when scanning upon a pseudo-powder bed	183
10.8	Surface profile view of the temperature distribution towards the end of scanning ($t = 0.499$ s) of the (5 x 5) mm single island above a thin-walled support structure	184
10.9	Profile views of the surface showing the residual stresses generated when scanning upon a thin-wall support structure	184
10.10	Cross-section through the thin-wall support structure showing the effect on the laser processed zone	185
10.11	Cross-section through the thin-wall support structure showing the effect on the laser processed zone	185
10.12	Profile views surface showing the residual stress generated when scanning on top of a double gyroid structure	186
10.13	Surface profile view showing the temperature and state when scanning a double gyroid structure	187
10.14	3D view showing the temperature distribution when scanning a double gyroid structure	187
10.15	3D view showing the temperature gradient when scanning a double gyroid structure	188
10.16	Views of the residual stresses generated when scanning a double gyroid structure	188
10.17	Profile views and cross-sections of the steady-state heat transfer through two types of support structures	189

10.18	Graph of the probability density functions of residual stresses generated in a layer scanned above various support mediums and structures	192
10.19	Material exposed underneath the scanned layer a thin-wall and double gyroid support structure	193
11.1	Illustration providing an overview of multi-scale method	198
11.2	Diagram showing the steps in the multi-scale methodology	199
11.3	Graph showing average temperature of solid elements observed after scanning the single (5 x 5) mm island	200
11.4	Rotation transformation applied to the stress tensor	202
11.5	Illustration of the <i>macro</i> -scale model used in the multi-scale method	203
11.6	Diagram showing the steps for initialising the elements in the <i>macro</i> -scale model	204
11.7	Hatched geometry used in the extension to the multi-scale method	205
11.8	Steps undertaken in the extension to the multi-scale method	206
11.9	Plot of bounding boxes generated in multi-scale method extension	206
11.10	Final input generated using the multi-scale model extension	207
11.11	Laser scan paths used in the transient thermo-mechanical analysis when compared to multi-scale method	209
11.12	3D pillar geometries used in the multi-scale analysis	210
11.13	(5 x 5) mm island inputs used in the multi-scale method	211
11.14	Sensitivity analysis of the pre-processed multi-scale inputs	212
11.15	Profile views of the residual stresses predicted in an un-transformed single island using the multi-scale method	213
11.16	Graphs of the probability density functions of residual stresses comparing the thermo-mechanical and multi-scale analyses	214
11.17	Total displacement of a single island obtained from the thermo-mechanical and the multi-scale analyses	215
11.18	Graph of displacement profiles of the single island obtained in the multi-scale analysis	215
11.19	Thermo-mechanical analysis of the 1 x 2 island case	216
11.20	Multi-scale analysis of the 1 x 2 island case	216
11.21	Profile view of the temperature taken midway through the scan of the second island in 1 x 2 island case	217
11.22	Comparison between all the 2 x 2 island cases	218
11.23	Probability density functions of residual stresses generated in the 2 x 2 island cases	219
11.24	Planar cross-sections of single island 3D pillar showing the residual stress components	220

11.25	3D View and diagonal cross-sections of single island 3D pillar showing displacement and residual stress components	221
11.26	Planar cross-sections of 2 x 2 island 3D pillar showing the residual stress components	221
11.27	3D View and diagonal cross-sections of 2 x 2 island 3D pillar showing displacement and residual stress components	222
11.28	Close-up of cross-section showing banding of the residual stresses	223
11.29	XY cross-section of residual stress at the base plate of the 2 x 2 island	224
11.30	Surface profile views of the residual stress encountered in complex geometry obtained using the thermo-mechanical analysis	224
11.31	Surface profile view of the von Mises stress of the complex geometric case obtained using the multi-scale method	225
11.32	Residual stress measurements of a 15 mm cube of Ti-6Al-4V	229
11.33	Illustration of jumping between scan vectors in the thermo-mechanical analysis of the complex geometry test case	231
11.34	Illustration showing bounding box regions of scan vector lengths which incorrectly and satisfactory map between	232

List of Tables

2.1	Absorption of wavelengths of a selection of materials taken from experiments performed by Tolochko et al. [17]	16
3.1	Overview of transient numerical simulations on powder-bed fusion processes arranged chronologically	62
4.1	Nominal composition of pre-alloyed Ti-6Al-4V powder	77
4.2	Temperature dependent material properties used for the powder form of Ti-6Al-4V	81
4.3	Temperature dependent material properties used for solid Ti-6Al-4V	81
4.4	Temperature dependent emissivity values used for both powder and solid	82
4.5	Temperature dependent thermal conductivity values of argon gas	82
4.6	Temperature dependent mechanical properties for bulk Ti-6Al-4V	85
5.1	Pre-processing parameters used for preparing the model for slicing	92
6.1	Scale factors used for relating the mechanical properties of powder phase with the solid phase	115
6.2	Performance metrics for adaptive mesh scheme	123
6.3	Median values of the stress component σ_{xx} using different levels of un-refinement	123
7.1	Laser style parameters used by a Realizer SLM 50 for Ti-6Al-4V used to generate the machine build files	134
7.2	Parameters used by a Realizer SLM 50 for Ti-6Al-4V to generate the laser geometry in the machine build files	134
7.3	Average values for von Mises stress and normal strain and stress components calculated from solid elements located in the first layer for multiple simulation cases	143

8.1	Selection of known laser parameters and machine parameters used for building Ti-6Al-4V available in literature	152
8.2	Properties used for calculating the normalised enthalpy for Ti-6Al-4V	152
10.1	Calculated average heat flux and effective thermal conductivity values through the support material. Percentages in brackets indicate the effective thermal conductivity relative to the solid material	190
10.2	Dimensions of the melt pool and the stability condition when scanning above different medium	191
11.1	Summary of the two models used at each scale in the multi-scale methodology	200
11.2	Computational timings for performing the analyses using the thermo-mechanical and multi-scale analysis methods	227

Abbreviations

ALE	Arbitrary Lagrange-Euler.
AM	Additive Manufacturing.
CAD	Computer Aided Manufacturing.
CAE	Computer Aided Engineering.
CFD	Computational Fluid Dynamics.
CFL	Courant-Friedrich-Lewy.
DDM	Domain Decomposition Method.
DED	Direct Energy Deposition.
DLP	Digital Light Projector.
DMD	Direct Metal Deposition.
DOD	Drop on demand.
DOE	Design of Experiment.
DOF	Degrees of Freedom.
DSC	Differential scanning calorimetry.
EBM	Electron Beam Melting.
FE	Finite Element.
FFT	Fast Fourier Transform.
FV	Finite Volume.
GAP	Gas Atomised Powder.
GL	Global-Local.
HAZ	Heat Affected Zone.
HIP	Hot Isostatic Pressing.
HPC	High Performance Computing.

LBM	Lattice Boltzman Method.
LFA	Laser Flash Analysis.
LHI	Least Heat Influence.
MPI	Message Passage Interface.
Nd:YAG	Neodymium-doped Yttrium Aluminium Garnet.
PDE	Partial Differential Equation.
PDF	Probability Density Function.
PREP	Plasma Rotating Electrode Processed.
RVE	Representative Volumetric Element.
SEM	Scanned Electron Microscopy.
SLM	Selective Laser Melting.
SLS	Selective Laser Sintering.
SMP	Shared Memory Processing.
SOR	Successive Over-Relaxation.
STL	Stereo Lithography.
TGM	Temperature Gradient Mechanism.
UTS	Ultimate Tensile Strength.
VOF	Volume of Fluid.
X-FEM	Extended Finite Element Method.
XRD	X-ray Diffraction.

Nomenclature

Scientific constants

σ_B Stefan-Boltzmann constant (5.67×10^{-8} W/ m²K⁴)

g Gravitational Constant (9.31 m/s²)

k_B Boltzmann constant (1.38×10^{-23} J/K)

L Lorentz number (2.44×10^{-8} W Ω K²)

N_a Avogadro's constant (6.022×10^{23} 1/Mol)

p_{atm} Atmospheric pressure (1.013×10^5 Pa)

R_0 universal gas constant [J/ mol K]

α Thermal diffusivity [m²/s]

α_{CTE} Linear thermal expansion coefficient [1/K]

β_{ex} Extinction coefficient

Γ Surface of domain

γ Surface tension [N/m]

μ Dynamic viscosity [kg/ms]

ν Poisson's ratio

Ω Domain

$\bar{\varepsilon}_p$ Total equivalent plastic strain

ϕ State variable

ρ Density [g/cm³]

ρ_h	Hemi-spherical reflectivity
ρ_h	Reflectivity
σ	Stress [MPa]
σ_y	Yield strength [MPa]
σ_{cond}	Electrical conductivity [S/m]
θ_h	Hatch angle
ε	Strain
ε_p	Plastic strain
ε_{em}	Emissivity
ε_{th}	Thermal strain
A	Absorption
Bo	Bond number
C	Specific heat capacity [kJ/kgK]
D_P	Spherical particle size [μm]
E	Young's modulus [GPa]
E_A	Aerial energy density [W/m^2]
E_L	Line energy density [W/m]
E_V	Volumetric energy density [W/m^3]
f_p	Powder packing factor
f_{po}	Spot point overlap factor
H	Enthalpy [J/kg]
h	Specific enthalpy [J/kg]
h_c	Heat transfer coefficient [$\text{W}/\text{m}^2\text{K}$]
h_d	Hatch offset distance [mm]
h_m	Enthalpy at melt [J]
H_p	Plastic tangent modulus [GPa]

k	Thermal conductivity [W/mK]
L_T	Layer thickness [mm]
L_{evap}	Latent heat of vaporisation [J/kg]
L_{fuse}	Latent heat of fusion [J/kg]
La	Laplace number
M_g	Molecular mass of gas [1/mol]
Ma	Marangoni number
P	Nominal laser power [W]
p	Pressure [Pa]
p_i	Partial pressure [Pa]
Pe	Peclet number
q_s	Surface heat flux [W/m ²]
q_v	Volumetric heat flux [W/m ³]
r_d	Laser spot radius [mm]
Re	Reynolds number
T	Temperature
T_A	Temperature (ambient) [°C]
T_B	Temperature (boiling point) [°C]
T_L	Temperature (liquidus) [°C]
T_S	Temperature (solidus) [°C]
v	Scanning velocity [mm/s]

Chapter 1

Introduction

1.1 Background

Additive manufacturing (AM) is a method of fabricating components directly from digital models, by additively depositing material to form a part. Geometrical representation of components is stored by computer aided manufacturing (CAD) supported by computer aided engineering (CAE) techniques. Fabrication of designs is directly achievable and not subjected to the many constraints, and expenses imposed by traditional manufacturing techniques. This new paradigm shift in manufacturing provides significant opportunities for improvements over pre-existing designs and be revolutionary in new novel applications. A broad family of AM process exist to cater for different end-users, with their taxonomy mostly dependent on the material choice (polymer, ceramic or metals). Each of these processes has their own limitations and challenges, although some of these may be overcome through further development and refinement of the process technique.

For the direct production of metal components, selective laser melting (SLM) is an attractive technology, which is now establishing itself as a certified production method in high-value industries. SLM offers the capability to manufacture light-weight structural components across a broad palette of metal alloys. The feature resolution obtainable enables intricate geometrical detail across a relatively large build volume, up to 300 mm in each direction, which is suitable for many applications. Yet, the production of structural metal components using this technology still has many challenges remaining for both industry and researchers. Critically, the reliable and consistent manufacture of parts is yet to resolved, which is essential for achieving manufacture at higher volumes. These problems arise from instabilities in the process, which require further understanding and mitigation. A pressing concern is systemic build failure during manufacture

caused by the build-up of excess residual stresses causing part distortion or failure. This issue adds large uncertainty to the production process.

The build-up of residual stresses is integral to thermal manufacturing processes such as SLM. However, due to the complex interactions in the process, experimental measurements provide little opportunity to understand the thermo-mechanical process that govern the generation of stresses within a complex part. The prediction of residual stress in welding has been long established, using analytical and computational models. This indicates that modelling can provide an insight into the generation of residual stresses in SLM, and form a basis of a computational framework for predicting and mitigating residual stresses.

1.2 Aim and objectives of the research

The overall aim of this research was to develop an efficient computational model of SLM, in order to investigate the generation of residual stresses generated within a typical part. The computational model should provide an insight into the mechanisms of residual stress generation across a part and provide guidance for the design of parts and their laser scan strategies. Ultimately this would help reduce the probability of part failure, which is critical for improving the adoption of SLM by industry. This aim was achieved through the following objectives:

- Investigate computational models for efficiently predicting the thermo-mechanical behaviour in SLM
- Develop an efficient computational model to predict the thermo-mechanical behaviour of a small part
- Using the model, perform a series of studies to understand the effects of the process inputs on the generation of residual stress
- Develop guidelines for reducing residual stress and an efficient multi-scale model for the prediction of residual stress in large components.

1.3 Significance and novelty of the research

The study of the thermo-mechanical behaviour in SLM is challenging, owing to the time and length scales involved in this process. Performing experiments to investigate the thermo-physical phenomena in the process zone, and specifically the build-up of residual stresses in the selective laser melting process remains limited due to the resolution offered by measurement techniques available, and the resources required.

In this work, a thermo-mechanical finite element model of the selective laser melting process was created to perform numerical investigations on the generation of residual stress. This work is significant because it has contributed greater understanding of the mechanisms that create residual stresses in SLM. Additionally, the work has investigated the effects of laser scan strategy, laser parameters, geometrical effects and support geometry on the generation of residual stresses in *macro*-scale parts, which was not available in the literature.

This work was supported by a volumetric hatching method, which had the ability to be used in both experiments and simulation. This has provided the opportunity to explore novel scan strategies and enable investigations into controlling the SLM process not previously available.

Furthermore, this work introduces a multi-scale approach for predicting residual stress and distortion in *macro*-scale regions, which may potentially be used for industrially sized parts.

1.4 Research methodology

Based on the research objectives outlined, a proposed modelling framework, as illustrated in Figure 1.1, was developed to study the effect of residual stress generation using a thermo-mechanical finite element analysis. The figure shows the breakdown of the research framework presented in this thesis, and the links between them.

The framework relies on the pre-processing methods, which are essential for generating the laser scan geometry for both the thermo-mechanical and multi-scale models. The thermo-mechanical model is described, and a variety of simulation studies were performed to better understand the thermo-mechanical response of various scenarios encountered during the selective laser melting process. The thermo-mechanical model was extended with an adaptive mesh scheme and also by using high performance computing facilities enabling a large scope of investigations to be performed. Combining these many elements together provide a foundation for developing a multi-scale methodology that could eventually provide a prediction of residual stresses and the distortion of large industrial parts. Through developing a multi-scale modelling strategy this will help achieve the aim for providing a predictive tool that can help designers and industrial users for building parts using selective laser melting correct the first time.

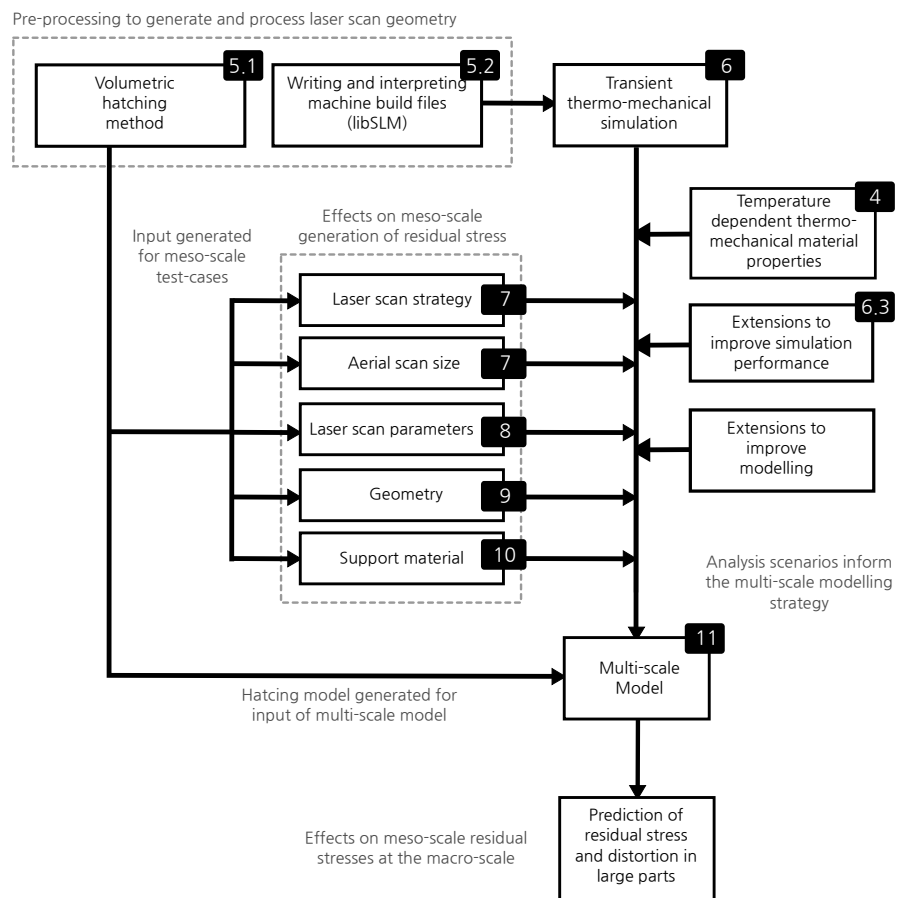


Figure 1.1: Framework for the research to determine the effects of residual stress through simulation and provide strategy for predicting residual stress and distortion in large parts (numbers indicate thesis chapters)

1.5 Thesis layout

A description of the content for each of the chapters is presented below.

Chapter 2 – Literature Review Part I: The selective laser melting process

In this chapter, a literature survey was performed to identify the relevant previous research in fields related to powder bed fusion processes, in particular selective laser melting. Firstly, a general summary of available additive manufacture methods for the production of metal components is presented, followed by an overview of the selective laser melting process. The remainder of the chapter examines in greater detail the thermo-physical phenomena present in the process that have been captured through experiments and modelling, along with related theory. Current knowledge of residual stresses is presented along with other issues associated with the process, and efforts by research to optimise the process.

Chapter 3 – Literature Review Part II: Numerical modelling of selective laser melting

In this chapter, a literature survey of techniques developed for modelling SLM and powder-bed fusion processes are presented. The SLM process is inherently multi-scale, and involves the presence of different physical phenomena at each scale required to be captured by the models. The modelling approaches are sectioned into the (*micro*, *meso* and *macro*) scales encountered in this process. Finally, analytical techniques are presented along with state of the art techniques for improving the simulation performance and capability of simulation.

Chapter 4 - Material properties used for simulation work

In this chapter, the measurements for the thermal conductivity of powder and solid form of Ti-6Al-4V material using the laser flash method are described. The thermal conductivity measurements for the powder are then compared with analytical models. Other temperature dependent thermal and mechanical properties are tabulated for reference in the modelling work.

Chapter 5 - Method for generating and processing laser scan geometry

In this chapter, a method for generating the laser scan geometry from volumetric models is presented. The structure of machine build files used by SLM systems is documented and a method for creating and interpreting these using the *libSLM*

library are shown. Finally, the role of this library in later simulation work is discussed.

Chapter 6 - Thermo-mechanical finite element modelling of selective laser melting

In this chapter, the finite element formulation and the methods for solving system of equations are presented. The definition of the transient thermo-mechanical model is then documented. In addition, extensions to this model to include adaptive meshing techniques and the use of high performance computing facilities are presented for improving the simulation throughput. Finally test cases for the thermo-mechanical model are described.

Chapter 7 - Investigations using transient thermo-mechanical model

In this chapter, a set of studies are performed using the thermo-mechanical model developed in this work. Firstly, investigations were performed to examine the mechanisms for the build-up of residual stresses in selective laser melting. Then, a set of studies were performed to study the effect of scan strategy and aerial size on the build-up of residual stresses. Finally, the adaptive mesh scheme developed in this work was benchmarked.

Chapter 8 - Investigation of the effect of laser parameters

In this chapter, a comprehensive parametric study on the role of laser parameters, including laser speed, power and hatch distance, is undertaken to observe any effects on the predicted melt pool geometry, and the residual stresses generated.

Chapter 9 - Investigation of geometrical effect on scan strategy

In this chapter, the effect of geometry across simple triangle and regular parameters, in addition to hatch orientation is investigated on the build-up of residual stresses. The distribution of residual stresses created are analysed to obtain a set of relationships.

Chapter 10 - Investigation of effect of support structures and overhang regions

In this chapter, a study is performed which examined the effect of material underneath the scanned region on the build-up of residual stresses. The study looks at the effect of a thin-wall and double gyroid support structures and the role of heat dissipation by comparing with a steady-state thermal analysis.

Chapter 11 - Multi-scale method for the prediction of residual stresses and distortion

In this chapter, the definition of a multi-scale methodology for the prediction of residual stress in large parts is presented. An extension to account for complex geometries is shown. Test cases are proposed for evaluating the performance and accuracy by comparing comparison with the previous thermo-mechanical model.

Chapter 12 - Conclusions and recommendations for future work

A summary of significant conclusions obtained from this research work is presented. Finally, recommendations for future work is presented following the outcomes of this work.

Chapter 2

Literature Review Part I: The selective laser melting process

The use of additive manufacturing has proliferated in recent years through enabling designers greater design freedoms than traditional manufacturing methods. AM provides the ability to include geometrically complex metallic structures [1], with a rapid design to manufacture cycle compared with conventional manufacturing methods [2]. Owing to its ability to incorporate advanced design techniques, such as topology optimisation [3, 4] and lattice structures into components [5], and individual customization, AM has gained significant attention from many industrial sectors, including aerospace and automotive.

2.1 Overview of Additive Manufacturing techniques for the production of metal components

The high melting temperatures required to fuse the metallic materials used in structural engineering applications limits the palette of additive manufactured techniques available, especially for the direct manufacture of fully dense metal parts. Current available families of technologies for the additive manufacture of metallic components include drop-on-demand systems, direct metal deposition, and powder-bed fusion techniques.

2.1.1 Drop on demand systems

Drop on demand (DOD) systems are less common than the other methods discussed for manufacturing metal components, but are commercially available. The use of ink-jetting binder technology has been developed by Höganäs in their ‘Digital Metal’ platform [6]. In their system, a metal powder is spread across a build platform at room temperature. Parts are formed by selectively depositing a binding ink to form a green compact. Afterwards, parts require sintering through hot isostatic pressing (HIPing) in order to obtain full density. This method offers a relatively high resolution – dependent on the powder morphology and resolution of the inkjet heads. Another benefit is the lack of protective atmosphere required during printing, or issues with distortion due to non-uniform thermal gradients. However, the use of HIPing is an undesirable extra step, and means the process doesn’t directly manufacture of metal parts.

Recently, a commercial solution by XJet used nano-particle ink-jetting to build parts directly without requiring post-treatment [7]. During the process, the ink containing suspended metal nanoparticles evaporates, depositing nano-particles. Due to their size, the particles can easily fuse together through solid state-diffusion. This specific solution, however, has not been reported in the academic literature. This technology has been used in 3D printing for thin electronics circuits, using silver nano-ink sintered with infrared heaters [8].

2.1.2 Direct metal deposition

Direct metal deposition (DMD) is a group of technologies originating from laser cladding, which involves progressively overlaying deposited weld beads to form a structure [9, 10]. The material deposited may originate from a powder source or solid wire feed-stock, which are fused thermally, either using a laser or by electric arc. These technologies currently offer the highest deposition rates and build volume for additive manufactured metal parts, at the expense of resolution.

2.1.3 Powder-bed fusion techniques

Currently the most favoured, and mature methods for the additive manufacture of metal components are based on the family of powder-bed fusion technologies [11], which are widely available commercial. These families of processes are classified by the use of a powder bed layer which is repeatedly exposed to a high density thermal flux causing powder particles to sinter or fully melt thereby, fusing into a consolidated structure upon cooling. Successive build-up of layers eventually produces the desired component and upon completion un-sintered loose powder material is removed from build.

A significant proportion of derivative technologies of this family are based on the ‘selective’ exposure of a powder bed using a point source: i.e. a focused laser beam or a directed electron beam. Manufacturing using areal sintering methods are desirable because of the potential significant speed gains for manufacturing components. This has been achieved for sintering polymer powders using digital light projector (DLP) systems [12], however, currently aerial methods do not exist for manufacturing metal components owing to the high energy input required.

For a single point exposure source to consolidate regions, a series of scan vectors are generated to enable the point to raster across the surface of the powder-bed. The scan path or vectors chosen are factors in the quality of the manufactured item. This is highly dependent on both the material, and machine it is manufactured on, and consequently this results in a broad parameter exploration space for optimisation [13]. Fundamentally, these scan vectors are designed based on the delivered energy density within a region.

Selective laser melting has gained significant attention from many industrial sectors, in particular aerospace and automotive. The SLM process uses a laser source under an inert atmosphere. Electron beam melting (EBM) is a competing technology for the production of metal components [14]. This technology differs considerably, and uses an electron beam to fuse metal powder under a high temperature and a near vacuum atmosphere. The use of an electron beam offers significantly faster scan velocities. Additionally, the high temperature available in EBM provides many benefits including in-build heat-treatment and negligible residual stress which reduces the need for support structures, and reduces part distortion during build. Both technologies have their advantages in production, yet laser melting technologies are far more popular to industry because of the greater availability and choice of systems.

2.2 Overview of selective laser melting

The machines have a typical design, as illustrated in Figure 2.1. The part is built on a heated substrate platform of a similar metal composition, which is lowered during the build along the Z-axis. After each successive laser scan across the powder layer, the platform is lowered, and the powder re-coating mechanism (wiper or blade) spreads an even distribution of powder of the desired layer thickness. The powder is not typically mechanically compressed, and relies on the free flow of powder, typically achieved using a powder packing factor f_p between 40-60% with single-component Gaussian distributed powders [15].

The process occurs in a build chamber with inert atmosphere to minimise the effects of oxidisation and external contamination that may cause build failure.

Oxide effects have been shown to have a profound effect on the process as described by Simonelli et al. [16].

In order to achieve an inert atmosphere, purging typically with argon is used to reduce oxygen levels to below 1000 PPM, without forming a vacuum. Throughout the build process, a continuous inert gas flow is directed across the surface displacing oxygen due to a buoyancy effect. The gas flow carries away undesirable molten material ejected from the melt pool caused by process instability, in addition to vapour plumes [16]. It has been observed that it is impractical to completely remove air trapped between pores in the powder bed and this further affects the absorptivity of the laser by the powder [17].

The profile of the laser beam is Gaussian, and a variable focus can be calibrated to change the effective laser spot size and the focal position within the layer [18, 19]. Various pulse modes are available, but conventional systems use a modulated pulsed or continuous laser which determines the exposure strategy dictating the energy delivered, as shown in Figure 2.2.

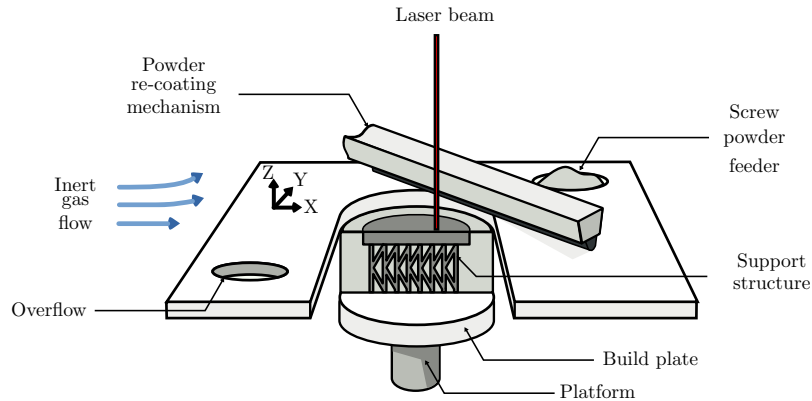


Figure 2.1: Illustration of the configuration of a typical SLM machine such as the Realizer SLM 50

Using the continuous laser, the laser remains active whilst scanning across the scan vector at a constant speed. Whereas the pulsed form delivers energy at series of points along the scan vector for a given exposure time and point distance. Despite the small nuances between the laser types, the exposure time and point distance is usually conveniently expressed as an ‘effective’ laser speed v . A combination of the common laser parameters are often defined using the energy density parameter, or apparent energy delivered to unit volume which is defined as

$$E_V = \frac{P}{vh_d L_T}, \quad (2.1)$$

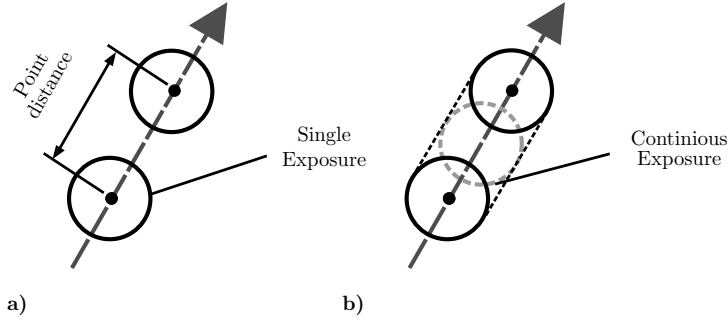


Figure 2.2: Illustration of the exposure mechanism along a scan track used by a) pulsed laser systems and b) continuous laser systems

where P is the nominal laser power, h_d the hatch spacing, and L_T is the layer thickness [20]. This measurement is often used as relative comparison between builds, and can alternatively be defined in two and one dimensional forms:

$$E_A = \frac{P}{vh_d}, \quad (2.2)$$

$$E_L = \frac{P}{v}. \quad (2.3)$$

These terms are rather simplistic, and largely ignore the majority of processing parameters and conditions that can affect build quality under certain situations within the process of SLM. A more complete method has been used by Wu et al. [21] who stated their laser parameters using the normalised enthalpy defined as,

$$\frac{\Delta H}{H_m} = \frac{\eta P}{\rho_{melt} H_m \sqrt{\pi \alpha r_d^3 v}}, \quad (2.4)$$

where η is the laser efficiency, ρ_{melt} is the density at melting, H_m is the enthalpy at melting, α is the thermal diffusivity, and r_d is the laser spot radius.

2.2.1 Laser scan strategy

The choice of laser parameters is seldom developed independently, and must often account for the laser scan strategy chosen, which is highly geometrically dependent. Generally, within SLM, three distinct classifications of laser paths exist: contour, hatching and point exposures, as shown in Figure 2.3.

The outer contour scan is offset from the part boundary by a spot compensation, usually the laser spot radius, r_d , to obtain the same dimensions of the part. Normally, a repeated number of contour scans are then offset from the part boundary to improve the surface finish quality and eliminates zones not fully

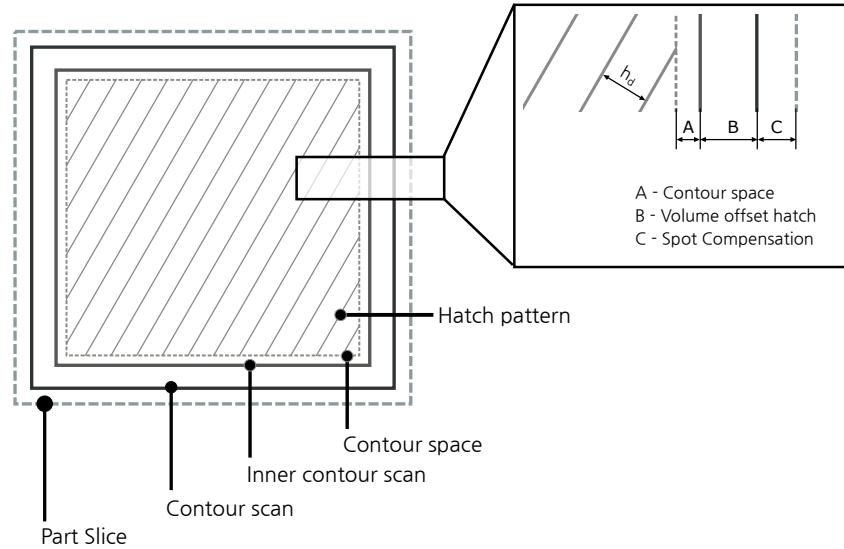


Figure 2.3: Illustration representing the composition of an applied scan strategy within a slice of a part geometry

scanned by the hatched region. The bulk of the material is consolidated using a hatch scan style, consisting of series of adjacent scan vectors with a given hatch spacing. The hatch spacing h_d for laser scan vectors is critical, and has been found to determine the level of porosity within a part, and the level of surface roughness [22]. There is a compromise for hatch spacing on build time and the quality of the part built. If the hatch spacing is greater than the track width, this results in un-sintered powder between tracks. Likewise, a hatch spacing equal to the track width results in irregular melt pool formation, leaving elongated pores within the built component [20]. On the contrary, reducing the hatch spacing has a variety of issues: increased build time, over heating in small regions, and increased susceptibility of porosity due to effect of denudation; explained in Section 2.3.8.

In order to minimise the effect of anisotropy within the XY plane of the build part, typically the hatch orientation is rotated incrementally for each layer by an angle θ_h . Regions are infilled with hatched regions using various scan strategies: conventionally a meander, checkerboard (island) or stripe scan strategy as illustrated in Figure 2.4. The choice of laser scan strategy is an additional method to provide a degree of localised control on the manufacturing process, which affects the stability, repeatability and quality of the parts produced using SLM.

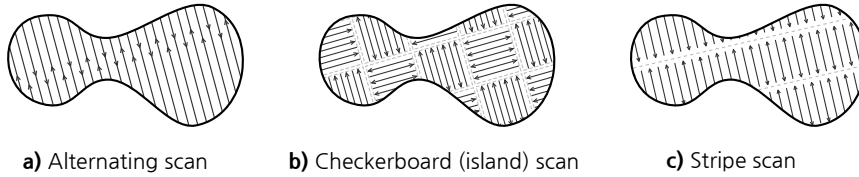


Figure 2.4: Common laser scan strategies used for pre-processing parts in SLM

2.3 Thermo-physical phenomena in the process

Owing to the nature of powder bed fusion processes such as SLM, a multitude of complex thermo-physical phenomena occur at a variety of different spatial and temporal time scales. Within this section, a review of the literature which analyses and discusses the underlying physics present during the manufacturing process using experiments and numerical simulations is reported. The interaction of the laser beam and powder including the effective transmission and absorption of energy with the multiple phases existing in the powder-bed medium is reported in Section 2.3.1. The effective transfer of heat generated due to exposure to the laser within the powder medium is then discussed in Section 2.3.2. The role of the sintering mechanisms of metal powders is discussed in Section 2.3.3, although much of the micro-scale behaviour is strongly tied to the thermo-fluid interactions within and surrounding the melt pool, which are reported in Sections 2.3.5-2.3.8.

2.3.1 Laser interaction with the powder bed

During the SLM process, the powder bed is irradiated by a laser focused onto the powder bed. Absorption of photons on the surface of the powder causes a transformation into thermal energy. Typical focused laser spot diameters range from 25 - 100 μm with a layer thickness varying between 25 - 50 μm depending on the powder morphology and the build material [23]. Two different types of irradiation sources are conventionally used for SLM: CO_2 and neodymium-doped yttrium aluminium garnet (Nd:YAG) with respective wavelengths of 10.6 μm and 1064 nm. The choice of laser depends on the absorptivity of the material, driven by the absorption mechanism [17]. Insulating materials, such as polymers, ceramics, and metal oxides, tend to favour the use of CO_2 lasers, whereas absorption with the Nd:YAG is better with metals, as shown in Table 2.1.

The interaction of the laser with the powder is particularly complicated. As illustrated in Figure 2.5, collimated rays are reflected off the oblique surface of particles through pores, and then is propagated and further scattered into a great depth of the powder [24]. The powder behaves as a homogeneous absorbing

Material	Absorption A	
	$\lambda = 1064 \text{ nm}$ (Nd:YAG)	$\lambda = 10.6 \text{ }\mu\text{m}$ (CO ₂)
Cu	0.59	0.26
Fe	0.64	0.45
Sn	0.66	0.23
Ti	0.77	0.59
Al ₂ O ₃	0.03	0.96
SiO ₂	0.04	0.96
NaCl	0.17	0.60
PTFE	0.05	0.73

Table 2.1: Absorption of wavelengths of a selection of materials taken from experiments performed by Tolochko et al. [17]

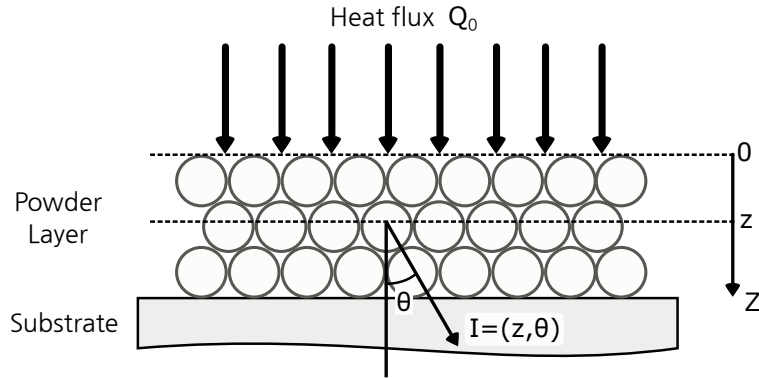


Figure 2.5: Illustration showing the intensity of the laser irradiation at the surface scattered into the powder medium

scattering medium, with an effective extinction coefficient β_{ex} . The scattering and multiple reflections allow the penetration of rays into the layer exceeding multiple-particle diameters [25] and spread into surrounding material at an angle θ , with an overall intensity characterised by $I(z, \theta)$.

The earliest analytical heat source model was proposed by Rosenthal for use in the application of welding metal plates together [26]. The analytical solution was derived from heat flow equations and assumed a moving point heat source on the surface with a constant thermal diffusivity α .

The analytical solution for a thick plate assumes a moving coordinate system $x_i = x - vt$, travelling at velocity v , with the resultant temperature distribution T defined as

$$T - T_0 = \frac{1}{r} \frac{P}{2\pi kd} \exp\left\{\frac{vx_i}{2\alpha}\right\} \exp\left\{-\frac{vr}{2\alpha}\right\}, \quad (2.5)$$

where d is the depth into the work piece, P is the heat input, k is the thermal

conductivity, T_0 is the ambient temperature, and r is the radial distance from the heat source. The Rosenthal solution, provides a reasonable estimate of the thermal distribution spatially over a large distance r , however, it is unsuitable close to the point heat source which tends towards infinity.

For laser applications such as SLM, beam characterisation has found the energy absorption profile to be Gaussian with a peak intensity and radial decay [27]. The application of a heat input as a boundary condition is a two dimensional stationary surface heat flux as

$$q = 2\pi P r_0^2 \exp\left\{-\frac{2r^2}{r_0^2}\right\}, \quad (2.6)$$

where r_0 is the laser spot radius. For welding applications Goldak proposed using a double ellipsoid Gaussian heat source to account for the absorption of energy at different depths in a moving heat source [28], with the definition

$$q_v = \frac{6\eta\sqrt{3}P}{\pi\sqrt{\pi}r_x r_y r_z} \exp\left\{-\frac{3x^2}{r_x^2}\right\} \exp\left\{-\frac{3y^2}{r_y^2}\right\} \exp\left\{-\frac{3z^2}{r_z^2}\right\}, \quad (2.7)$$

with a variable laser power P , laser spot radii r_x , r_y , and r_z , and a lumped efficiency term η to account for the relative absorption of laser energy into the material, that can change according to the material phase. Calibrating the efficiency term may be necessary by comparing the melt pool penetration with that of the model. However, using this formulation, Kolosov et al. recommended that a sufficient mesh resolution in the model is required for accurate representation of the heat source [29]. Zeng et al. [30] performed experimental validation using thermal imaging to measure the size and peak temperature of melt pool and found in good agreement with their simulations. This method is often preferred due to its simplicity.

The absorption in a dense medium is described by the Bouger-Beer-Lambert law, which is a logarithmic relationship between the transmission of light of intensity I through a medium [31], and is defined as

$$I = I_0(1 - \rho_h) \exp\{-\alpha_{abs}\delta\}, \quad (2.8)$$

where I_0 [W/m²] is the incident radiation, ρ_h is the reflectivity, α_{abs} is the absorption coefficient and δ is the path length. The Bouger-Beer-Lambert law is only applicable for pure absorption. Due to multiple reflectance of radiation between the bodies in the particle bed, scattering is created rendering this law unsuitable for modelling absorption of energy into the powder bed.

Further advances have been made in predicted the absorption characteristics of powder. Gusarov et al. proposed a radiation-conduction model of the powder bed and the effect on absorbance A and implicitly the transmission of

an energy flux from the surface into the powder bed [32] which has been used in subsequent simulation studies [33, 34]. This model considered penetration into the powder medium by assuming a statistically isotropic powder bed considering the importance of optical thickness λ defined as

$$\lambda = \beta_{ex} L_T = \frac{3}{2} \frac{1 - f_p}{f_p} \frac{1}{D_p}, \quad (2.9)$$

where β_{ex} is the extinction coefficient, L_T is the powder layer thickness, f_p is the powder packing factor and D_p is the powder's spherical particle size. The distribution of energy in the powder bed depends on these parameters, in addition to the reflectivity ρ_h of the material, and the effective scattering properties of the medium defined by the effective scatter coefficient $\sigma_{scatter}$. In the model proposed by Gusarov, the expression of the normalised power density \bar{q} applied was defined as

$$\begin{aligned} \bar{q} = \frac{Q}{Q_0} = & \frac{\rho_h a}{(4\rho_h - 3)D} \times ([1 - \rho_h^2]e^{-\lambda}[(1 - a)e^{-2a\xi'} + (1 + a)e^{2a\xi'}] \dots \\ & - [3 + \rho_h e^{-2\lambda}][(1 + a - \rho_h(1 - a))e^{2a(\lambda - \xi')} + (1 - a - \rho_h(1 + a))e^{2a(\xi' - \lambda)}]) \dots \\ & - 3 \frac{(1 - \rho_h)(e^{-\xi'} - \rho_h e^{\xi' - 2\lambda})}{4\rho_h - 3}, \end{aligned} \quad (2.10)$$

where constant a is defined $a = \sqrt{1 - \rho_h}$, the optical thickness in the powder medium $\lambda = \beta_{ex} L_t$, the dimensionless coordinate in the Z' direction of the powder thickness $\xi' = \beta_{ex} z'$, and D is an additional constant where

$$D = (1 - a)[1 - a - \rho_h(1 + a)]e^{-2a\lambda} - (1 + a)[1 + a - \rho_h(1 - a)]e^{2a\lambda}. \quad (2.11)$$

The volumetric heat source term q_v , used in subsequent models can be found by the partial derivative of the normalised power density in equation 2.10 multiplied by the surface irradiation such that

$$q_v = -\beta_{ex} Q_0 \frac{\partial \bar{q}}{\partial \xi'}, \quad (2.12)$$

with the equivalent surface irradiance Q_0 , projected onto the surface. This is spatially varying according to a Gaussian profile at the laser origin determined by:

$$Q_0 = 3 \frac{\eta P}{\pi r_d^2} \left(1 - \frac{r}{r_d}\right)^2 \left(1 + \frac{r}{r_d}\right)^2, \quad \text{for } 0 < r < R, \quad (2.13)$$

with the radial coordinate system $r^2 = x'^2 + y'^2$ positioned at the laser origin. The author acknowledges that the model does not account for any effects on the powder associated with energy losses caused by the effects of vaporisation, and therefore includes an additional efficiency term η . In this model, the effective deposition of energy into the powder bed is shown in Figure 2.6, and the effect of the optical thickness is shown in Figure 2.7. It can be seen, that this model better accounts for the scattering of the heat flux throughout the powder-bed, and unlike other models, the effect of the optical depth (the layer thickness) changes the profile of deposited energy into the powder bed. Their transient thermal model showed the formed melt pool was in good agreement with experiment. This model provides a means to capture more accurately the behaviour of the powder compared to the volumetric Gaussian models used typically for homogeneous solid regions in welding applications.

The model proposed by Gusarov assumes the optical thickness of the powder medium is homogeneous and is composed of particles substantially smaller in diameter than the layer thickness. In practice, when scanning across a single layer, the particle size distribution of the powder present in SLM typically will have particle sizes equal or greater than the layer thickness, and of a similar order as the laser beam spot. This condition would not let the scattering and transmission of the energy deposited into the effective layer and it raises questions about validity of the model when scanning across a single layer. However, this model may provide a better representation when scanning directly into a powder medium without a substrate, such as an overhang region.

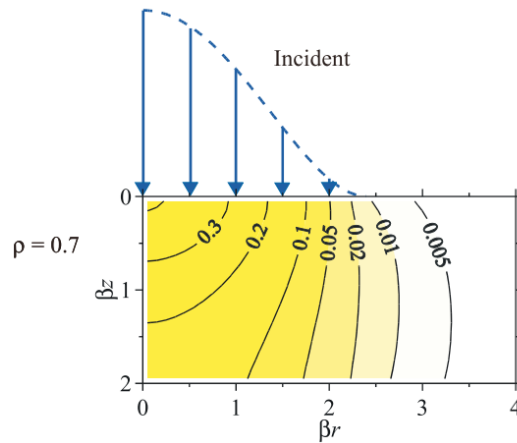


Figure 2.6: Normalised energy deposited in the powder layer with an optical thickness $\lambda = 2$ using the model proposed by Gusarov et al. [24]

An additional means for modelling the interaction of the powder with the laser is the use of raytracing. Raytracing involves tracing the path of rays

emitted from a source and interacting with surfaces according to Maxwell's equations. Depending on the material surface and the ray path, it may be absorbed, reflected or transmitted, aiming to replicate the physical behaviour of the powder bed. Raytracing has been used in the simulation of stationary laser welding to determine the mechanism of keyhole formation and the stability of the process [35]. Raytracing has been incorporated into two selective laser sintering (SLS) models for determining the penetration of different laser types into the powder bed [25, 36]. Boley et al. performed calculations on random Gaussian and bi-modal powder beds obtained from rain models to determine the absolute absorption coefficient for different metals [37]. They observed a significant increase in absorption over flat surfaces due to the scattering behaviour in powder discussed by Gusarov [32]. Additionally, the absorptance could be changed by altering the powder morphology. Through optimisation of the morphology of the powder bed, they obtained two-fold increase in absorptivity for highly reflective materials such as gold and silver. Boley et al. noted that the non-uniform energy absorption due to the stochastic nature of the powder distribution and morphology could be a cause of instabilities in the melt pool [37].

2.3.2 Effective thermal heat transfer within powder mediums

Bulk conduction between the substrate, melt pool and the surrounding powder occurs according to the thermal diffusivity of the materials. This effect influences the size and geometry of the melt pool created. The high thermal conductivity of some metals (e.g. copper, aluminium, gold) increases the dissipation of heat from the melt pool into surrounding solid regions and as a result makes the melt pool relatively small. For low thermal conductivity materials, more heat is retained within the melt pool because of the slow dissipation of heat into the solid region resulting in relatively large melt pools [38].

The thermal conduction in a solid substrate can be readily found. The temperature dependent thermal conductivity $k(T)$ for homogeneous metals in both solid and liquid states can be calculated from the electrical conductivity σ_{cond} of the metal using the *Wiedemann–Franz* law, defined as

$$\frac{k}{\sigma_{cond}} = LT \quad (2.14)$$

where L is the Lorentz number, which remains generally constant for most metals up to high temperatures. Alternatively, steady-state or transient experimental measurements such as a laser flash analysis may be used to find the temperature dependent thermal conductivity.

The thermal properties of the powder are dependent on many parameters

including the packing factor f_p , powder morphology, powder distribution and the constituent material including the resident gas insides the pores. The prediction of the effective thermal conductivity of powders, k_e , was first established by Maxwell [36], assuming randomly packed spheres in a continuous medium

$$\frac{k_e}{k_g} = \left(1 - 2f_p \frac{1 - k_s/k_g}{2 + k_s/k_g}\right) / \left(1 + f_p \frac{1 - k_s/k_g}{2 + k_s/k_g}\right), \quad (2.15)$$

$$\lim_{\frac{k_s}{k_g} \rightarrow \infty} \frac{k_e}{k_g} = \frac{1 + 2f_p}{1 - f_p},$$

with the thermal conductivities of the discrete phase k_s and continuous phase k_g in the medium. This model is only suitable for low packing factors because the model neglect thermal interaction between the discrete phases. In contrast, the model proposed by Bruggeman [39] takes into account these interactions giving

$$1 - f_p = \frac{k_s - k_e}{k_s - k_g} \sqrt[3]{\frac{k_g}{k_e}}, \quad (2.16)$$

$$\lim_{\frac{k_s}{k_g} \rightarrow \infty} \frac{k_e}{k_g} = \frac{1}{(1 - f_p)^3}.$$

Other models have been proposed to improve the accuracy at higher packing factors [40, 41]. However, such models are suitable only at room temperature and fail to account for the high temperatures experienced during SLM where the radiative conductivity, k_r , becomes significant due to the Stefan-Boltzmann law, where $q_{rad} \propto T^4$.

Various studies have proposed models for the effective conductivity in powders, such as the Yagi-Kunii [42] and Zehner-Schlünder [43] models. The latter model only considered conductive terms but Sih and Barlow [44] made further corrections with the additional Damköler's radiation term to give

$$\frac{k_e}{k_g} = (1 - \sqrt{1 - f_p}) \left(1 + \frac{f_p}{k_r} k_s\right) + \sqrt{1 - f_p} \times \dots$$

$$\left[(1 - \phi) \left(\frac{2}{1 - \frac{Bk_g}{k_s}} \left(\frac{B}{(1 - \frac{Bk_g}{k_s})^2} (1 - \frac{k_g}{k_s}) \ln \left(\frac{k_s}{Bk_g} \right) - \frac{B+1}{2} - \frac{B-1}{1 - \frac{Bk_g}{k_s}} \right) + \frac{k_r}{k_g} \right) + \phi \frac{k_s}{k_g} \right] \quad (2.17)$$

where k_r is the thermal conductivity due to radiation calculated from Damköler's equation 2.19, ϕ is the flattened surface fraction of particle in-contact, and B is the deformation parameter for particle which may be calculated from

$$r^2 + \left(\frac{z}{B - (B-1)z} \right)^2 = 1, \quad (2.18)$$

with the radius r and the height z , and parameter B defining the cylindrical shape. The following conditions define the particle shape: $B = 0$ represents the Z -axis, $B > 0$ is a barrel like shape and $B = 1$ is a sphere. The thermal conductivity term k_r due to radiation is calculated from the Damköler equation as follows

$$k_r \Delta T = \xi D_p \varepsilon_{em} \sigma_b (T^4 - T_0^4), \quad (2.19)$$

$$k_r \approx 4\xi D_p \varepsilon_{em} \sigma_b T^3 \quad (2.20)$$

where ξ is the area fraction occupied by canals per unit area, D_p is the powder particle diameter, ε_{em} is the emissivity, and σ_b is the Stefan-Boltzmann constant. An alternative definition for k_r exists dependent on the extinction coefficient β_{ex} , which is estimated by the Rosseland term [43], and is approximated as

$$k_r = \frac{16}{3} \frac{\sigma_b T^3}{\beta_{ex}}, \quad (2.21)$$

where β_{ex} is the extinction coefficient in a powder medium determined by the power-void fraction f_p ,

$$\beta_{ex} = \frac{3}{2} \frac{1 - f_p}{f_p} \frac{1}{D_p}. \quad (2.22)$$

The Zehner-Schlünder model was used in laser melting of a metal and ceramic powder bed by Dai and Shaw [44] who assumed perfect spheres ($B = 1$), the view factor $F = 1/3$, and no flattening of contact surfaces ($\phi = 0$).

Another more recent analytical model proposed by Gusarov and Kovalev [32] exists for the thermal conductivity value of powder by considering the particles as a network of thermal resistances, resulting in the relation

$$\frac{k_e}{k_g} = \frac{f_p N}{2} \left[\frac{1}{2} \ln(1 + L) + \ln(1 + \sqrt{L}) + \frac{1}{1 + \sqrt{L}} - 1 \right], \quad (2.23)$$

where N is the mean coordination number and the parameter L is defined as

$$L = \frac{\gamma_g + 1}{9\gamma_g - 5} \frac{3}{4\sqrt{\pi}Kn}, \quad (2.24)$$

with the adiabatic exponent of the gas γ_g . The definition of the Knudsen number Kn is stated as

$$Kn = \frac{l}{D_p} \quad (2.25)$$

which is defined by the mean free path length l within the gas pore

$$l = \frac{\gamma_g - 1}{9\gamma_g - 5} \frac{k_g}{p_{pore}} \sqrt{\frac{M_g T}{2k_b}}, \quad (2.26)$$

where p_{pore} is the pressure of the gas pore, M_g is the molecular mass of the gas and k_b is the Boltzmann constant.

The effective thermal conductivity of the powder medium depends on the particle size and the gas pressure and may be evaluated at different orders of scale. Gusarov and Smurov acknowledged there was a discrepancy with experimental data because the model cannot reflect the non-uniform powder diameter distribution and non-uniform geometries of powder manufactured for use in powder-bed fusion applications [32].

Experimental data for the thermal conductivity of different powders at high temperature remains scarce, however, a doctoral thesis work has predicted the thermal conductivity of stock gas atomised powder (GAP) and plasma rotating electrode processed (PREP) Ti-6Al-4V powder for EBM [45]. A linear relationship between thermal conductivity and temperature up to ~ 700 °C was apparent, but the thermal conductivity become non-linear and steadily increased above this temperature.

2.3.3 Sintering kinetics of particles

The absorption and conversion of energy within the powder raises the temperature of the medium. Upon reaching a high enough temperature sintering will occur. The process of sintering is generally defined as the coalescence of two particles, as illustrated in Figure 2.8, which can occur at the order of milliseconds [46]. The principle sintering behaviour is characterised into two phases. Through solid state diffusion, sintering necks first form between adjacent particles. In the second phase, the increased connectivity provides an additional mechanism for heat transfer to occur in the powder, thereby accelerating the sintering mechanism.

Klocke et al. performed experimental measurements the sintering of two stainless steel particles at various powers [45]. In their study, when using a laser power > 125 W, the coalesce time was found to be approximately 2 ms. Additionally, dimensional analysis and numerical simulation by Attar et al. [46] showed the interaction time to be of the same order in powder-bed fusion processes, which is further discussed in Section 2.6.2.

Solid state sintering is driven by three key mechanisms: surface and volume diffusion, vapour transport and grain boundary diffusion, with the latter present at lower homologous temperatures [47, 48]. The sintering kinetics were observed

to occur at a homologous temperature between $0.7 < T/T_m < 1$ [48]. It was reported that surface diffusion occurs at lower particle sizes and volume diffusion at large particle sizes, accounting for the large necking between adjacent particles [47].

A variety of theories for predicting the relative neck radius uniting two sintering particles have been considered. Kuczynski's theory [49], determined the change in neck radius with time,

$$\frac{dx}{dt} = \frac{1}{t_o x^4} \quad (2.27)$$

with the characteristic time

$$t_o = \frac{N_o k_b T R^3}{8 \gamma_e D_s}, \quad (2.28)$$

where N_o is the number density of solid material, R is the particle radius, γ_e is the surface free energy and D_s is the self-diffusion coefficient. Another model was proposed by Frenkel [50]

$$\left(\frac{x}{R}\right)^2 = \frac{3}{2} \left(\frac{\gamma t}{R \eta}\right), \quad (2.29)$$

where γ is the particle surface tension, η is the thermally activated particle viscosity and t is the time of sintering. Studies of sintering behaviour in selective laser melting remain largely unexplored, possibly because of the instantaneous melting that occurs in the process.

2.3.4 Thermo-fluid physics

Upon the formation of a melt pool, the high thermal gradients and energy input create a highly complex set of thermo-fluid physical-phenomena, providing a great challenge for researchers to identify and understand. The melt pool is subject to a variety of forces acting upon it including buoyancy, gravity, surface tension and capillary forces. The interplay between these forces determine the stability, hence, the final geometry of the overall melt-track formed. At these length and time-scales, dimensional analysis, as discussed in Section 2.6.3, indicates that the fluid flow is largely dominated by surface tension effects, rather than buoyancy and gravity.

The surface tension has a significant influence on the formation of the melt pool. The high surface tension and wettability of molten metals facilitate the formation of smooth surfaces under favourable conditions, permitting the creation of continuous elongated cylindrical tracks, as shown in Figure 2.9. Yadroitsev et al. showed experimentally that elongated melt pools with high

aspect ratios were susceptible to instability, due to capillary forces [51].

Plateau-Rayleigh instability analysis of an infinitely long cylinder, as shown in Figure 2.10(a), informs that a cylinder is stable if the axial harmonic disturbances of its radius with wavelengths λ are less than its circumference [51]. The criterion is satisfied provided the following condition is met

$$\frac{\pi D}{L} \geq 1, \quad (2.30)$$

where D is the track diameter and L is the track length [52]. In the case of SLM, the melt pool track has a finite length, and features contact with the substrate, at a given contact angle ϕ , as shown in Figure 2.10(a). Gusarov et al. [24] determined the stability criterion to be

$$\frac{\pi D}{L} > \sqrt{2} \sqrt{\frac{\phi(1 + 2\cos(2\phi)) - \sin(2\phi)}{2\phi(2 + \cos(2\phi)) - 3\sin(2\phi)}}. \quad (2.31)$$

It was concluded that stability could be achieved for any wavelength, provided the contact angle $\phi < \frac{\pi}{2}$ - equivalent to a half a cylinder, as shown in Figure 2.10(b).

Understanding the previous behaviour would further explain the balling phenomenon discussed by Gusarov et al. [31]. Fundamentally, surface tension drives the melt pool to minimise the surface energy towards its lowest energy state - a sphere. During this deformation, the track melt pool begins to recede from the substrate, as shown in Figure 2.11(b). Depending on the resultant track geometry, detachment can occur, resulting in the formation of a ball.

The balling effect occurs with high aspect ratio melt pool geometry; i.e. the melt pool becomes larger than equivalent sphere of the same volume, which is observed typically with high aspect ratio melt pools [53]. Tolocko et al. investigated the mechanisms for the balling effect, and showed this instability is dependent on the laser parameters chosen [53]. The balling affect can be avoided by limiting excess power into the powder and controlling the laser scan speeds to ensure a stable melt pool shape is achieved [32, 54]. A study by Yadroitsev and Gusarov intuitively found the penetration into the substrate was linearly dependent on the scanning velocity, therefore the contact angle and aspect ratio of the melt pool could be controlled [51]. Their investigation resulted in a process map shown in Figure 2.9, and it was highlighted that re-melting of the substrate was crucial for obtaining stability during the process. Instability at higher powers was attributed to fluidic effects created by Marangoni flow, and the key-hole phenomena both further discussed in Sections 2.3.5 and 2.3.7.

2.3.5 The effects of Marangoni flow

The second consequence of surface tension forces are within the melt pool itself, namely surface tension driven Marangoni convective flow. Marangoni flow is induced by a shear force τ acting parallel to the melt pool's free-surface, created by a surface tension gradient $\frac{\partial\gamma}{\partial T}$ induced by the temperature gradient. Marangoni forces dominate the flow in the melt pool, and have a strong effect on the melt pool dimensions and surface temperature depending on the flow direction and magnitude of the convection. The shear force may be derived using the chain rule assuming a radial coordinate system around the melt pool centre [57],

$$\tau = -\mu \frac{\partial u}{\partial z} = -\mu \frac{\partial\gamma}{\partial T} \frac{\partial T}{\partial r}, \quad (2.32)$$

where μ is the dynamic viscosity of the molten metal. The strength and direction of the flows can be characterised by the non-dimensional Marangoni number Ma , stated as

$$Ma = \frac{\partial\gamma}{\partial T} \frac{\partial T}{\partial r} \frac{L}{2\mu\alpha}, \quad (2.33)$$

where L is the chosen characteristic length [55]. The Marangoni number typically varies between 10^3 and 10^6 , with its sign indicating the direction of the convective flows. The direction of the Marangoni force, and consequently recirculation behaviour, changes based on the surface tension gradient $\partial\gamma/\partial T$. Characteristic melt pool shapes as a result of Marangoni flow are shown in Figure 2.12. A negative surface tension gradient ($\partial\gamma/\partial T < 0$) results in a shallow melt pool and a positive surface tension gradient ($\partial\gamma/\partial T > 0$) results in narrow deeper melt pool with.

A positive surface gradient induces an inward flow, with heat energy transferred downwards towards the solid-liquid interface at the bottom of the melt pool, resulting in preferentially greater melting downwards rather than at the corners [55]. This effect results in greater penetration into the medium. The relative importance of convective over conductive heat transfer within the melt pool can be characterised according to the Peclet number,

$$Pe = \frac{u\rho c_p L}{k}, \quad (2.34)$$

where u is the characteristic fluid velocity, ρ is the fluid density, c_p the specific heat capacity, L is the chosen characteristic length, and k is the thermal conductivity of the fluid. Flow within the melt pool varies, and the high velocity region near the melt pool surface will have a higher Peclet number, compared to the interior regions and the 'mushy-zone' at the solid-liquid interface [38]. Marangoni flow

tends to decrease with increasing temperature but the inclusion of surface active elements have a profound influence and conversely increase its strength with temperature [55]. Zhao and Richardson [56, 57] proposed the following expression for the influence of oxygen and temperature on the surface gradient

$$\gamma = \gamma_m^0 - A(T - T_m) - RT\Gamma_s \ln \left[1 + k_i a_i \exp \left\{ -\frac{\delta H^0}{R_0 T} \right\} \right], \quad (2.35)$$

where A [N/mK] is the negative temperature coefficient of surface tension ($\partial\gamma/\partial T$), Γ_s [Mol/m²] is the surface excess concentration at saturation, k_i is a constant related to the entropy of segregation of the alloy species i , a_i is the activity of species i in the alloy solution, and H^0 [J/Mol] is the standard heat of adsorption of the alloy system. Their experimental analysis of laser welding of pure iron in conjunction with their model, showed that even at low concentrations of oxygen between 100-1000 PPM, positive surface tension could be experienced at lower temperatures. It further shows the complexity and subtle effects of parameters on the physics at the *micro*-scale within the process.

Gas entrapment during SLM is a known problem [54]. Gas species resident in powder medium coalesce and cannot escape from the melt pool surface because the Marangoni convection within the fluid is too great. Upon solidification, gas is trapped leaving an undesirable void or pore with characteristic spherical shape, as shown in Figure 2.13, contributing to undesirable porosity [58]. The source of these gases are

- Trapped gas resident in powder pores
- Evaporation of residual chemical alloying elements with high vapour pressure P_i
- Chemical reactions

The residual pores left through gas entrapment are an undesirable manufacturing artefact which affects the mechanical properties, especially the fatigue performance, as discussed in Section 2.5.2.

2.3.6 Vaporisation

Owing to the laser intensity in the SLM process, evaporation of metallic elements will occur at the surface of the melt pool, and this contributes greatly to the complex phenomena occurring [16, 33]. Given enough energy, a plume of metal vapour can form in the chamber, and then condense on the lens attenuating the laser beam, degraded performance, especially for builds of long duration

[16]. Evaporation is a probabilistic process and is a function of the equilibrium vapour pressure p_s with an Arrhenius relationship described by

$$p_{s,i} = p_0 \exp \left\{ -\frac{\Delta G}{R_0 T} \right\} = p_0 \exp \left\{ \frac{L_{evap}(T - T_B)}{R_0(T - T_B)} \right\}, \quad (2.36)$$

where ΔG is the Gibbs free energy, p_0 is the ambient pressure, L_{evap} is the latent heat of vaporisation, T_B is the boiling point temperature, and R_0 is the universal gas constant. The partial pressure calculated in equation 2.36 can then be used to calculate the rate of evaporation J_i using the Langmuir equation;

$$J_i = \frac{M_i p_{s,i}}{\sqrt{2\pi M_i R_0 T}}, \quad (2.37)$$

which is dependent on the atomic mass M_i of the alloying species and their partial vapour pressure p_i . The model may be further improved by summing the constituent components of an alloy instead of the bulk as some alloying species may have high partial pressures [59, 60],

$$J_i = \frac{\gamma_i p_{s,i}^0 C_i^s}{\rho_m \sqrt{2\pi M_i R_0 T}}, \quad (2.38)$$

where γ_i is the activity coefficient, p_i^0 is the vapour pressure of the alloy, C_i^s is the volumetric concentration at the surface, and ρ_m is the molar density of the alloy. Furthermore, an estimate of the overall surface heat loss contribution q_{loss} is

$$q_{loss} = \sum J_i L_{evap,i}. \quad (2.39)$$

The effect of latent heat of vaporisation, L_{evap} , is far greater in strength compared to the latent heat of fusion, L_{fuse} , and limits the maximum surface temperature of the melt pool [33, 55]. There is a preferential evaporation of each metal component in metal alloys [61] and Juechter et al. [62] showed that the final alloy composition of Ti-6Al-4V in a part could be changed by altering the scan speeds when processing using EBM. In their study, there was preferential evaporation of aluminium, owing to its relatively lower boiling temperature ($T_B = 2470$ °C), and the concentration of this component was effectively found to increase with the line energy density, E_L (equation 2.3), as predicted. Therefore, it was recommended that overheating should be avoided to prevent changes of the chemical composition in the melt pool, and the final built part.

The rapid process of vaporisation of molten material results in the generation of a recoil pressure p_r on the melt pool, which has the effect of flattening the melt pool and pushing material in the lateral direction [33]. It also provides the

driving force behind the many thermo-fluid phenomena leading to instabilities in the process: such as keyhole and laser spatter formation, and the creation denudation zones.

2.3.7 Keyhole and spatter formation

The evaporation of alloying constituents in the melt pool, has the potential to form a keyhole pore: a narrow vapour cavity [38], with the potential to trap un-melted powders, as shown in Figure 2.14.

In laser welding, keyhole formation is desirable, and can improve the energy efficiency caused by reflection and scattering inside the cavity, enabling deeper penetration of the weld during the joining processes. However, keyhole formation is detrimental to stability in powder-bed fusion process. Expansion of gas and plasma within the melt pool cavity could further increase the instability of the melt pool [63]. Additionally, due to high energy density of the laser, metal vapour can become excited and ionise resulting in the formation of a plasma that can adversely affect the attenuation of the laser beam [16].

The recoil pressure, p_r , produced by the ablated material exerts a force on the melt pool. It is calculated from kinetic theory and is approximately related to the saturation vapour pressure, p_s [64]:

$$p_r \approx 0.56p_s, \quad (2.40)$$

with the saturation vapour pressure, p_s , described by;

$$p_r > \frac{\gamma}{r_d}, \quad (2.41)$$

where γ is the surface tension [65]. Given the small laser spot size, between 10-100 μm , material ejection occurs at the material boiling point T_B . Using a combination of the laser parameters, and material properties involved in the process, King et al. [65] derived an estimate of the threshold speed v_t for keyhole formation, stated as

$$v_t = \frac{4\alpha}{r_d} \left[\frac{\sqrt{\pi}kT_b}{AIr_d} \right]^{-2} \quad (2.42)$$

with the absorptivity A , and the laser intensity $I = P/2\pi r_d^2$. The keyhole generated is in equilibrium between forces opening the cavity, and those forces causing collapse (gravity and surface tension) [66]. Fluctuation forces can eventually lead to self-collapse, resulting in the undesirable formation of the keyhole pores often exhibited in SLM.

It has been identified that keyhole formation commonly occurs along the

border of parts [20, 67]. This can be attributed to the acceleration of the galvo-mirrors not letting the laser reach its nominal velocity [20], and instability of the keyhole after the laser has switched off at the end of the scan vector [67]. Khairallah et al. recommended ramping down the laser power, to provide enough time for surface tension to smooth the surface, however, current SLM machines do not have this facility [67]. Kempen [20] recommended the use of ‘skywriting’ or ‘ghost-vectors’ at the beginning of scan vectors, as shown in Figure 2.15. During the ghost vector, the laser is turned off, but provides the galvo-mirrors enough time to accelerate to their nominal velocities.

Laser spatter consist of large particles ejected at high speeds from the melt pool, and are the source of ‘visible sparks’ seen within the chamber [68]. Simonelli et al. analysed the ejecta, and observed regardless of the material processed, the creation of spherical particles exceeding the pre-alloyed particle sizes[16]. Laser spatter that lands on the powder-bed can lead to disastrous consequences. Their large size prevents complete homogeneous melting when scanned by the laser because of the lack of energy available, given the laser parameters are tuned for the particle distribution size of the powder feed-stock. Additionally, large particles prevent correct spreading of powder in the next layer; creating a trail in the direction of the power re-coating mechanism [69].

According to Khairallah et al. spatter is created by metal vapour plumes creating a pressure forces acting on the melt pool [67]. Owing to the key-hole depression, the advancing front of the melt pool begins to accumulates liquid like a ‘bow-wave’. There is a tendency for the liquid to become elongated and pinch caused by high surface tension forces. Eventually this breaks away, forming spheres that are ejected at high speed, ~ 10 m/s, due to pressure [70]. This has been observed in numerical simulations [67] and is in agreement with high speed video recordings by Mathews et al. [70]. Their video footage showed unheated particles were ejected in a rearward direction at ~ 2 m/s. Particles formed at the front and sides of the melt pool (observed by their high incandescence) were ejected forward at 10 m/s with particles sizes approximately equal to the width of the track, agreeing with the measured particles sizes observed by Simonelli et al. [16]. They also suggested that the vaporisation generated above the melt pool either expands or narrows into a jet depending on the ambient pressure. This jet can provide significant vertical momentum, up to 10 m/s, causing particles to escape the melt pool.

2.3.8 Denudation of powder

Denudation, or the absence of powder particles adjacent to the scan track, is shown in Figure 2.16, and is characterised by an observable light halo surrounding

the scan [22]. Denudation is suspected to be the cause of elongated longitudinal pores being generated parallel to scan tracks [71]. This porosity formation is often encountered when the scan spacing is small enough that a neighbouring scan track lies completely in the first track's denudation zone [20, 72].

Numerical modelling carried out by Khairallah et al. showed that as a result of recoil pressure acting upon the surface of the melt pool overcoming surface tension, the liquid is accelerated away from the centre [67]. This results in the creation of depressions and spatter. Marangoni flow aids cooling in the depression and create additional denudation regions.

Mathews et al. [70] acknowledged that their colleagues' computational model [73] cannot alone fully resolve the causes of denudation due to the lack of two phases needed to account for the complex flow within the build chamber. Their experimental work used optical micrographs supported by high speed imaging, as shown in Figure 2.17, to understand the role of gas flow within the chamber.

The denudation widths, and additionally track height, were found to be heavily dependent on the gas pressure within the chamber, as shown in Figure 2.18. They concluded that the dominant driving force for denudation was the entrainment of surrounding gas flow, due to the Bernoulli effect created by the intensive vaporisation above the melt pool. Two opposing regimes are evident, dependant on the ambient pressure in the chamber, which are affected by the Knudsen number, Kn , defined previously in equation 2.25. At high pressures ($Kn < 1$), a metal vapour jet is formed creating a low pressure zone due to the Bernoulli effect, as shown in Figure 2.19(a). This induces particles to be drawn into the melt pool, increasing consolidation or alternatively being ejected upwards or to the rear. At low pressures ($Kn > 1$), metal vapour can freely expand outwards pushing particles away, as shown in Figure 2.19(b), creating a denudation zone adjacent to the melt track.

2.3.9 Summary

The turbulent and chaotic behaviour of the SLM process zone at the micro-scale, in particular the thermo-fluidic physics of the melt pool and with the surrounding powder-bed is a highly stochastic process. The behaviour is extremely sensitive to the input parameters, and small changes can have a profound effect on the stability of the melt pool. Fundamentally these instabilities are caused by vaporisation and the surface tension effects of Marangoni flow, which result in the formation of laser spatter, keyholes pores, and denudation zones, which all contribute to part level porosity.

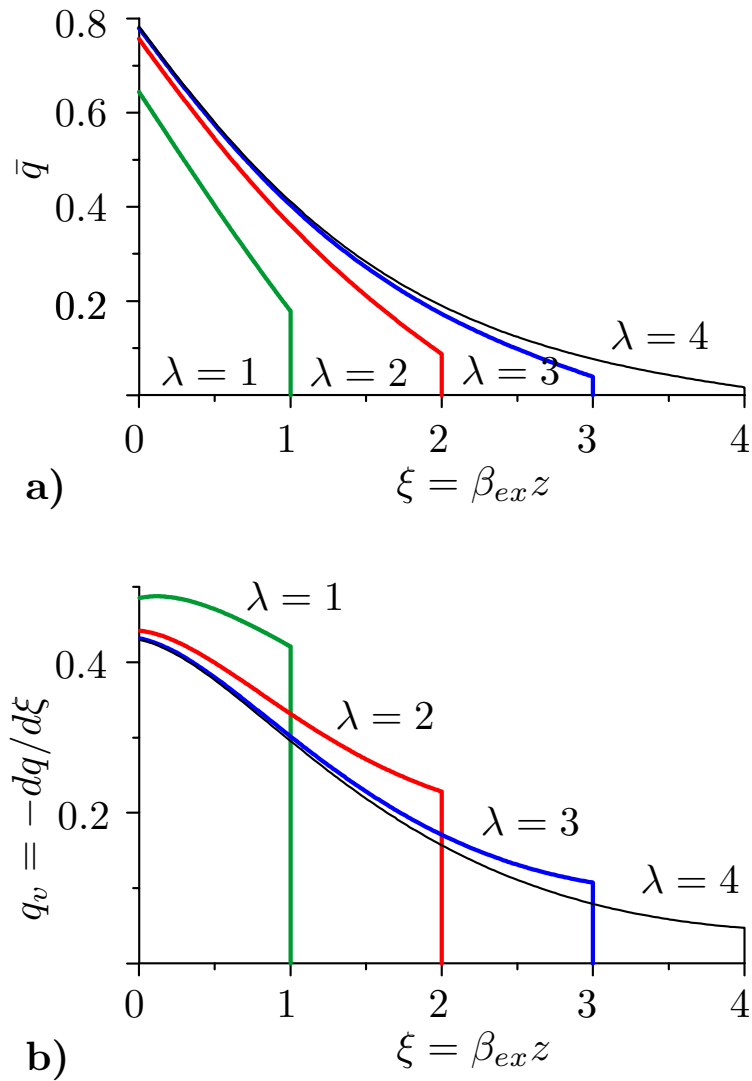


Figure 2.7: Profiles showing the effect of the optical thickness λ , on a) the normalised power density \bar{q} and b) the volumetric heat source q_v against the dimensionless depth ξ' in the model proposed by Gusarov et al. [32]

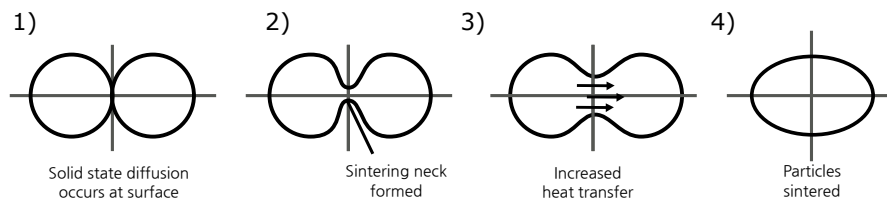


Figure 2.8: Illustration showing the coalescence of two particles undergoing sintering

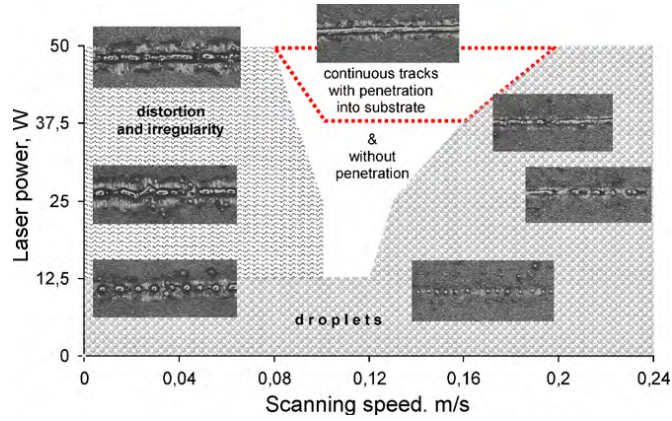


Figure 2.9: Single track process map of Stainless Steel 316L with a layer thickness of $50\ \mu\text{m}$ taken from a study performed by Yadroitsev and Gusarov [51]

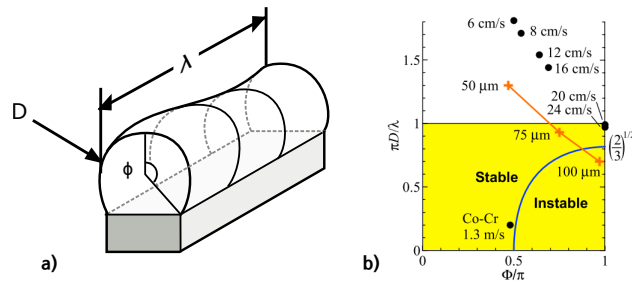


Figure 2.10: a) Illustration showing the capillary stability of a cylinder track on a solid substrate, and b) diagram showing theoretical stability plotted against experiments by Yadroitsev et al. [51]

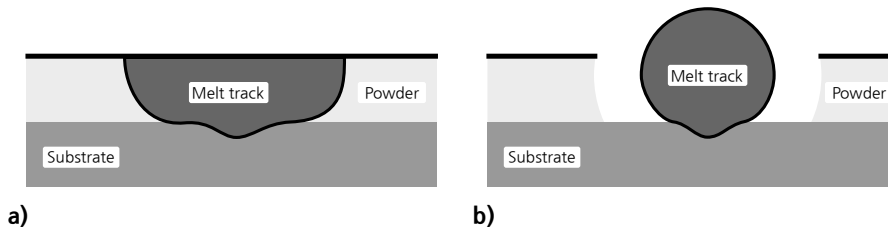


Figure 2.11: Illustration showing the role of surface tension affecting the track geometry upon consolidation when a) just melted and b) after minimising the surface energy of the melt track surface.

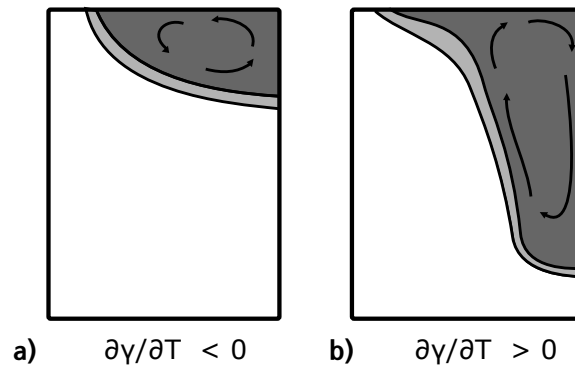


Figure 2.12: Illustration showing the effect of the surface tension gradient on the shape of the melt pool: a) a negative gradient forms a shallow profile and b) a positive gradient produces a narrow deep depression.

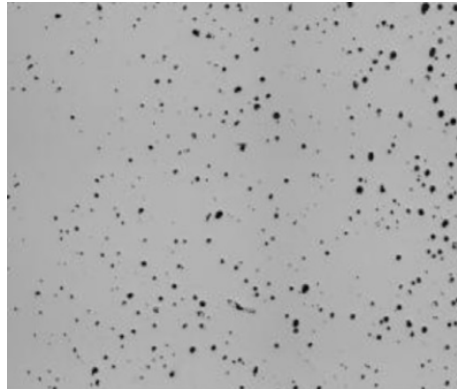


Figure 2.13: Microscopy image of spherical porosity observed in AlSi10Mg processed using SLM by Aboulkhair et al. [58]

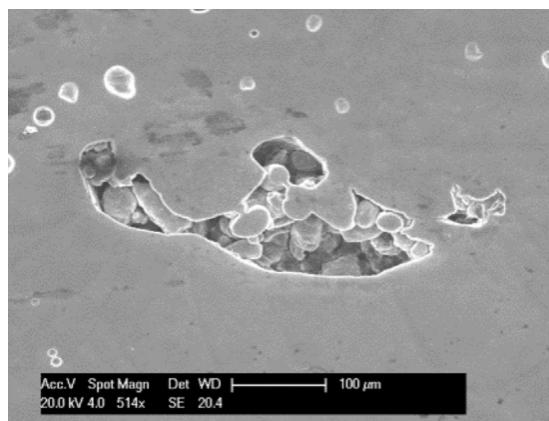


Figure 2.14: scanned electron microscopy (SEM) image of keyhole pore formation enclosing un-melted powders when processing AlSi10Mg in a study by Aboulkhair et al. [58]

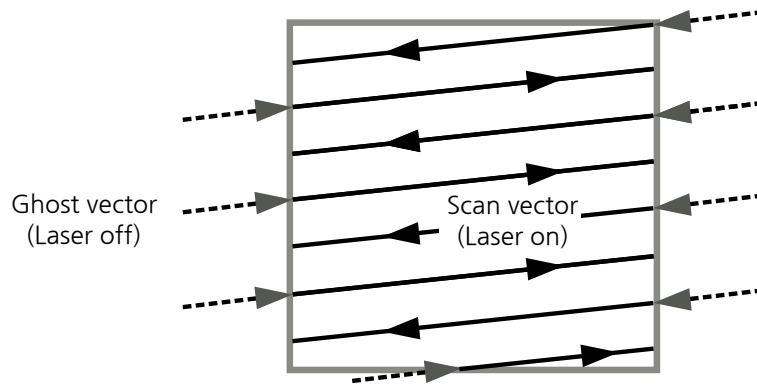


Figure 2.15: Illustration of the ‘sky-writing’ technique using ‘ghost’ vectors to assist accelerating the galvo-mirrors when scanning in SLM

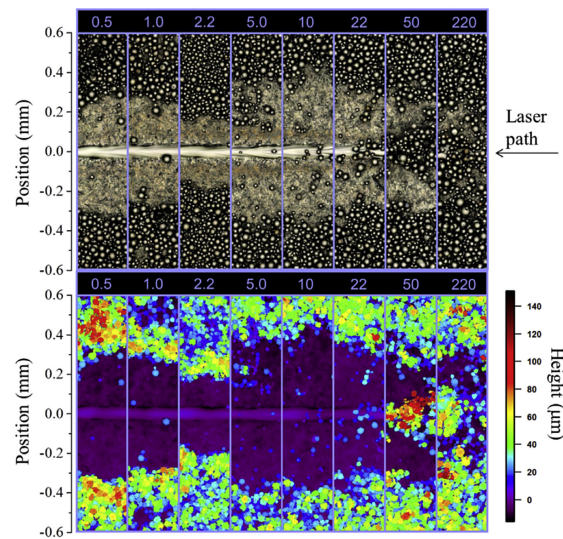


Figure 2.16: Optical micrograph (top) and height map (bottom) showing the powder denudation zone surrounding a single scan track. Taken from Matthews et al. [70]

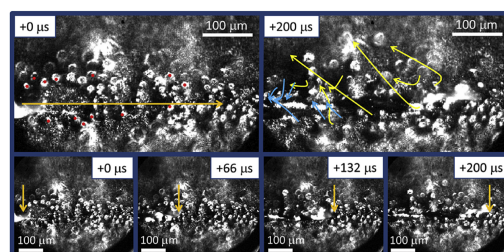


Figure 2.17: High-speed imaging showing the track progression and movement of particles during scanning. Taken from Matthews et al. [70]

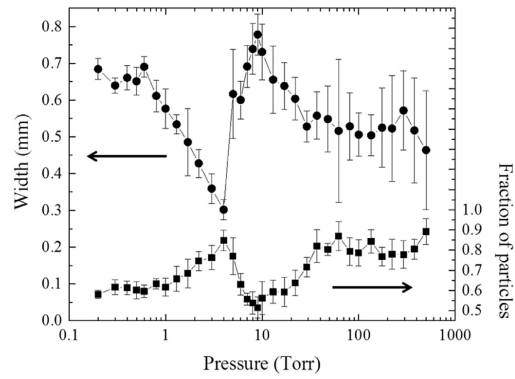


Figure 2.18: Graph showing the width of the denudation zone as a function of the ambient argon pressure over the surface. Taken from Matthews et al. [70]

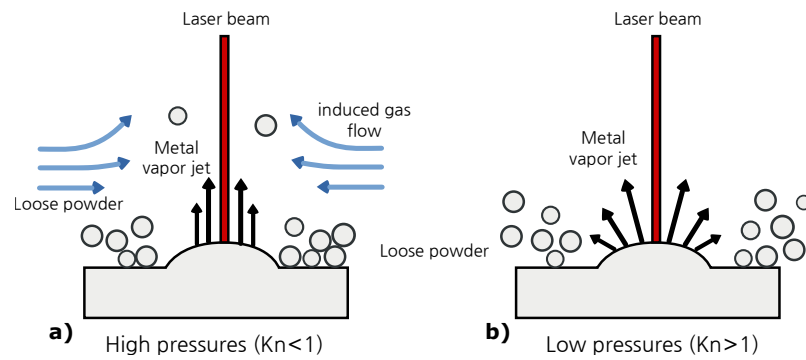


Figure 2.19: Illustration showing the effect of surface pressure as a result of the Bernoulli effect on the movement of powder particles near the laser interaction zone. Effect of a) high pressure ($Kn < 1$) and b) low pressure ($Kn > 1$)

2.4 Residual stress in selective laser melting

Probably the most significant concern to industry in the use of SLM for structural parts is the ability to predict and mitigate the residual stresses generated in parts during manufacture. These are the primary cause of build failure, and indirectly, they impose severe design restrictions and reduce the reliability of components, driving up costs, which impede the adoption of SLM in industry.

In metals, residual stresses develop from the inhomogeneous plastic deformation created by thermal, mechanical and chemical manufacturing methods. Residual stresses are not necessarily detrimental to part quality, and can be exploited to enhance the performance of a component. In particular, compressive stresses can be introduced at the surface to improve the mechanical and physical performance. For example, high strength tempered glass is formed by quenching the outer surface at high temperature, which creates compressive stresses at the surface and tensile stresses at the interior [74]. Shot peening is used to plastically deform the surface of metals inducing compressive stresses in the surface layers. This improves the surface hardness, wear resistance, and can effectively improve fatigue performance by increasing resistance to the nucleation and propagation of fatigue cracks [75]. Thermo-chemical treatment, such as surface nitriding, is used in carbon and alloyed steels to improve the surface properties for similar benefits. Chemical diffusion of nitrogen introduces nitrides into the metal matrix in a thin surface layer, (0.5 – 7) mm, improving hardness and mechanical properties, but additionally introduces compressive stresses [76]. Unfortunately, in manufacturing processes such as welding and SLM, residual stress is often detrimental.

Multi-length scales are associated with residual stresses [77]. Type I macro stresses vary largely across the part, and generally result in large part deformation. Type II and III occur at a much smaller scale, occurring at atomic and micro-structural levels but are largely ignored due to the higher resolution needed to measure these experimentally. Nevertheless, the smaller scale stresses, can have a significant impact on the ‘weldability’ of some metal alloys, further discussed in Section 2.4.3.

2.4.1 Mechanisms for the generation of residual stress

Laser based manufacturing processes are extremely susceptible to the generation of residual stresses owing to the highly localised heating. The primary mechanism for the creation of residual stress is the temperature gradient mechanism (TGM) [77, 78]. High temperature gradients and non-uniform thermal expansions and contractions in the heat affected zone (HAZ) result in the formation of residual stresses within the finished component, as shown in Figure 2.20. These are

created by incompatible thermal-strains generated during thermal expansion and contraction. Underneath the melt pool, tensile stresses are created due to restricted thermal shrinkage. Previously colder material surrounding this is heated up rapidly and thermally expanding, which results in compressive stresses.

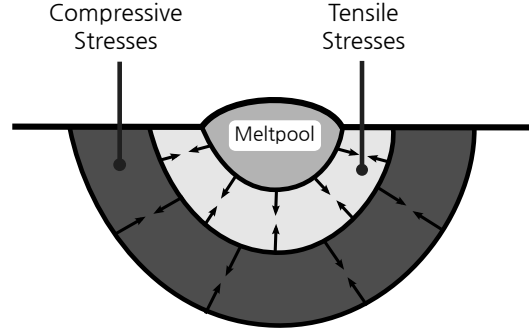


Figure 2.20: Illustration showing the temperature gradient mechanism for the generation of residual stresses in the heat affected zone

At high temperatures, plastic deformation also occurs through yielding because the yield strength, σ_y , invariably decreases with temperature. After cooling, these transient thermal stresses achieve an equilibrium state, leaving residual stresses within the part [74, 79].

The ability of a material to resist cracking under high temperature gradients is dependent on the ultimate tensile strength of the material σ_{UTS} . An indication of this is measured by the thermal shock resistance τ in equation 2.43, and is observed to be the ratio between material strength and the ability to generate residual stresses [74].

$$\tau = \frac{\sigma_{UTS}k}{E\alpha_{CTE}} \quad (2.43)$$

2.4.2 Consequences of residual stress in SLM

Residual stresses unmanaged, have the immediate consequence of causing failure during manufacture, as shown in Figure 2.21. Unlike laser sintering and to some extent EBM systems, parts produced by SLM require additional support structures to prevent build failure. Support structures constrain the part to restrict ‘curling’ or distortion during the build to prevent collisions with the powder re-coating mechanism. In extreme cases, high residual stresses cause the material to fail and rupture, allowing the part to freely deform and again collide with the re-coating mechanism. Other undesirable artefacts of residual stress at post-build are distortion, increased susceptibility to crack formation



Figure 2.21: Failure during manufacturing of a Ti-6Al-4V component caused by the build-up of residual stress

and reduced fatigue performance, as discussed in Section 2.5.2.

Ultimately, some part distortion and residual stress development are inevitable even with robust thick supports since bending is possible within the build plate. Complete removal of residual stresses, therefore, requires further post processing either by heat treatment to stress relieve the component, or through hot isostatic pressing [23].

2.4.3 Influence of material properties

In theory, materials with a low thermal expansion coefficient α_{CTE} , and low melting temperature T_M should experience a reduction in the residual stresses generated due to a smaller rate of strain accumulation over a smaller temperature range [74]. As previously discussed, reducing thermal gradients experienced in the process can have a profound effect. Materials with a high thermal diffusivity α , such as aluminium, copper and gold, are able to dissipate heat efficiently into the surround material, which effectively reduces the thermal gradients. If sufficiently high, stresses generated will result in yielding, and therefore the material yield strength σ_y limits the maximum stresses generated. The yielding behaviour is highly dependent on the material, especially for high temperature metal alloys. A significant reduction in the yield strength with temperature reduces the extent of the maximum residual stresses generated. However, an investigation of the effect of thermal material properties, namely the specific heat capacity, c_p , and the linear thermal expansion coefficient, α_{CTE} , on the creation of residual stress, failed to reveal any systematic correlations in a previous study [74].

A method to mitigate the need for support structures was proposed Mumtaz et al. [80] by utilising the eutectic point of a zinc alloy (Bi3Zn) to minimise the melt temperature required thereby reducing the direct energy input. This enabled them to build parts without support structures although they did not report the effects of distortion caused by residual stress. This method, however, is considerably limited in the choice of alloys and alloy compositions. A metallurgical factor coexists with residual stresses, and this exasperates the problem depending on the choice of material processed. Some metal alloys, especially nickel super-alloys [81], silicon steels [82] and Waspaloy [83], are particularly susceptible to thermally induced micro-cracking during solidification [84]. To a limited extent, this micro-cracking can be mitigated through process optimisation and scan strategies [81–83]. A study by Tomus et al. [81] suggested that an increase of some alloying elements (Mn, Si, S and C) increased crack susceptibility by reducing the solidification temperature T_S , and that grain boundaries provide the most likely sites for the nucleation and propagation of cracks due to the segregation of minor elements towards these regions.

Harrison et al. [84] performed a design of experiment (DOE) on a nickel super-alloy Hastelloy X, and concluded that the laser power had the greatest influence on crack density, whilst energy density held a stronger relationship with porosity but could not eliminate the presence of micro-cracking. A modified composition of the original alloy with an increase in the proportion of solid solution strengthening elements to the nominal, led to an average reduction in crack density of 65%. The strengthening mechanism allowed small gains in the ultimate tensile strength (UTS), yield strength σ_y , and reduction in ductility at higher temperatures (> 768 °C). They attributed this strengthening effect as the method for reducing the crack density, contrary to the conclusions drawn by Tomus et al. [81].

2.4.4 Influence of laser scan parameters

Experiments to optimise the laser scan parameters for materials, as discussed in Section 2.6, are namely focused on the stability of the melt-track formation in order to obtain high material densities. Thermo-mechanical models of SLM provide an insight into the effect of laser parameters on the build-up of stress. These models provide an opportunity to explore parameters combinations unsuitable for building dense parts. Nevertheless, the effect of laser scan parameters on residual stress remains largely unknown and inconsistent. Vasinonta et al. investigated the effect of laser speed and found temperature gradients decrease with slower scan speeds [85]. Experiments performed by Wu et al. indicated that increasing the laser power and the laser speed increased the length of

the melt pool, and reduced the magnitude of residual stresses, as measured by neutron diffraction [21]. The melt pool length was also shown to increase with laser power also in a model by Vasinonta et al. [85]. The hatch distance was investigated by Pohl et al. who found the distortion measured decreased with an increase in hatch distance [86], however, no further investigations have been done since. It was suggested by Vrancken, that varying the hatch distance could effectively control the accumulation of heat during the layer scan, which may reduce thermal-gradients [87].

A parametric experimental study was performed by Vrancken to study the effect of laser speed, laser power, and layer thickness on the residual stress generated using X-ray diffraction (XRD) measurements [87]. Their results indicated that an increase in the layer thickness increased residual stress and was attributed to less thermal accumulation using larger layer thicknesses. During each scanned layer, heat accumulates in the build volume and substrate, which they note using smaller layer thicknesses having more of pre-heating effect. Also, their results showed that increasing the scan speed elongates the melt pool, which increased the magnitude and anisotropy of residual stress found.

2.4.5 Influence of laser scan strategy

The correct choice of laser scan strategy is critical in generating the desired microstructure [58, 88] and is also known to affect the build-up of residual stress in components [77]. Numerous studies have observed that the largest planar residual stress component is generated parallel to the scan vector and increases with scan vector length [77, 86, 89].

Scan strategies which limit the length of the scan vector such as the checkerboard island or ‘stripe’ scan strategy have the greatest impact on reducing the levels of residual stresses within components. The use of the checkerboard island scan strategy has been shown to be an effective method for reducing the build-up in residual stress, especially in large parts because the maximum length of the scan vectors is restricted to the scan island size or stripe width [77, 90]. This is attributed to the size and geometric independence irrespective of the part, achieved by uniformly rotating scan vectors orthogonally and restricting the length of the scan vectors throughout the part, as shown in Figure 2.4(b). However, it was found that reducing the island size did not further reduce the magnitude of residual stress [87]. The checkerboard island strategy is a very effective strategy for making the scan vectors independent of the part manufactured, since each layer is decomposed into smaller regions.

However, the published work to date has not definitively shown the influence of island scan order on the formation of residual stress. The least heat influence

(LHI) strategy has been stated to reduce residual stress by scanning the islands randomly to minimise the thermal influence between islands. A possible explanation suggested isolated islands are not constrained along their edges and therefore have zero normal stresses along their edges [77]. However, currently there is insufficient evidence to show how, and the extent to which, the island scanning order affects the build-up of residual stress.

Alternative scan strategies have been proposed, such as spiral or helix strategy, whereby contours are offset gradually from the border inwards towards the centre [86]. The scan vector lengths remain substantially long, but the directionality is spread evenly across the layer. Nickel et al. investigated this for a thin sheet experimentally by measuring the distortion of a single square using meander and a spiral scan strategies, and then compared this with a FE model [91]. Using the spiral scan strategy, the stress distribution was symmetrical and more uniform than the normal meander strategy, but the deformation was greater. Qian et al. [92] developed a spiral strategy further for use on more complex components, as shown in Figure 2.22(b). They had success building parts using the spiral scan strategy, whilst the meander scan failed and suffered great deformation, resulting in more failures. The parts built with the spiral strategy suffered less distortion in the both in the Z direction and the XY plane compared to those built using the meander strategy. They suggested that when using the spiral strategy, the bending moment created by the residual stresses was more uniform radially, and therefore parts suffered less distortion.

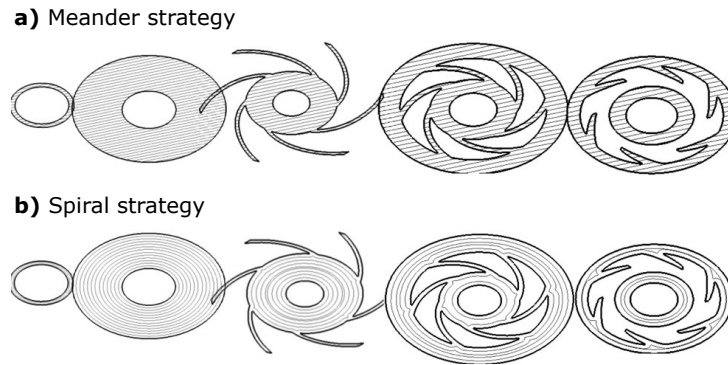


Figure 2.22: Application of a) meander and b) spiral scan strategy used by Qian et al. [95] to build a complex component

The use of fractal based scanning strategies also has been considered. Yang et al. used a fractal scan strategy, as shown in Figure 2.23, for use with SLS [93]. In their method, a Hilbert filling curve was trimmed to the shape boundaries, however, the effectiveness of this strategy was not conclusive. Ma and Bin

performed a thermo-mechanical finite element (FE) simulation of SLM with a fractal Hilbert curve geometry, and compared this with the meander strategy [94]. They reported a symmetrical temperature field and distortion in the final component built. However, the dimensions of the model were not representative of the process, and a coarse mesh was used.

Vrancken suggested complex strategies haven't been investigated due to the difficulty generated compatible scan vector definition for commercial machines [87]. However, recently this has been experimentally applied to SLM of 'unweldable' nickel based super-alloy CM247LC [95], made possible by the pre-processing methods developed in this thesis. In their work, the Hilbert and Peano-Gosper curves were applied to manufacture 3D samples. The use of these fractal scan strategies increased the bulk density of the parts by 2% over the island scan strategy. It also resulted in a significant reduction in crack length density, although the crack area density remained relatively the same. The authors acknowledged further work was required to explore other fractal scan strategies and optimise these to improve the quality of parts manufactured.

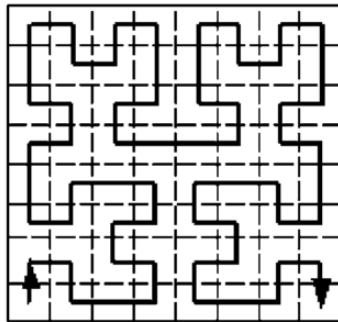


Figure 2.23: Illustration of Hilbert area filling curve fractal scan strategy used by Yang et al. [93]

The use of surface re-melting to reduce residual stress is inconclusive. Shiomi et al. suggested residual stresses could be reduced by surface re-melting [96]. A re-melting technique was successfully used for the selective laser melting of a metallic glass ($\text{Al}_{85}\text{Ni}_5\text{Y}_6\text{CO}_2\text{Fe}_2$) by Li et al. with no presence of micro-cracking [97]. In their approach, the material was scanned at high power (200 W), followed by a rescan at low power (80 W). However, a study by Mercelis and Kruth [77] showed no substantial reduction could be gained by re-scanning further, as discussed in Section 2.6.2.

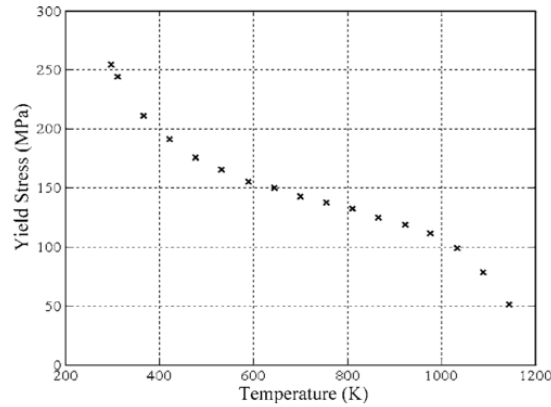


Figure 2.24: The yield strength for stainless steel 304, taken from Vasinonta et al. [85]

2.4.6 Effect of pre-heating

Pre-heating the build chamber has been considered as an effective strategy for reducing residual stresses in SLM and was first investigated in work by Klingbel et al. [98]. It has been claimed to be the most effective method for reducing the effect of residual stress during. This is achieved by raising the build chamber to high temperatures, in order to reduce global thermal gradients throughout the part [99]. However, an additional effect of the increased temperature is the reduction of the yield strength, as shown in Figure 2.24, for stainless steel 304. The yielding behaviour at high temperature limits the maximum residual stresses within the process.

Vasinonta et al. developed a thermo-mechanical FE model of thin-wall structures to aid understanding of the effect of pre-heating on both the temperature gradient and the residual stress generated [85]. As shown in Figure 2.25, varying the scan parameters (power, and laser speed) at room temperature, shown as the solid line, did not vary the maximum residual stress even at small temperature gradients. Increasing the pre-heat temperature using the same parameters (shown as curved lines), considerably reduces the maximum residual stress.

The use of a localised pre-heating source was first experimented by Abe et al. who used an additional CO₂ laser offset in front (pre-heating) and behind (re-heating) the laser scanning across the surface [101]. They reported improved ductility in the material using the dual laser source. Aggarangsi and Beuth developed a thermo-mechanical FE model to investigate the effect of using a localised pre-heating source [102]. They concluded that temperature gradients barely changed using a localised heat source compared to using uniform surface pre-heating, which reduced residual stresses by 18%. They acknowledged that

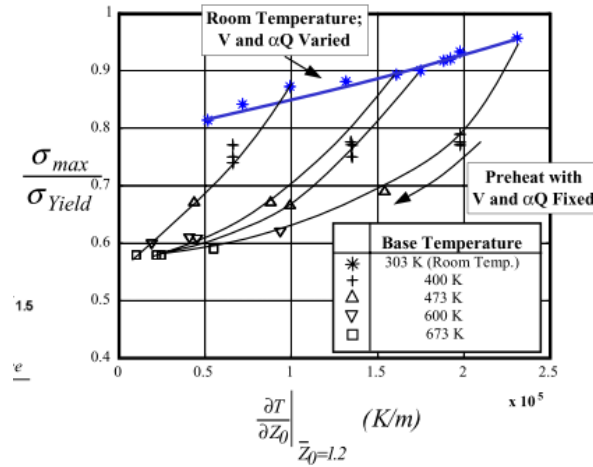


Figure 2.25: Process map by Vasinonta et al. [100] showing the maximum residual stress generated against the temperature gradient at different pre-heating temperatures, and laser parameters

uniform pre-heating of the part is more effective, but is impractical to achieve. Buchbinder et al. investigated the effect of pre-heating an aluminium alloy, AlSi10Mg, using SLM, and reported that a preheat temperature of 250 °C was sufficient in order to reduce part distortion and improve reliability [99].

Parts produced by EBM are significantly less prone to the effects of residual stresses. Through the use of a vacuum atmosphere, the build chambers can be raised to high temperatures, 750 °C in the case of Ti-6Al-4V [14]. Nevertheless, there is still residual shrinkage in the final part as the build chamber cools, and the parts are not completely impervious to distortion in the process.

2.5 Other manufacturing issues present in selective laser melting

As described in Section 2.3, the complexity of the underlying thermo-physical phenomenon in SLM contribute to defect formation, such as porosity and inadequate layer adhesion due to laser spatter. These defects provide routes for material failure when combined with residual stress. The random nature of defect generation reduces confidence in the mechanical performance of AM built parts. Even parts successfully built, are limited by the surface roughness (Section 2.5.1) and in-built material anisotropy (Section 2.5.2), which affects the mechanical properties and the overall mechanical performance including resistance to fatigue failure. These issues are discussed further below.

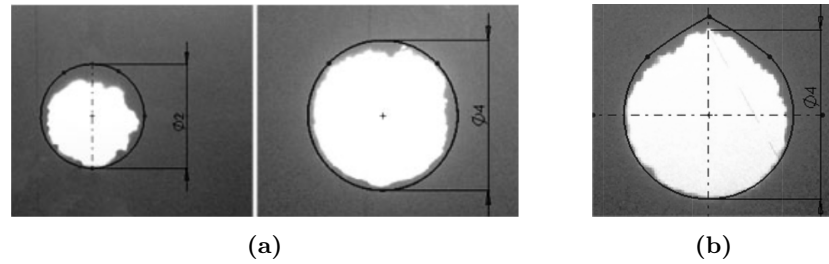


Figure 2.26: Unsupported overhang regions are susceptible to dross formation shown in a) two holes performed in an experiment by Thomas [105]. Design workarounds such as b) ‘tear-drop’ geometry can mitigate manufacturing constraints in SLM.

2.5.1 Surface roughness

Other factors that affect the production of parts by selective laser melting are surface roughness and porosity, which are dependent on numerous factors such as reliability of the machine, quality of powder material and most crucially optimisation of the laser build parameters [103]. Surface roughness in the as-built part taken from SLM is visually noticeable by inspection and is approximately 30-40 μm . Surface roughness is a source of crack initiation that promotes fatigue failure to occur [104]. A study by Edwards et al. found as-built parts in the Z direction experienced reduced fatigue performance, which was attributed to the surface roughness, and material anisotropy [104]. Surface polishing techniques can result in satisfactory finishing, however, inaccessible internal voids or cavities are a challenge for current surface treatment techniques and remain unsolved.

SLM is susceptible to poor surface roughness and sagging on geometrical features with low surface angles and is dependent on the overall part orientation relative to the build platform. Problematic areas often include holes, fillets and areas containing overhangs, which unsupported result in the formation of dross, as shown in 2.26(a). Unsupported areas are prone to dimensionally deviate from the original design geometry, and critical assembly interfaces features will need additional post-machining to reach desired tolerances.

The development of design rules was studied in doctoral work by Thomas [105]. Their research investigated the buildability of CAD geometry, and identified rules for self-supporting geometry by modifying original CAD geometry using chamfers, bosses or additional in-built support structures could remove. Hole features were noted to be susceptible to dross formation, and deviating in size from the original geometry, as shown in Figure 2.26(a). By designing holes using ‘tear-drop’ geometries, as shown in Figure 2.26(b), these can mitigate against the issue of over-hang areas. These design techniques can mitigate these issues and reduce the dependency on additional support material that requires removal

during post processing. However, these techniques involve manual operations for parts suitable for simplistic CAD geometry features. These manual workarounds become time-consuming to incorporate, and it is therefore desirable the part is automatically designed to be manufactured to account for the manufacturing constraints in AM.

2.5.2 Anisotropy of built components and fatigue performance

The orientation and size of poly-crystalline grain structures are dependent on the direction and magnitude of the temperature gradient field. Rapid cooling induces a martensitic transformation in of the microstructure in steel and titanium alloys [82, 106]. In SLM, there is a tendency for the generation of small dendritic or needle-like columnar grain structures pointing vertically (Z direction) that are greater than the layer thickness [104]. These vertically orientated grains are explained by heat dissipating preferentially downwards through the part into the base plate, during the build-process [107].

The effect this has on the bulk material is profound since these are highly dependent on their inherent microstructure. Numerous works [104, 107, 108] for various metals have shown the anisotropic mechanical behaviour where mechanical properties differ between the planar (X and Y direction) compared to the Z direction. Both static and dynamic mechanical properties are affected by material anisotropy, with a tendency for poor performance in the Z direction for yield strength, tensile strength and fatigue performance [104]. Investigations often involve building the part in different orientation planes (longitudinal, perpendicular, transverse) and at various locations on the build platform to also determine if build quality varies with the position inside the build platform.

Work by Vrancken concluded that for non-heat treated samples, the anisotropy of the residual stresses generated in conjunction with the developed grain structure had a strong influence on the anisotropy of the mechanical performance [87]. These factors have yet to be exploited practically in manufactured designs or methodologies to enhance the part performance, but was noted by Yadroitsev et al. [22].

A study by Dadbakhsh et al. [109] investigated the effect of part orientation and placement in the build chamber to understand the effect of protective flow of gas over the powder bed and on the mechanical properties of the final part. Despite showing a substantive difference when orientating the part on the powder bed parallel and perpendicular to the gas flow, the high level of porosity 17% was insufficient for a definitive conclusion.

Producing a reliable part with homogeneous material properties and negligible porosity requires further post processing such as hot isostatic pressing (HIP),

stress relieving or annealing. These processes relieve residual stress from within a component, however, only HIPing is able to reduce porosity, but this remains an undesirable step in production because of the additional cost and complexity imposed [23]. Tammis-Williams et al. [110] identified another potential issue: spherical pores containing trapped argon gas come under high pressure following HIPing and were found to progressively re-appear and grow compared to the as-built specimens. Hence, there is a significant motivation to avoid the use of HIPing for metal parts produced in SLM.

2.6 Process optimisation

The overall quality of built parts is governed by the number of in-built defects which arise through process instabilities created through the complex thermo-physical process involved in the melt pool as discussed in Section 2.3. Developing and improving the palette of materials available for manufacture by SLM begins with building specimens with low porosity. This is achieved by optimising and tuning the laser scan parameters in conjunction with the laser scan strategy. Further exploration of the parameter space can then account for different geometries, support areas and overhang regions to potentially reduce the magnitude of residual stresses generated and improving the surface finish.

2.6.1 Identifying the process window

Careful choice of laser power, point exposure time and point distance effectively control the rate of consolidation (build speed), part density, and most crucially the stability of the process; and together directly impact on build quality. Typically, process optimisation begins with the stable formation of single tracks and thin walls [51, 103, 111]. Accomplishing this across a parameter space, produces process maps, as illustrated in Figure 2.27. These are created through experimental methods, as shown in Figure 2.28, to identify a satisfactory operating window [89].

These process maps provide a guide to identify parameters where there is stable formation of the melt pool, and its solidification forms stable continuous tracks with low aspect ratios. These studies provide an insight into two or three laser parameters, but neglect a large number of process parameters [13, 69, 108]. Typical experimental methods are exhaustive trial and error approaches, since the parameter space is large and this further reduces the understanding of process.

A case study was presented by Elsen [13], who observed that the balling behaviour occurring on a single track differed greatly between work conducted

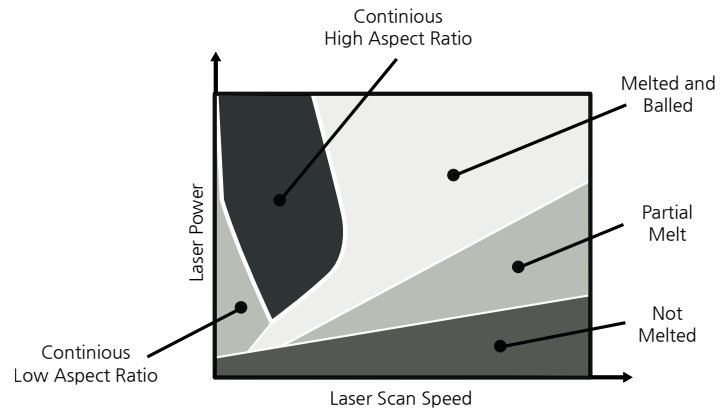


Figure 2.27: Process map of a tool steel experiment adapted from Hauser et al. [89]

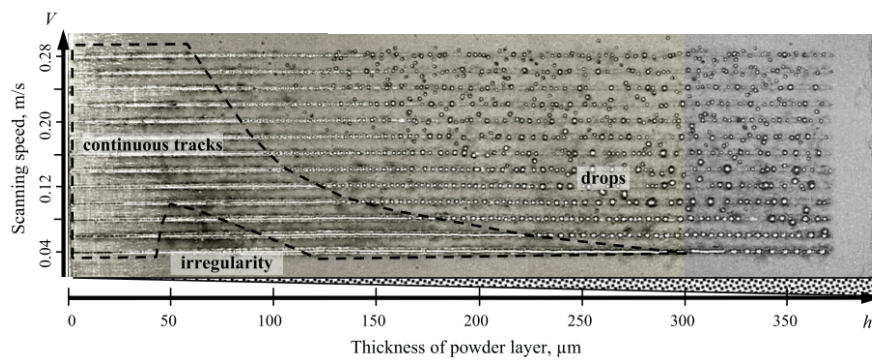


Figure 2.28: Process map performed by Yadroitsev et al. [103] showing melt pool formation and stability of a single track with varying scan speed and layer thickness

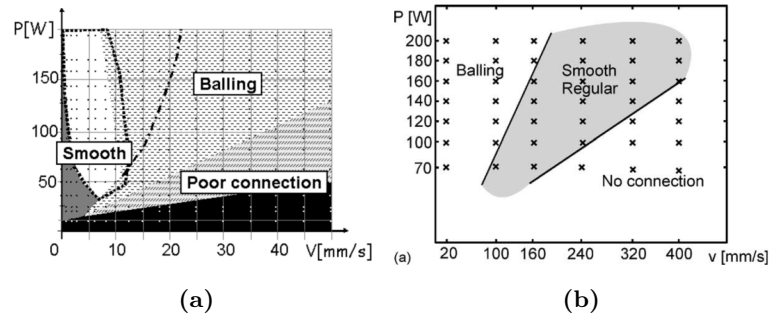


Figure 2.29: Process window taken from experiments of iron powders performed by a) Hauser [89] and b) Kruth et al. [78]

by Hauser [89] and Kruth et al. [78], as shown in Figure 2.29. The discrepancy between the results was observed to be caused by different laser spot size r_d and laser scan speed v , resulting in an incompatible Peclet number (equation 2.34) between the studies.

The optimal laser parameters are highly dependent on the material, the powder morphology and the capabilities of the machine, which are currently problematic for standardisation and certification of the process. Therefore, care must be taken when comparing research owing to the difference in known stated parameters and those unknown within the sub-process.

2.6.2 Pre-sintering and laser surface re-melting

Laser scan strategies are often employed to improve the processability and mechanical integrity of components produced using SLM [58]. Laser surface re-melting has been used to significantly reduce levels of porosity to achieve high density parts ($>99.9\%$), with improved surface finishing but at the expense of approximately doubling the build time [112, 113]. This is achieved by scanning the current layer twice (or multiple times) with the same or a different hatching regime, with the aim being to remove any residual porosity created by process instability. The second scan could be orientated perpendicular or be shifted to overlap between scan vectors, referred as the ‘two-zones technique’ [58, 108]. Morgan et al. successfully applied re-melting to remove inter-layer porosity, achieving porosities of $\sim 1\%$ [114]. This technique has also been used to improve surface quality: Lamikiz et al. selectively applied this to top surfaces and improved surface roughness by 80.1% from $7.5\text{--}7.8\ \mu\text{m Ra}$ to $1.49\ \mu\text{m Ra}$ [115]. Also, Pinto et al. investigated the use of re-melting to improve the micro-hardness of the surface [116]. Yasa and Kruth carried out an investigation to determine if the ‘stair-stepping’ effect could be suppressed, but discovered only a modest reduction of 10-15% could be gained [113].

Despite the increased production time, surface remelting can be cost and time effective if it removes the requirement for expensive HIPing and reduces surface polishing required on the part. This performance penalty using re-melting could be improved significantly by applying this more selectively to areas containing defects using in-situ monitoring or restricting to problematic or performance critical regions.

The pre-sintering technique relies on scanning the layer using a relatively lower power setting to sinter powder prior to melting in a second scan. Aboulkhair et al. [58] improved the processability of AlSi10Mg using this technique, achieving densities, 99.8%, demonstrating a significant improvement over a variety of re-melting scan strategies employed in their study. An added benefit was that their method could be achieved using a lower power laser, 100 W, compared to 200 W used in a previous study by Thijs et al. [71]. A detailed investigation of the pre-sintering mechanism has not been reported, but the act of sintering powder particles will flatten the surface, removing surface irregularities and the likelihood of pore formation. Since particles are anchored, denudation is less likely to occur, reducing inter-track porosity. Also, because sintering necks increase thermal conductivity, this should effectively reduce the instantaneous power requirement to fully melt powder, reducing the potential formation of key-hole pores.

Both the use of re-melting and pre-sintering [82] have been considered in reducing the effect of residual stresses generated during the build. Mercelis and Kruth [77] investigated the use of re-melting to reduce residual stresses. Their study revealed that only using 50% of the nominal laser power used for hatched zones, reduced the level of stress, whereas repeated exposure at full intensity had no effect on the residual stress. The surface re-melting technique does not seem to be an effective solution to reduce residual stress because a new melt pool is re-created. This induces another HAZ, and thus generates another set of residual stresses of a similar magnitude to those in the initial scan.

2.6.3 Dimensional analysis

The large parameter space in SLM makes it important to understand the relative importance, and the effect of variability of the process parameters to ensure repeatability and consistency in the build process. Consequently, the large parameter space requires time-consuming and expensive experiments are needed to obtain an optimised set of parameters specific to the material, machine manufacturer, and powder supplier. Elsen et al. [13] investigated approaches to improve process optimisation through a dimensional analysis using the Buckingham Pi theorem in order to reduce the number of factors affecting the process. This

helps deliver a more systematic approach using experimental design methodologies. Considering the thermo-fluid phenomena occurring in the process, the dimensional reduction still required nine non-dimensional input parameters, as shown in equation 2.44, and remained considerably exhaustive.

$$\theta = f_3\left(\frac{L_T}{r_d}, \frac{h_d}{r_d}, \frac{vr_d}{\alpha}, \frac{P}{\alpha r_d \delta h}, \frac{\sigma_b r_d}{\mu \alpha}, \frac{\rho^2 \delta h \alpha^3}{\mu \sigma_b^2}, \right. \\ \left. Pr, M^2, \%O_2, St, \frac{\rho_p}{\rho}, \frac{x}{r_x}, \frac{y}{r_y}, \frac{z}{r_z}, \right) \quad (2.44)$$

δh	Melt enthalphy
Pr	Prandtl number
M	Beam quality
St	Stefan number
ρ_p	Density of powder

Dimensional reduction has also been considered in work by Körner et al. [117] and by Megahed et al. [69], which characterised the effect of dimensionless numbers on the process parameters, in particular during the melting regime and laser interaction with the powder. Körner identified several dimensionless numbers that characterised the fluid behaviour in the melt pool and compared these with their numerical simulations. The Bond number Bo , is a measure for comparing gravity verse the surface tension forces and is defined as

$$Bo = \frac{\rho g L^2}{\gamma} \quad (2.45)$$

where L is the chosen characteristic length, and g is the gravitational constant. Another method for characterising the free-surface fluid dynamics of the melt pool is the Laplace number, La , which is the ratio between the inertia and capillary effects against the viscous forces, and is defined as

$$La = \frac{\gamma \rho L}{\mu^2} \quad (2.46)$$

where μ is the dynamic viscosity of the liquid, and L is the chosen characteristic length. Using common parameters associated with the electron beam melting of titanium, the dimensional parameters were found to be $Bo = 10^{-4}$ and $La = 10^5$, which indicated the system is largely driven by surface tension effects, and gravity and viscous forces are negligible.

2.7 Summary of literature and identified gaps in the literature

Despite additive manufacturing's proposition for offering unlimited design freedoms, many limitations, such as those discussed in Section 2.5 remain a challenge to industry. The manufacturing issues for SLM systems remain largely un-accounted for with the current design methodologies and tools available, hence, manufacturability relies on the competent experience of technicians operating the AM machines.

In addition to the exhaustive list of parameters associated with these processes, as discussed in Section 2.6, the manufacturing process remains significantly dependent on the design geometry. This dictates the pre-processing steps including part orientation, support structure generation, and, critically, the laser scan strategy employed during the build. Building a knowledge-base to support design guidelines and rules, alongside predictive tools to support design methods is critical to unlocking all the available manufacturing freedoms.

Powder-bed fusion processes such as SLM inherently manifest a variety of complex thermo-physical behaviour, as discussed in Section 2.3. These processes embody highly non-linear and transient behaviour as a result of the complex interaction between the irradiation of laser energy, the powder layer, the melt pool and the heat affected zone. The chaotic behaviour inside the melt pool and its interaction with the random distribution of powder, are the precursors for the generation of process instabilities such as pore formation and laser spatter, as discussed in Sections 2.3.7-2.3.8. The generation of these defects have repercussions on mechanical performance such as fatigue failure, which hinder adoption in industrial applications requiring high reliability. At the micro-scale the random distribution of powder results in highly stochastic behaviour, requiring extremely high resolution measurement methods to capture or predict these. Research to understand the complex thermo-physical phenomena occurring inside the melt pool remains immensely challenging, both experimentally and numerically.

Artefacts of this process caused by process instabilities include key-hole porosity, formation of laser spatter, and the elongation of pores, as discussed in Sections 2.3.7-2.3.8. Several methods are available to mitigate against these instabilities such as altering scan strategies and the use of pre-sintering or surface re-melting for the removal of random porosity present within the part. The aim of current research is the development of in-situ monitoring and repair systems that will provide certification of parts produced in SLM, and more efficient methods for the removal of porosity and cracks.

The thermo-fluidic phenomena and their effects on built parts occurring at the *micro*-scale have not been shown to have direct implications on the residual stress generated within larger *macro*-scale regions or within parts. Nevertheless

it is important to understand the physics governing the melt pool because this will determine the penetration into the substrate below and also change the heat input into the process. Potentially, this will drive the development of different micro-structural behaviour and in some materials induce micro-cracking. Ultimately, the ability to predict the melt pool geometry and its stability will help identify suitable processing parameters for this process, which in turn will have the most influence on the residual stresses generated.

As discussed in Section 2.4, the most pressing issue hindering successful adoption of SLM are the currently unpredictable build failures caused by excess distortion of parts caused by residual stresses. The effect of laser parameters remains inconclusive, and the practically infinite combinations of laser scan strategies has little been explored due to the difficulty of generating and deploying custom scan strategies on SLM machines.

The limited resolution, repeatability and resources required for experiment measurement of residual stress in SLM creates significant challenges. Process modelling can address these issues and guide experimental work. Following the review of literature of current research into selective laser melting, the key gaps in research are outlined below

1. Understanding behind the thermo-fluid phenomena that causes melt-track instability, and the generation of defects such as pores, and spatter remain very challenging to capture experimentally. The effect of laser parameters and scan strategy on defect generation remains largely unknown. However, many defects can be mitigated through re-scanning in-order to produce near fully dense parts.
2. Prediction and mitigation of residual stress remains the most significant concern for manufacturing components. The effect of laser scan strategy on residual stress has been explored experimentally, with conclusions that short scan vectors reduce the effect of residual stress, and the largest stress component is orientated parallel to the scan vector. However, there is a lack of understanding at the fundamental mechanisms of how residual stress is generated, with respect to laser scan parameters, scan strategy and size of the scan area. Other influences remain largely unexplored, such as the response of residual stress depending on the geometry, and underlying support material whilst scanning.

Chapter 3

Literature Review Part II: Numerical modelling of selective laser melting

The extremely high temporal and spatial resolution required to capture the complex physics occurring in the manufacturing process severely limits the knowledge and understanding that can be obtained solely through physical experiments. Additionally, to fully explore the extent of the large parameter space specific to the material consumed on machine platform would incur a significant resource cost. These fundamental issues provide an incentive to model the process of selective laser melting.

The first work in simulating a rapid prototyping process of laser sintering was carried out by Nelson et al. [118]. Owing to the complexity of the process, a significant trade-off is required between accurately modelling all known thermo-physical phenomena in the melt pool, HAZ, and the global response of the part. The combination of the physical time scale and the extremely large number of degrees of freedom (DOF) created by discretising the domain create a significant computational burden. Therefore, modelling efforts by researchers have segregated towards scales appropriate for modelling the phenomena of interest at resolutions feasible with different modelling techniques. Modelling scales are generally classified under three scales: *micro*, *meso* and *macro*, which account for the different physics occurring at different length and time scales.

These are classified as the following:

1. **Micro-scale** consists of modelling the interactions between the laser and particles at the ‘powder scale’. The sintering behaviour and the dynamic

formation of the melt pool can be tracked. The models must to some degree account for the thermo-fluid physics involved and provide information on the formation and stability of the melt pool along a track or layers. Simulations at the micro-scale are inherently expensive owing to the high resolution required.

2. **Meso-scale** consists of modelling sub-regions of the process, typically a number of scan vectors over a series of layers. Given the coarser resolution and large time-frame required, the thermo-mechanical behaviour is usually captured, and can predict the residual stress distribution within the zone. The thermal response provides an input to determine the micro-structural evolution of the metallurgy for a built material.
3. **Macro-scale** consists of modelling information (e.g. stress distribution, distortion) for large regions or parts. Model abstractions are used to reduce the complexity of the underlying physics captured downwards at the *micro* and *meso* scales.

3.1 Micro-scale modelling

At this scale, models account for the individual geometry of the powder particles, and broadly encompass the region surrounding the interactions of the laser, the powder bed and melt pool. The hydrodynamics within the melt pool must be captured at high resolution in time in order to capture the high velocity flows present. *Micro*-scale analyses require element sizes of the order of microns, and may consist of millions of elements during discretisation. A stochastic element must be accounted for when generating the model because of the random distribution and morphology of powder particles. This leads to irregular absorption, heat dissipation and contact leading to the process instability arising as previously discussed in Sections 2.3.4 to 2.3.8.

The governing equations are modelled through a combination the Navier-Stokes, mass conservation, and energy conservation equations together with extensions to account for multi-phases, body forces and surface tension effects, resulting in a highly non-linear system [20, 69]. In these equations, the molten metal is assumed incompressible. Many hydrodynamic effects are dependent on tracking the free surface. This can be obtained through Volume of fluid (VOF) or level set methods. The VOF method tracks the volume of each liquid phase within each element (metal or gaseous phase). This can account for evaporative losses in the system, since each phase is separable. The level set method instead tracks the distance to the surface from each element centroid. A disadvantage of computational fluid dynamics (CFD) analysis is the use of explicit time

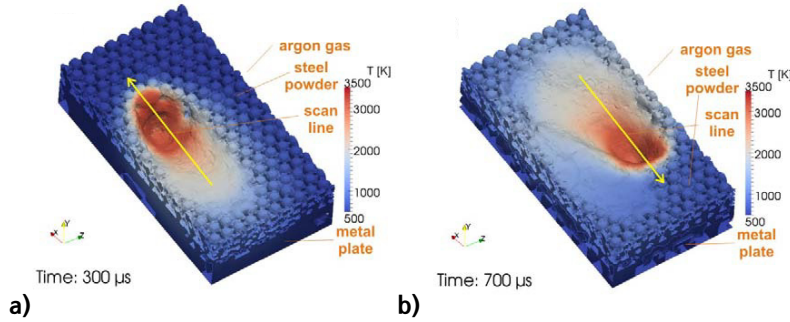


Figure 3.1: CFD simulation of selective laser melting using the finite volume method taken from a study performed by Gürtler et al. [119]

integration. Numerical stability or convergence can only be guaranteed when the Courant-Friedrich-Lewy (CFL) condition is satisfied, such that

$$\frac{u\Delta t}{\Delta x} < 1, \quad (3.1)$$

where u is the fluid velocity, Δt is the time step, and Δx is the finite length scale. Essentially, the timestep must be less than the transit time of a sound wave across the smallest element size [67]. This limits the timestep permitted in these simulations, due to the high fluid velocities present.

Various numerical implementations have been developed by different researchers. Gürtler et al. [119] developed a 3D model for the SLM of steel, as shown in Figure 3.1, using OpenFOAM - a c++ framework for solving continuum, mechanical and dynamic problems using the finite volume (FV) method. Multiple phases and tracking of the free-surface was modelled using the VOF method, and the model could account for latent heat and the effect of vaporisation. Their model used a volumetric Gaussian heat source, with the absorption coefficient given by the Fresnel equation, and the attenuation of the laser beam driven by the Beer-Lambert law (Section 2.3.2). A powder packing factor of 60% was used to represent the sphere packing. The author acknowledges that to improve performance, artificial sintering necks were made between particles to increase thermal conductivity, and reduce the melting time. Qiu et al. [63] also used the openFOAM framework and expanded this further to comprehensively model the fluid forces, and also compared the results with experimental work.

Khairallah et al. [73] developed a hybrid finite element and finite volume for the inclusion of multi-physics in the problem based on an in-house arbitrary Lagrange-Euler (ALE) framework. Their implementation used a uniform Cartesian grid as the background mesh to discretise the domain which was mapped between each physics analysis step. Their method used ‘operator splitting’ to model the

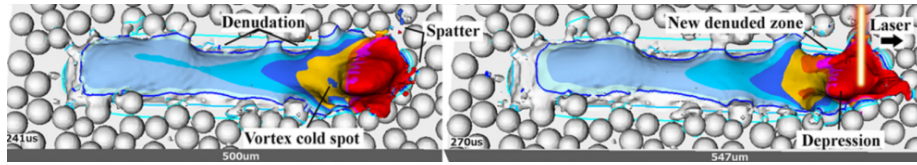


Figure 3.2: Micro-scale simulation of the melt pool formation by Khairallah et al. [67], showing the creation of the defects such as denudation zones and laser spatter

hydrodynamics and thermal dissipation independently. A Lagrangian motion phase translated material adiabatically in response to forces using single point Gauss quadrature for mapping strain and nodal forces. A thermal analysis was performed without material movement by integrating nodal temperatures, and the results were advected back onto the original background mesh. To reduce the simulation time, the material densities were artificially increased to bypass the CFL condition (equation 3.1) resulting in a 3-10x speed-up whilst ensuring numerical convergence was stable. Nevertheless, the simulations exceed 10^5 CPU hours, requiring High performance computing (HPC) facilities. Their model had the ability to predict a variety of effects including Marangoni flow, the generation of keyholes and the associated formation of keyhole pores and laser spatter, as shown in Figure 3.2 [67].

The lattice Boltzmann method (LBM) has been used to simulate power-bed fusion in two dimensions by Körner and Attar [120]. Their approach is especially beneficial for problems with complex interfaces, such as flows in porous media, and the presence of multiple phases [121]. Their study could account for the surface roughness because it could track the wetting behaviour, and therefore the melt pool formation and fragmentation under different laser parameters. Later they extended their model to account for the successive build-up of layers, as shown in Figure 3.3. Their model had a stochastic element by distributing particles randomly using a ‘rain-drop’ model and this had a significant effect on the build-up of the scan tracks. The author acknowledged that Marangoni flow, and vaporisation effects were not included in their model, and that the results could not be directly compared with a 3D solution.

All the previous *micro*-scale models focus on capturing the fluid flow, and tracking the surface boundaries of the melt pool to understand the formation of the scan tracks and generation of porous defects. They neglect any strong mechanical interaction such as the creation of residual stress in consolidated material and the substrate. Jamshidinia et al. developed a coupled CFD/FE model for the EBM of Ti-6Al-4V, using ANSYS, a commercial multi-physics simulation package [123]. A ‘weak’ physics coupling was used, in which the resultant mesh geometry and the thermal state acquired from the CFD solution

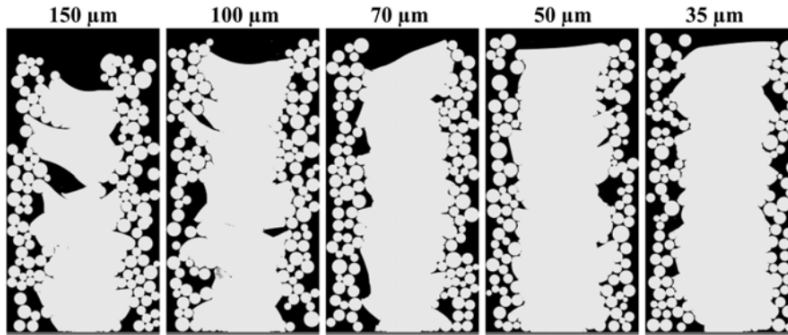


Figure 3.3: A multi-layer LBM simulation of EBM performed by Körner et al. [122] showing the effect of layer thickness on the melt-track stability over multiple layers

was transferred to the thermo-mechanical FE analysis for each time step. Their simulation was limited to 50 time steps at 0.06-0.6 ms per time step and used a relatively small mesh size (11×10^3 elements), owing to the inefficiency of transferring between analysis types. The CFD analysis could track the formation and geometry of the melt pool and showed that a relationship existed between the scan speed and the magnitude of residual stress. The hydrodynamic coupling at these time-scales does not present any significant advantage except to obtain more accurate geometry and temperature distribution of the melt pool to apply boundary conditions in their FE model. This would allow the model to incorporate the effects heat transfer within the melt pool due to Marangoni flow and the mushy zone, as discussed in Section 2.3.5.

Micro-scale analyses requiring the use of CFD offer a wealth of information on the interactions between laser and the powder bed at this scale. These simulations provide an insight to the mechanism that result in the formation of instabilities of the melt pool, and the formation of defects occurring with these processes.

Ultimately, the resolution required for capturing the *macro*-scale response, i.e. the thermo-mechanical behaviour of a component, does not require capture of the high-fidelity physics. In order to better determine the factors influencing the build-up of residual stress, continuum based thermo-mechanical models are a more suitable modelling choice.

3.2 Meso and macro-scale modelling

Currently, *macro*-scale models aim to capture the thermal behaviour during manufacture, and the development and fully resolved mechanical state post-build. The modelling scales using continuum approaches varies, from capturing small

regions (single or series of scan tracks) at the *meso*-scale towards simulating industrial size components at the *macro*-scale. The resolution and accuracy required dictates the modelling strategies chosen.

An approach to reduce the computational burden is to treat the powder bed and substrate as a continuum, which coarsens the discretisation required, both spatially and in time. Typically, the continuum consists of elements modelled using a state variable, ϕ , to account for the transformation between the powder, liquid and solid phases present. The nature of thermo-mechanical system, allows a ‘weak coupling’ to be used for further model simplification. First, a transient heat-transfer analysis is performed, and the resultant temperature field is used as input during the mechanical modelling step, both sharing the same mesh.

Flexibility at these length and time scales does not necessarily require all the physics to be explicitly modelled. Generally improving the performance is favoured whilst still capturing the important relevant physics during the process. Additionally, the stochastic nature at these scales is largely un-important compared to models at the *micro*-scale, because the bulk properties in material phases are homogenised. Nevertheless, the underlying problem remains a transient one, and highly non-linear due to the large temperature range, and multiple phases present.

3.2.1 Development of continuum models in powder-bed fusion processes

Most modelling approaches, as summarised in Table 3.1, have used the finite element method to solve the heat-transfer problem and mechanical analyses. The earliest work, which was applied to laser sintering, by Nelson et al., who used a 1D heat transfer model to predict the sintering behaviour (track depth) of polymer powders [118]. Methods for the thermo-mechanical modelling of powder-bed melting systems were developed by Dai and Shaw [124]. Unlike previous work, their method fully accounted for the powder-solid phase transition phase, using a state variable, with independent temperature dependent thermo-physical material properties. The powder thermal conductivity used the model proposed by Sih et al. [44] described in Section 2.3.2. A crude moving laser heat source was used, where 3 x 3 elements were irradiated at an instance. Forced heat convection and radiation terms were applied to the surface. A quasi-static mesh was used with an ‘element-birth’ technique to activate a new layer of power elements to mimic the process, without the requirement to change the mesh. Kolossov et al. [29] developed a 3D thermal model of the laser sintering process

and defined the state variable representing the powder phase as

$$\phi(x, t) = 1 - \exp - \int_0^t \zeta(T(x, s)) ds \quad (3.2)$$

where $\zeta(T)$ represents the ‘sintering rate’ to account for the sintering kinetics. The sintering rate $\zeta(T)$ in their model was defined by that proposed by Frenkel in equation 2.29, based on the surface tension γ and the viscosity μ of the liquid phase.

Further development in techniques for modelling the laser melting process were made by Roberts et al. who introduced a moving surface based Gaussian laser heat source, with the ability for scanning a complex pattern over multiple layers using the element ‘birth and death’ technique [127]. Gusarov et al. [32] developed a 1st order explicit finite difference model of the process. Their model incorporated a proposed radiation transfer equation (Section 2.3.1) for modelling the irradiance of the laser onto the powder bed, along with a set of equations that modelled the effective thermal conductivity of the powder (Section 2.3.2). Evolution of the solidification interface of the melt pool was tracked by the transport equation applied to the state variable ϕ ,

$$\frac{\partial \phi}{\partial t} - v \frac{\partial \phi}{\partial \mathbf{x}} = 0, \quad (3.3)$$

where v is the interface velocity. Despite the restrictions of the numerical scheme used, a small timestep of $\Delta t = 7 \times 10^{-6}$, the final geometry of the melt pool was in good agreement. Similarly, Hodge et al. considered tracking the phase change at the interfaces based on the Stefan-Neumann equations [34]. However, the author acknowledged that this required reducing the time step significantly in order to satisfy convergence with the non-linearity imposed by the solidification equations.

3.2.2 Accounting for shrinkage

A general difficulty in continuum models is accounting for material shrinkage during transformation from powder to its final state and material ablation due to vaporisation. This has been considered a by Chen and Zhang in a study of SLS [126]. Their model incorporated a dimensionless shrinking velocity as a coefficient for their energy equation with respect to the Z direction. An iterative algorithm was proposed by Verhaeghe et al. [33] to account for shrinkage in the Z direction with three distinct states, powder, solid and voids (the effect of material removal by vaporisation).

The shrinkage is calculated in a column of ‘cells’ in the Z direction, as shown in Figure 3.4. Through heat transfer, there is an effective mixing of enthalpies

Simulation Type	Materials	Validation Method	Element Size [mm]	Domain Size [mm]	Laser Power [W]	Laser Speed [mm/s]	Laser Beam Diameter [mm]	Reference
SLS (FE)	Bisphenol-A Polycarbonate	Sintering Dimensions	N/A	N/A	15	551	0.5	[118]
SLS (FE)	Fe-Cu & WC-Co	Sintering Dimensions	N/K	N/K	28.9,8.18	0.01	0.8	[36] [125]
SLM (FE)	Ni & Porcelain	-	0.67 x 0.67 x 0.5	20 x 20 x 1	2.0	0.01	2	[124]
SLS (FE)	Ti	Thermal imaging	0.1(C) 0.01(F)	5 x 5 x 2	2.0	1.0	0.25	[29]
SLS(CFD)	Nickel(40%) Steel(60%)	Sintering dimensions	N/A	N/A	150	N/A	N/A	[126]
SLM(FE)	Ti6Al4V	N/A	0.025	1 x 1 x 0.15	120	220	0.1	[127]
SLM(FE)	Steel Alloy	Neutron diffraction, deformation displacement	0.025	1 x 1 x 0.15	200	500	N/A	[128]
SLM(FVM)	Ti6Al4V	Melt pool dimensions	0.002	0.36 x 0.24 x 0.36	20-80	200	0.026	[33]
SLM(FE)	W-Ni-Fe	-	0.05	2 x 3 x 1.5	100	20-140	0.03	[129]
SLM(FE)	Steel 316L, Cu	-	N/K	N/K	30-120	100-200	N/K	[24]
SLM(FE)	Steel 316L	Melt pool dimensions	0.056	6 x 9 x 1	100	400	0.2	[130]
EBM(LBM)	Ti6Al4V	Melt pool dimensions	N/A	N/A	N/A	N/A	N/K	[46]
SLM (FE)	Steel 316L	Melt pool dimensions	0.025	N/K	50	150-300	0.03	[19]
SLM (FE)	Ti6Al4V	Thermal Imaging	0.04 (C)	1 x 1 1.5	180	1250	0.1	[30]
SLM (CFD)	Ti6Al4V	-	N/A	0.6 x 0.32 x 0.2	200	1000	0.05	[119]
EBM (CFD,FE)	Ti6Al4V	-	0.04	3.6 x 0.8 x 0.4	840	100-1000	0.4	[123]
EBM (FE)	Ti6Al4V	-	N/A	4 x 3 x3	40.60	1000	0.2	[131]
SLM (FE/CFD)	Steel 316L	High speed video, Thermal Imaging	0.003	1 x 2 x 0.1	100-400	700-7500	0.05	[73]
SLM (FE)	Steel 316L	Comparison	0.002 (F) 0.6 x 0.6 x 0.2	167,33	1600	180	0.06	[34]
SLM (FE)	Inconel 718	-	N/K	70 x 10 x 4.5	-	-	-	[134]
SLM (FE)	Steel 316L	Distortion, Melt Pool	N/K	5 x 5	200	800	0.06 x 0.05	[132]
SLM (FV)	Ti6Al4V	-	N/K	0.25 x 0.25 x 0.5	400	3500	-	[63]
SLM (FE)	Steel 316L	Distortion	0.05 x 0.05 x 0.0375	N/K	300	50	0.6	[133]

Table 3.1: Overview of transient numerical simulations on powder-bed fusion processes arranged chronologically

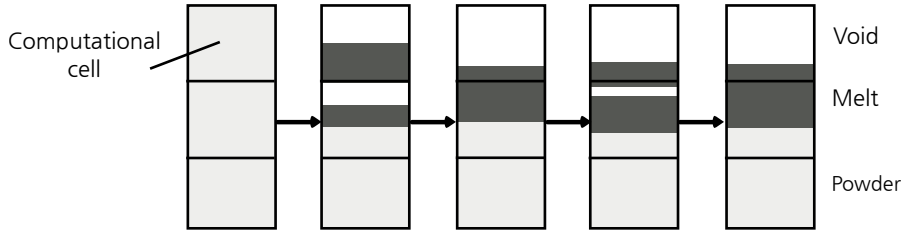


Figure 3.4: Illustration of the iterative scheme for shrinking and re-melting algorithm applied per element by Verhaeghe et al. [33]

between these states which allows the powder above and below the melt-pool to melt. Another method was proposed by Hodge et al. [34] by incorporating a virtual shrinkage strain ε_ϕ , to account for shrinkage associated with phase transformation from powder to solid, and thermal shrinkage ε_{th} , as exhibited during casting processes

$$\varepsilon = \varepsilon_e + \varepsilon_{th} + \varepsilon_\phi \quad (3.4)$$

and

$$\varepsilon_\phi = \phi_1\beta_1 + \phi_2\beta_2, \quad (3.5)$$

where β_1 is the phase transformation shrinkage coefficient and β_2 is the contraction resulting from the total loss of porosity from the powder to solid. The element shrinkage factor was discovered to be important during the application of new layers, causing some layers to not fully melt, as shown in Figure 3.5, because the final layer thickness varied throughout the part. This effectively models the inconsistent build-up of layers; however, the relative importance of this effect in the process does not seem significant for the calculation of residual stresses within a component.

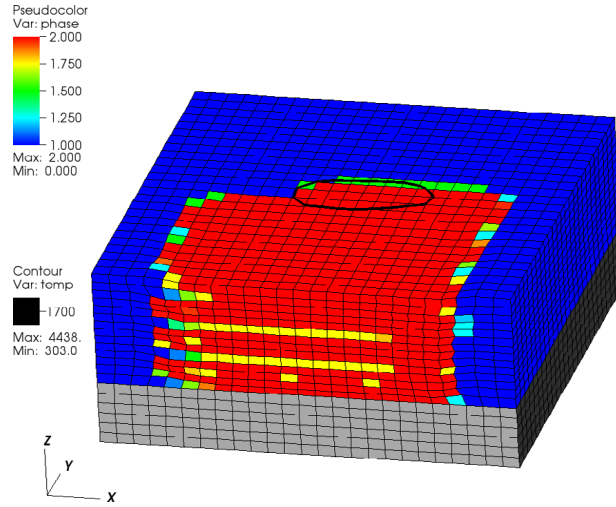


Figure 3.5: Multi-layer thermo-mechanical simulation showing the inter-layer porosity as a result of accounting for shrinkage between layers. Taken from Hodge et al. [34]

3.3 Analytical modelling methods for prediction of residual stress

The non-linearity present in the manufacturing process provides significant issues for modelling the process analytically. Nevertheless, there has been development of analytical models for SLM that have modelled the build-up of residual stresses. The first analytical model intended for the prediction of residual stress in SLM was proposed by Shimoi et al. [96]. In their model, experiments were performed to obtain the longitudinal and parallel strain components in the XY plane on the build plate during the build process using a strain-gauge, as shown in Figure 3.6. It was seen that strain accumulates linearly with the addition of each layer.

In their model, it was assumed that the accumulation of strain $\delta\varepsilon$ throughout the part and the base plate increased linearly with build height such that

$$\delta\varepsilon = a_1 + \delta\varepsilon_1, \quad (3.6)$$

where a_1 is some constant to be determined by the measurement of $\delta\varepsilon_1$ in their experiment. Their model was based on simple bending theory of two beam elements (model and base plate), with Young's moduli E_b , for the base plate and E_m for the part, as illustrated in Figure 3.7. By using equilibrium of forces and moments in the X direction, the residual stress distribution σ_R , can be

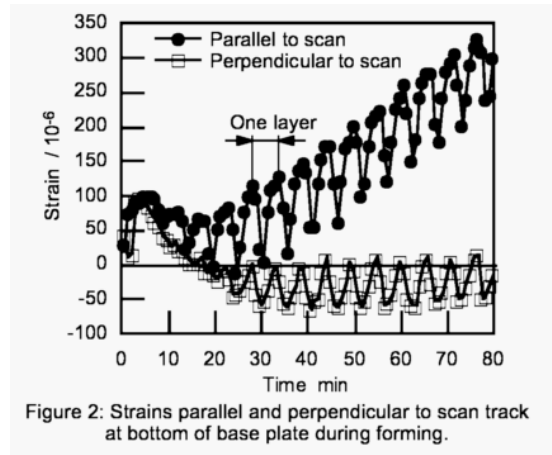


Figure 3.6: Longitudinal and transverse strains at the bottom of the base plate obtained from a strain-gauge during the build from an experiment by Shimoi et al. [96]

obtained for the first layer

$$w_b \int_0^{h_b} E_b(a_1 z + \delta \varepsilon_1) dz + w_m \int_{h_b}^{H-b+h)m-L_T} E_m(a_1 z + \delta \varepsilon_1) dz - w_m L_T \sigma_R = 0, \quad (3.7)$$

and with subsequent removal of the base plate,

$$w_b \int_0^{h_b} E_b(a_1 z + \delta \varepsilon_1) dz + w_m \int_{h_b}^{H-b+h)m-L_T} E_m(a_1 z + \delta \varepsilon_1) dz - \dots \quad (3.8)$$

$$w_m L_T \sigma_R \left(h_b + h_m - \frac{L_T}{2} \right) = 0.$$

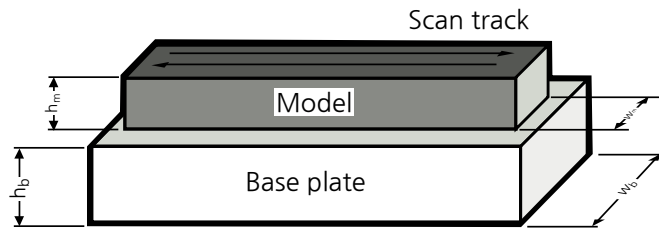


Figure 3.7: Illustration of bending beam model proposed by Shiomi et al. [96]

The residual stress distribution during the build can be determined in a similar fashion, but their assumption was that the residual stress created in each new layer never exceeded the yield stress σ_y , and that the increment of

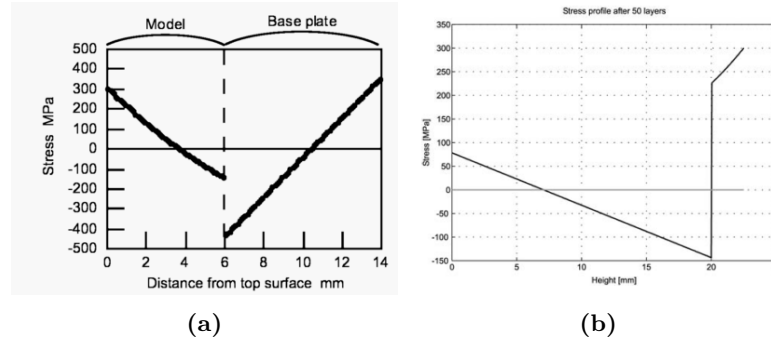


Figure 3.8: Graphs of residual stress profiles in built samples, taken from analytical models developed by a) Shiomi et al. [96], and b) Mercelis and Kruth [77]

stress increases linearly with layer addition as

$$\delta\sigma_R = cz + d, \quad (3.9)$$

with constants c and d to be determined. Through equilibrium of forces and moments, they showed the residual stress profile in the Z direction could be modelled as

$$\sigma_R(z) = -6\frac{\delta h}{h_b^2}\sigma_y z + 2\frac{\delta h}{h_b}\sigma_y, \quad (3.10)$$

where δh is the thickness of the formed layer. This results in the calculated stress profile shown in Figure 3.8(a). Similar work was carried out by Mercelis and Kruth [77], who used a similar approach. They made the same assumption that the incremental residual added per layer $\delta\sigma_R = \sigma_y$, and found the stress profile shown in Figure 3.8(b), to be similar to that of Shiomi et al. Both analytical models predict high compressive stresses near the interface between the model and the base plate. With the gradual addition of layers, tensile stresses build up linearly.

These analytical mechanical models follow simple assumptions, and remove non-linearity from the process. Additionally, they require knowing the incremental residual stress added per layer $\delta\sigma_R$ which must be obtained through experiments. Therefore, they are not suitable as a predictive tool. Nevertheless, they provide an insight into predicting the residual stress within a structure as the part is built up gradually.

3.4 Methods for improving simulation throughput

The actual build process for powder bed systems is considerably long, with some industrial parts requiring upwards of several days to manufacture. Attempting to accurately account for the movement of the laser across each scan vector building an entire industrial component is not currently feasible. Realistically, achieving this in a feasible time requires developing suitable model strategies and abstractions to gain substantial improvements in capturing model details, in particular the residual stresses and part distortion.

3.4.1 Alternate heat flux models

Zäh et al. [128] identified that significant model simplifications were required to improve simulation throughput. In their approach, they applied a uniform heat flux instantaneously to the entire cross-sectional surface of the part on an active layer, as shown in Figure 3.9. This approach attempts to replicate the equivalent energy deposited by raster scanning across the surface. Adiabatic conditions were imposed on the remaining part surface, through the assumption that conduction through the powder is negligible. In order to reduce the number of DOF used, a further simplification was aggregating layers such that 1 model layer (1 mm) was equivalent to 20 physical layers (50 μm). The layer heat flux approach significantly reduces the time dependency when modelling using this approach, becoming only a function of the part volume.

Experimental measurements to measure both the residual stresses and distortion on a T-shape cantilever, using neutron diffraction, and cantilever testing method showed a deviation of 10% with their FE model, although some regions such as the upper surface the residual stress values varied significantly. This error was attributed to the measurement resolution using neutron diffraction. This modelling strategy was adopted subsequently by Neugebauer et al. on industrial problems [134], however, the method is limited by its inability to resolve the effect of laser scan strategy on residual stress.

To overcome the previous limitation, a layer based model was proposed by Keller et al., which used a characteristic strain determined using a *meso*-scale thermo-mechanical model [135]. The anisotropic characteristic strain tensor was calculated using the average strain $\bar{\epsilon}$ in a hatched area obtained using the *meso*-scale model, as shown in Figure 3.10(a). Various test cases were developed with different characteristic strains to account for different laser scan strategies. The characteristic strain was then used as the initial stresses in a mechanical analysis, with each model layer activated gradually, as illustrated in Figure 3.10(b). The difficulty with this method is that it cannot resolve geometrical effects of the laser scan strategy because the inherent strain is constant across

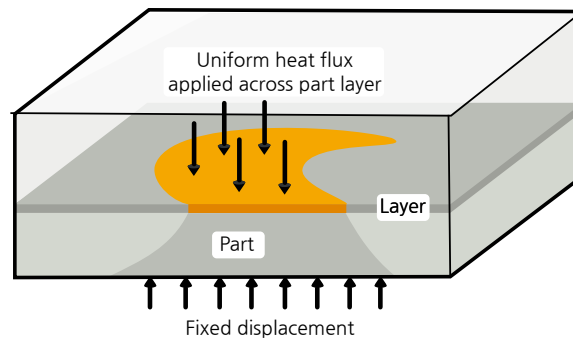


Figure 3.9: Illustration of the uniform instantaneous heat flux layer approach used for building a component

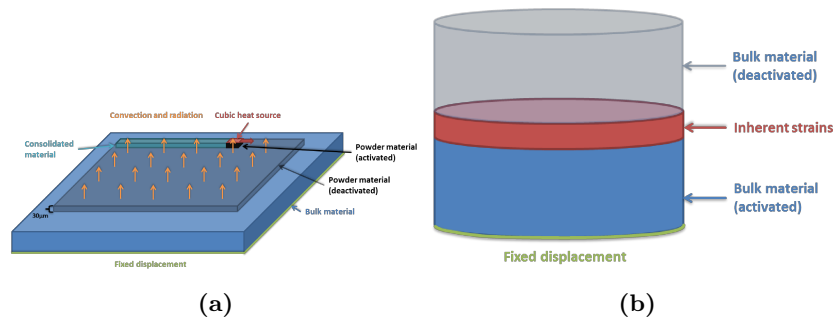


Figure 3.10: Illustration of multi-scale methodology proposed by Keller et al. [135] showing a) their thermo-mechanical simulation of a hatched region to obtain an inherent strain used in b) their *macro*-scale model to simulate the part deformation

the entire part volume. Further approaches have been developed by Seidel et al. [136] and Li et al. [137] by applying a non-uniform heat flux across a sub-region within a layer, as shown in Figure 3.11. This could account to some degree the influence of laser scan strategy employed, since localised thermal gradients were created across the layer geometry.

Francois et al. developed a thermal model using an equivalent line based Gaussian heat flux across each scan vector, with an equivalent line energy density of a moving laser source [138]. This method is restricted to thermal analysis only, because the thermal gradients parallel to each scan vector cannot correctly develop the residual stresses. However, it is an alternative approach to improve the throughput in order to understand the thermal dissipation within a large structure.

Wang et al. demonstrated a ‘sub-area’ method for improving performance when simulating the direct energy deposition (DED) process [139]. Essentially, their method was a form of domain decomposition method (DDM), but regions were isolated based on physical separation within the process. Unlike conventional

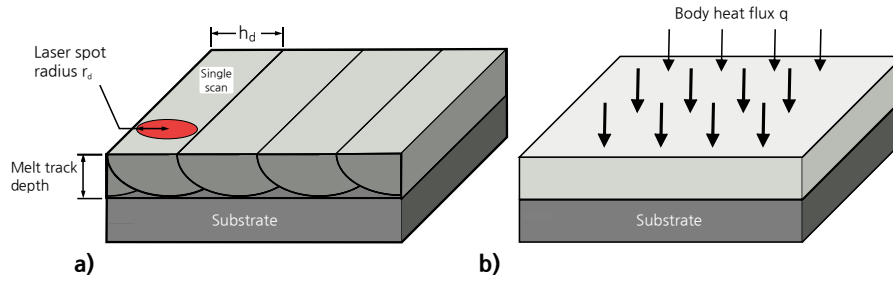


Figure 3.11: Equivalent heat source model proposed by Li et al. [137] showing a) the equivalent energy deposited using a series of hatches into b) the aerial equivalent using a volumetric heat flux

DDM methods, these are solved completely independently and in parallel. In their model, thermal state and residual stress distributions from each sub-analysis were superimposed together because each region was assumed to have negligible influence on each other. The overall benefits are increasing concurrency by segmenting regions to multiple computers and reducing the maximum memory required. This form of DDM is not trivial to apply to every process, but applying the principles of DDM can significantly improve the scalability of process simulations.

3.4.2 Adaptive meshing techniques (HP-FEM) and XFEM

Adaptive refinement of elements within the domain is a suitable approach for improving the convergence of non-linear problems, by specifically reducing the discretisation errors near the melt pool and regions featuring high temperature gradients. Adaptive refinement of mesh elements can be achieved either by

- **h** - element subdivision
- **p** - polynomial degree within an element.

Solvers can provide automatic refinement based on a local error function, such as temperature gradient, plastic deformation etc., however, usually only the h-refinement is available in commercial FE packages. For the simulation of AM processes, element subdivision has been applied based on a temperature gradient criterion by Riedlbauer et al. [131], and an octree coarsening routine performed was used layer-wise by Denlinger et al. [140]. The performance benefits were not quantified by the authors. Zeng et al. focused on applying a dynamic adaptive mesh localised to the melt pool. Their model used a moving mesh strategy to reduce discretisation errors created by the high thermal gradients within the melt pool [30]. In their method, a fine resolution irregular mesh of a fixed size,

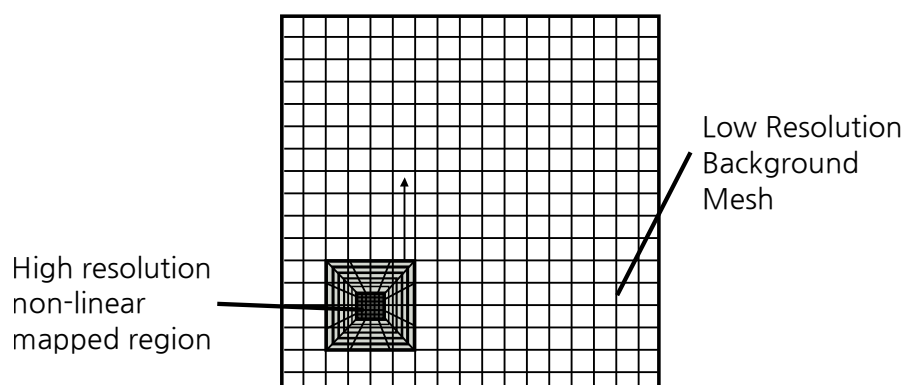


Figure 3.12: Illustration of dynamic adaptive mesh localised to position of the laser position proposed by Zeng et al. [30]

as shown in Figure 3.12, was translated by one coarse element to reduce the complexity of mapping between dual meshes.

The non-linear thermal behaviour was isolated into the fine detailed sub-region. The benefit of fixed moving meshes (with fixed nodal positions) is the potential improvement in performance. Time is gained by removing the need for complete re-assembly of the entire global stiffness matrix by substituting those only changed in the detailed sub-region. It was found that their own custom FE code using Matlab was approximately 66x faster than the same model created in ANSYS FE Package (11 hours to complete) for scanning one layer. This method poses the problem that it assumes complex thermo-mechanical behaviour is isolated inside a small region, and if this region is not sufficiently large enough it will fail to account for the elongated melt pool and heat tail occurring during the process. The performance of this method for coupled thermo-mechanical analysis was not reported.

Spectral finite element frameworks such as Nektar++ [141], which include hp adaptivity are far less common. These enable variable and arbitrary polynomial order for elements within a domain, and can capture efficiently the high thermal gradients associated with this process. High order polynomials offer significant improvement in convergence for the equivalent number of DOF when using solely h-adaptivity [142]. A high-order polynomial finite element framework has been developed by Kollmannsberger et al. with multi-level hierarchical h and p adaptivity for modelling the laser melting process [143]. The application of hp finite element models are less mature compared to established commercial FE packages which at most provide 2nd order element formulations.

The extended finite element method (X-FEM) is used to provide local enrichment without requiring modifications to the original mesh. It has been extensively

used for modelling crack propagation in materials by allowing the crack interface to be modelled without re-meshing techniques. X-FEM potentially has the advantage that regions consisting of singularities can be accounted for using special enrichment functions. X-FEM has not been widely used in the context of SLM modelling, however, because of its limited availability in commercial FE packages.

3.4.3 Global-local analysis

The global-local (GL) method first solves the local solution either using a higher resolution model, or using an enrichment technique such as HP-FEM or X-FEM. The solution of the local boundary conditions is applied to the global domain and solved.

1. A set of local domains Ω_L within the global domain Ω_G are specified
2. The coarse global domain is solved
3. Boundary conditions applied to local domain Ω_L from global domain Ω_G
4. Enrichment using HP-FEM and/or XFEM is used and then solved
5. Local domain boundary conditions applied to global domain and solved

Two computational studies have looked at the advantage of such refinements using a global-local method [144, 145]. Their motivation for using the global-local approach was to improve convergence and accuracy for highly-localised non-linear behaviour in both plasticity and thermal problems. Their results showed GL technique improved accuracy and reduced the number of DOF compared to using a global HP-FEM method alone. The other benefit is the local domain size should remain independent of the global domain.

The application of the GL technique is not necessarily restricted to incorporating element based refinement techniques into the local model. This technique could be used to isolate behaviour within models, to improve performance. For instance, the global domain may be treated as a linear, steady-state analysis, whereas the local model may be treated as a transient non-linear analysis; the former requiring less computational time [146]. Thus, the performance can be tuned appropriately as seen in the simulation of welding large assembled structures [147].

3.4.4 Spectral methods

A dual-scale thermal analysis method of selective laser melting was developed by Patil et al. who mapped a *micro*-scale model onto the mesh of their *macro*-scale

model [148, 149]. The *fine*-scale model used a conventional non-linear FE analysis to obtain an accurate prediction of the thermal history in the melt pool and surrounding HAZ. Their *macro*-scale model relied on slow temperature evolution throughout the powder bed, and therefore assumed steady-state thermal behaviour as part of their dimensional reduction scheme for each layer. To obtain the solution to the system, the eigenvalues and modes were calculated to reduce the computation complexity of the problem. The overall performance and potential limitations of this method have not been reported in the literature.

Another approach for potentially reducing the computational cost of the thermal system, is the use of discrete fast fourier transform (FFT) to solve the set of Partial differential equation (PDE)s. The system of equations is transformed into the time domain, and the inverse transform is used to find the solution to the system. FFT are extremely fast for solving systems compared to FE formulations. This maths has been applied in microstructural simulations for the prediction of grain growth, and the prediction of bulk mechanical properties from the grain structure, obtained from crystallography measurements [150]. A major difficulty with this method, however, is re-formulation of boundary conditions so they are periodic.

3.4.5 Multi-scale modelling

Even after considering the model simplifications and techniques described in the previous section, thermo-mechanical models of SLM are too expensive to be feasibly used for the prediction of residual stress in industrial parts. Simulations which account for each scan vector during the build process are too expensive to be used in iterative based topology optimisation techniques during the design stage. The use of multi-scale methodology is a far more efficient solution for simulating the entire build envelope in SLM, and naturally the process of SLM lends can be decomposed into three distinct scales (*micro*, *meso* and *macro*).

Li et al. used three analyses steps at the *micro*, *meso*, and *macro* scale to develop their multi-scale model [140]. A transient thermal simulation was performed for the interaction of the laser and the powder bed, which was subsequently used to find a representative temperature history. Afterwards a thermo-mechanical analysis consolidated the previous thermal history by sequentially activating each region in the *macro*-scale part. However, their method cannot accurately capture the creation of residual stresses in the hatched area because a distributed volumetric heat flux was applied. Additionally, it required an expensive transient thermo-mechanical analysis to be performed.

The use of an applied plastic inherent strain was proposed by Ueda et al. [151], and subsequently used in the process modelling of welding [152]. A

significant reduction in computation time was achieved for mechanical analyses because the time dependency of the process was removed by not having to explicitly model the movement of the laser across each weld bead. The method is summarised as follows [152]:

1. High-resolution transient thermo-mechanical analysis is performed
2. Plastic strain tensor is calculated across whole domain after cooling to ambient temperature T_A
3. Plastic strain tensor is mapped to *macro*-scale model
4. Mechanical analysis is performed with the *macro*-model to estimate the final distortions.

This method was incorporated as an anisotropic strain component to define a homogeneous stress property for solid material in SLM simulations by Keller et al. [135], and also by Denlinger et al. [153]. Li et al. developed a multi-scale model using three analysis scales [153]. In their *micro*-scale model the temperature profile for a single scan vector was obtained. The temperature profiles were used as boundary conditions in an intermediate thermo-mechanical (*meso*-scale) analysis to obtain the stress field for a hatch zone. The residual stress fields for these hatch zones were later mapped onto a mechanical (*macro*-scale) analysis. Their method was only performed for a single layer, assuming an orthogonal 0-90° rotation of scan vectors. However, the assumption that both thermal and mechanical response behave independently between hatch island regions was not validated.

Incorporating the stress field obtained in the *macro*-scale analysis onto a larger domain is a potential methodology for reducing the computational resources required for simulating this process. The literature has indicated that decomposing regions into small areas could make this method feasible, because island regions appear to behave independently and inherent stresses are not dependent on the overall part geometry. This is complemented that the overall distortion and resolved stress field within a part is mainly dependent on the geometrical combination of planar stresses inherent in the material generated by the scan vectors within a layer [77].

3.5 Summary of literature and identified gaps in the literature

In order to understand the factors affecting residual stress and its prediction requires the creation of a thermo-mechanical model. Coupled thermo-mechanical

analyses of SLM have been reported by several researchers, as discussed in Section 3.2, yet the underlying mechanisms for the generation of residual stress remain less understood. Thermo-mechanical models of SLM in the literature tend to be line based (either single tracks or thin walls), with the exception of Hodge et al. [34] and Roberts [154], however, the resolution has been insufficient to capture any significant understanding of the process. Crucially, the aerial effect of scan strategy and the thermal history have not been thoroughly investigated.

Current models have not identified the geometrical relationship between the choices of laser scan strategy with the generation of residual stress. Also, there is a lack of knowledge relating the temperature field created with the residual stress generated by the choice of laser scan strategy. Patil et al. concluded that due to rapid cooling in sub-regions, the choice of laser scan strategy could potentially control the temperature history and magnitude of the residuals stresses generated [149]. Additionally, knowledge related to the effect of the substrate remains largely unexplored. This information would help process optimisation and the development of new scan strategies that could potentially mitigate the extent of residual stresses.

Currently, the performance limitations of methods used in FE based *meso*-scale simulations restrict their analysis to small regions, and severely limit their utility for research. As discussed in Section 3.2, there is a need to improve current modelling strategies to improve the simulation throughput in order to increase the size of region captured beyond a 1 mm square with a satisfactory resolution. This would enable better understanding of the effect of scan strategies and develop more optimal solutions.

Multi-scale methods, discussed in Section 3.4.5, show great potential for providing a modelling framework that can incorporate the hierarchy of physics at different scales, in a computationally efficient manner. This modelling approach has been considered, but has yet to be thoroughly investigated or developed, in order to provide feasible and reasonably accurate prediction of residual stress and distortion for use in design tools.

Following the literature review into numerical approaches of modelling SLM, the identified gaps in research are outlined below:

1. The *micro*-scale behaviour is experimentally very difficult to capture due to the random nature of powder, and the complex thermo-physical phenomena at this scale. Therefore, highly detailed *micro*-models, require very high spatial and time resolution, which is computationally very expensive. As a result, this area of modelling remains challenging.
2. Understanding of the build-up of residual stress at the *meso*-scale is limited by the performance and resolution of thermo-mechanical models. Suitable

strategies have been suggested, but have not reported any meaningful results with respect to residual stress.

3. There is interest towards developing multi-scale methods to couple the analysis scales together from different simulation types, especially for part scale prediction of residual stress and distortion. These strategies remain undeveloped and their underlying assumptions require further investigation.
4. Design tools available for supporting research on experiments and models are currently restrictive for commercial SLM platforms. Without these, it becomes significantly difficult to fully explore the effects of scan strategy experimentally.

Chapter 4

Material properties used for simulation work

Thermo-mechanical numerical simulation requires an extensive list of temperature dependent thermo-physical properties for a given material. This work accounts for the manufacturing of components using Ti-6Al-4V favoured for its use in the aerospace industry [2, 155]. This chapter documents the powder morphology of Ti-6Al-4V in Section 4.2, with the temperature dependent properties obtained using the laser flash analysis method in Section 4.2.1 and compiled sources obtained from literature which are presented in Section 4.2.2. The thermal conductivity measurements of the powder obtained using the laser flash method are then compared with powder thermal-conductivity models in Section 4.2.3. Finally, the temperature dependent mechanical properties obtained through the literature are presented in Section 4.3.

4.1 Powder properties

The Ti-6Al-4V powder used in the selective laser melting process was supplied by LPW Technology UK, produced through the plasma atomisation process. Nominal compositions of the pre-alloyed metal powder are listed in Table 4.1.

The particle size distribution was measured using a Malvern Mastersizer

	Ti	Al	V	Fe	C	N	H
%	89.7	6.10	4.10	0.07	0.01	0.01	0.01

Table 4.1: Nominal composition of pre-alloyed Ti-6Al-4V powder produced in the plasma atomisation process

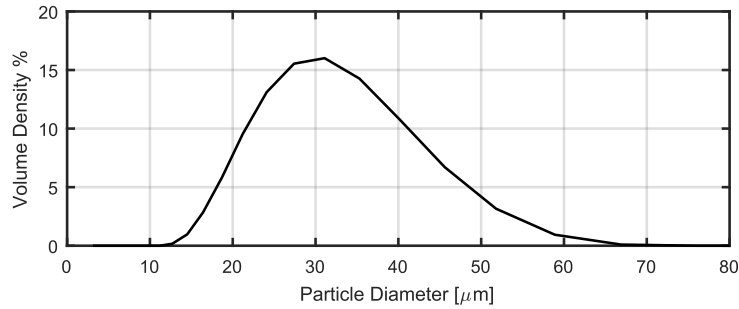


Figure 4.1: Measured particle size distribution for Ti-6Al-4V virgin powder stock

particle analyser with virgin powder stock material. The powder distribution is shown in Figure 4.1, and was found to have a mean diameter size $D_p = 30.5 \mu\text{m}$.

4.2 Temperature dependent thermal properties

Temperature dependent properties are required for the thermo-mechanical model in Chapter 6. A set of measurements for the temperature dependent thermal conductivity values of SLM powders were undertaken by Alderson et al. [156]. However, the values reported did not appear to agree with analytical models of powder thermal conductivity presented in literature [32, 44]. Therefore, measurements were made using the laser flash analysis technique to obtain the temperature dependent thermal conductivity values.

4.2.1 Measurement of thermal conductivity using laser flash analysis

The laser flash analysis (LFA) technique measures the thermal diffusivity of a sample with uniform thickness inside a controlled heated chamber under a protective atmosphere, as shown in Figure 4.2(a). The machine emits a laser pulse onto the bottom surface, and the temperature difference ΔT on the upper surface is measured by a detector. The half-time signal shown in Figure 4.3 is captured showing the temperature difference against time.

The thermal diffusivity of a material is obtained by locating the half-time signal, $t_{1/2}$, where the temperature rise is half of the maximum observed temperature ΔT_∞ . The thermal diffusivity is then estimated using the following relation [157],

$$\alpha = \frac{1.38}{\pi^2} \frac{L^2}{t_{1/2}}, \quad (4.1)$$

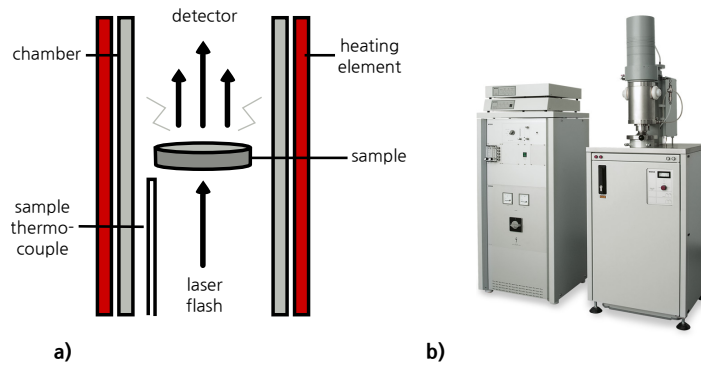


Figure 4.2: Illustration of the laser flash apparatus for measuring the thermal diffusivity of a sample and b) the Netzsch LFA 427 laser flash analysis machine used for the measurement

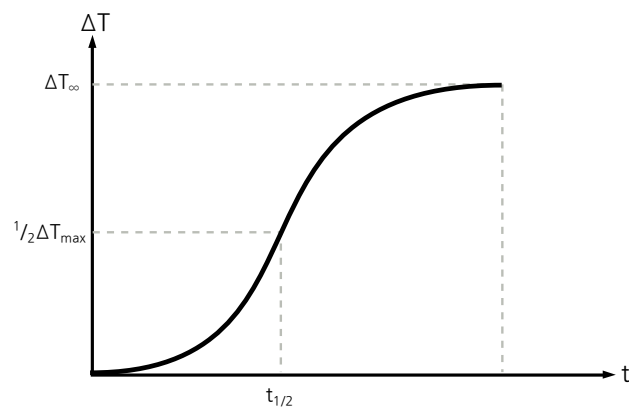


Figure 4.3: Diagram showing the half-time signal measured by the detector after the laser pulse has been emitted and conducted through the sample

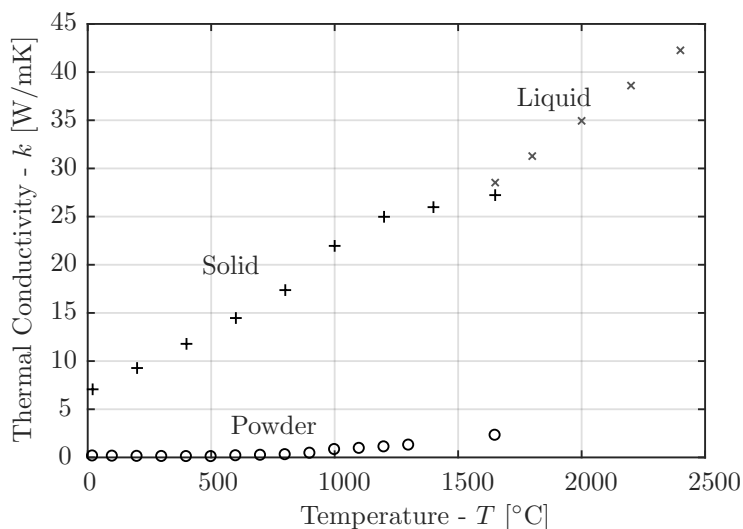


Figure 4.4: Graph of compiled thermal conductivity values for the powder, solid and liquid states of Ti-6Al-4V.

where L is the characteristic uniform thickness of the sample. The temperature dependent thermal conductivity $k(T)$ for the specimen can then be calculated from the thermal diffusivity α , using the relationship

$$K(T) = \alpha(T)\rho(T)c_p(T). \quad (4.2)$$

Independent measurements of thermal diffusivity were made for Ti-6Al-4V powder and solid SLM built samples. Both samples were tested using a Netzsch LFA 427 laser flash analysis machine (Figure 4.2(b)) under a vacuum atmosphere purged with an argon backflow, from room temperature up to 1400 °C. A cylindrical specimen with a diameter of 12.7 mm and 2 mm depth was prepared using a Realizer SLM 50 to measure the thermal diffusivity of the solid specimen. The powder sample was placed inside an 85 μ L sapphire crucible and spray coated with graphite on the top and bottom surfaces to increase absorptivity and emissivity of the sample.

4.2.2 Measured thermal properties

The thermal conductivity values for the liquid state were taken from experiments performed by Bovineau et al. [158]. The thermal conductivity values for all states are presented in Figure 4.4, and the supporting properties required for its calculation are listed in Table 4.2 and Table 4.2. The values of emissivity ε_{em} for Ti-6Al-4V shown in Table 4.4 were compiled using two sources [158, 159].

Temperature [°C]	Specific heat capacity c_p [J/KgK]	Density ρ [g/cm ³]	Thermal diffusivity α [$\times 10^{-6}$ m ² s]	Thermal conductivity k [W/mK]
20	520	2.65	0.11	0.145
100	516	2.65	0.09	0.125
200	505	2.64	0.08	0.104
300	492	2.63	0.07	0.092
400	480	2.62	0.07	0.083
500	473	2.61	0.06	0.078
600	472	2.6	0.14	0.167
700	483	2.59	0.17	0.216
800	507	2.58	0.21	0.279
900	548	2.57	0.31	0.43
1000	610	2.56	0.52	0.813
1100	696	2.55	0.53	0.934
1200	808	2.54	0.53	1.09
1300	951	2.53	0.53	1.27

Table 4.2: Temperature dependent material properties used for the powder form of Ti-6Al-4V. Specific heat capacity and density taken from [156]

Temperature [°C]	Specific heat capacity c_p [J/KgK]	Density ρ [g/cm ³]	Thermal diffusivity α [$\times 10^{-6}$ m ² s]	Thermal conductivity k [W/mK]
20	543	4.42	2.95	7.07
200	566	4.39	3.74	9.28
400	599	4.36	4.51	11.8
600	636	4.33	5.25	14.5
800	675	4.30	5.98	17.4
1000	713	4.27	7.22	22.0
1200	745	4.24	7.91	25.0
1400	770	4.21	8.02	26.0

Table 4.3: Temperature dependent material properties used for solid Ti-6Al-4V. Specific heat capacity and density taken from [156].

Temperature [°C]	Emissivity ε_{em}
25	0.121
100	0.155
200	0.178
300	0.205
400	0.228
500	0.331
600	0.561
700	0.591
900	0.600
1500	0.600
1650	0.405
1900	0.402
2100	0.400
2300	0.398
2600	0.395

Table 4.4: Temperature dependent emissivity values used for both powder and solid compiled from two sources ([158, 159])

4.2.3 Comparison of experimental measurements with analytical models

The experimental measurements for Ti-6Al-4V powder were compared with two different powder thermal-conductivity models proposed by Zehner-Schlünder and Gusarov-Kovalev in Section 2.3.2. The emissivity of the solid particles ε_{em} were taken from Table 4.4. The gaseous phase was assumed to be argon at atmospheric pressure ($p_{atm} = 1.01 \times 10^5$ Pa), with the temperature dependent thermal conductivity k_g listed in Table 4.5. Intermediate values of these properties were linearly interpolated over the temperature range as necessary. Both models were calculated using a powder packing factor $f_p = 0.6$ [19], with a mean powder particle diameter $D_p = 30.1 \mu\text{m}$.

Temperature [°C]	300	400	500	600	800	1000
Thermal conductivity k_g [W/mK]	0.0177	0.0223	0.0264	0.0302	0.0368	0.0427

Table 4.5: Temperature dependent thermal conductivity values of argon gas taken from Roger and Mayhew [160]

When using the proposed Zehner-Schlünder model in equation 2.17, the following non-dimensional parameters were used as suggested by Dai and Shaw [124]: the deformation parameter for the particle $B = 1$, the view factor $F = \frac{1}{3}$, and flattened surface fraction of particle in contact $\phi_{fs} = 0$.

In the model proposed by Gusarov-Kovalev in equation 2.23, the following parameters were used: the adiabatic exponent of argon gas, $\gamma_g = \frac{5}{3}$, the

molecular mass of argon $M_g = 39.95 \times 10^{-3}$ kg/Mol, and the mean coordination number $N = 7$.

A comparison of the measured thermal conductivity presented in Section 4.2.2 with that predicted with the two models can be seen in Figure 4.5. The measured thermal conductivity measurements decreases from 0.15 W/mK to 0.78 W/mK at ~ 500 °C, whilst the proposed models show a continuous increase in thermal conductivity. The Zehner-Schlünder model does not show agreement with experimental measurements, throughout the entire temperature range. The Gusarov-Kovalev prediction shows a good agreement with the thermal conductivity at room temperature, but again does not follow the decreasing trend.

This decrease in thermal-diffusivity of the powder with temperature has not been reported previously, although previously reported values by Alderson et al. [156], also do not show agreement between experimental measurements and the models. The significant increase in thermal conductivity beyond 500 °C is associated with initial exothermic sintering behaviour at this point. The effect of sintering is identified from a small peak in the specific heat capacity at 525 °C, as shown in Figure 4.6. The temperature dependent specific heat capacity $c_p(T)$, was obtained using differential scanning calorimetry (DSC). The process of sintering increases the network of path connections between adjacent particles, and therefore improves thermal conduction throughout the medium.

Both proposed models consider thermal conduction between touching particles. The Gusarov-Kovalev model accounts for thermal convection of the gaseous phase between pores, whereas the Zehner-Schlünder model includes the Damköler radiation term k_r (equation 2.19). However, it was acknowledged by Gusarov et al. to provide a negligible contribution at low temperatures ranges.

Fundamentally these models are limited because they cannot account for the sintering mechanisms observed when processing these powders. However, the relative inaccuracy using the model should not be significantly important in the finite element model, since the time-scales involved in melting the powder are very small. The sintering behaviour would only become important specifically for laser scan strategies involving a pre-sintering phase.

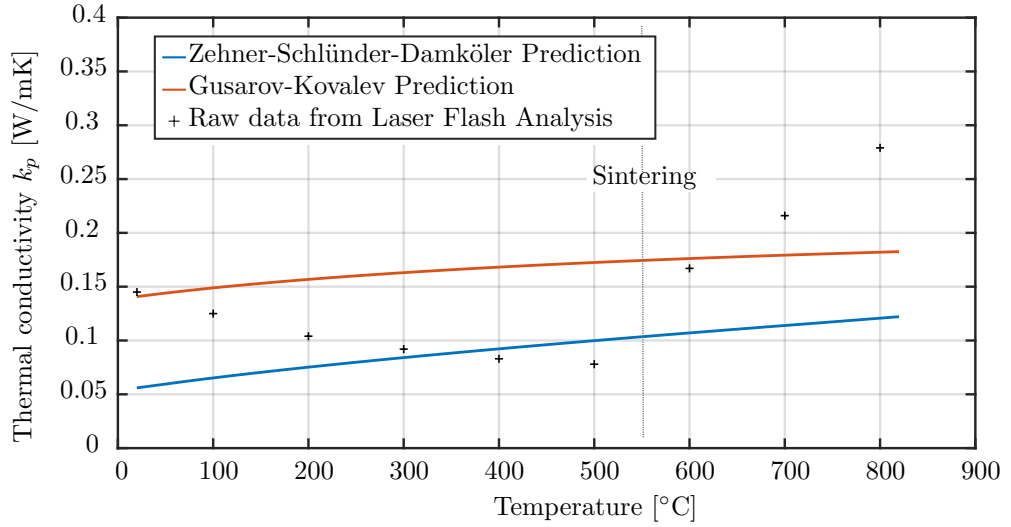


Figure 4.5: Graph showing effective thermal conductivity of Ti-6Al-4V powder k_p , obtained from the laser flash measurements compared with predictions obtained from the Zehner-Schlünder and Gusarov-Kovalev models.

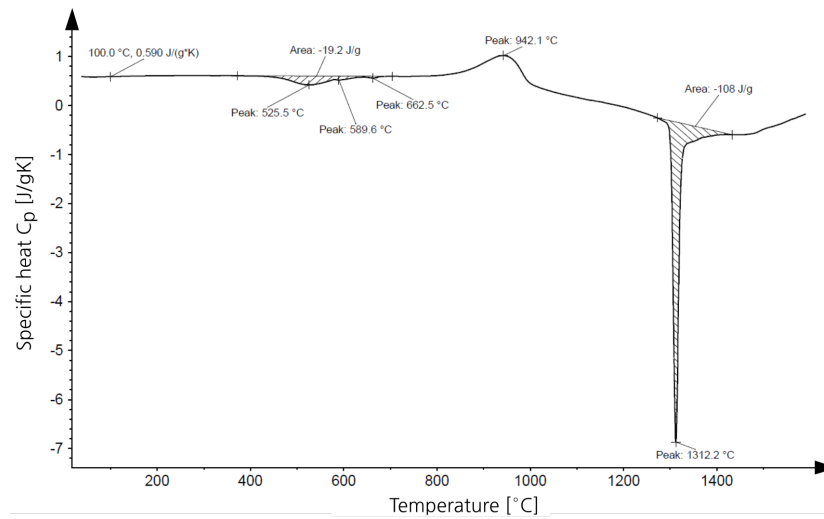


Figure 4.6: Measurements of the temperature dependent specific heat capacity $c_p(T)$ obtained using DSC.

4.3 Temperature dependent mechanical properties

The temperature dependent mechanical properties for Ti-6Al-4V were obtained from sources available in the literature. The linear coefficient of thermal expansion, α_{CTE} , is listed in Table 4.6 for Ti-6Al-4V. The Poisson's ratio is assumed to be $\nu = 0.342$. Temperature dependent properties for the yield stress σ_y and the plastic tangent modulus H_p are listed in Table 4.6.

Temperature [°C]	Linear CTE $\alpha_{CTE} [\times 10^{-6} \text{ 1/K}]$	Young's modulus E [GPa]	Yield stress σ_y [MPa]	Plastic tangent modulus H_p [GPa]
24	8.78	125	1000	0.7
94	9.83	110	630	2.2
205	10.0	100	630	2.2
317	10.7	100	525	2.2
428	11.1	80	500	1.9
539	11.2	74	446	1.9
650	11.7	55	300	1.9
761	12.2	27	45	2
872	12.3	20	25	2
1094	12.4	5	5	2
1650*	12.5	0.1	0.1	0.1

Table 4.6: Temperature dependent mechanical properties for bulk Ti-6Al-4V [154, 161]. * linearly extrapolated values

4.4 Summary

The temperature dependent thermal conductivity of Ti-6Al-4V powder used in SLM and the solid parts obtained using processing were obtained experimentally using the laser flash method. The experimental thermal conductivity measurements were then compared with two analytical models proposed by Zehner-Schünder and Gusarov-Kovalev. It was found in both models that the order of magnitude of the prediction was correct at room temperature. However, the thermal conductivity steadily decreased until 500 °C in the experimental measurements. Above this temperature, sintering behaviour in the powder was observed in DSC measurements causing the thermal conductivity to increase. Both analytical models exclude the effect of sintering, therefore these models are only suitable for the prediction of thermal conductivity at low temperatures. Finally, the temperature dependent thermo-mechanical properties used for both the thermo-mechanical analysis (Chapter 6) and the multi-scale method (Chapter 11) were presented.

Chapter 5

Method for generating and processing laser scan geometry

It was identified in the review of the literature that a strong coupling between the triad of design, pre-processing, and simulation are required in order to fully exploit the manufacturing process. The ability to perform specific experiments to understand the effect of scan strategy, laser parameters, and directly manufacture components is not feasible with current commercial programs. Established commercial tools were designed solely for manufacturing 3D parts and offered no opportunity to experiment with novel scan strategies and design methods. Additionally, there was no scope to make a direct comparison within simulation studies, since the generated laser scan geometry couldn't be extracted.

To fully investigate the effectiveness of scan strategies through numerical and physical experiments, requires the ability to generate the scan vector geometry and export these directly to the SLM systems. In particular, using the multi-scale method in Chapter 11, the simulation model uses scan islands generated when using the checkerboard scan strategy and requires information of the individual laser scan vectors hatched for each clipped island.

A method for slicing and hatching volumetric representation of the geometry into machine build file is presented in Section 5.1 to support the experiments and simulations, because this is not available in commercial pre-processing software. After generating the laser scan vectors for a part, these can be exported directly into compatible machine build files or processed directly by the simulation using a custom developed library called, *libSLM*, which is presented in Section 5.2.

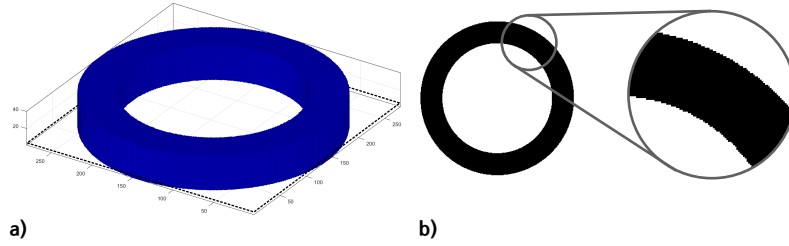


Figure 5.1: a) Volumetric model of a ring and b) a cross-section taken through the model showing the aliasing effects to discretise the model

5.1 Volume hatching method

The generation of scan vector geometry for a slice-layer is achieved by a series of geometric operations infilling and offsetting sliced boundaries. All current, commercial pre-existing pre-processing methods use triangular mesh representations for the surface geometry of a part. In this work, a volumetric (voxel) representation was chosen because this enables an efficient, direct mapping with the computational models, which use a structured grid. Potentially, volumetric quantities can also be stored and referenced with the geometry. The method was implemented using Matlab [162] to ease prototyping custom scan strategies, and take advantage of existing image processing algorithms.

5.1.1 Slicing the voxel representation

This method assumes a uniform binary segmented voxel grid is provided as input with (void = 0, solid = 1) representing the structure. The resolution of the voxel model determines the level of pre-processing required, as shown in Figure 5.1.

Aliasing or ‘terracing’ of surfaces are often encountered along regions of high curvature in low resolution voxel grids. Convolution filters can, to an extent, smooth-out these effects [163]. A simple pre-processing routine was used to smooth the voxel model. Firstly, the voxel model was upsampled by a factor f_{scale} using Matlab’s *imresize* function to allow for diffusion when applying a 3D Gaussian blur convolution filter $G(\sigma)$ to this grid. Then the binary grid was reproduced using a threshold operator of factor $f_{limit} = 0.5$, to rebuild the boundary. The effect of this smoothing process in a 1D image is illustrated in Figure 5.2.

The slicing mechanism is trivial to implement in a voxel environment compared to stereo lithography (STL) files, where slice edges require sorting to guarantee correct shape orientation. Given the layer thickness desired, the slice’s Z position

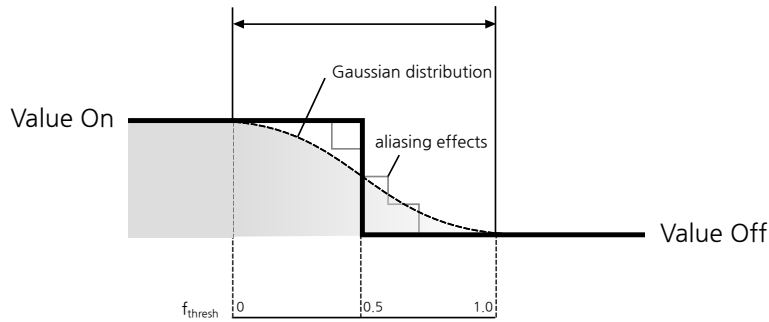


Figure 5.2: Illustration showing the smoothing effect applied in 1D. Upscaling reduces the effect of aliasing whilst increasing the value of σ broadens the Gaussian distribution, increasing smoothing

is calculated to scale correctly with the voxel unit scale size and image upscaling factor, as shown in Figure 5.2. The SLM machine has a fixed layer thickness, and therefore adaptive layer slicing algorithms cannot be used.

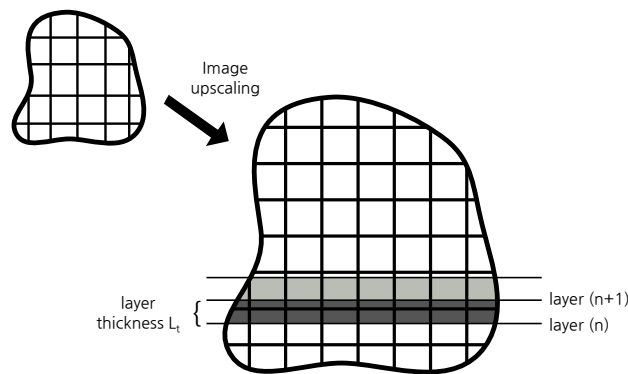


Figure 5.3: Diagram showing cross-sections for each slice are taken based on the layer's z-position after upscaling the image and based on the voxel unit scale used for the model

Having obtained a slice of a voxel model (2D image), an image segmentation algorithm was then performed to identify the boundaries of each cross-section using the built-in Matlab function `bwboundaries`, which is based upon a modified Moore-Neighborhood tracing algorithm with Jacob's stopping criteria [164]. This algorithm traces edges of binary images in clockwise order, as shown in Figure 5.4, and guarantees closed polygons are detected with the correct fill order.

The results of this algorithm are edges with a length of the voxel unit, and this will create aliasing when using a combination of low resolution input voxel models with large voxel unit size. To reduce the number of line segments, line

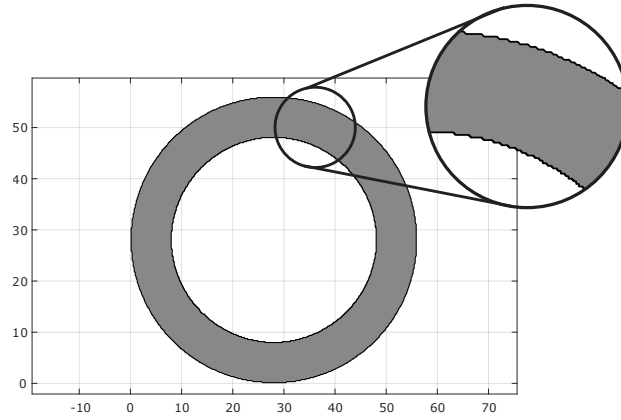


Figure 5.4: Identification of closed boundaries obtaining using Moore-Neighbourhood tracing algorithm

simplification was performed using the Douglas-Peucker algorithm [165] with the added effect of smoothing the contour, as shown in Figure 5.5.

The resultant edges are transformed into closed polygons which can contain holes. The edge sorting was done using the libClipper library [166], which provides geometrical operations such as polygon clipping, offsetting and the calculation of complex hulls. In Matlab, MEX can be used to interface between a c++ library and perform commands natively within the Matlab environment. A MEX interface was created to perform the functions available in the libClipper library natively from within Matlab.

5.1.2 The hatching process

The hatching process generates both the contour and hatch laser scan geometries used for manufacturing a component from the boundaries created in the previous section. Upon obtaining a set of closed contours for each layer, these are separated and processed independently. Geometric properties such as the region's centroid and area are trivial to obtain, which could assist the development of custom geometry specific laser scan strategies.

Firstly, boundaries are offset to form the contours for each cross-section. Interior regions require infilling using a chosen scan strategy, such as the meander, checkerboard and spiral scan strategies shown in Figure 5.6. Regardless of choice, a series of vectors covering the region are intersected with the boundary. When generating the checkerboard islands, hatched square tiles are replicated in X,Y, and are then intersected with the boundary. Geometrical information (centroid, rotation, clipped coordinates) for each island was stored, which was used for generating the input for the multi-scale model presented in Chapter 11.

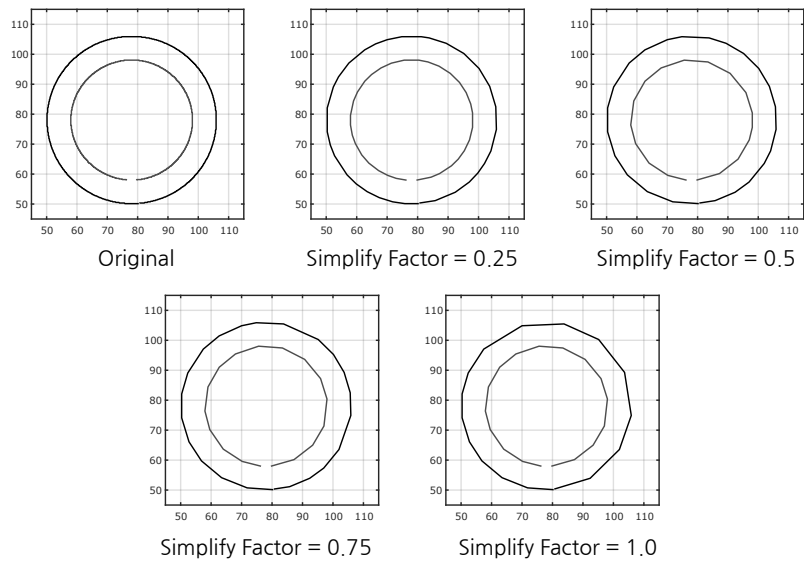


Figure 5.5: Different levels of line simplification applied to ring model boundaries

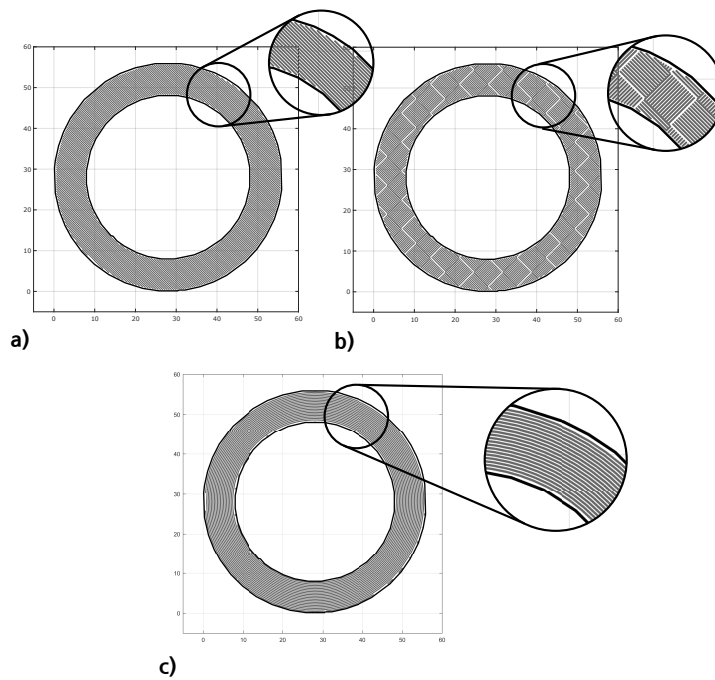


Figure 5.6: The hatching procedures applied on the ring model using the typical a) alternating meander scan strategy and b) checkerboard scan strategy, and using an unconventional custom c) a spiral infill.

Voxel unit [mm/voxel]	0.1
Upscaling Factor f_{scale}	2
Gaussian blur sigma σ	5
Greyscale threshold factor f_{thresh}	0.5
Line simplification tolerance	0.2

Table 5.1: Pre-processing parameters used for preparing the model for slicing



Figure 5.7: Photograph of a ring geometry manufactured in Ti-6Al-4V using SLM with the volumetric hatching method

After completion of the hatching process, the laser scan geometry is stored in a generic data structure that can be exported using *libSLM* into a suitable format depending on its intended use, as discussed in Section 5.2. The volumetric hatching method is demonstrated using the ring geometry shown in Figure 5 1(a), which was sliced and hatched using a 3 mm checkerboard island strategy with parameters in Table 5.1 and with additional support structures generated through Magics [167]. The ring was produced in Ti-6Al-4V using a Realizer SLM 50 and is shown in Figure 5.7.

5.2 Functionality for interpreting machine build files - *libSLM*

A library, *libSLM*, was created in order to simulate the manufacturing process more efficiently and closely integrate laser scan geometry into a design methodology. The library was built using c++, and the Qt library [168] to provide a method for reading and processing the machine build files in commercial SLM systems.

The role of this library is to provide facilities to read and parse generated build file formats generated for commercial SLM machines, which ultimately

could be used in both design and simulation, as illustrated in Figure 5.8. Additionally, it can write directly to these formats using a universal schema for defining the laser parameters and geometry, either within a c++ or Matlab environment. Currently, no research tools exist offering this ability to explicitly control the laser parameters and geometry. The library provides routines that integrate with a simulation for providing the current position and parameters of the laser at time t , along with additional statistics such as the build time prediction.

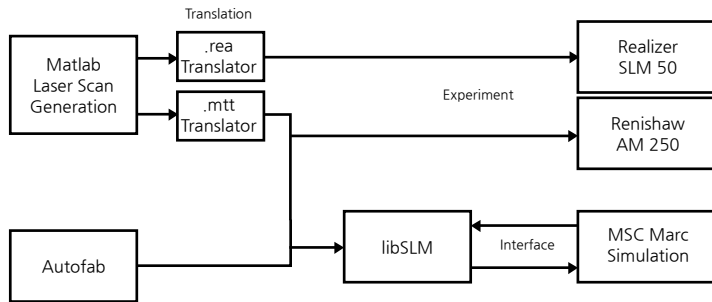


Figure 5.8: Illustration showing an overview of the transformation between generated scan vectors from Matlab translated into compatible build files, which are either used directly by the SLM platform, or interpreted by libSLM for use in simulation or design.

5.2.1 Machine build file formats used in SLM and SLS

Currently, before a component can be built, a pre-processing step is required to ‘slice’ and ‘hatch’ a set of 3D components into a representation that the SLM and SLS machine systems can interpret. This generates a series of laser scan vectors, with given laser parameters that represent the raster motion of the laser across the powder bed surface and are stored in machine build files. The size of the build file is determined by the part volume, its complexity, and the density of scan geometry used. The increased popularity for using functional-representation, and complex geometrical structures such as lattices [5], further complicates the issues of generation and portability. Currently, no reported real-time method exists in commercial systems to generate the laser scan geometry ‘on-the-fly’ from a volumetric or surface representation. Interest is currently focused on providing a closed feedback loop for responding to changing environmental conditions or the stability of the melt pool [169].

Currently, machine build files remain the preferred approach for controlling these AM systems. These files offer a compact higher-level representation compared to G-Code, which instead provide explicit commands to operate a physical component within the machine. Binary encoding provides a more compact storage format, which is essential for representing large complex volumes.

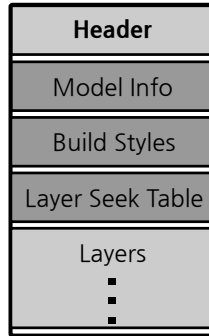


Figure 5.9: Diagram showing the typical structure of a machine build file used on SLM systems

No standardised universal format exists, and these proprietary file formats are specific to each manufacturing system. The general structure observed in these machine build files is illustrated in Figure 5.9. At the beginning, a header section defines the machine operating configuration, a set of laser parameters for each part within a build, and in some cases an address table for looking up layer slice sections. The remainder of the file consists of a series of individual layer definitions.

Each individual layer definition consists of a series of laser geometry groups that define a series of scan vectors representing a primitive type

- **Contour** - a connected series of scan lines
- **Hatches** - a series of disconnected scan lines
- **Points** - individual point exposures.

The groups are often assigned a set of laser parameters governing the exposure time, point distance (effective laser speed), and the laser power. However, some systems (e.g. Realizer SLM) permit setting laser parameters individually per scan vector within a laser geometry group. The 2D scan vector coordinates are usually stored as a consecutive list of IEEE754 floating point numbers. Some formats (e.g. Renishaw .MTT), define their own representation for storing primitive integer numbers.

The specification for the MTT file format used by SLM systems produced by Renishaw was available internally, however, the build volume of the AM 250 system, shown in Figure 5.10(a), is unsuitable for performing small experiments. The Realizer SLM 50 system shown in Figure 5.10(b) was, hence, the preferred platform for experiments, however their proprietary format was unavailable.

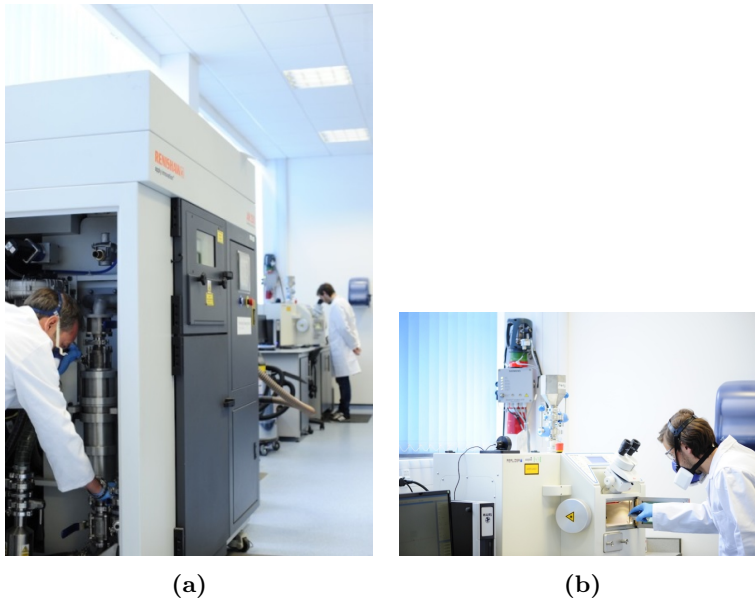


Figure 5.10: Photographs of commercial SLM systems: a) Renishaw AM 250 System and b) Realizer SLM 50

5.2.2 Disassembling the Realizer .rea format

The previous procedure for generating the realizer .rea format involved generated slices (part contour geometry) into the Focker&Schwarze .F&S format using the Magics pre-processing software [167]. The realizer control software imports the boundary slices, and implements its own hatching routines to generate the scan vectors into the Realizer .rea machine file format used by the machine. The .rea file format was disassembled, and the specification of the file format was discovered by interpreting integer and floating point binary values stored in the file and cross-referencing these to known positions and laser parameters within the geometry. Having this specification, enables complete direct control over scan geometry used and provided greater capability to perform experiments.

5.2.3 Structure of the *libSLM* library

The library consists of machine manufacture specific importers and exporters that translate between a generic storage schema and the machine build file. Additionally, functionality is built around processing the generic representation of machine build files.

A generic schema, independent from any SLM system, was used to define the laser scan geometry and laser parameters used to represent a machine build file. The representation, as illustrated in Figure 5.9, consists of a header, model

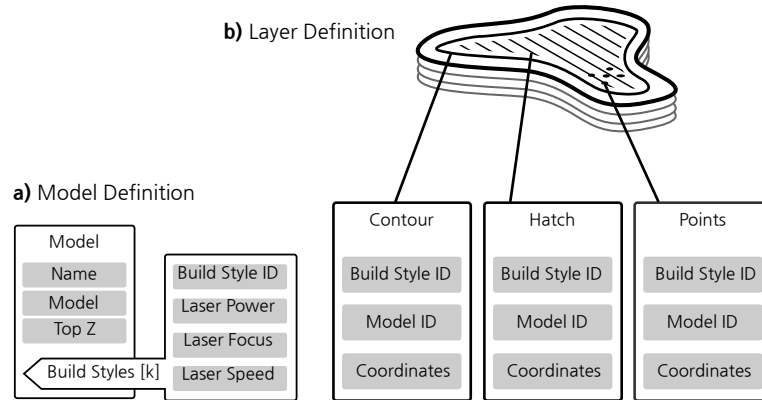


Figure 5.11: Illustration showing a) the model definition and the build styles used per model, and b) the structure of layer geometry defined in a machine build file

section, and a list of layers, and can be translated to specific machine build formats used by different vendors.

In the schema, a header provides a structure for attaching vendor specific build parameters and global values, such as layer thickness, which can be interpreted by each translator. Each part within a build contains a model that contains a set of build-styles, as shown in Figure 5.11(a), which define the set of laser parameters used for the part. As shown in Figure 5.11(b), the layer consists of a series of geometry groups, which are assigned a build-style from a model, with a section containing coordinates representing geometry of a specific type.

The thermo-mechanical simulation in Chapter 6 required a method for iterating over the scan vector geometry in the machine build file. This provides the simulation with the current scan vector, and, specifically, the state and position of the laser at the current time t , and at an increment ahead $t + \Delta t$. This functionality was added to provide better control over adaptive mesh refinement in the thermo-mechanical simulation (Sections 6.3.1 to 6.3.3), and for obtaining the previous laser scan position to enable a restart option during analyses.

The position of the laser in absolute time is found by the accumulation of time scanning previous scan vectors. In between adding layers during the build, a constant time was added to account for time taken adding a new layer during the powder re-coat operation. In order to calculate the exact position of the laser, interpolation was carried out over the current vector path, based on the effective laser speed to calculate the position and the state at time t .

Taking advantage of the static nature of scan geometry, caching mechanisms were used to reduce the performance penalty of accessing the scan vector geometry randomly. This was done by decomposing the geometry structure into a wide-spanning tree structure, as illustrated in Figure 5.12, and caching the total time taken to

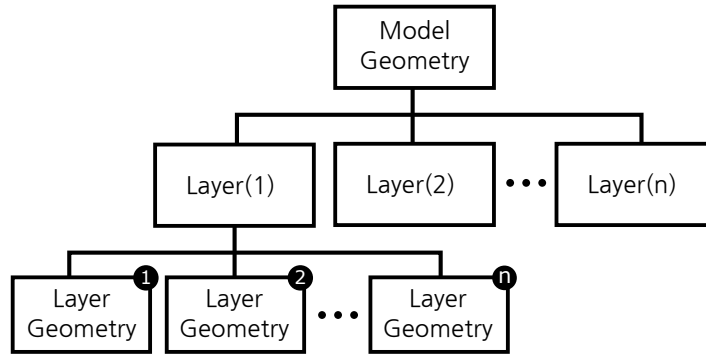


Figure 5.12: Diagram showing the decomposition of the build file into layers and the layer geometry to provide a caching mechanism

scan each layer geometry, and subsequently for each layer. The calculations of these times were computed in parallel. Iterator functions allow directly traversing linearly across the build tree, between layer geometries, and individual scan vectors, which was used in the thermo-mechanical simulation. The overall build time and the mean scan vector length can be calculated to inform decisions when designing scan strategies, or potentially locating the suitable orientation of a part within a build.

5.3 Summary

The volumetric hatching method shown in Section 5.1 provides a valuable tool for prototyping custom laser scan strategies for direct use in both numerical simulation and in physical experiments using commercial SLM systems. Having the laser scan geometry directly available enables the generation of the specific inputs required in the multi-scale model, which cannot solely be achieved through importing the part geometry itself. Therefore, it is essential that both the design and simulation tools associated with producing parts through SLM have a tight integration with the pre-processing stage which generate the laser scan geometry.

Aiding the pre-processing stage, the *libSLM* library provides a valuable utility for interfacing and processing machine build files used by SLM and potentially SLS systems. It reduces the number of utilities required to translate scan vector geometry into a machine ready format, and provides essential capability to help perform a direct comparison between experimental and simulation studies. In addition, the library provides a facility to predict the overall build time, which could potentially provide feedback when designing, or pre-processing a component for a chosen laser scan strategy. Both are crucial within the toolchain in order to fully integrate the triad of design, manufacturing and simulation.

Chapter 6

Thermo-mechanical finite element modelling of selective laser melting

In this chapter, the finite element method and the general techniques used for solving sets of non-linear equations are presented as reference in Section 6.1. The implementation of the coupled thermo-mechanical finite element model is established in Section 6.2 with the definitions of the governing equations used for the thermal and mechanical analysis. This model is then used to determine the implications of the temperature history created by the choice of laser scan strategy and scan area size on the development of residual stress during selective laser melting. Extensions to the model to improve the performance using an adaptive meshing technique are presented in Section 6.3.

Background on the finite element method and the established numerical techniques used in order to obtain solutions to a non-linear problem are presented for convenience to the reader.

6.1 Finite element formulation

The FE method is a numerical technique for the approximate solution to a set of continuous PDEs encountered when modelling physical phenomena. The method involves discretising a domain Ω , into a mesh of connected elements, with a set of boundary conditions on the surface Γ , as shown in Figure 6.1.

Each element corresponds to a finite region, with nodes that are shared between elements. Often a family of element formulations are available in 2D and 3D to build a mesh. The Galerkin method is used to convert a continuous

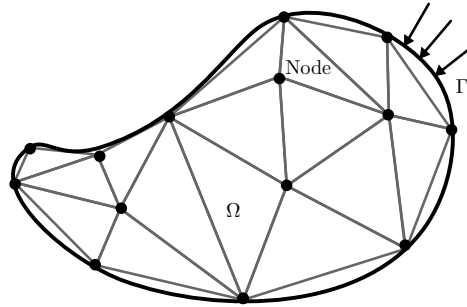


Figure 6.1: Illustration showing discretisation of the domain Ω into finite element mesh using triangle elements

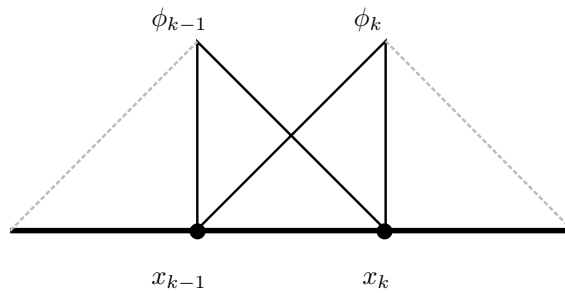


Figure 6.2: Illustration of 1D piecewise linear trial functions

problem into a discrete problem that can be solved numerically. The method uses the weighted sum of a finite number of basis or trial functions ϕ_i across a small sub-domain (element) to approximate the PDE. Typically, linear piece-wise trial functions are used, which interpolate quantities from each element node i anywhere inside the element, as shown in Figure 6.2.

This Galerkin method requires a variational statement of the problem by transforming the strong-form of the PDE into its the weak-form [170]. This has the effect of relaxing the problem over a small sub-domain, by satisfying the strong-form on average across the domain. By assembling the trial functions for each element across the whole domain, a system of linear equations is formed

$$Ku = F. \tag{6.1}$$

6.1.1 Solution to non-linear systems

The presence of non-linearity due to changes in material properties result in the element stiffness matrix K_e being a function of the nodal displacement u ,

resulting in the form

$$k(u)u = F, \quad (6.2)$$

with the external nodal-load force vector, F . The non-linear equation can be solved by adding a residual term, the nodal-load force vector R , to obtain the state of equilibrium such that

$$R(u) - F = 0. \quad (6.3)$$

and substituting equation 6.2 into equation 6.3 results in

$$K(u)u = F - R(u) = 0. \quad (6.4)$$

The internal nodal-load force vector is calculated from the internal stresses across all elements using

$$R = \sum_{el} \int_V B^T \sigma d\Omega, \quad (6.5)$$

with the non-linear strain-displacement differential operator B defined as,

$$[B] = [\partial][N], \quad (6.6)$$

where N is the matrix of shape functions. The strain-displacement differential operator maps nodal displacements to strains across the element. The procedure attempts to minimise the residual between external and interior forces within the structure until effectively the body is at an equilibrium state. The Newton-Raphson iterative method can be used to solve the set of non-linear equilibrium equations with the iterative scheme in the form

$$u^i = u^{(i-1)} - K_T^{-1} \left(u^{(i-1)} \left(F - R(u^{(i-1)}) \right) \right), \quad (6.7)$$

where K_T is the tangent-stiffness matrix, and i denotes the iteration. A more convenient representation of this equation which can be solved as system of linear equations is

$$K_T(u^{(i-1)})\delta u^{(i)} = F - R(u^{(i-1)}), \quad (6.8)$$

with the incremental correction to the displacement vector $\delta u^{(i)} = u^{(i)} - u^{(i-1)}$. The solution of the displacement at the next time increment, $t + 1$, is obtained

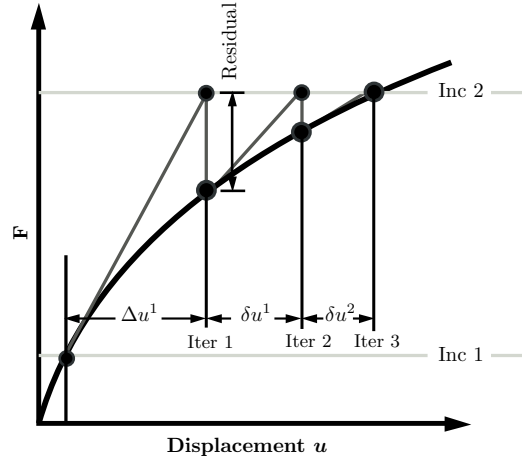


Figure 6.3: Illustration showing the convergence towards the solution across a single time-step, using the Newton-Raphson method

as follows

$$\begin{aligned}\delta u^{(i)} &= u^{(i-1)} + \delta u^{(i)} \\ u_{(t+1)}^{(i)} &= u_t + \Delta u^{(i)}\end{aligned}\quad (6.9)$$

with the superscript, i , for the iteration number and the subscript, t , for the time increment. The whole Newton-Raphson procedure is illustrated in Figure 6.3, which shows the iterative solution converging towards the solution based on the required tolerance.

The convergence of the iterative solution for a non-linear mechanical solution can be determined by checking the maximum force residuals and the incremental change in displacement within the system. The force residual is based on the absolute maximum residual, $F_{residual}$, and the reaction forces $F_{reaction}$ across all elements under the criterion

$$\left\| \frac{F_{residual}}{F_{reaction}} \right\| < TOL_1, \quad (6.10)$$

where TOL_1 is the relative force convergence tolerance chosen by the user. The relative incremental displacement convergence is determined at each iteration based on the maximum absolute value of the current displacement increment vector Δu , and the correction to the increment displacement vector δu , with the criterion

$$\left\| \frac{\delta u}{\Delta u} \right\| < TOL_2, \quad (6.11)$$

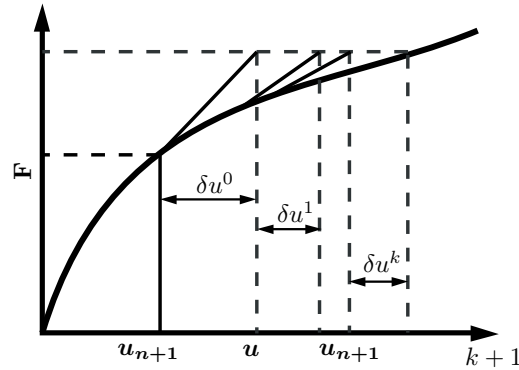


Figure 6.4: Illustration showing the iterative convergence tolerance using the maximum relative displacement

where TOL_2 is the relative displacement convergence tolerance chosen by the user. The relative displacement convergence criteria checks that the maximum change in incremental displacement does converges across all elements, as illustrated in Figure 6.4.

The maximum error in temperate estimate prediction is used as a heuristic method for determining convergence during a thermal analysis. During each iteration, the predicted element temperature T_p is based on the previous temperature iteration, $T_{(i-1)}$, such that

$$T_P = T_{i-1} + \left(\frac{dT}{dt} \right)_{i-1}, \quad (6.12)$$

with the rate of change in temperature (dT/dt) based on the current material properties evaluated. Convergence is obtained when the maximum absolute difference across all elements is achieved within a tolerance TOL_3 , such that

$$\|T_P - T_i\| < TOL_3. \quad (6.13)$$

The Newton-Raphson method tends to provide good convergence at the computational expense of requiring re-assembly of the tangent stiffness matrix, K_T , for each iteration. The modified Newton-Raphson method only requires a single calculation of the tangent stiffness matrix at the beginning of the timestep. This reduces the expensive assembly of the tangent stiffness matrix, at the expense of a greater number of iterations. However, in practice these methods are only suitable for mildly non-linear problems. As with all gradient based solutions, these do not provide a guarantee for global convergence, and can converge towards local solutions, which in some cases can be fixed by reducing the timestep.

6.1.2 Solutions to systems of linear equations

The finite element formulation of the non-linear system presented in equation 6.8 is assembled from element-wise contributions to the global stiffness matrix K_G . This is solved as a general set of linear equations presented in the standard form of

$$Ax = B, \tag{6.14}$$

where A is a $N \times N$ sparse matrix corresponding to N degrees of freedom within the system. The nature of the system solved in thermo-mechanical problems should result in a symmetric positive-definite matrix, with a bandwidth as shown in Figure 6.5, which is well suited for solving efficiently with direct and iterative matrix solvers. Efficient storage schemes can take advantage of the sparse nature of these matrices.

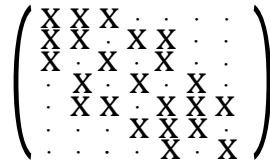


Figure 6.5: Illustration of the bandwidth in a sparse matrix

Direct solution methods, such as those offered by MUMPS [171], PARADISO [172] offer a reliable solution for well-conditioned systems of equations, at a predictable cost. Direct methods are based on numerical Cholesky factorisation, by decomposition of a positive-definite matrix A , such that

$$A = LL^T \tag{6.15}$$

where L is the lower triangle with positive diagonal elements. The solution is obtained through forward and backward substitution:

$$\begin{aligned} Lz &= b, \\ L^T x &= z. \end{aligned} \tag{6.16}$$

The level of sparsity within matrix A determines the number of operations required during forward and backward substitution. This can be improved through permutation of rows and columns, which effectively reduces the matrix bandwidth, such that

$$\begin{aligned} A &= PLL^T P^T, \\ \tilde{b} &= Pb, \end{aligned} \tag{6.17}$$

with permutation matrix P . Careful choice of P can reduce the number of operations required during forward and backward substitution. Depending on the level of sparseness, the computation complexity required for factorisation is $O(\frac{1}{3}N^3)$, and the substitution phase, $O(2N^2)$. The scaling of the problem is predictable, and therefore the number of DOF (elements) within the finite element model determines the cost of the solution. Additional problems associated with direct methods are excess memory consumption required to keep the matrices entirely in memory (in-core) for large systems, and difficulty efficiently in splitting and distributing the computation.

Iterative methods find a solution that has a significant reduction in computation cost compared to direct methods, with a computational complexity of $O(N)$ for well-conditioned systems. Iterative schemes are formed based on minimising equation 6.8 into the form

$$\psi(\delta u) = \frac{1}{2} \delta u^T K_T(u) \delta u - \delta u^T (F - R(u)), \quad (6.18)$$

and in a general form,

$$\psi(u) = \frac{1}{2} u^T A u - u b. \quad (6.19)$$

This is solved by an iterative scheme in the general form

$$u_{k+1} = u_k + \alpha_k r_k, \quad (6.20)$$

which can be solved through established techniques such as Jacobi, Gauss-Seidel and the successive over-relaxation (SOR) technique. Modern methods such as (bi)conjugate stabilised gradient method use pre-conditioning for improving the rate of convergence. For convergence, the theoretical maximum number of operations required is N - the size of the system. However, depending on the conditioning of the matrix and choice of iterative scheme, this can be significantly reduced with better performance than direct methods, requiring significant less memory.

Fundamentally, the overall computational cost for the simulation of a finite element problem is determined by two factors: the number of DOF within the system, and the convergence of the set of non-linear equations. Unlike linear problems, non-linearity requires the re-calculation of the tangent stiffness matrix which is expensive computationally, and in some situations can be slower than solving the system of equations. Therefore, reducing the number of elements required for discretisation where not required, provides the most efficient means for solving these problems. For improvement of the simulation throughput, the use of adaptive mesh refinement in Section 6.3 was developed in this work as

an extension to the original implementation of the thermo-mechanical model in Section 6.2.

6.2 Details of the thermo-mechanical implementation

A commercial FE solution was deemed sufficient to provide a robust solution whilst reducing development time required in the work. MSC Marc [173] was chosen because of its competency in modelling non-linear multi-physics manufacturing processes and the ability to extend models and functionality with user defined Fortran subroutines.

The overall modelling strategy attempts to replicate the SLM process by directly simulating the machine build files to enable a direct comparison with experiments. The workflow is shown in Figure 6.6 where two main inputs are required: an extensive list of material properties and the machine build file.

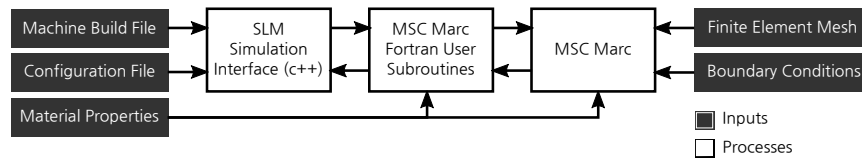


Figure 6.6: An overview of inputs required by the simulation and the inter-dependency of the processes

The simulation process interacts between Fortran user subroutines and an external c++ interface to control the simulation behaviour whilst running (Figure 6.7). The c++ interface has several responsibilities. Firstly, it parses the machine build file using the developed *libSLM* library discussed in Section 5.2. Using the previously developed library, the laser position, laser power and state are made available at a given simulation time. Finally, it provides an interface for managing the state variable of each element. For each simulation, an additional configuration file is created to define additional material properties, activate various models, and parameters associated with the simulation.

This functionality is integrated separately with a general purpose multi-physics FE solver to enable future additions of more complex modelling.

In the following sections, the classical thermal and mechanical definitions which govern the relevant physics in the process at this scale are presented as reference to the reader.

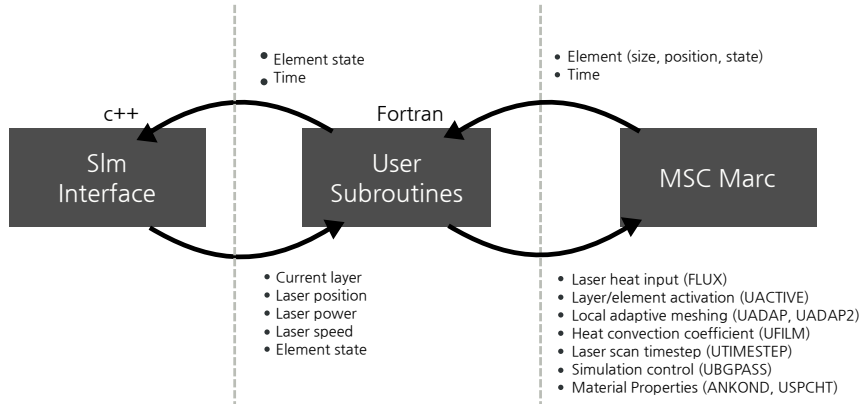


Figure 6.7: The interaction between c++ interface, *Fortran* user subroutines and MSC Marc

6.2.1 Thermal definition

The thermal problem is governed by the enthalpy within a system, defined as

$$H = \int_{T_{ref}}^T \rho c_p dT \quad (6.21)$$

with the heat transfer defined by the heat equation in a volume, Ω , as given in equation 6.22.

$$\frac{\partial H}{\partial t} = \nabla(k(T)\nabla T) + q_v + q_s, \text{ in } \Omega \quad (6.22)$$

The volumetric heat input term, q_v , is the heat input from the laser source defined in equation 2.7. The surface heat source term, q_s , is the sum of the convective and radiation terms defined in equation 6.23, which was applied to the exposed powder bed surface, Γ , having a surface normal \mathbf{n} such that

$$k(T) = \frac{\partial T}{\partial \mathbf{n}} = h_c(T - T_A) + \varepsilon_{em}\sigma_b(T^4 - T_A^4) \text{ on } d\Gamma. \quad (6.23)$$

The values of emissivity ε_{em} used in equation 6.23 are listed in Table 4.4 (Section 4.2.2) and a heat convection coefficient, $h_c = 14.73 \text{ W/m}^2\text{K}$ [19] was used.

Three material phases were considered in the simulation: powder, solid and liquid. Both the liquid and solid state represent the ‘consolidated’ form. A unidirectional transformation occurs during consolidation from powder to liquid and there is a bidirectional transformation between solid and liquid during (re)melt. Each state requires a set of temperature dependent material properties, with the powder state having an assumed packing factor $f_p = 0.6$ [154].

In order to assign appropriate material properties, a state variable was used to track the state of each element, using a discrete variable, ϕ , with the three exclusive conditions

$$\phi = \begin{cases} -1 & \text{Powder state} \\ 0 & \text{Liquid state} \\ 1 & \text{Solid state} \end{cases} \quad (6.24)$$

During the transition to the liquid phase, stresses and any previously accumulated strains were reset by becoming temporarily deactivated using the *UACTIVE* subroutine during the simulation to emulate annealing and prevent unrealistic accumulation of plastic strains.

6.2.2 Laser heat input

The laser heat input was modelled using the volumetric Gaussian heat source proposed by Goldak [28] in equation 2.7 using a laser spot radius $r_d = 32 \mu\text{m}$. Caution is expressed when choosing η because these values vary widely between experimental studies for both powder and solid medium [154]. For powder, this is assumed to be the same as pure titanium powder $\eta = 0.77$ [48] and for the solid substrate is assumed to be $\eta = 0.3$ [174]. Normally, to account for latent heat, the specific heat is modified in a finite interval between the solidus T_S and liquidus T_L temperatures. This was excluded in this work because accounting for latent heat requires a small enough timestep to ensure the temperature change does not overshoot this interval and is relatively insignificant compared with loss of heat through radiation.

The transmission efficiency of the laser source in SLM has not been accurately measured, both in general and specifically for the Realizer SLM 50. It is expected that many factors during the build will affect this, such as the release of a metal condensate into the path of the laser [16] or the lens focal position. Hence, the inclusion of an empirical laser absorption efficiency term in this work.

A constant point overlap factor f_{po} was used to control the relative position of the laser point between each simulation time step, as shown in equation 6.25. This ensures that irrespective of the laser speed, v , and the fixed laser spot size, r_d , the heat flux traverses across the whole scan path without any intermittent gaps, as illustrated in Figure 6.8.

$$\Delta t = \frac{f_{po} r_d}{v} \quad (6.25)$$

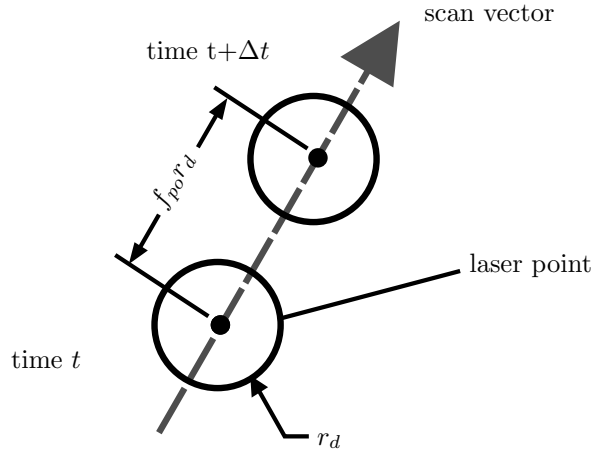


Figure 6.8: Illustration showing the point overlap factor, f_{po} , which ensures the timestep remains constant with the scan speed.

6.2.3 Mechanical definition

The mechanical analysis assumes a small strain and small deformation formulation using an elasto-plastic constitutive model. The total strain tensor, ε , within a material is the superposition of three strains terms

$$\varepsilon = \varepsilon_e + \varepsilon_p + \varepsilon_{th}, \quad (6.26)$$

which are the elastic strain, ε_e , the plastic strain, ε_p , and the thermal strain, ε_{th} . Upon yielding, plastic deformation occurs and the plastic strain ε_p must be accounted for. In this model, the incremental J_2 plasticity small strain formulation was used. The yield behaviour was determined using the Mises yield criterion, shown in equation 6.27, which is applicable for metals.

$$\sigma_y = \sqrt{3J_2} = \left[\frac{3}{2} \left((\sigma_{11} - \sigma_{22})^2 + (\sigma_{22} - \sigma_{33})^2 + (\sigma_{33} - \sigma_{11})^2 + 6(\sigma_{12}^2 + \sigma_{23}^2 + \sigma_{31}^2) \right) \right]^{1/2}. \quad (6.27)$$

The computational procedure requires determining the prior deformation history, and incrementally calculating small changes in the plastic strain $d\varepsilon_p$. This can be calculated using the flow rule,

$$d\varepsilon_p = d\lambda \frac{\partial f}{\partial \boldsymbol{\sigma}}, \quad (6.28)$$

where $d\lambda$ is a positive proportional scale factor and ∂f is the loading function

representing the yield surface. The associative flow rule can be determined based on the elasto-plastic constitutive relation used in the model (i.e. perfect plasticity, isotropic and kinematic work hardening). The effective plastic strain ε_p is found based on the accumulated plastic loading history,

$$\varepsilon_p = \int \sqrt{d\varepsilon_p d\varepsilon_p}. \quad (6.29)$$

Finally, the thermal strain ε_{th} is defined as

$$\varepsilon_{th}(T) = \int_{T_{ref}}^T \alpha_{CTE}(T) dT. \quad (6.30)$$

By obtaining the total strain tensor, the Cauchy stress tensor, $\boldsymbol{\sigma}$, can be resolved using

$$\{\boldsymbol{\sigma}\} = [D]\{\boldsymbol{\varepsilon}\}, \quad (6.31)$$

where D is the element stiffness matrix.

The linear coefficient of thermal expansion, α_{CTE} , is listed in Table 4.6. The Poisson's ratio is assumed to be $\nu = 0.342$. For modelling time-independent plasticity, a kinematic plasticity model with a von Mises yield criterion was chosen because this captures the cyclic non-linear work hardening (Baushinger) effect [175]. Temperature dependent properties for the yield stress σ_y and the plastic tangent modulus H_p are listed in Table 4.6.

If re-melting of previously consolidated elements does occur, previously accumulated strains for the element are reset to zero and are removed subsequently from the structural analysis pass. De-activating elements prevent any extrapolation of material properties exhibited in the melt pool undergoing extreme temperatures.

6.2.4 Finite element mesh

The single layer simulations were scanned directly over a solid substrate to enable comparison with previous work. The domain was discretised with a static mesh, consisting of powder bed composed of uniform 0.02 mm 8 noded hexahedral elements and a substrate region with an overall thickness of 1.56 mm.

On the bottom surface, a fixed displacement boundary condition is applied. On this surface, a fixed temperature of 200 °C was used to represent the pre-heated platform which remains fixed at this temperature throughout the process. The side walls of the model were assumed isothermal due to the insulative properties of the powder and the large volume of solid material in the substrate acting as an effective heat sink. The top surface has an aerial heat flux applied to permit heat convection into the environment and surface

radiation losses. The mesh and the applied boundary conditions are illustrated in Figure 6.9.

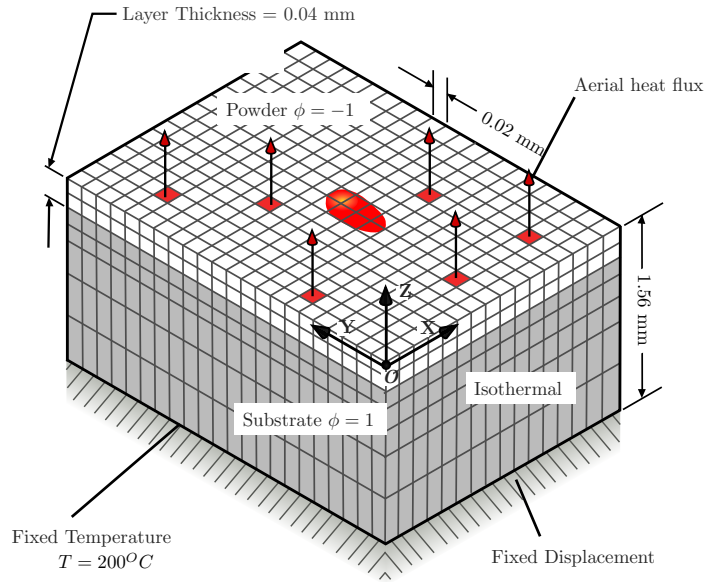


Figure 6.9: Illustration showing the fixed mesh implementation and the applied boundary conditions used in the thermo-mechanical model

The ‘assumed strain’ option within MSC Marc was used to improve the bending performance of these elements by internally modifying the interpolation functions with further enrichment. The ‘constant dilation’ option was also used to improve the performance of hexahedral elements undergoing compression within the elasto-plastic analyses [173].

6.2.5 Simulation options

The relative displacement tolerance and force residual convergence criteria in equations 6.10 and 6.11 were used to satisfy convergence during the mechanical analysis. These were both set to a value of 0.1, and are based on the maximum value obtained across every element within the domain. If convergence during a timestep was not satisfied, the time-step was repeatedly ‘cutback’ by a factor of a half and the current iteration was performed again.

6.2.6 Post-processing the results

Post-processing of the results was accomplished using a set of *Python* scripts using the *PyMentat* and *PyPost* functions available within MSC Marc. The

average quantities of the scalar values were obtained from consolidated elements with a state variable $\phi > 0.95$. These results were then exported to Matlab using SciPy [176] for further processing and analysis.

The results obtained from the thermo-mechanical analyses were found to be fairly complex both spatially and in time. Probability density distributions offers a method for characterising the magnitude of a quantity (e.g. stress component or temperature) across a region by decomposing into a 1D form. This greatly simplifies comparing and analysing the results under different conditions and test cases. The probability density distributions were created by building a histogram of the chosen quantity across the scanned region, and then producing a curve tracing its profile.

6.3 Extension of the thermo-mechanical model

Extreme non-linearity is present in the SLM process zone, caused by the high localised temperature gradients created by exposure from a moving laser, which result in phase changes in the temperature dependent material. Therefore, a sufficiently high discretisation resolution spatially and temporally must be used to capture the thermal-mechanical response over time for this region.

This presents a great challenge to model the problem efficiently in order to understand the effect of scan strategies on the development of residuals stresses as a function of the local and global response within the domain.

The previous implementation of the thermo-mechanical finite element model in Section 6.2 used a static mesh with a fixed resolution throughout the entire domain during the analysis. It was soon discovered that the scalability of the solution was highly dependent on the volumetric area required to be simulated. This was determined by the number of elements within the domain, and the physical time required for the laser to scan across the region.

6.3.1 Adaptive meshing technique for improving simulation performance

Octree mesh refinement was used by Riedelbauer et al. [177] for modelling the selective laser melting of PA12, however, the performance of their method was not discussed. The review of the literature identified that the use of moving adaptive meshes [30, 178] could gain significant improvements in performance whilst conserving discretisation accuracy in the melt pool. In the method proposed by Zeng et al. [30], they used a quasi global-local approach to model the high non-linearity exhibited near the melt pool. The domain is decomposed into a sub-problem, with a fixed size dynamic mesh that overlaps directly

on the global domain, which follows the current point of the laser. Their method performs the analysis at both scales transferring the material state and properties, along with the temperature boundary conditions through their own interpolation scheme to transfer between meshes. The advantage of this approach over traditional mesh refinement is that no renumbering of nodes is required during the assembly stage of the global stiffness matrix because no elements are changed. This can be taken advantage of during the Cholesky factorisation when solving the solution of the global stiffness matrix [179].

From the results of performing the thermo-mechanical simulations in relatively small regions in Sections 7.2.2 and 7.2.3, the HAZ was not necessarily isolated to a small region around the location of the melt pool, as shown in Figure 3 12 . The thermo-mechanical response extended into previously scanned tracks, which was shown to affect the generation of transverse stresses, and the creation of plastic strain in previously consolidated regions. Also, the high aspect-ratio of the melt pool, and the spatial length of the thermal gradients across the currently scanned track increases the refinement area required to be captured. Restricting the adaptivity of the mesh solely within the melt pool region as proposed by Zeng et al. seems insufficient when also considering the mechanical response.

An octree-based decomposition was chosen as the implementation for improving the performance of the thermo-mechanical model. A bi-directional refinement scheme was developed to both refine regions exhibiting a very non-linear localised behaviour and coarsen regions exhibiting a more steady-state global response.

6.3.2 Octree mesh refinement

The use of a structure grid consisting of hexahedral 'Hex8' elements in the previous implementation, lends itself to the use octree-based refinement which is natively supported within MSC Marc [173]. The in-built refinement procedure in MSC Marc subdivides an element by one level (1:2 refinement), guaranteeing that a balanced tree is form. This is illustrated in principle for a quad tree implementation in Figure 6.10, which requires the two newly created elements sharing one edge of the neighbouring element. During the refinement phase, when a selected element is refined, new nodes N are created along the shared edge with the neighbouring element . An additional nodal constraint is used on node N to be the average of solutions shared between the two vertices shared along the same edge.

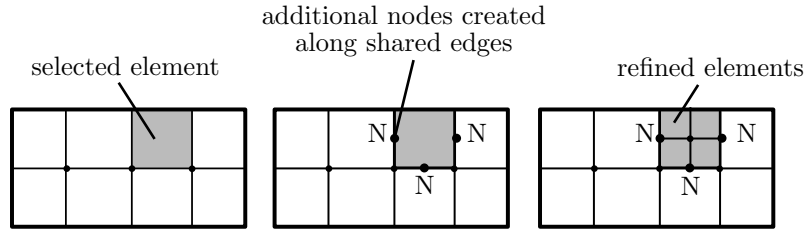


Figure 6.10: Illustration showing balanced refinement scheme with at most two elements sharing one edge

6.3.3 Implementation of adaptive meshing scheme

Originally, the state and transformation between phases was tracked using a discrete state variable ϕ . However, in-order to be compatible with the adaptive scheme, the values of the states were changed to

$$\phi = \begin{cases} -1 & \text{Liquid state} \\ 0 & \text{Powder state ,} \\ 1 & \text{Solid state} \end{cases} \quad (6.32)$$

with properties that can linearly vary between the powder and solid phases ($0 \leq \phi \leq 1$). During the element un-refinement phase, the mean value of quantities is taken as the average from the previous sub-divided elements, and are used in the un-refined element as shown in Figure 6.11. This also affected the state variable ϕ , and as of consequence may result in intermediate values between the powder and solid phases. These are only likely to occur along boundaries regions formed between consolidated regions and powder.

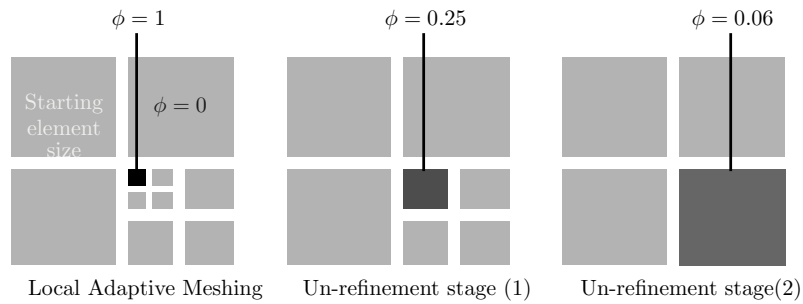


Figure 6.11: Illustration of the un-refinement phase, showing the mean quantities are obtained from the previously refined elements

Material properties were linearly interpolated between those defined at the powder and solid phase. It was assumed that there was negligible mechanical interaction of the powder phase, therefore the mechanical material properties

	Property	Scale Factor
	Young's Modulus E	0.1
Linear coefficient of thermal expansion	α_{CTE}	0.1
	Yield stress σ_y	0.1

Table 6.1: Scale factors used for relating the mechanical properties of powder phase with the solid phase

were scaled for the powder phase using the factors in Table 6.1.

The implementation of octree refinement occurs spatially in all three dimensions, and using a balanced (2:1) tree, required changing the starting mesh and strategically placing the mesh along the Z direction. Having the active layer placed arbitrarily within the mesh volume creates several issues. During un-refinement, these elements can be larger than the active layer thickness, as shown in Figure 6.12(a). This prevents assigning the surface thermal boundary conditions, since these can only be applied when initialising the simulation at start-up. Instead, the domain was shifted, as illustrated in Figure 6.12(b), which requires the top surface of the starting mesh to be aligned at the same height of the first layer. After continuously refining the mesh, elements will all be aligned to the bottom of the active layer positioned at $z = 0$.

The benefit of this refinement approach is that the surface boundary conditions remain static on the top surface irrespective of refinement level. As a result, a coarse starting mesh can be used, which significantly reduces the time taken to apply the surface boundary conditions and initial conditions to the model within the pre-processor. The caveat of this scheme is that the mesh is dependent on the layer thickness, requiring the starting mesh element size to be a multiple of the layer thickness. This is needed because during the refinement procedure, the top scanned layer need to be set to a powder-phase. An additional problem is that multiple-layers cannot be simulated within one analysis. This would require performing a subsequent analysis for the next layer and applying the state (stresses, phase) of the previous layer as part of the substrate.

For the simulation to operate from a coarse starting mesh, without advancing the simulation in time, an algorithm was developed to control both refinement and the time-stepping procedure. This is necessary since the adaptive meshing routine in MSC Marc is called at a fixed number of timesteps set by the user. The refinement criteria were implemented inside the *UADAP* and *UTIMESTEP* Fortran subroutines, and are outlined in Figure 6.13.

First, the position of the laser at time $t + \Delta t$ is determined using the *libSLM* library. If the position of the laser lies within the volume of the element with an edge length than minimum length, h_{min} , the element requires further

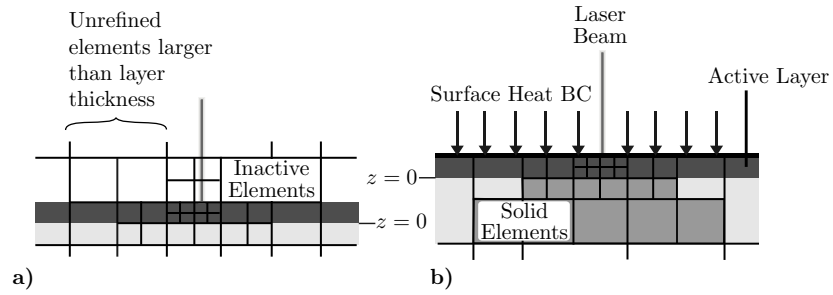


Figure 6.12: Illustration showing the placement of the starting mesh when aligning with a) an arbitrary starting position, and b) aligning the bottom of the actively refined layer at $z = 0$

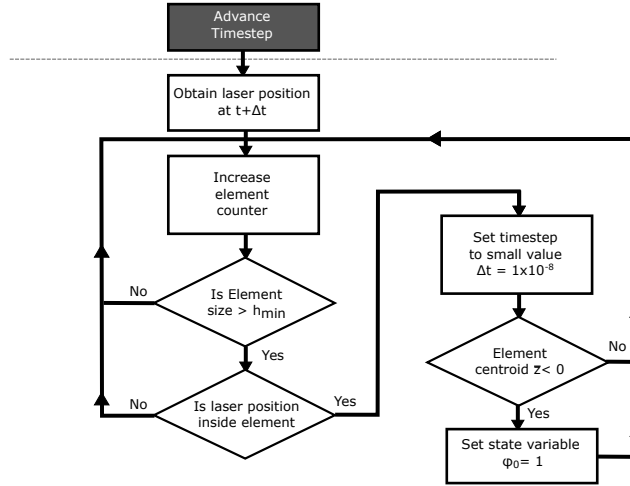


Figure 6.13: Flow diagram of the adaptive meshing algorithm to refine elements across multiple timesteps

refinement.

The centroid, element size and the nodal coordinates to calculate these are not conveniently available within the user subroutines. The element sizes were approximately calculated by taking the distance between the positions of two Gaussian integration points situated at opposing corners of an element, as shown in Figure 6.14, and taking the inverse between two-point Gauss-Legendre quadrature points distributed at intervals

$$x_i = \pm \sqrt{\frac{1}{3}}, \quad (6.33)$$

such that the length of the elements can be found

$$\delta l_z = \sqrt{3}\delta z. \quad (6.34)$$

These lengths are only used for differentiating the position and element size for use during refinement, so the accuracy of this calculation is not crucial.

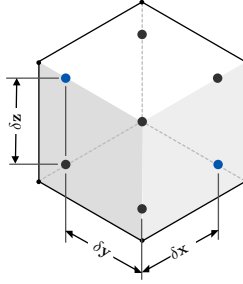


Figure 6.14: Illustration of Gaussian quadrature in a Hex8 element for obtaining the approximate size and centroid of the element

If refinement occurs, the timestep is set to an extremely small value, $\Delta t = 1 \times 10^{-8}$ s, to effectively prevent any advancement of the simulation. Refinement continues until the laser position lies within the specific smallest refined element size, and the timestep returns to the value determined by the spot overlap factor calculated in equation 6.25. During this process of refinement, if the maximum point of an element lies below the layer ($z = 0$), the state of the material is changed to that of the substrate ($\phi_0 = 1$), or an arbitrary pseudo-phase of choice, as illustrated in Figure 6.15.

Refinement was performed based on a radial distance from the laser spot, to capture the high thermal gradients within the melt pool. An additional refinement was made on solid elements ($\phi = 1$), determined by the maximum absolute component of the temperature gradient such that

$$\max \left\| \frac{\partial T}{\partial x_i} \right\| > f_{grad}, \quad (6.35)$$

with the refinement parameter $f_{grad} = 500$. This parameter was arbitrarily chosen and found to satisfactory refine elements exhibiting high temperature gradients near the SLM process zone. When the criterion was not met, an un-refinement procedure coarsened previously refined elements to an intermediate size with an element length of 0.08 mm, to improve the performance of the simulation. The final size was determined by performing the same simulations for a (3 x 3) mm island with different final refinement element sizes found in Section 6.3.5.

For the simulation of Ti-6Al-4V, 7 levels of refinement were used: the original

mesh has a uniform element size of 1.28 mm with the minimum element length $h_{min} = 0.02$ mm, set to half the layer thickness, as illustrated in Figure 6.15.

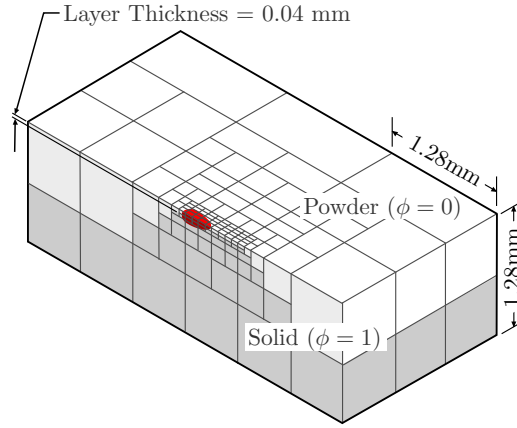


Figure 6.15: Illustration of the adaptive-mesh for the thermo-mechanical analysis

6.3.4 Extension of adaptive meshing scheme for custom geometry

The use of adaptive meshing provides significant opportunity to broaden the aerial region scanned by the laser to fully understand the implications of scan strategy and geometrical effect on the build-up of residual stresses. In order to fully capture the behaviour of the process in the multi-scale methodology presented in Chapter 11, there is a requirement to understand the many potential scenarios that could arise through the process. The previous adaptive scheme assumes a homogeneous distribution of phase ϕ_0 , below the active layer, which can be used for modelling either a solid substrate or an overhang region with a powder phase. The region below the active layer in practice can encounter a variety of geometries, such as support structures, or more complex structures such as lattices. The spatially varying structures will have a localised effect on heat dissipation, and therefore affect the generation of residual stress on the scanned layer. It is currently infeasible to simulate scanning multiple layers in the thermo-mechanical model. However, a representative geometry can be analysed to understand the behaviour on both this structure and the scanned layer above.

The use of a structured fixed, resolution mesh is prohibitively expensive when used in conjunction with a transient thermo-mechanical analysis. It was found that there was no straightforward method to generate and integrate a compatible octree mesh which could account for a heterogeneous domain (solid

structure and powder) using commercial meshing tools. Additionally, a mesh with large number of elements becomes cumbersome to use in the pre-processor.

An alternative method was developed using the in-built adaptive mesh refinement in Marc. Fortran subroutines provide a technique for generating an octree mesh representation of the geometry below the layer dynamically whilst running the simulation. Firstly, a voxel representation of the geometry is generated within Matlab. For representation of solid manifold using STL files, this is readily done using the *VOXELISE* function [180]. For geometry represented by shells e.g. supports structures generated through Magics software, this was transformed into a voxel model at a given voxel density using the *Polygon2Voxel* function [181]. The voxel representation was then transferred into the openVDB format [182], and was then used directly when the simulation was run. The starting mesh shown in Figure 6.16 is extended into the negative Z direction by z_{offset} to incorporate the geometry and a solid substrate. A fixed displacement boundary condition was applied on the bottom surface.

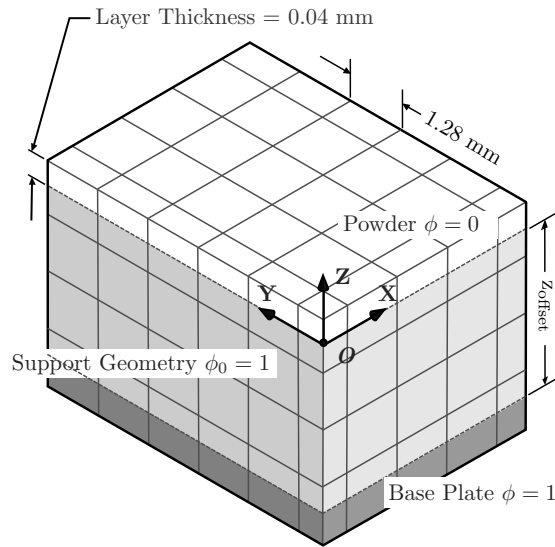


Figure 6.16: Illustration of the starting mesh used in the adaptive analysis when incorporating geometry underneath the active layer during the analysis

The overall procedure for generating the adaptive mesh is illustrated in Figure 6.17. At the beginning of the analysis, during each increment, the element's centroid and lengths were determined. These were used as bounds for sampling across the corresponding volume of geometry grid to obtain the mean value ($\overline{\phi_{geom}}$) across the element, as illustrated in Figure 6.18. When the average value was above zero, geometry exists within the coarse element, indicating element refinement is required. This element was flagged for refinement in a

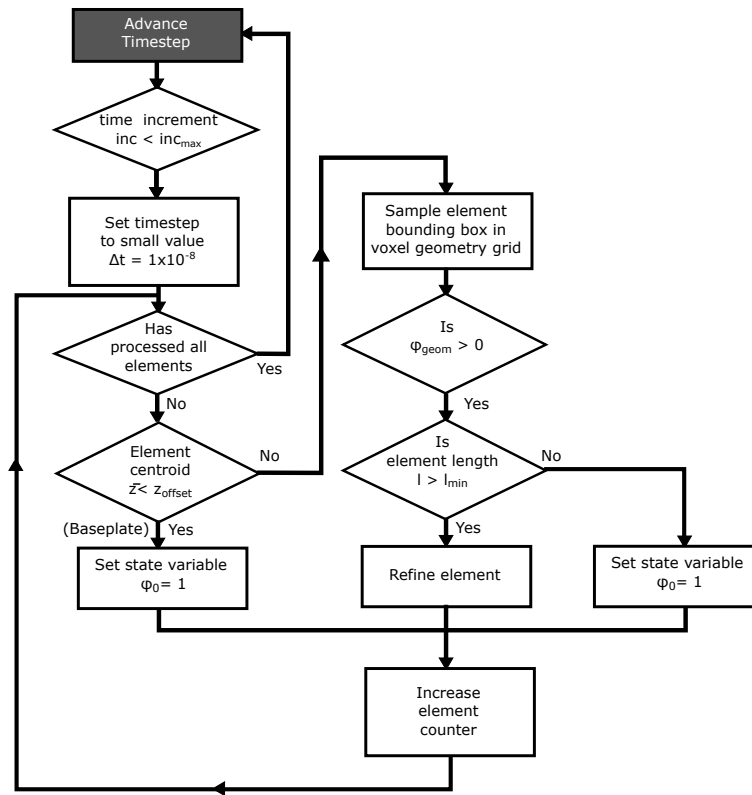


Figure 6.17: Flow diagram of the adaptive meshing routine used for incorporating an additional geometry underneath the active layer during the analysis.

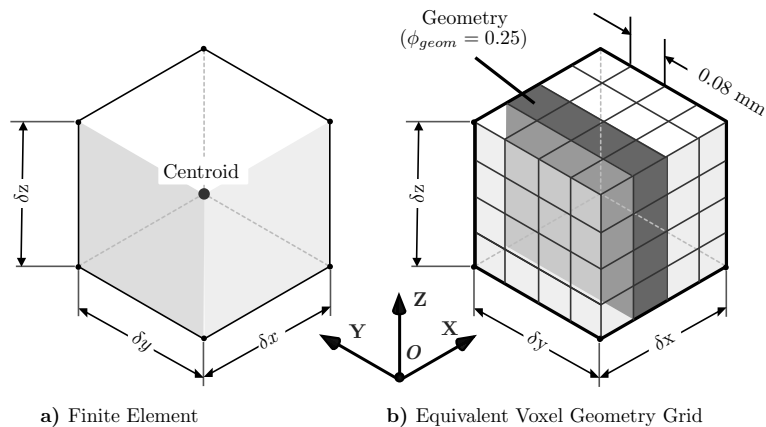


Figure 6.18: Illustration showing the procedure for refining an element by sampling a) the bounding box of the finite element across b) the voxel geometry grid in order to calculate the value $\overline{\phi_{geom}}$ used to toggle the element refinement

second state variable ϕ_{geom} , and the timestep is set to a small value ($\Delta t = 1 \times 10^{-8}$ s) to prevent the simulation from advancing.

Elements with $\phi_{geom} \neq 0$ are refined within the *UADAP* subroutine, and the iterative procedure continues until the level of refinement matches the corresponding resolution of the geometry grid. When this is achieved, the element's first state variable is set to solid ($\phi = 1$). This process continues until stopped after a number of increments set by the user.

6.3.5 Benchmarking of the adaptive meshing scheme

The benchmark of the adaptive meshing scheme was carried out on the (3 x 3) mm island region and compared with the same result obtained using the fixed grid approach. In this study, the chosen final un-refinement levels varied between 0.04 – 0.32 mm to benchmark sensitivity of this parameter on performance and accuracy. The highest level of refinement using the adaptive meshing scheme was chosen to be the same as the same as the fixed mesh, with the smallest element length, $l = 0.02$ mm.

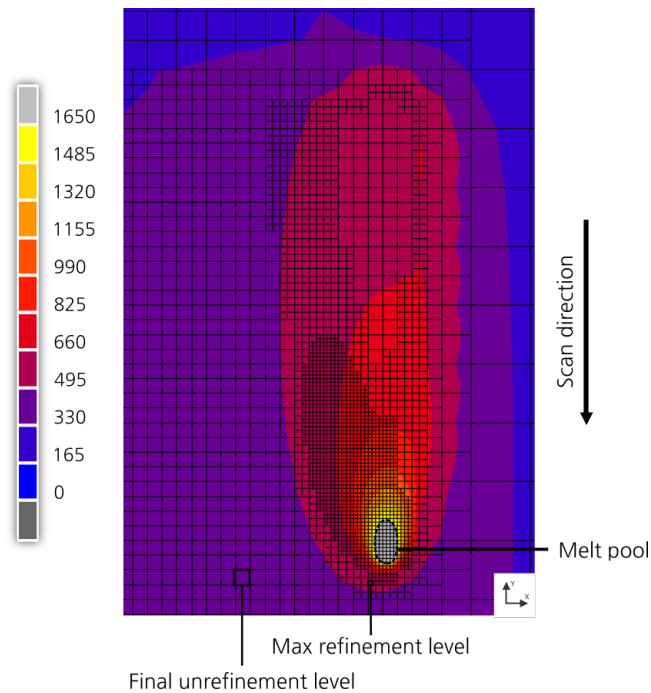


Figure 6.19: Profile view of temperature showing the levels of adaptive mesh refinement in the thermo-mechanical model

The element adaptivity after scanning several scan tracks is shown in Figure 6.19, which used two levels of un-refinement to achieve a final un-refined element size of 0.08 mm. Elements are refined adjacent to the heat-tail in the previously scanned region due to the high thermal gradients occurring in this region. This shows that the thermal behaviour does extend into the previous scanned region. This indicates that in-order to use a moving adaptive grid, as proposed by Zeng et al. [30], a sufficiently large moving mesh is required to fully capture the high thermal gradients in the previously consolidated regions. Element un-refinement occurs along the current scan vector and additionally in previous consolidated regions, where thermal gradients are lower. A time-lapse of the adaptivity scheme at the start of the analysis is shown in Figure 6.20, showing

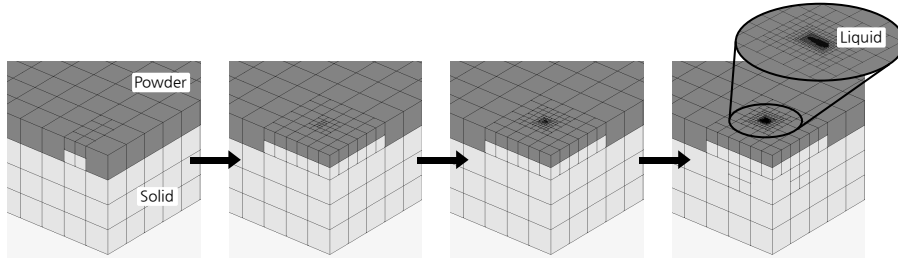


Figure 6.20: Time lapse showing the initial mesh refinement at the beginning of the analysis

the development from the initial coarse mesh to the locally refined zone.

The overall run-time to perform the simulations and the final element count are listed in Table 6.2. Profile views of the final state of the residual stresses are presented in Figure 6.21, when the temperature of the regions had cooled uniformly to ~ 200 °C.

	Number of un-refinement levels			
	0	1	2	3
Final element size [mm]	0.02	0.04	0.08	0.16
Run time [s]	183 757 (-)	68 975 (37.5%)	35 980 (19.6%)	29 850 (16.3%)
Final element count	114 753 (-)	34 568 (30%)	13 057 (11.4%)	7 338 (6.4%)
Peak memory consumption [Mb]	5 336 (-)	3 374 (63.2%)	2 964 (55.5%)	2 839 (53.2%)

Table 6.2: Performance metrics (run time and final element count) for the un-refinement levels used in the analyses with adaptive mesh and the fixed mesh

The final probability distributions for both the longitudinal and transverse stresses are compared between all the un-refinement levels in Figure 6.22. For all the un-refinement levels chosen up to a final un-refinement element length of 0.16 mm, the longitudinal stress distribution does not vary significantly, as shown in 6.22(b). However, it can be seen in Figure 6.22(a) that the σ_{xx} stress distribution does begin to change when using more than one level of un-refinement. This was expected to be caused by the element un-refinement capturing stresses that are developed into the substrate as well as the scanner layer. Overall, this has an effect of reducing the effective magnitude of the σ_{xx} sample across the region from the finest to the coarsest resolution by 77 MPa, when comparing the median values as listed in Table 6.3.

	no un-refinement	1 level of un-refinement	2 levels of un-refinement	3 levels of un-refinement
Median σ_{xx} [MPa]	275	252	215	198

Table 6.3: Median values of the stress component σ_{xx} using different levels of un-refinement

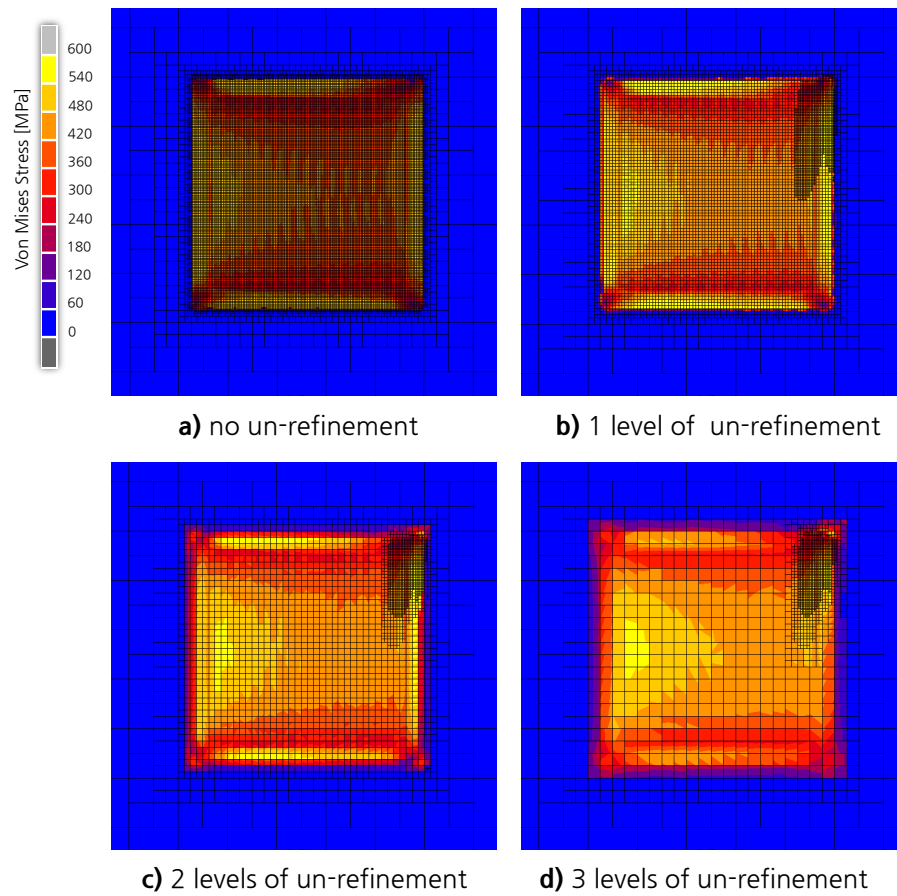


Figure 6.21: Profile views showing the von Mises stress distribution of (3 x 3) mm islands scanned using various un-refinement levels with a final un-refinement element sizes: a) 0.02 mm, b) 0.04 mm, c) 0.08 mm and d) 0.16 mm

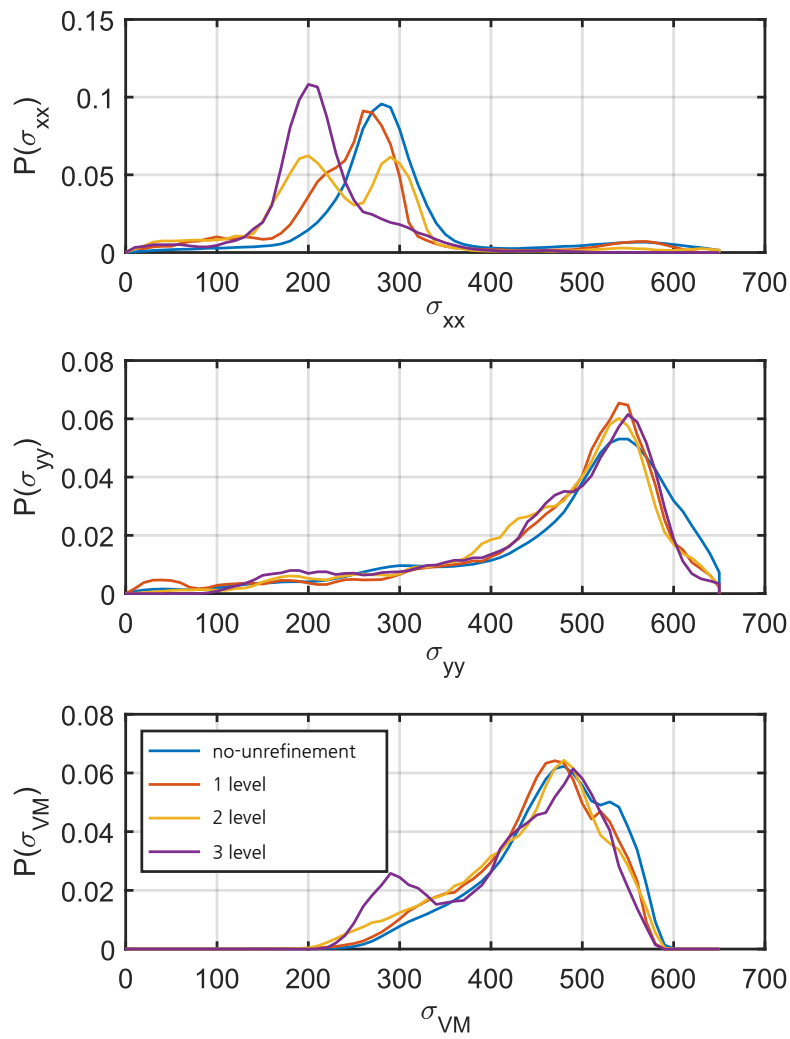


Figure 6.22: probability density function (PDF)s of a) $p(\sigma_{xx})$, b) $p(\sigma_{yy})$ and c) $p(\sigma_{zz})$ for different levels of un-refinement chosen in the analysis of the adaptive mesh scheme

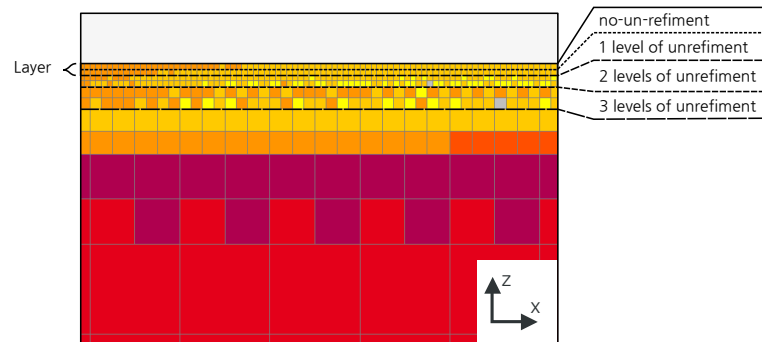


Figure 6.23: Cross-section view along the ZX plane showing the σ_{xx} stress distribution, with the depths corresponding with the levels of un-refinement chosen.

This does not necessarily mean a reduction in accuracy when using higher level of un-refinement. This an additional side effect of sampling greater variance in the composition of stress across a larger depth. This change in the σ_{xx} stress distribution with depth can be seen in Figure 6.23, with the depths captured using different un-refinement-levels.

The final element count does not provide a good indicator of the performance of the adaptive meshing during the analysis, therefore a plot of the total number of elements with analysis time for all un-refinement is shown in 6.24. During the analysis, the total number of elements increases linearly at a rate dependent on the level of element un-refinement chosen. The use of adaptive mesh provides a predictable linear behaviour for the total number of elements used, depending on the un-refinement level chosen, which can provide an estimate of overall run time required. Crucially, the use of the un-refinement procedure provides a significant increase to the computational throughput.

The implementation of the thermo-mechanical model using the adaptive meshing scheme provides a significant boost to the simulation throughput, as shown in the overall timings and resource consumption in Table 6.2. A single level of un-refinement can reduce the overall run time by 62.5%, and is further improved by using a higher level of un-refinement. The number of elements within the model increases linearly with scan time, as shown in Figure 6.24, the rate dependent on the un-refinement level. This shows that to effectively increase the scan area available, a higher level of un-refinement becomes necessary using the technique.

When the un-refinement level was increased such that the final size of the un-refined elements was greater than the layer thickness, this did reduce the median stress sampled, because of the change in residual stresses generated below the layer, as shown in Figure 6.23. This fact should be considered when

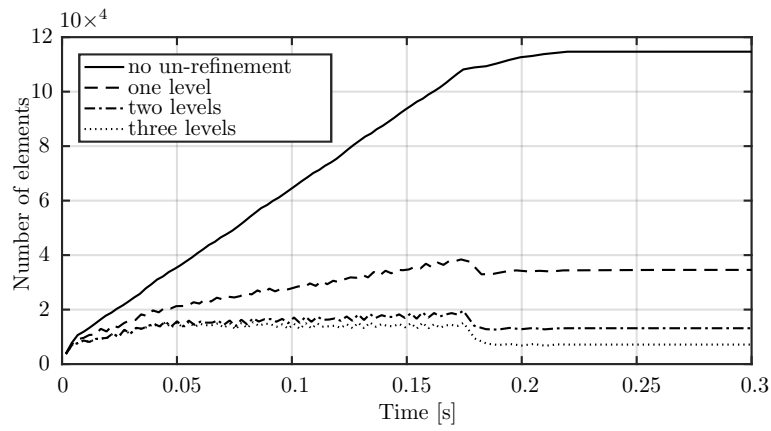


Figure 6.24: Graph showing the total number of elements against time when scanning the (3 x 3) mm island using the adaptive un-refinement

measuring the absolute value of residual stress present within the scanned layer.

6.3.6 Improving scalability through high performance computing facilities

Attempting to perform the adaptive meshing scheme still requires significant computing resources. The memory consumption of a single layer adaptive mesh model is significantly reduced compared to the fixed mesh in Section 6.2. Nevertheless, the simulation run time remains a significant issue, and the capability to simulate large regions greater than (> 3 mm), becomes infeasible, especially when exploring different scenarios, and simulating these in parallel. HPC facilities were available to provide a resource that could be exploited to improve simulation throughput.

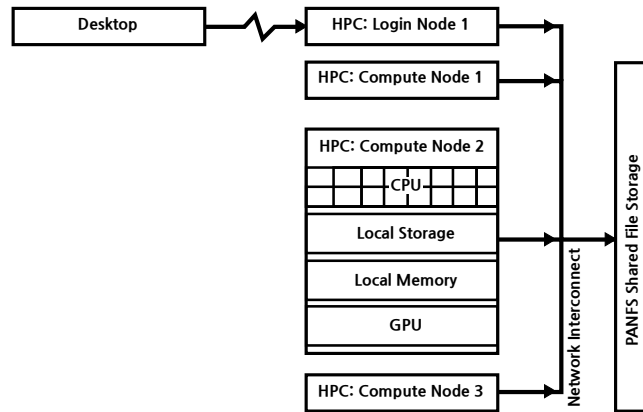


Figure 6.25: Illustration showing the infrastructure provided of the HPC facilities available at the University of Nottingham

The HPC facility provides simultaneous access to approximately 170 high performance compute nodes, each consisting of 16 compute cores, with a minimum memory capacity of 32Gb, as illustrated in Figure 6.25. All the compute nodes are connected using a low-latency high bandwidth network interconnect to enable an efficient multi-processor ‘distributed memory’ computing environment, supported through *OpenMPI*. A proprietary distributed *PANFS* file system provides concurrent shared storage between each compute node, in addition to providing ‘local’ storage on each compute node. The system uses a headless Linux environment, requiring the use of a *BASH* scripting terminal. Native versions of software must be available or be compatible to use on this operating system when performing simulations.

The HPC system uses a prioritised queuing system which requires users to submit a job request, before they are executed by the scheduler, as illustrated in Figure 6.26. A significant advantage of this approach is that it enables running concurrently multiple job analyses. Each job is allocated with specified required

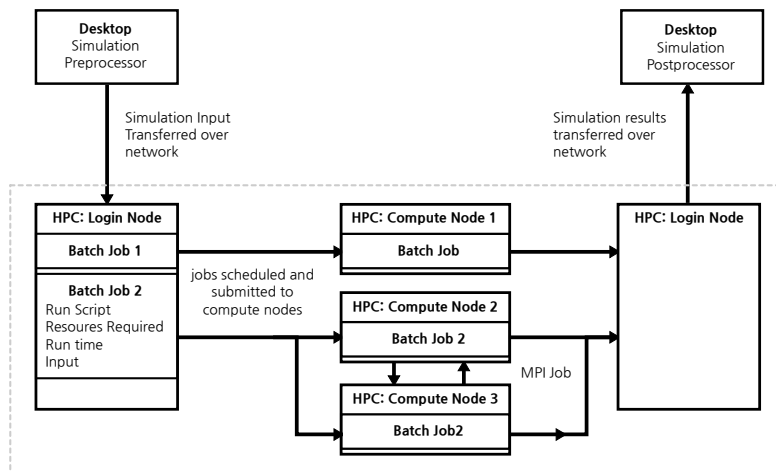


Figure 6.26: Illustration showing the job scheduling system used by the HPC system

resources stated by the user, which determines the job start time, depending on the current available capacity. The job resources required to be stated are:

1. Estimated job execution time
2. Number of compute nodes
3. Number of CPU cores and memory required
4. Specific high performance (enhanced storage, large memory, GPGPU facilities).

Jobs with low resource requirement can jump the queue. Another method for reducing the waiting time is distributing the job over many compute nodes with few CPU cores, and memory. This effectively allows the scheduler to allocate the job onto compute nodes that are not used at their full capacity. However, this is at the expense of reduced efficiency performing the computing task using a distributed memory environment compared to the shared memory architecture when using a single node. MSC Marc provides the capability to perform parallel computation on both shared memory and distributed memory systems.

6.3.7 Shared memory parallel computation of finite element systems

For shared memory processing (SMP), Marc can concurrently utilise each CPU core within the system for all stages of solving the finite element analysis. The element loop phase is performed completely in parallel, which includes the Fortran subroutines, assembly of the element stiffness matrices, and the stress

recovery phase. Depending on the choice of the matrix solver – *PARDISO* direct solver, or the *CASI* iterative solver, these can obtain the solution of the system matrix, utilising all CPU cores. With the efficiency of modern matrix solvers, the assembly of the stiffness matrix can typically be the most computationally expensive phase of the analysis, however, usually with modern computing methods near linear scaling can be achieved. There is no effort required on the user to take advantage of these in-built parallel facilities. SMP systems provide the most efficient environment for solving the computational problem because of data locality.

6.3.8 Distributed memory parallel computation of finite element systems

Distributed memory systems requiring use of the DDM, for splitting the finite element mesh into sub-domains that are distributed to each system. The analysis is controlled by a master node, which distributes and coordinates child nodes which hold the subdomain during the analysis. Elements remain independent from other sub-domains, however, nodes that are co-located along the boundaries between sub-domains are duplicated, and are known as inter-domain nodes. Communication between each domain on the system uses the message passage interface (MPI) to transfer data and synchronise between nodes. Inter-domain data transfer is a serial process and significantly reduces the throughput. The *METIS* algorithm in the DDM method splits the domain to reduce the number of inter-domain nodes, reducing data transfer between each sub-domains. Within each sub-domain, the same procedure is performed for assembling the element stiffness matrix. The strategy for obtaining the solution to the global system depends on the choice of solver. When using the *PARDISO* solver the global stiffness matrix is assembled from each sub-domain, and is then transferred and solved on the master node. The results are then re-distributed back to each child node. Some direct solvers solve the global system using two phases. In the first phase, fixed displacements are applied on the inter-domain nodes, and the solution is obtained for the sub-domain. In the second phase, the fixed displacements are removed, and an iterative conjugate gradient solver is used across the inter-domain nodes to determine the final global solution. Another method uses the iterative conjugate gradient solver across all domains, which attempts to minimise the residual across the inter-domain nodes.

6.3.9 Implementation of the thermo-mechanical model on the HPC system

A native version of MSC Marc was installed on the HPC System. All the c++ code was developed using the Qt library [168] and the CMake build system [183], which together provide a platform agnostic method for building software. This removed difficulty migrating the simulation between environments, and it also ensures consistent behaviour of the simulation across platforms, regardless of the system it was developed on. Additionally, the Fortran subroutines did not require any modification, except changing the name of the log file to prevent conflict when using simulations performed over several compute nodes using DDM. The input deck, configuration file, and machine build file used for simulation do not explicitly require change, unless the DDM method was used to solve over a distributed system.

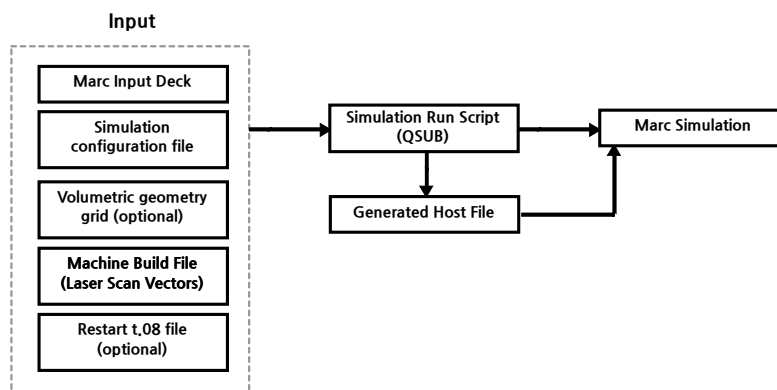


Figure 6.27: Illustration showing the procedure for submitting a simulation job on the HPC system

The overall procedure for submitting a job onto the HPC is illustrated in Figure 6.27. A job submission script was used to submit the job to the HPC scheduler. When using the DDM method across several compute nodes, a host file was generated using Python to correctly configure the MPI settings within Marc. An example job submission command is

```

qsub {N JOBNAME -P PROJECTNAME -l walltime=1:00:00 -l select=1
:ncpus=8:mem=9000mb -v SIM_NAME="simname",NUM_CPU_SOLVER=8,
NUM_EL_THREADS=8,NUM_DOMAIN=1 ~/bin/runSLMSim
  
```

The ability to restart a previous simulation was important. The maximum simulation time permitted on the HPC system (192 hours) presents a challenge when simulating larger problems, especially since the overall simulation time for a given study is often unknown. During the analysis, at pre-defined intervals,

Marc saves the current element state of the analysis to a *.t08* restart file. When restarting a simulation, Marc restarts using the previous state of the domain. Additionally, a subroutine obtains the current analysis time within the restart file, which is used by the *libSLM* library to ‘seek’ through the machine build file to locate the state and position of the laser.

Chapter 7

Investigations using transient thermo-mechanical model

The thermo-mechanical model developed using the fixed mesh is first used in Chapter 6 was used to understand the physical mechanisms that generate the residual stress during the process. In addition, the effect of scan area and the choice of scan strategy are investigated.

The extensions to the thermo-mechanical model, in particular the combination of the adaptive meshing technique with the computational performance offered through the HPC facilities provide greater opportunities to study the *meso*-scale behaviour of the process.

7.1 Methodology

In order to investigate the importance of the chosen laser scan strategy on the residual stresses in the built component, two scan strategies were chosen: unidirectional and alternating (meander). Both laser paths were generated with the Matlab script described in Section 5.1, using compatible laser machine parameters, listed in Table 7.1, and scan parameters in Table 7.2.

The hatched region is scanned first followed by the scan of a single outer contour for each case, as illustrated in Figure 7.1. A direct comparison of the two scanning strategies can be made since the total scanning times are equivalent.

The entire domain had an initial temperature set to 200 °C with a cooling time of 5 seconds. Six simulation cases were chosen: two scan strategies with three different cross-sectional widths each (1-3 mm). To validate the thermal

Laser style configuration	Laser power [W]	Point exposure time [μ s]	Point distance [μ m]
Contour (Border)	40.0	40	10
Hatching	82.5	40	20

Table 7.1: Laser style parameters used by a Realizer SLM 50 for Ti-6Al-4V used to generate the machine build files

Hatch distance h_d [mm]	0.09
Border offset [mm]	0.07
Spot compensation [mm]	0.14
Layer Thickness L_t [mm]	0.04

Table 7.2: Parameters used by a Realizer SLM 50 for Ti-6Al-4V to generate the laser geometry in the machine build files

simulation, a study was conducted to compare the melted track widths observed experimentally with those found in the simulation results. A (3 x 3) mm square region was processed on a Realizer SLM 50 for a single layer using the same parameters as the simulation. An evenly distributed layer was created by manually spreading the powder on the surface of the base plate. Optical measurements were then taken for the melted track widths to be compared with the results obtained from the simulation.

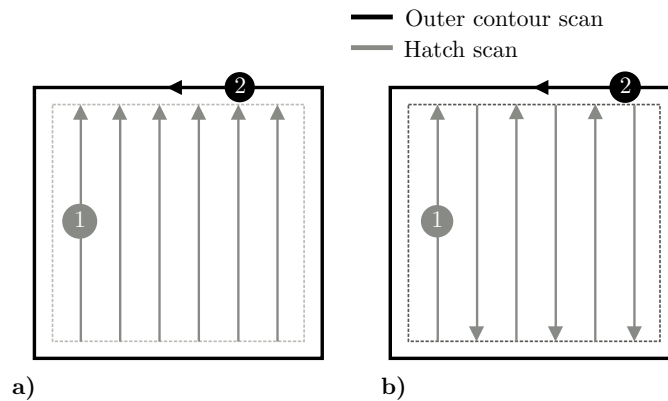


Figure 7.1: Laser scan strategies chosen: a) unidirectional and b) alternating

7.2 Results obtained from the thermo-mechanical model

The results obtained from the thermo-mechanical are presented in this section. Firstly, the validation between the model and the experiment are presented in Section 7.2.2. Followed by a more thorough analysis of the effect of scan strategy and scan area, which are shown in Sections 7.2.2 to 7.2.4. Finally, the results obtained from benchmarking the adaptive meshing scheme are presented in Section 6.3.5.

7.2.1 Validation of thermal analysis with experiment

The surface temperature for a single scan vector in Figure 7.2(a) shows an approximate melt pool width of 0.14 mm. The peak temperature is an isolated singularity inside the melt pool region above the vaporisation temperature of Ti-6Al-4V. A micrograph was taken for the single layer experiment, as shown in Figure 7.3. It can be seen from comparing Figure 7.3(a) and Figure 7.3(b) that the track width in simulation and experiment varies by approximately 14%, taking into account adjacent track re-melting due to overlap. This provides confidence in the modelling approach and material parameters used in the simulations.

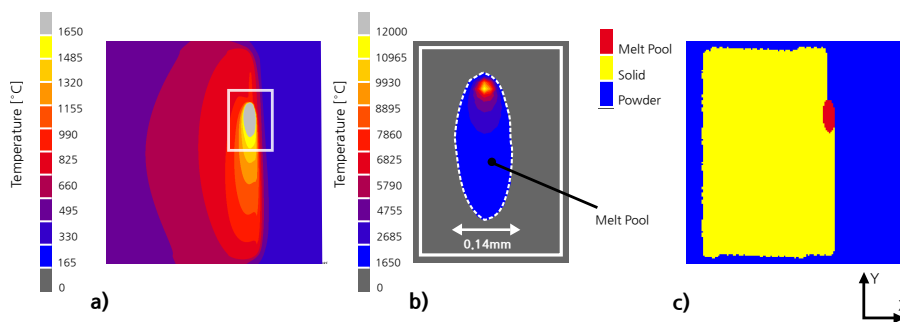


Figure 7.2: Temperature distribution whilst scanning, showing a) the temperature in the hatched region, b) temperature inside the melt pool and c) the element state variable.

7.2.2 Thermal analysis of single layer sections

Due to the inclusion of multiple material phases, non-symmetric thermal behaviour is seen, as illustrated in Figure 7.2(a). An asymmetric melt pool is formed during the laser scan in the hatched area due to the position of powder and solid regions on each side of the scan vector, as shown in Figure 7.2(c). The

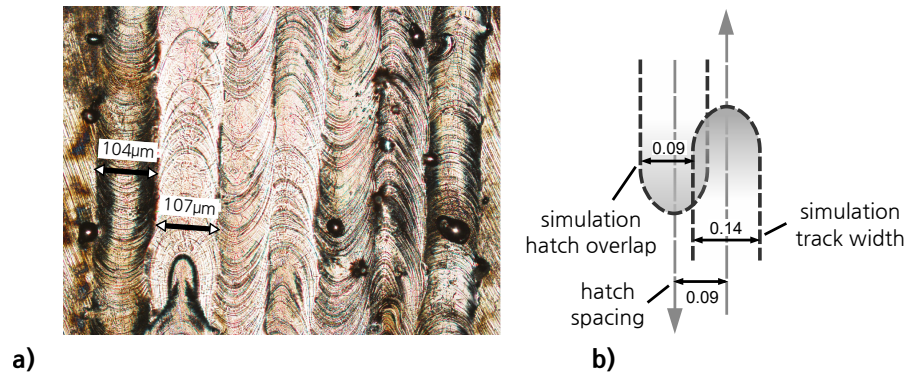


Figure 7.3: a) Single layer laser scan on a base plate using Ti-6Al-4V of adjacent tracks and b) diagram illustrating the calculated overlap of adjacent scan tracks for the simulation.

melt pool becomes asymmetric through preferential heat conduction into the previously scanned consolidated region which has a higher conductivity than the neighbouring powder region.

The transient thermal histories of the simulations are shown in Figure 7.4 by taking the average temperature for solidified elements in the first layer. For all scanned areas, the average temperature decreases with scanning time. The discontinuities in temperature, shown in Figure 7.4, indicate the change from hatch to contour scan and the end of scanning. Overall, the average element temperature is the highest in the smallest scan area but is held for a short duration, compared with the larger region sustaining a lower temperature over a greater period of time. This is caused by higher thermal losses associated with the higher temperature the smallest region is held at, and the increased storage of thermal energy into the substrate, thereby reduction conductive losses from the consolidated layer. Oscillations in the temperature correspond to the scanning of adjacent tracks and are shown for a single node in (3 x 3) mm cases in Figure 7.5. The oscillations resemble a damped ‘saw tooth’ wave with the peaks corresponding to the position of the laser at the end of each scan vector. The temperature oscillations are damped and tend towards a steady state of 400 °C, because of the energy balance of the heat input and losses in the system, as defined in equation 6.22.

In Figure 7.6, the total area held above 825 °C, the point at which Ti-6Al-4V begins to acquire super-plastic behaviour [184], increases with time. This indicates the accumulation of heat in the part since the power is kept constant throughout scanning the hatched region.

The probability density distribution $P(T, t)$ in Figure 7.8 shows the current temperature state throughout the scanning history of the hatched regions. A

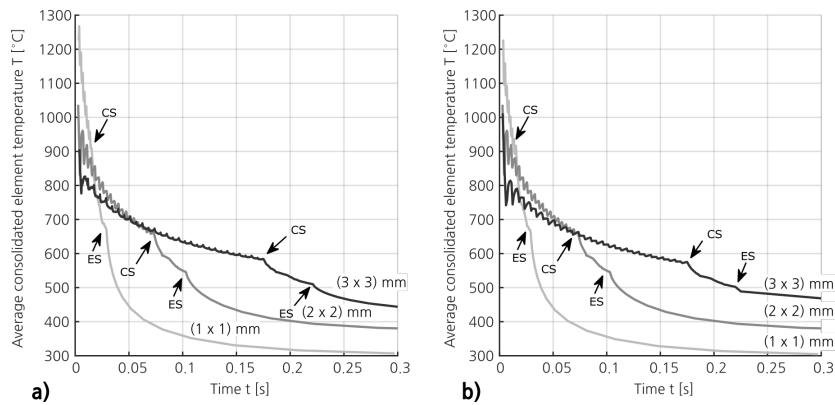


Figure 7.4: Average solidified element temperature over time for different scan area sizes (CS – Start of the Contour Scan and ES – End of Scanning) for a) alternating and b) unidirectional scan strategy

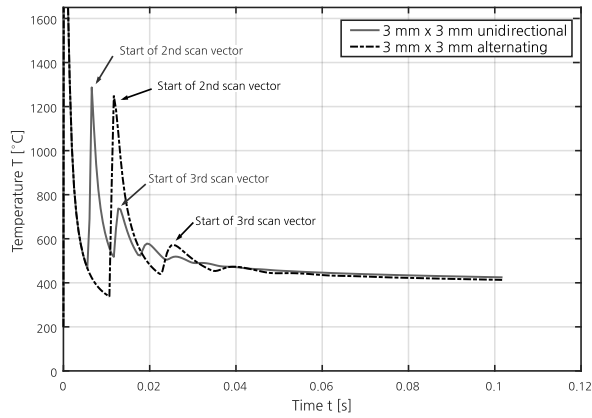


Figure 7.5: Temperature profile for a single node taken at top left corner of the hatch region for the unidirectional and alternating scan strategies

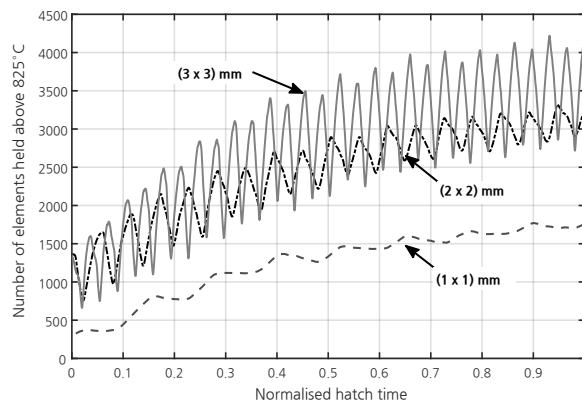


Figure 7.6: Total number of elements held above 825 °C the three different scan cases when using the alternating strategy.

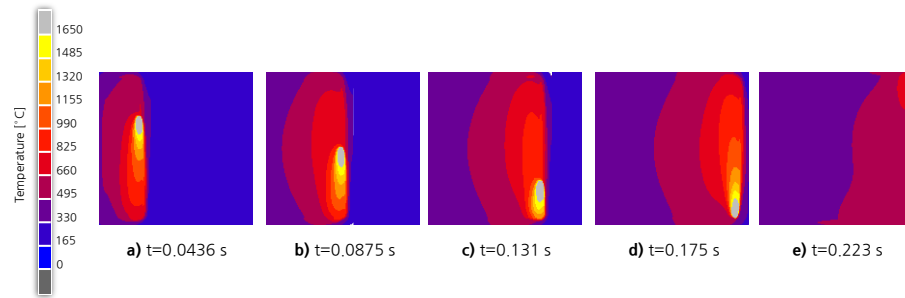


Figure 7.7: Profile views of temperature for (3 x 3) mm test case using the alternating scan strategy. The time intervals were taken for a) $\frac{1}{4}$ hatch scan time, b) $\frac{1}{2}$ hatch scan time, c) $\frac{3}{4}$ hatch scan time, d) end of scanning hatch, and e) the end of contour scan

skewed distribution is present, with the presence of oscillations (ridges) throughout the scanning history in all cases. When scanning the smallest region, as shown in Figure 7.8(a,d), a large proportion of elements are held above 825°C. Towards the end of scanning, the distribution in the larger regions become narrower, with the peak centred at approximately 500°C. During the early phase of scanning using the alternate strategy, as shown in Figure 7.8(a,b,c), the troughs in the temperature are lower compared to the unidirectional strategy.

The temperature history for the (3 x 3) mm test case with the alternating scan strategy, as illustrated in Figure 7.7, shows a localised heat tail in the direction of the scan vector situated near recently scanned tracks. Over time heat becomes uniformly dissipated into previously consolidated regions.

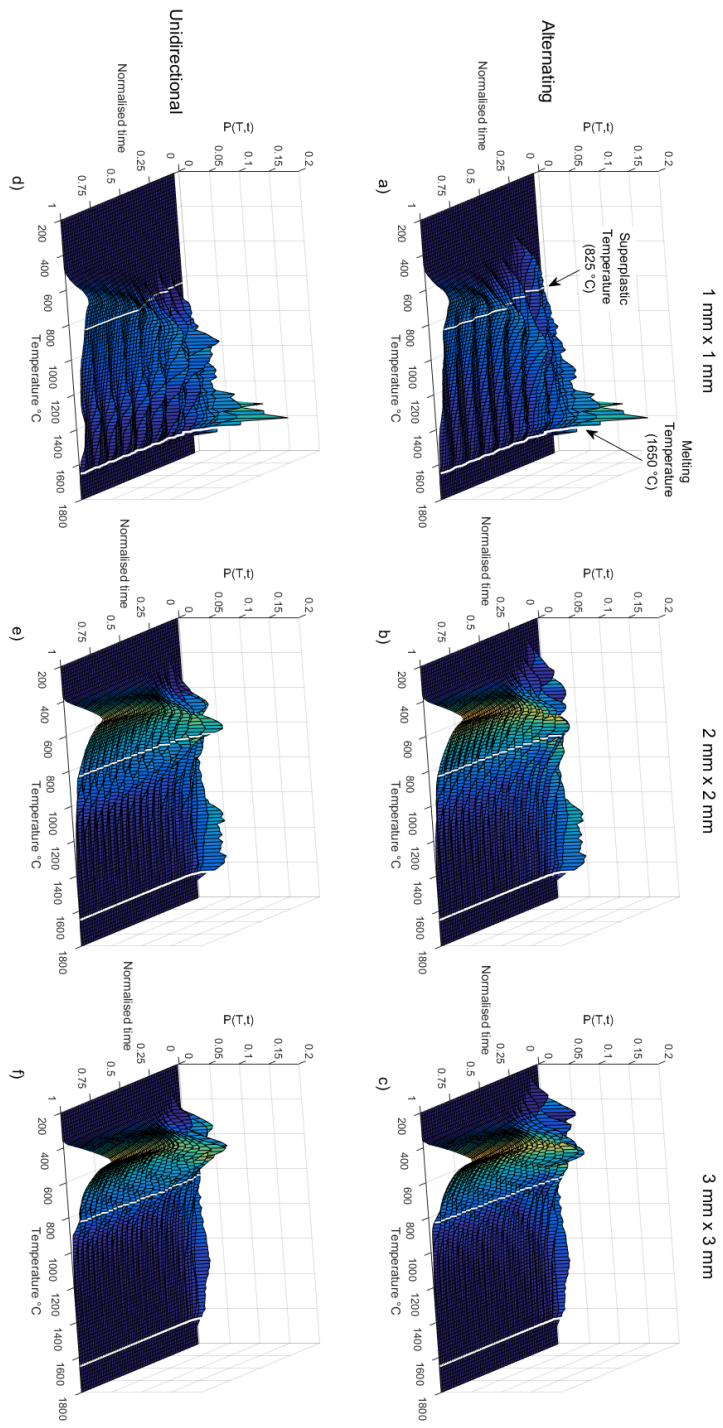


Figure 7.8: Transient probability density distribution $P(T,t)$ for consolidated elements normalised to the scanning time of the hatched region. Distributions are shown for the alternating strategy with sizes a) (1 x 1) mm, b) (2 x 2) mm and c) (3 x 3) mm, and unidirectional strategy with sizes d) (1 x 1) mm, e) (2 x 2) mm and f) (3 x 3) mm

7.2.3 Stress analysis of single layer regions

The state of a single scan vector track at an instance is shown in Figure 7.9. It can be seen that longitudinal stress, σ_{yy} , as shown in Figure 7.9(d), is generated as consolidated material behind the melt pool cools and contracts. The transverse stress, σ_{xx} , shown in Figure 7.9(e) is lower due to the lack of solid material inhibiting thermal expansion and a lower temperature gradient perpendicular than parallel to the scan vector, respectively shown in Figure 7.9(b) and Figure 7.9(c).

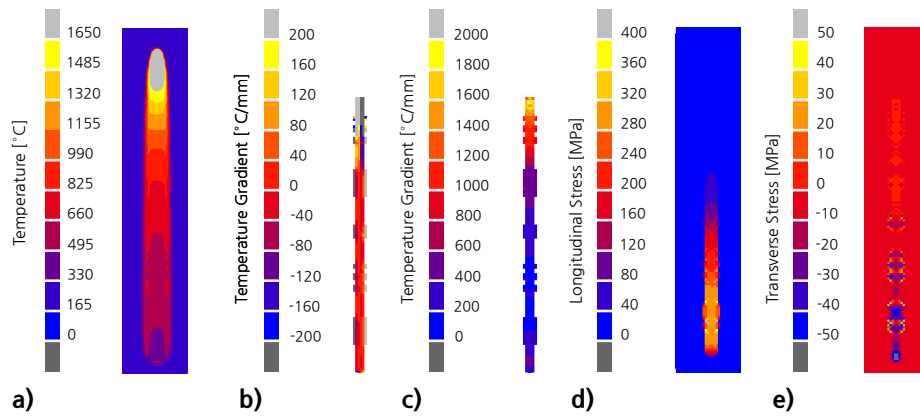


Figure 7.9: Profile views during the first scan vector of a) temperature, b) temperature gradient in solid elements in X direction c) temperature gradient in solid elements in Y direction, d) σ_{yy} stress component, and e) σ_{xx} stress component

Upon the accumulation of several tracks, there is a progressive build-up of transverse stress, as shown in Figure 7.10(c), due to material inhibiting thermal expansion in the previously scanned track. The thermal expansion in the region surrounding the melt pool creates a compressive stress in the neighbouring region. Due to the high temperature in the HAZ, yielding occurs, which creates regions of plastic strain between each adjacent scan track in the hatch region, as shown in Figure 7.10(d).

A non-uniform, anisotropic stress distribution in the component is generated, as shown in Figure 7.11 and Figure 7.12. The stress distributions in the XY plane are mostly dominated by the σ_{yy} component which decreased in magnitude from the start to the end of the hatched region, as shown in Figure 7.12(a). The largest σ_{yy} stresses were situated centrally along the hatch region and decrease towards the end of the scan vectors in the hatched region. A ‘ripple’ effect was observed in both the transverse and longitudinal stress components, when using the alternating scan strategy (Figure 7.12(a)).

To identify the cause for the longitudinal stress varying in the X direction for both scan strategies, a series of comparisons were made near the beginning

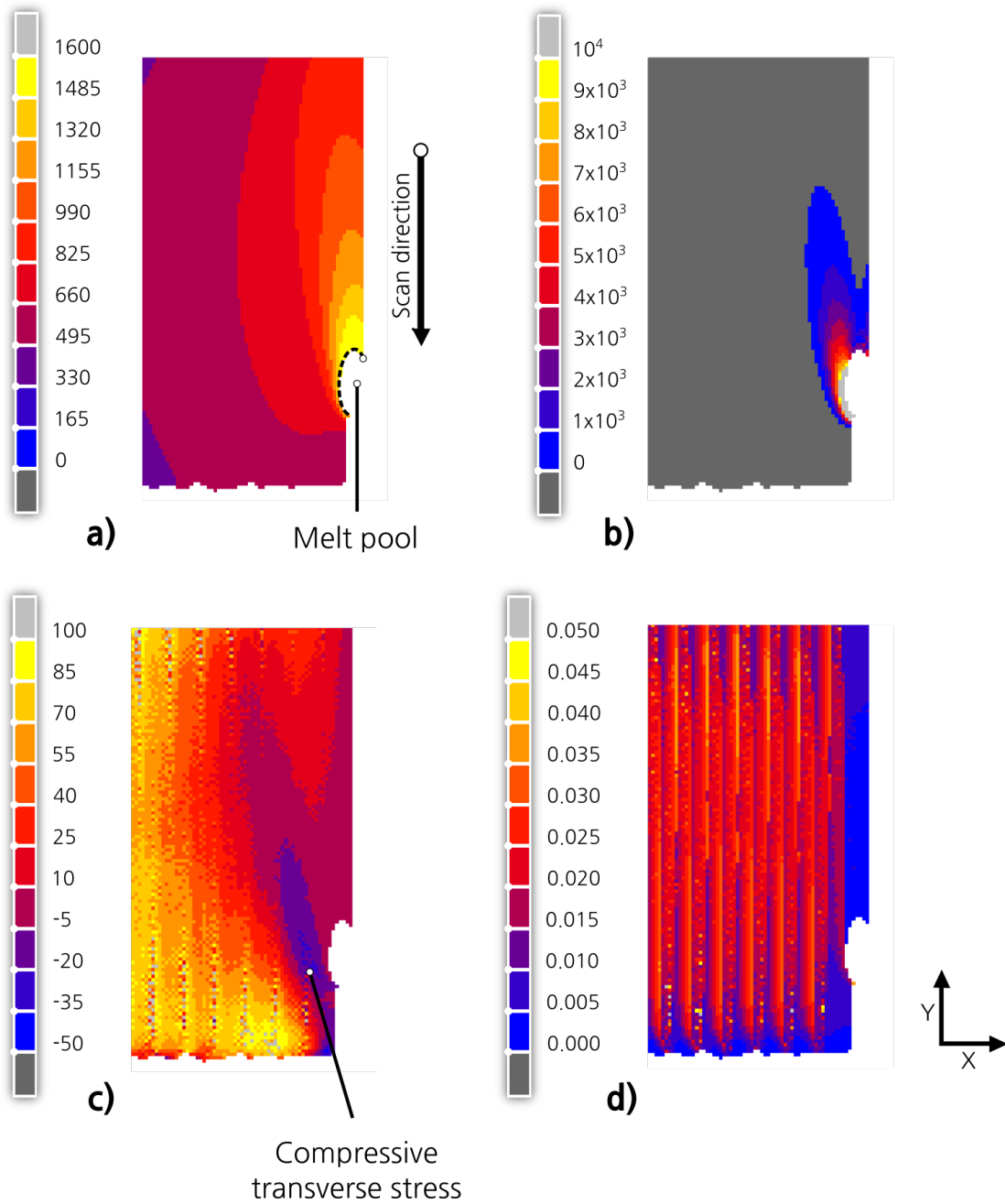


Figure 7.10: Profile views of a) temperature [°C] b) temperature gradient [°C/mm], c) σ_{xx} [MPa] and d) $\bar{\epsilon}_p$ whilst scanning the (3 x 3) mm unidirectional test case at $t = 0.092$ s. Dashed line indicates position of the melt pool region.

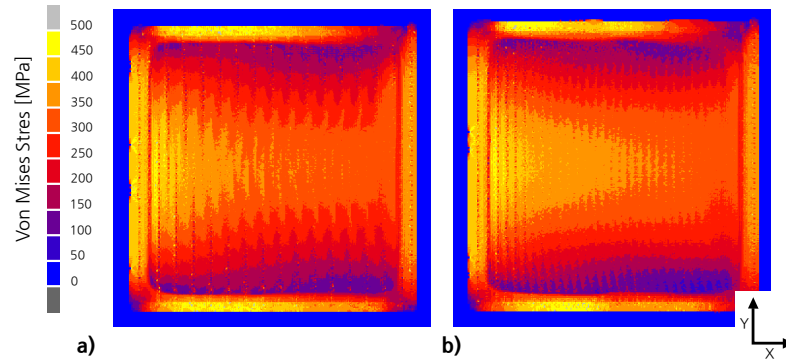


Figure 7.11: Profiles views of von Mises stress distribution for (3 x 3) mm test case when using a) unidirectional, and b) alternating scan strategies.

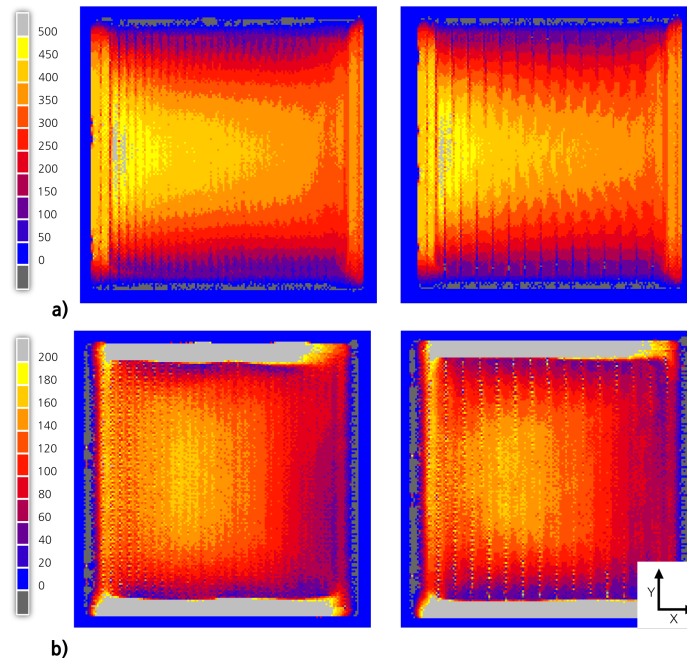


Figure 7.12: Profile view of surface normal stresses a) σ_{yy} and b) σ_{xx} when using unidirectional (left) and alternating (right) scan strategies

and the end of scanning the hatch region, as shown in Figure 7.13. Towards the end of scanning the hatched zone, the surrounding region was held at a higher temperature, as shown in Figure 7.13(a) and exhibited a smaller temperature gradient behind the melt pool region, illustrated in Figure 7.13(b). During the initial development of the longitudinal stress behind the melt pool, as shown in Figure 7.13(c), the magnitude of these stresses was found to be lower towards the end of scanning for the hatched region.

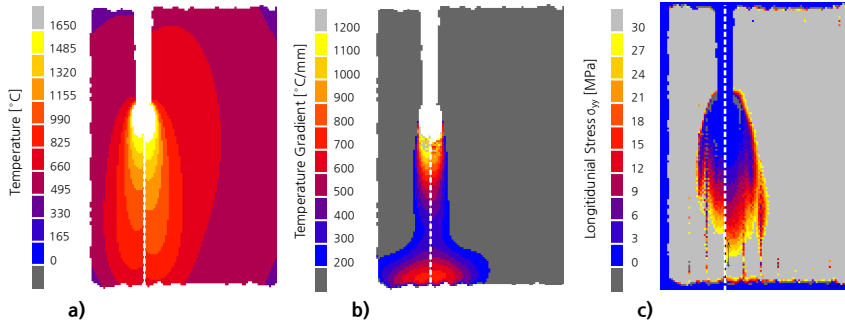


Figure 7.13: Mirrored profile views of a) the temperature, b) the temperature gradient in the Y direction, and c) σ_{yy} taken at $t = 0.0320$ s (left half) and at $t = 0.156$ s (right half)

Scan Area	Scan Strategy	Total Strain Component $\times 10^{-3}$			Stress Components [MPa]			Von Mises Stress [MPa]
		ϵ_{xx}	ϵ_{yy}	ϵ_{zz}	σ_{xx}	σ_{yy}	σ_{zz}	
(1 x 1) mm	Alternate	-13.5	-9.0	-22.9	151.8	189.3	0.0	236.0
	Unidirectional	-13.8	-9.1	-22.5	145.1	183.6	0.0	221.0
(2 x 2) mm	Alternate	-13.5	-6.2	-23.7	161.8	270.1	0.0	289.0
	Unidirectional	-13.5	-6.1	-23.4	166.8	273.5	0.0	289.3
(3 x 3) mm	Alternate	-13.9	-4.5	-23.6	140.2	302.0	0.0	307.0
	Unidirectional	-13.8	-4.4	-23.5	143.9	305.2	0.0	307.0

Table 7.3: Average values for von Mises stress and normal strain and stress components calculated from solid elements located in the first layer for multiple simulation cases

7.2.4 Comparison between laser scan strategies

To enable comparison of the different scan areas sizes and scan strategies on the mechanical response, the mean values were calculated for the normal strain and stress components and the von Mises stress, which are listed in Table 7.3. The average values of these measurements were sampled from all consolidated elements on the final time step of the simulation.

The greatest strain component was ϵ_{zz} followed by ϵ_{xx} and ϵ_{yy} . The von Mises stress increases with the scan area size. Throughout each test case, the largest magnitude of stress exists in the σ_{yy} component, followed by σ_{xx} with a small value for the σ_{zz} component. Measuring the average for stress and strain, reveals no substantial difference between the two scan strategies, but, there is clearly a difference in the distribution of stress components, as shown in Figure 7.11 and Figure 7.12.

A comparison of the temperature at the start and the end of scan vectors between scan strategies is shown in Figure 7.14 to Figure 7.16 to better understand the difference in the distribution of stress components during the process. When

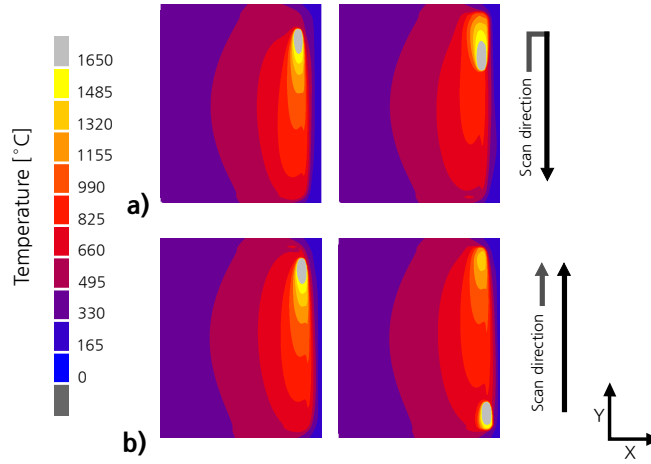


Figure 7.14: Profile view of temperature distribution at the approach and exit of the laser scan vector when using a) alternating scan strategy and b) unidirectional scan strategy

the alternating scan strategy was used, the next scan vector began in a higher temperature region compared to the unidirectional scan due to the prior scan vector finishing nearby. The elevated temperature in the alternate scan reduces the magnitude of the temperature gradient for the alternating scan, as shown in Figure 7.15(b), which is less at the start of the scan vector compared to the unidirectional scan shown in 7.16(b). After the duration of 2 ms, the distributions of the temperature gradients become independent of their position along the scan vector for both scan strategies. The transverse stress at the start of the scan vectors differed between strategies. At the beginning of the scan vector, a larger region is subjected to a compressive transverse stress when using the alternating strategy, as shown in Figure 7.15(a), compared to the unidirectional strategy shown in Figure 7.16(a).

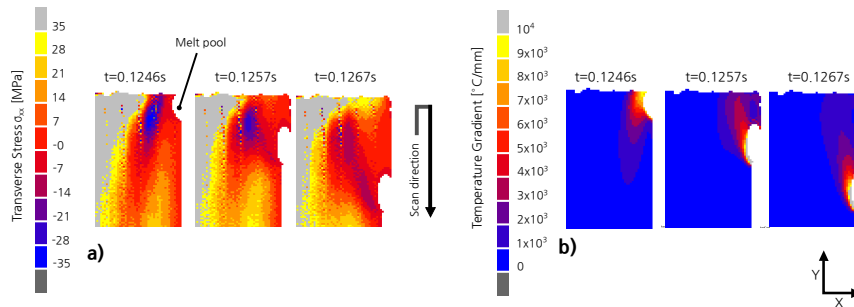


Figure 7.15: Profile views of a) σ_{xx} stress and b) temperature gradient for solid elements at the beginning of the scan vector using the alternating strategy

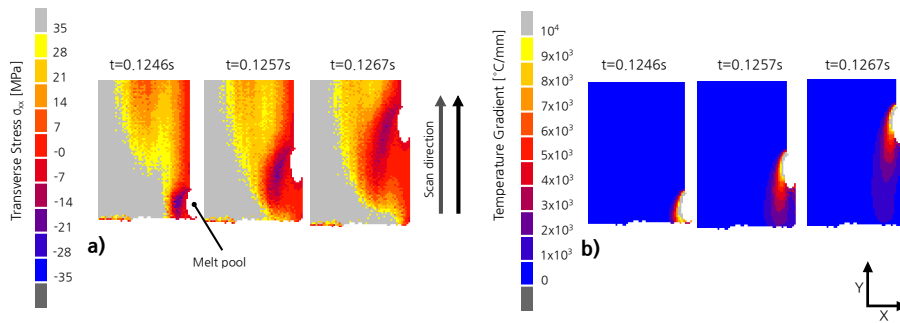


Figure 7.16: Profile views of a) σ_{xx} stress and b) temperature gradient for solid elements at the beginning of the scan vector using the unidirectional strategy

The previously described temperature effect also caused a difference in the distribution of plastic strain between scan strategies. When using the unidirectional scan strategy, a uniform distribution of plastic strain is present throughout the hatch region, as shown in Figure 7.17(b), whereas the alternating scan strategy features decreased levels of plastic strain towards the end of the scan vectors, as shown in 7.17(a).

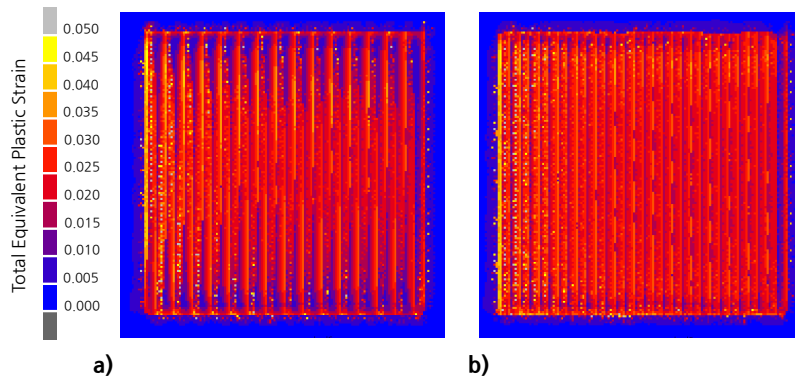


Figure 7.17: Profile view of total equivalent plastic strain fields $\bar{\epsilon}_p$ for a) alternating strategy and b) unidirectional strategy

7.3 Discussion

The single layer experiment showed that the melted track width in the simulation varied with the experiment by 14%. However, potential error does exist in the experiment, such as accurately levelling the base plate, exact lens focal position, and inconsistency in the thickness of the powder layer created manually. Nevertheless, the peak temperature is in good agreement with another work that used a similar

spot size of $50\ \mu\text{m}$ [185]. This work excluded the effect of vaporization although it is acknowledged this effect will influence the melt pool depth and geometry, and limit the maximum surface temperature to some degree. However, this is not expected to cause a significant change in the thermal and stress values generated by the simulation because the effect will be isolated to the temperature singularity inside the melt pool, as shown in Figure 7.2.

The temperature history shown in Figure 7.4 and 7.5 reveals the importance of the sizing effect in the physical problem. It was found that the temperature distribution achieved and length of time temperature is sustained is dependent on the size of scan area, as shown in Figure 7.4 and Figure 7.8. The smallest scan area sustains a high temperature for a short period but due to its size cools rapidly after scanning has completed, whereas the largest region holds a lower temperature for longer with a lower cooling rate. This is caused by the accumulation of thermal energy into the consolidated regions and substrate over the duration of the scan.

A large proportion of material in the (1 x 1) mm test cases, as shown in Figure 7.8, is held above the super-plastic temperature. In Table 7.3, this test case has the greatest longitudinal strain (ε_{yy}), and has the smallest transverse stress which indicates that plastic deformation has occurred. In super-plastic forming of Ti-6Al-4V, parts can be manufactured without suffering from residual stress or spring back, at low shear rates [184] and likewise shows that the formation of residuals stresses can be controlled by temperature. Depending on the substrate (powder or solid), varying the scan area size will enable control over the sustained temperature achieved in a scanned region. Potentially, this will enable control over the build-up residual stress and generation of the microstructure by elevating the temperature and reducing the rate of cooling [99].

Oscillations in the temperature exist, as shown between Figure 7.4 and Figure 7.8, and have different frequencies for the laser scan strategies due to the interval of time between adjacent scanning. The period of the oscillations is, therefore, affected directly by the scan vector length. The unidirectional strategy has a more stable minimum temperature, due to a smaller period between adjacent scans, as shown in Figure 7.5 and Figure 7.8, but this also affected by the lack of thermal mass available early in the scanning history. Also, it is evident in Figure 7.5 that the heating effect from the laser in previously consolidated areas diminishes between three to four adjacent scan tracks, and this is also visible in Figure 7.7. Potentially, a performance improvement for simulating SLM could be gained by modelling regions far from the melt pool using a steady-state analysis, but retaining the transient behaviour in region near the melt pool.

The analysis of stress in Section 7.2.3 showed that the main contributor

of stress is created parallel to the scan vector. Observing the behaviour in a single scan track, the longitudinal stress was considerably higher than the transverse stress, due to the higher temperature gradient component parallel to the scan vector, as shown in Figure 7.9(c). Table 7.3 shows that increasing the scan area size effectively increases the overall stress in the region. This is caused by the dominating longitudinal stress which increases with scan vector length, as reported previously in the literature [155]. Therefore, when designing laser scan strategies, it is important to minimise the scan vector lengths for all orientations.

For all test cases, a non-uniform anisotropic stress distribution was generated, as illustrated in Figure 7.11 and Figure 7.12. The calculated averages for the normal stress components match observations in experimental studies using experimental X-ray diffraction measurements conducted by Simonelli et al. [186] and numerically by Roberts [154]. Overall, the laser scan strategy chosen for a component should factor in the anisotropic build-up of stress created during this process. A further study is required to determine the viability of orientating the scan vectors in an optimal way to equalise the overall stress field whilst considering other processing constraints such as porosity.

Longitudinal stress tended to decrease in the X direction, which was caused by a combination of a higher elevated temperature, and a lower temperature gradient, as shown in Figure 7.13. This corresponds with the temperature history, as shown in Figure 7.6 with the region of higher temperature (>825 °C) increasing in area towards a plateau throughout the scanning history.

After successive scanning of tracks, as shown in Figure 7.10, the mechanism for the generation of transverse stress was found to be caused by the temperature gradient mechanism shown in Figure 7.10(b). The thermal expansion of solid material surrounding the melt pool area creates a region of compressive transverse stress (Figure 7.10(c)). Additionally, regions of plastic strain were created by re-melting between adjacent scan tracks at high temperature (Figure 7.10(d)). The distributions of the total strain components correspond to the large values in the X and Z direction for the total strains, as shown in Table 7.3, which includes contributions from the plastic strains. This indicates that in a full sized part, distortion will occur normal to the XY plane, where the total strain component in the Z direction is greatest. This results in the ‘curling’ effect typically observed in failed builds. These findings raise concerns about mechanical testing on the as-built specimens produced in SLM because they will contain geometrically dependent residual stress and plastic deformation, which will affect the bulk material strength and ductility in the final component.

The average stresses calculated in Table 7.3 indicate that scanning small regions with the same laser parameters for these two scan strategies do not

strongly affect the magnitude of residual stress. This was suspected to be caused by the small scale of the analysis. Nevertheless, a difference was shown between the two scan strategies for the distribution of planar normal stresses, and the plastic strain towards the end of the scan vectors, as shown in Figure 7.12 and Figure 7.17. The ‘rippled’ stress distribution present in the alternating strategy is attributed to reversing the scan vector direction. Both effects are caused by the high temperature and smaller temperature gradients found in this region, as shown in Figure 7.15, when using the alternating scan strategy. Inevitably, increasing the substrate temperature prior to scanning will reduce the magnitude of residual stress and plastic deformation in a part, as reported by other researchers [77, 80]. This, however, is currently not practical to perform with current commercial SLM technologies.

The use of adaptive meshing showed that refinement was required to capture the thermal gradients which extended outwards into previously consolidated material, as shown in Figure 6.19. This raises questions if the use of moving meshes, with a coarse fixed background mesh compared to the melt pool, such as that proposed by Zeng et al. [178] will capture the residual stresses. Their proposed technique has not been analysed for thermo-mechanical analyses or is not available in reported literature.

7.4 Conclusions and summary

A coupled thermo-mechanical simulation has been established that is capable of predicting the effect of scan strategy on residual stress and has been demonstrated for two different scan strategies with single layer cross-sections of 1-3 mm. This work demonstrates that even at a macro scale, complex transient behaviour is inherent to the process of selective laser melting.

The simulation based investigation has identified the interactions between temperature history, the mechanical response and the effects of laser scan strategy. Specific conclusions drawn from the results that have been confirmed with observations and findings present in current literature are:

- The temperature oscillates with a frequency dependent on the scan vector length.
- The larger scanned regions had a lower average temperature but temperature was sustained for a longer duration due to the accumulation of heat.
- Longitudinal stress (parallel to the scan vector) increases with scan vector length and is the main contribution to stress due to the presence of the larger thermal gradient parallel to the scan vector.

The investigation also revealed new findings that have advanced knowledge in understanding the role of thermal history created by choice of scan strategy and the build-up of residual stress. The specific conclusions found are:

- The process generates a non-uniform anisotropic stress fields, which have regions of lower transverse and longitudinal stresses situated towards the end of the scan vectors.
- No substantial difference in the magnitude of stress was observed between the two scan strategies investigated. However, the distribution of stress and plastic strain did vary between laser scan strategies and was shown to be caused by the thermal history.
- Reduced levels of stress and plastic strain are exhibited at the end of scan vectors when using the alternate scan strategy due to the reduced temperature gradients at the end of each vector.

Chapter 8

Investigation of the effect of laser parameters

8.1 Introduction

The effect of laser process parameters on the generation of residual stress, as discussed in Section 2.4.4, is little understood. Experimental work was done by Vrancken [87] to study of the effect of ‘buildable’ laser parameters on residual stresses measured using XRD measurements and through the method of cantilever distortion. Preliminary conclusions from their results were summarised as follows:

- Increase in layer thickness increases the generation of residual stresses
- Increase in scan speed increases both residual stress and anisotropy of stresses
- Laser power has the smallest effect on residual stress

Due to variability between some of their experimental results, further confidence in their results is required. Their overall recommendation was that thermo-mechanical models could support understanding of the effect of laser parameters.

8.2 Methodology

Considering the large parameter space for exploration, and the model design, the following laser parameters were considered for investigation in this work:

Laser power [W]	Laser scan speed [mm/s]	Hatch distance [μm]	Layer thickness [μm]	Laser spot size [μm]	Energy density [W/mm^3]	Normalised enthalpy	Reference
170	1250	100	30	100	45	8.6	[187]
200	600	150	50	70	44	25.0	Renishaw AM250
157	225	100	50	70	140	32.1	[186]
82.5	500	90	40	60	46	14.2	[188]
42	200	75	30	52	93	14.2	
42	200	50	30	52	140	14.2	
42	200	100	30	52	70	14.2	
42	200	75	30	52	93	14.2	[71]
42	100	75	30	52	187	20.1	
42	50	75	30	52	373	28.4	
42	225	74	30	80	84	7.0	[90]
170	1250	100	30	100	45	8.6	[189]

Table 8.1: Selection of known laser parameters and machine parameters used for building Ti-6Al-4V available in literature

Thermal diffusivity α [$\times 10^{-6} \text{ m}^2/\text{s}$]	8.02
Enthalpy at melt H_m [$\times 10^6 \text{ J}$]	1.49
Density at melt ρ_m [kg/m^3]	4000

Table 8.2: Properties used for calculating the normalised enthalpy for Ti-6Al-4V. Enthalpy at melt taken from Rai et al. [38]

- laser power
- laser scan speed
- hatch distance.

In order to reduce the number of studies required, infeasible combinations of laser power and speeds that would likely create low density parts were excluded to reduce the parameter space. These were determined by calculating the normalised enthalpy definition in equation 2.4, based on known laser parameters available throughout literature for different commercial systems listed in Table 8.1, and material properties in Table 8.2.

The use of the normalised enthalpy provides a non-dimensional parameter for comparing laser parameters by ignoring hatch distance and layer thickness, which are simplistic measures of energy deposition. Based on the normalised enthalpies calculated in equation 2.4, a combination of laser power and scan speeds with normalised enthalpies between 12 – 25 was arbitrarily chosen as a sufficient process window.

Based on the normalised enthalpy range, the combination of laser speeds and powers within this process window applicable for the Realizer SLM 50 were calculated at intervals of 100 mm/s for the laser speed, and 10 W for the laser power using a laser spot size $r_d = 30 \mu\text{m}$. The process window for this is shown in Figure 8.1, revealing a window widening with increase in both laser power and speed.

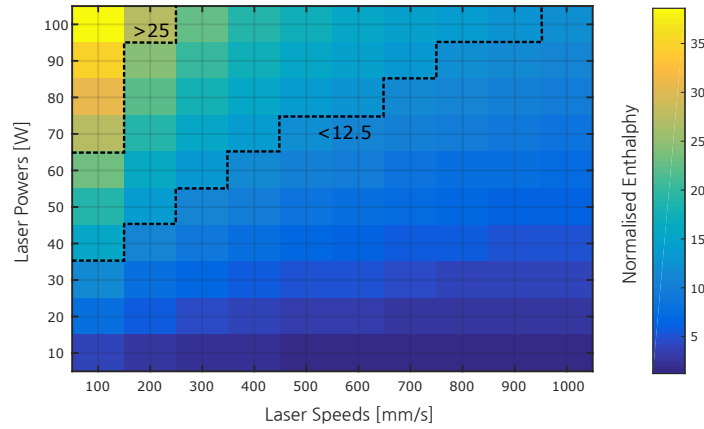


Figure 8.1: Plot of the normalised enthalpies calculated for laser power and speeds suitable for the Realizer SLM 50. Dashed area shows an arbitrary chosen processing window with a normalised enthalpy between 12.5 and 25

The first parametric studies aimed to investigate the effect of laser parameters on the shape and dimensions of melt pool. It was only necessary for these to be performed with a thermal analysis – achieved by disabling the mechanical pass in the thermo-mechanical model.

The analysis was performed over the combination of laser scan speed and powers within the process window, using a fixed hatch distance $h_d = 0.09$ mm, layer thickness $L_T = 0.04$ mm. Each parametric study was performed over two adjacent scan vectors of 5 mm length, as shown in Figure 8.2. The length was chosen to find the quasi-steady behaviour of the melt pool after it stabilises. Three scan vectors were chosen, since previous studies in the literature were only concerned with the behaviour for single scan tracks. It is expected that scanning along the second track would change the melt pool shape, and the thermal dissipation behind the melt pool.

In order to increase the resolution and accuracy for capturing the melt pool, the analyses used an additional level of refinement (smallest element length = 0.01 mm), and the use of a shorter point overlap factor $f_{po} = 0.3$ to improve stability across the large range of laser scan speeds chosen. The simulations were performed using the HPC system described in Section 6.3.6.

The dimensions of the melt pool were extracted from the results using a *Python* post-processing script to obtain the state variable, which were then exported to and processed in Matlab. The overall dimensions of the melt pool were automatically extracted for each timestep of the results using Matlab’s connected component algorithm *bwconncomp* and region properties tool *regionprops*. The average melt pool dimensions were obtained across each scan vector.

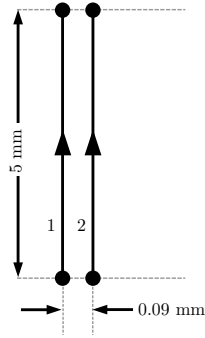


Figure 8.2: Illustration of the scan vectors used for thermal analysis in the parametric study

Following the thermal analysis, a full thermo-mechanical analysis using the same parameter study was performed on the same laser parameter set. In this analysis, the laser parameter set was instead scanned across a (5 x 5) mm square, using the same hatch distance $h_d = 0.09$ mm. The large region was chosen to understand the implications of the laser parameters when scanning across large components. It is expected that the parameter set will behave differently for smaller regions.

In order to increase simulation throughput, the thermo-mechanical simulation returned to the normal refinement level (smallest element length = 0.02 mm), however, retained the same point overlap factor as the thermal analysis study. A final study was performed by varying the hatch distance across a single laser power and speed combination.

8.3 Results

8.3.1 Parametric study for the thermal analysis

The parametric study using only the thermal analysis was completed successfully except for a few combinations of parameters which resulted in simulation crashes. A parameter map (laser speed and laser power) of the extracted profiles of the melt pools for the first scan vector is shown in Figure 8.3. It can be seen that an increase in laser speed, and to a lesser extent laser power, elongates the melt pool, and increases the aspect ratio

The stable melt pool shape was extracted for the first and second scan vectors and their geometries are shown in Figure 8.4, and respectively their aspect ratios in Figure 8.5. It can be seen the melt pool length is both dependent on both the laser power and speed whilst the melt pool width is mostly dependent on

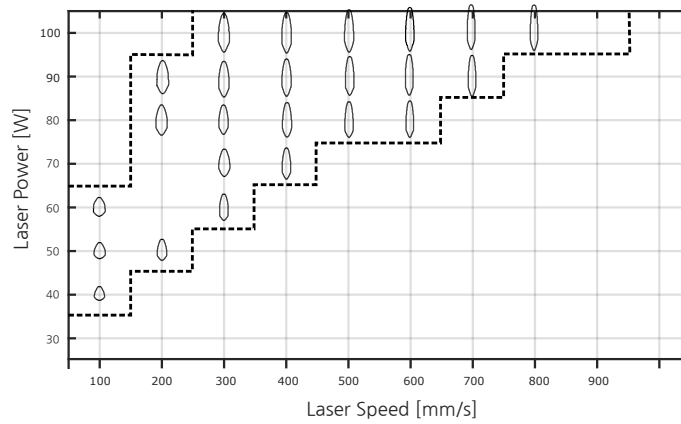


Figure 8.3: Process map showing the effect on melt pool geometry based on the combination of laser powers and scan speeds

the scan speed. In the parameter window explored, the aspect ratio varied from 1.5 to 5.5 for both the first and second scan vector, and it was found to be more dependent on the scan speed than laser power. When comparing the melt pool dimensions when scanning the first and second track, as shown in Figure 8.4, there is a decrease in melt pool width and length. This can be attributed to the previous scan vector providing an additional heat sink for the dissipation of heat away from the melt pool.

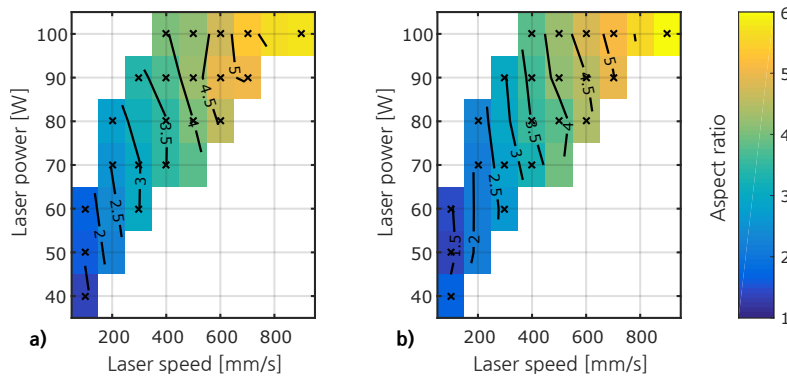


Figure 8.5: Parameter map showing the melt pool aspect ratio for a) the first scan vector and b) the second scan vector

8.3.2 Parametric study for the thermo-mechanical analysis

A parametric study was performed using the full thermo-mechanical model to investigate the effect on the residual stress generated across a (5 x 5) mm island

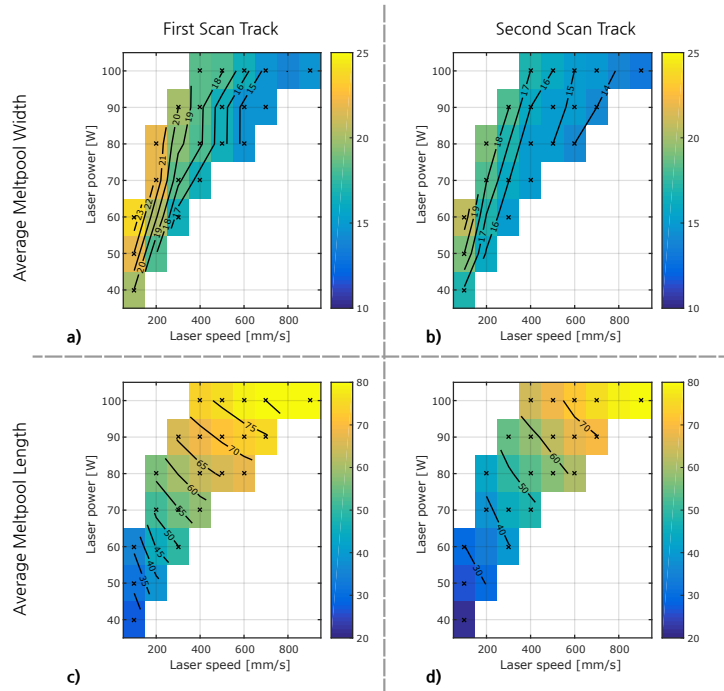


Figure 8.4: Parameter map showing interpolated average melt pool widths along a) the first scan vector and b) the second scan vector, and the average melt pool length along c) the first scan vector, and d) the second scan vector. Crosses indicate parameter combinations that were successfully analysed

region, across a range of laser power and speed combinations. The profiles of the transverse, longitudinal residual stresses and the total equivalent plastic strain $\bar{\varepsilon}_p$ shown in Figure 8.6 were extracted from the results by taking a section through the centre of the scanned square region perpendicular to the scan vector.

Across the parameter combinations investigated, the observed transverse stresses (Figure 8.6(a)) varied by ~ 150 MPa, whilst for the majority of parameters the longitudinal stresses (Figure 8.6(b)) varied less than 75 MPa, when excluding the cases ($P = 50$ W, $v = 100$ mm/s) and ($P = 60$ W, $v = 100$ mm/s). The equivalent plastic strain (Figure 8.6(c)) varied from 0.02 to 0.036 across the parameters combinations indicating a various degree of yielding occur based on the parameters.

To establish a relationship between residual stresses and total equivalent plastic strain between the parameter combinations, a single measure was used. Instead of using an average value, a linear fit was taken across the profiles shown in Figure 8.6, and the interpolated value at the mid-point was used. From these sampled values, the process maps in Figure 8.7 were generated.

It can be seen in Figure 8.7(b) that the longitudinal stress is only highly

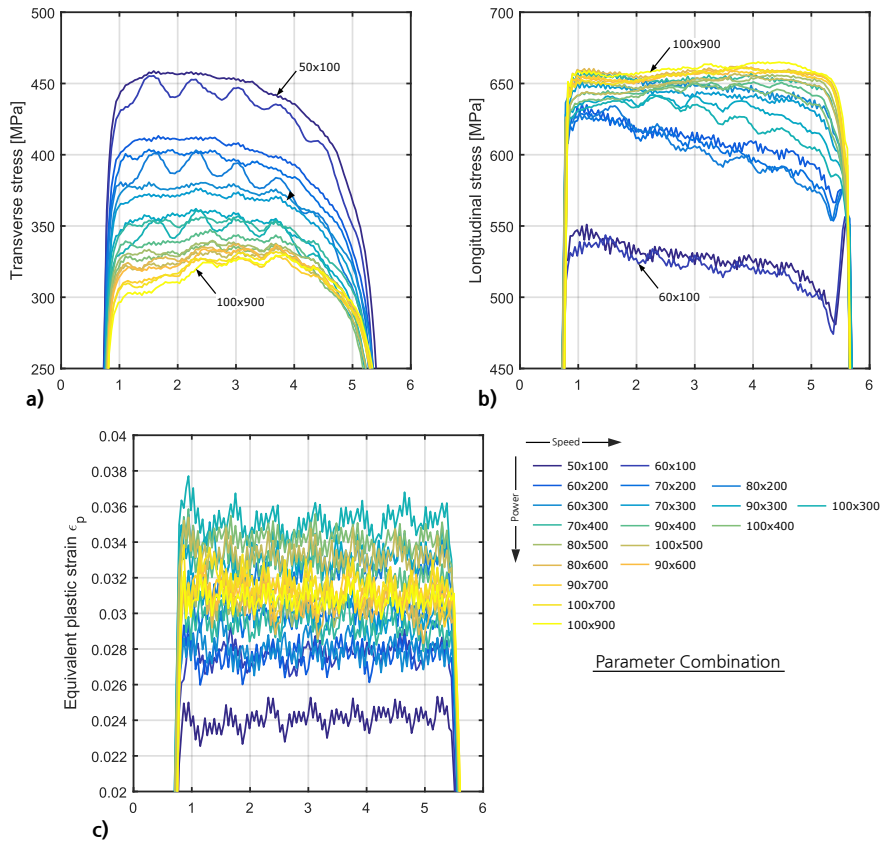


Figure 8.6: Profiles taken through the centre of the (5 x 5) mm square showing a) the transverse stresses, b) the longitudinal stresses and c) the total equivalent plastic strain

dependent on the laser scan speed chosen. The longitudinal stresses increased with the laser scan speed plateauing towards an effective limit of ~ 660 MPa – also observed in Figure 8.6(b). Conversely, by increasing the scan speed, this reduced the transverse stresses, as shown in Figure 8.7(a).

From this parametric study, it appears that varying laser power has negligible effect on the overall magnitude of residual stresses generated. However, increasing the laser power used, increased the level of yielding in the scanned layer, as shown in Figure 8.7(c). This may correspond with the normalised enthalpy (Figure 8.1), for each laser parameter combination, but there are not enough samples to conclude this. The increase in levels of plastic deformation does not necessarily correlate directly with the magnitude of the transverse and longitudinal stresses generated. This yielding behaviour explains the limit on the maximum residual stresses observed in the scanned layer.

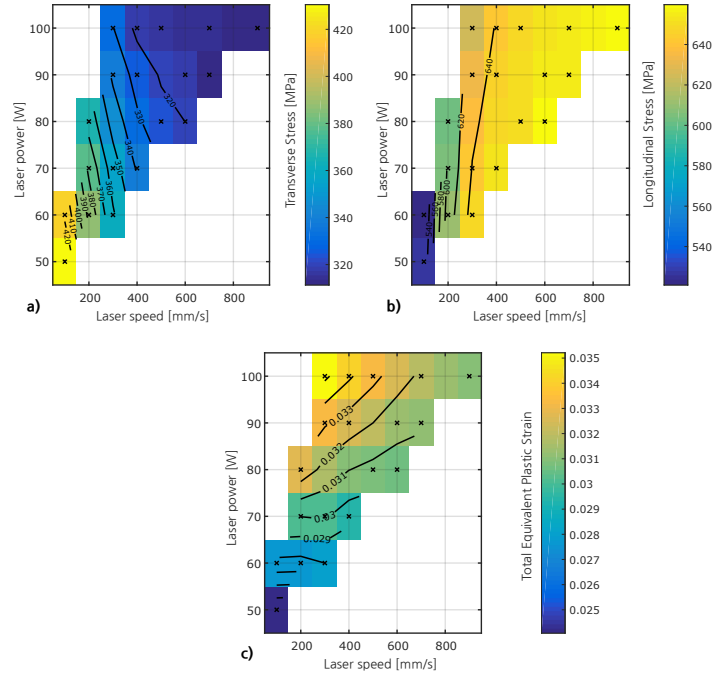


Figure 8.7: Process maps of the laser power and speed showing their effect on a) the transverse stresses, b) the longitudinal stresses and c) the total equivalent plastic strain $\bar{\epsilon}_p$, generated in the (5 x 5) mm island regions

The final part of this parametric investigation looked at varying the hatch distance with a laser parameter combination of $P = 80$ W, $v = 500$ mm/s, which is similar to that used with the Realizer SLM 50. The hatch distance h_d was chosen to vary from 0.07 to 0.15 mm in equal intervals. The plots of the longitudinal and transverse stresses, along with the total equivalent plastic strain are shown in Figure 8.8. It was found that hatch distances of 0.13 mm and 0.15 mm were too large, and were therefore excluded in the results. It can be seen in both Figure 8.8(a) and Figure 8.8(b) that there is negligible difference between longitudinal and transverse stresses generated at different hatch distances. However, there is a significant difference in the total equivalent plastic strain generated, as shown in Figure 8.8(c). A decrease in the hatch distance increased the level of equivalent plastic strain observed, indicating a greater level of yielding occurred.

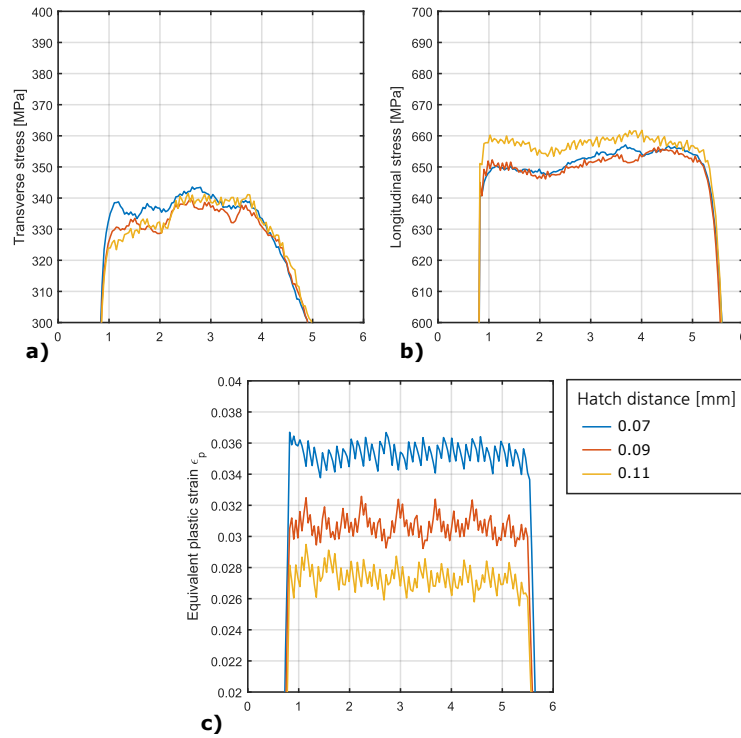


Figure 8.8: Graphs of a) the longitudinal stresses, b) the transverse stresses, and c) the total equivalent plastic strain across the centre section of the (5 x 5) mm square, when varying the hatch distance

8.4 Discussion

A parametric study was performed to discover the effect of laser parameters on the generation of residual stresses. The first study was a thermal analysis along two scan vectors for a variety of power combinations to observe the melt pool behaviour. The geometry of the melt pool corresponding with observations long observed in welding literature [190] and the following was found

- An increase in scan speed increased the melt pool aspect ratio
- An increase in laser power increased the melt pool width.

There was a consistent decrease in the melt pool dimensions across all parameters when scanning between the first and second scan vectors. This was expected due to the additional material available in the previously scanned track for heat to dissipate away from the melt pool whilst scanning the second scan vector. This result highlights whether previous simulations of single tracks are valid, since the thermal behaviour will largely depend on the inclusion of

the surrounding melt-track.

The parametric study consisting of a full transient thermo-mechanical analysis of a 5 mm square island (typical dimensions used in checkerboard island strategy), revealed more on the effect of laser parameters on residual stress, which has been unavailable in literature. The compiled process maps shown in Figure 8.7(a) and 8.7(b) revealed that the laser speed was the most dominate parameter that influenced the magnitude of both longitudinal and transverse residual stresses. Increasing the laser scan speed increased the longitudinal stress generated towards a limit of ~ 660 MPa, whilst decreasing the transverse stresses generated. Similar behaviour was noted from experiments performed by Vrancken, who concluded that increasing the laser speed increased the level of anisotropy of the residual stresses generated [87]. Additionally it was shown in both Figure 8.7(a), and Figure 8.7(b) that varying the laser power had a small effect on the generation of both transverse and longitudinal residual stresses, which was also concluded in work by Vrancken [87]. However, increasing the laser power had a considerable effect of increasing the level of yielding occurring in the scanned layer, as shown in Figure 8.7(c).

It is acknowledged that a potential limitation with the thermo-mechanical model is that a single layer analysis cannot account for the gradual accumulation of heat across multiple layers which is inherent with samples manufactured during an experiment. Ideally, the influence of laser power on long build durations needs further investigation, but a compromise could be made by performing a sensitivity analysis on the residual stress obtained at different substrate temperatures. It is difficult to compare results by Wu et al. who used high scan speeds and laser powers ($P = 400$ W, $v = 1800$ mm/s), on a small 'L' shaped geometry [21]. They concluded that a decrease in residual stress could be obtained by increasing the energy per unit length (E_L). However, at such high speeds and powers, temperature accumulation in previous scan vectors could have more of a profound effect owing to the reduced time available for heat to dissipate away. It is recommended that the parameter space should be expanded to look at any potential effects that could arise at extremely high scan speeds (>1000 mm/s).

Varying the hatch distance across one parameter combination ($P = 80$ W, $v = 500$ mm/s), as shown in Figure 8.8, revealed that the hatch distance has negligible effect on the longitudinal and transverse stress, but influenced the level of plastic strain generated. Decreasing the hatch distance increased the level of yielding that occurred in the scanned layer. Although the distortion is not measured, the increase in plastic deformation coincides with experimental observations from Pohl et al. who showed increasing hatch distance reduced the overall distortion at the edges [86]. The equivalent plastic strain provides an additional indication of in-built distortion during the manufactured process.

The increase in yielding when decreasing the hatch distance is anticipated to be caused by the increased frequency of scanning across the equivalent area. This has the effect of accumulating temperature, reducing the yield stress σ_y , and therefore increasing the plastic deformation.

Ideally, these relationships should be validated experimentally both for a single layer and for cubic samples produced. This parametric study only considers laser parameter combinations that are likely to produce fully dense parts, and this itself creates a narrow process window that may reduce the observed influence of these parameters on the generation of residual stress. Despite some parameter combinations being infeasible, these should be explored too.

The overall study considers the exploration of the parameter space across a fixed geometry size. (scan vector length of 5 mm). It is expected that change in geometry, in particular reducing the scan vector length, will potentially change the temperature history and the residual stresses generated. Further investigation of the geometrical interplay with process parameters, may provide an opportunity for optimising the laser scan strategy and parameters more specifically for different geometry types.

8.5 Conclusions and summary

The parametric study to investigate the effect of laser parameters revealed conclusions consistent with the published literature. The effect of the laser parameters on the dimensions were found to be as follows:

- an increase in laser scan speed increased the melt pool aspect ratio
- an increase in laser power increased the melt pool width.

Another parametric study was performed using the thermo-mechanical model to analyse the effect of laser parameters on the generation of residual stress found in a 5 mm square across a single layer. The following conclusions were reached:

- Increasing the laser scan speed had the most significant influence on the magnitude and anisotropy of the residual stresses generated.
- Increasing the laser scan speed increased the magnitude of longitudinal stress whilst decreasing the transverse stresses generated.
- Increasing the laser power had a small effect on the residual stress, but did increase the level of yielding that occurred.
- Varying the hatch distance had little effect on the maximum magnitude of residual stresses generated, but decreasing the hatch distance significantly increased the level of yielding that occurred

The conclusions drawn from this investigation are in good agreement with experimental observations available in literature. These trends observed for the generation of residual stress varying with laser parameters corresponds with those experimental measurements made by Vrancken [87]. Altogether this gives greater confidence in the thermo-mechanical model for predicting the residual stresses generated in selective laser melting.

Further work is needed to observe if these conclusions remain the same on different sized geometries across both single and multiple-layers. This would help identify if the accumulation of heat over time is the cause for the change in the residual stress. Potentially, this would also provide a route for optimising the laser scan strategy specific to geometry.

Chapter 9

Investigation of geometrical effects on scan strategy

9.1 Introduction

The principle advantage for using AM is the ability to realise intricate and complex part geometries at little cost penalty. The investigation of the elementary scan strategies was undertaken on square island geometries, which always featured a constant scan vector length parallel to its edge. This is an overly simplified test case and such scan vectors are only encountered when scanning regions with a large cross-sectional area. In order to develop the understanding how to optimise the generation of scan vector geometry for a real part, and to help to develop a multi-scale methodology, an investigation into the effect of geometry on the generation of residual stresses was performed.

There has been no reported literature to date that has investigated the effect

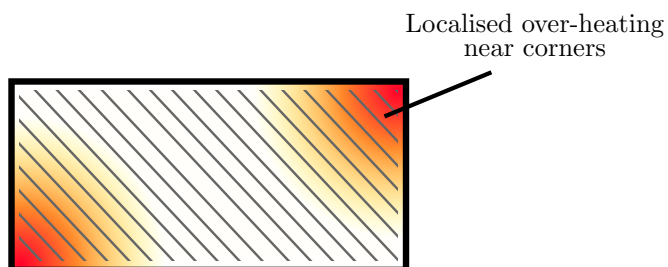


Figure 9.1: Illustration showing the localised build-up of heat created when scanning towards the corners of geometries

of the geometrical scan vector geometry on residual stress. It is suspected that under some situations, the choice of scan vector geometry can have a localised heating effect within hatch regions, such as corners of geometry as illustrated in Figure 9.1. This potentially can result in excess heat build-up within regions, which could affect the instabilities of the process. Additionally, it is suspected that the thermal history with varying scan geometry profiles would affect the generation of residual stress.

The directionality and length of scan vectors was expected to dominate the generation of residual stress. It is known in the literature that the magnitude of the longitudinal residual stresses generated parallel to the scan vectors was found to be highly dependent on the scan vector length [77, 86, 90]. The transient thermal effects during the processing affected the distribution and magnitude of the transverse stress component generated perpendicular to the scan vector.

9.2 Methodology

In order to understand the role of geometry dependency in relation to the scan strategy, a series of geometrical primitives (triangles and squares) of different aspect ratios was considered. The use of triangles creates scan vectors with lengths that vary linearly across the geometry, at a rate dependent on the aspect ratio chosen. In theory, this can characterise the influence of the thermal history of a scanned region on the build-up of residual stresses caused by the previously accumulated heat.

Both the triangles and squares had a maximum length $l = 5$ mm, and their size varied, using ten different aspect ratios by changing the height h , as illustrated in Figure 9.2. The triangles were hatched in two directions, to fully explore the effect of scan strategy on different aspect ratio geometry. The collections of hatched primitives are shown in Figure 9.3 using larger hatch distance for illustration.

It was hypothesised that by reducing the overall mean and variance of the scan vector length, it could effectively reduce the overall magnitude of residual stresses within a region. Additionally, by reducing the variance, this reduces the opportunity for creating localised zones with excess build-up of heat. In order to determine the validity of the hypothesis, a simple geometrical test was performed by varying the hatch angle, θ_h , when hatching different aspect ratio triangles. This obtained the distribution of scan vector lengths, with varying angles, as shown in Figure 9.4.

Performing the geometrical test for the triangles, it was observed that irrespective of aspect ratio, the local minima for the mean and variance was found when the hatch angle was perpendicular to the triangle's hypotenuse. Based on

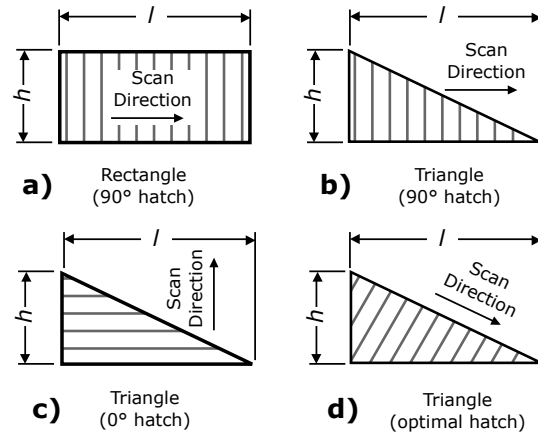


Figure 9.2: Illustration showing the geometrical test cases with varying length h : a) rectangle hatched at 90° , and triangles hatched at b) 90° , c) 0° , and d) perpendicular to hypotenuse

this knowledge, another set of test cases were developed with the hatch-angle perpendicular to the hypotenuse, as shown in Figure 9.4(d).

For this investigation, over 40 primitive geometries were considered to investigate the geometrical effect of scan strategy, and this required the use of the HPC facilities to automate this process. A Matlab script was generated to automate this process of generating the scan strategies, and additionally a job submission script was used to automatically submit a batch of jobs on the HPC. In the simulation, the same laser and hatch parameters were used as listed in Table 7.1 and Table 7.2.

In order to examine the transverse and longitudinal residual stress distributions generated across the geometries, the σ_{xx} and σ_{yy} stress fields were extracted from the results when the scanned region cooled to a uniform temperature of 200°C . The stress fields were exported to Matlab using a *Python* script within the active layer and the layer below the scanned region ($-L_T < z < L_T$). This was done to automate the stress profile distribution, and provide additional stress fields in the multi-scale analysis described in Chapter 11.

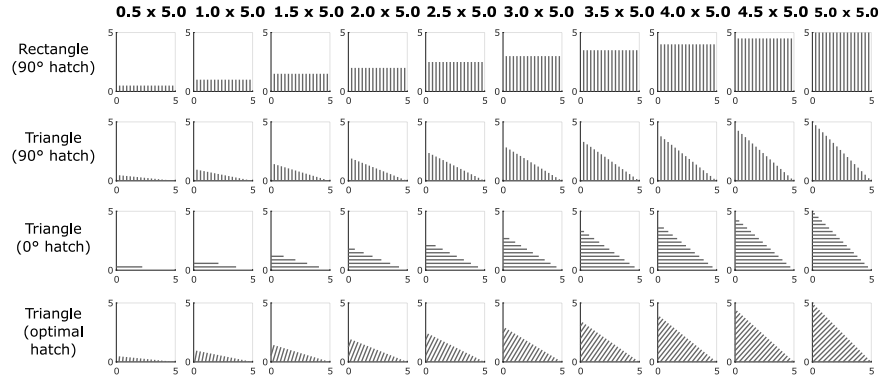


Figure 9.3: The hatched geometrical primitives generated for the geometrical study, scanned from left to right. For illustration, the hatch spacing has been increased.

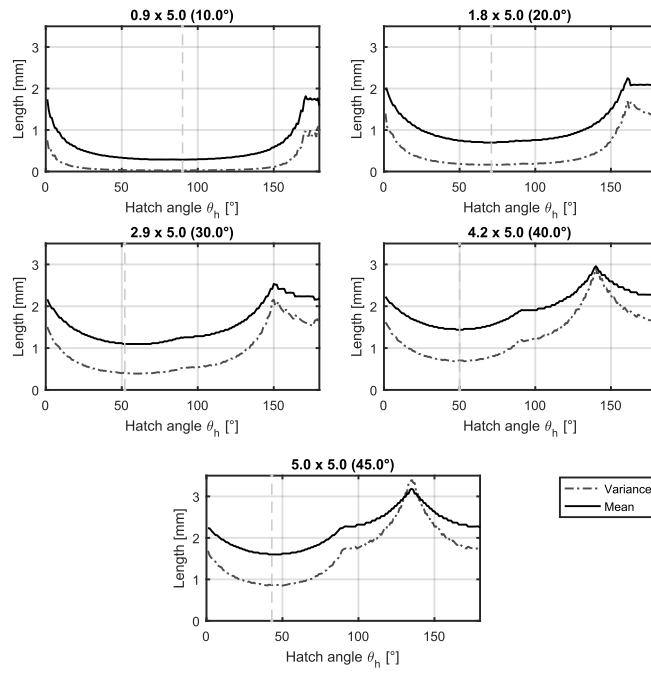


Figure 9.4: Graphs of the mean and variance of the scan vector lengths plotted against the hatch angle θ_h for different aspect ratio triangles

9.3 Results

The stress distribution plots for all the analyses are shown in Figure 9.5. It is clear from the triangle geometries shown in Figure 9.5(a-c), that the orientation of the scan vector used for hatching geometrical primitives has a significant effect on the magnitude and distribution of residual stresses. The aspect ratio of the scanned shape does determine the overall magnitude of the residual stresses generated, since this primarily determines the scan vector length.

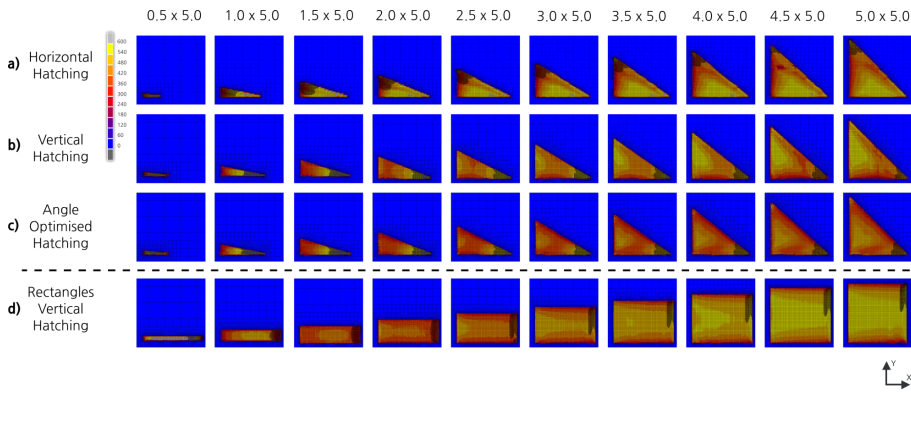


Figure 9.5: Profile views showing the von Mises stress distribution of scanned triangle primitives with a) horizontal hatching, b) vertical hatching, c) angle optimised scanning, and d) rectangles hatched vertically

As seen in the surface plots of the von Mises stress in Figure 9.5, it appears that orientating the hatch angle to follow the hypotenuse of the triangle tends to reduce the magnitude of the residual stresses generated throughout the scanned geometry. The probability density function of the von Mises stresses for each triangle test case with each hatch orientation is shown in Figure 9.6. The PDFs show that the peak of optimised hatch angle remains narrow and stationary at 450 MPa irrespective of the aspect ratio, except for the high aspect ratio cases (1.5 x 5.0, 2.0 x 5.0) mm. The narrow distribution observed for the optimised hatch angle, corresponds to low variance in the scan vector length.

The residual stress distribution using the horizontal and vertical hatching are more heavily influenced by the aspect ratio of the geometry. In the low aspect ratio, triangular geometries (Figure 9.6(f)-(h)), the distribution of the stresses for both the vertical and horizontal hatching become bi-modal. Of the two peaks, the higher magnitude peak is associated with regions of long scan vector lengths whilst the smaller magnitude peak is associated with the shorter scan vectors towards the end of scanning the geometry. Generally, horizontal hatching results in higher magnitude of residual stress for the given area, especially for high

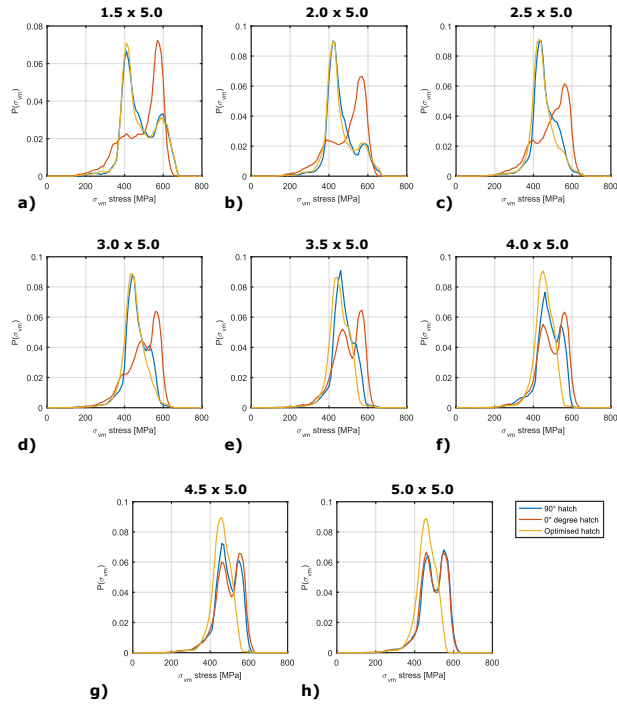


Figure 9.6: Comparison of the von Mises PDFs $p(\sigma_{vm})$ for the different aspect ratio triangles using the 0° , 90° and optimised hatching

aspect triangles, as shown in Figure 9.6(a)-(c). This is expected to be caused by these scanned geometry cases always having a full scan vector length (5 mm) along the bottom edge. When using the vertical hatching, the maximum length of the scan vectors are based on the shortest length of the triangle. In the higher aspect ratios, higher magnitudes of residual stresses are generated towards the corner of the triangle (regions with shorter scan vectors). It would be expected that these regions would also suffer from the effect of localised over-heating. This can be observed when comparing the temperature distribution towards the shortest scan vectors at the acute angle of the triangle for the (2.0 x 5.0) mm triangles between horizontal and vertical hatching in Figure 9.7(a) and Figure 9.7(b).

The aerial distribution of the stresses within the triangles scanned using the horizontal and vertical hatching tend to be similar in shape, as demonstrated in all the cases in Figure 9.6(a) and in Figure 9.6(b). The peaks of the longitudinal and transverse stresses tended to be located through a line X-X extending through the triangle's centroid, as shown in Figure 9.8(a).

The transverse and longitudinal residual stresses generated in the geometries of different aspect ratios are plotted against the distance along line X-X normalised

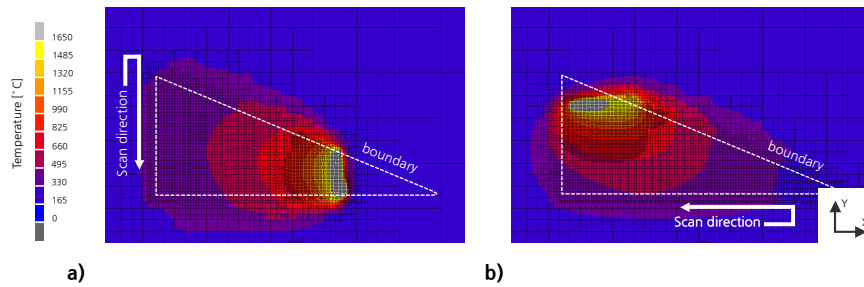


Figure 9.7: Profile of the surface showing the temperature distribution towards the end of scanning for a (2 x 5) mm triangle using a) vertical hatching and b) horizontal hatching

with the effective scan vector length in Figure 9.9 for the vertical hatching, and Figure 9.10 for the horizontal hatching. It can be seen in both Figure 9.9(b) and Figure 9.10(b) that the longitudinal stresses increased linearly with the scan vector length, and begin to plateau when the scan vector length becomes greater than 3 mm.

The transverse residual stresses generated perpendicular to the scan vectors vary considerably, irrespective of the aspect ratio and hatch angle, as shown in Figure 9.9(a) and Figure 9.10(b). Reducing the effective scan vector length increases the magnitude of the transverse stresses which plateau towards a limit depending on the aspect ratio of the triangle chosen. This shows the strong influence of previous thermal history on the generation of the transverse stresses within a structure which is specific to the geometry scanned.

The transverse and longitudinal residual stresses generated in the rectangular geometries were sampled across the centre, and their distributions are shown in Figure 9.11. The transverse stresses (Figure 9.11(a)) generally have a slightly asymmetric, flat profile along the width of the rectangular geometry, which decreases rapidly at the far edges. This rapid decrease in the transverse stress can be attributed to the fact that transverse stresses aren't generated towards the end of scanning the region. The general curvature of the transverse stress distribution along the central profile was associated with the resultant deformation of the layer at this temperature (200 °C). Using the shortest scan vectors, ranged between 1.5 mm and 2.5 mm, significantly increased the magnitude of the transverse stresses generated. For the longer scan vectors, the magnitude of transverse stresses varied by ~ 30 MPa. This shows similarities with the observations of the residual stresses generated in high aspect ratio triangles.

The longitudinal stresses shown in Figure 9.11(b) decayed exponentially from the highest point at the start of scanning before tending towards a constant

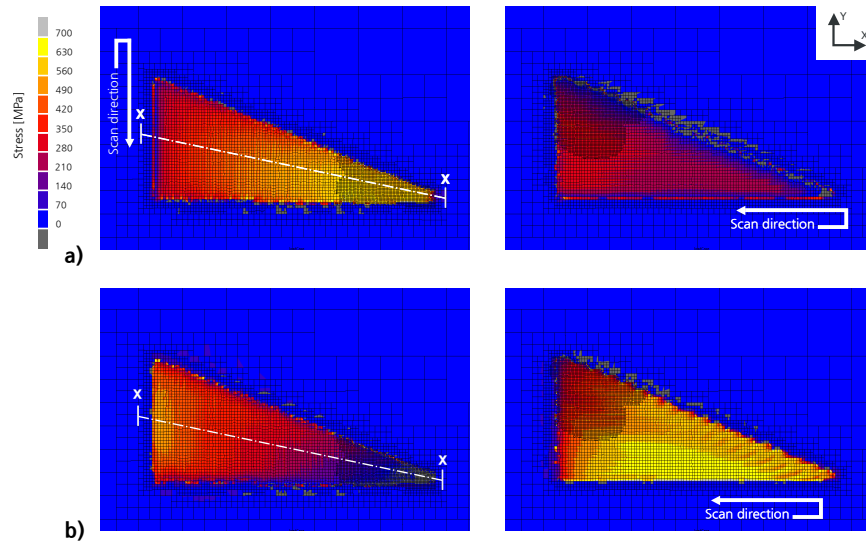


Figure 9.8: Profile of the surface showing a) the transverse and b) longitudinal stresses using vertical hatching (left), and horizontal hatching (right) for the (2 x 5) mm triangle geometry

stress value dependent on the scan vector length. This largest decrease at the beginning of scanning was observed using the shortest scan vector lengths between 1.5 and 2.5 mm. This expected to correspond to an overheating effect due to the lack of material available at the beginning of a scan for the dissipation of heat.

In order to examine the thermal history on the effect of the build-up of the transverse residual stresses, the mean temperature of consolidated elements ($\phi = 1$) in the scanned layer was plotted against the scan time in Figure 9.13. The temperature profile plot showed that irrespective of geometry, increasing the area scanned or the effective scan length tended to reduce the mean temperature across the entire duration of scanning. In the rectangular cases with scan vector lengths less than 2.5 mm, these experienced the highest sustained average temperatures.

Shorter scan vectors such as those in the rectangular case in Figure 9.13(c) may initially have the highest average temperatures but experienced a higher rate of temperature loss across the normalised scanning duration. For the rectangles which have constant scan vector lengths, the average temperature decreased linearly with time.

The deltas between the longitudinal and transverse stresses for all aspect ratio triangles hatched vertically are shown in Figure 9.12. For all aspect ratio

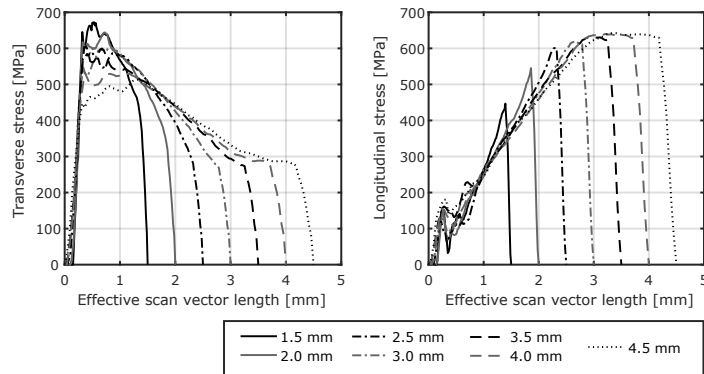


Figure 9.9: Graph showing a) the transverse and b) the longitudinal stresses plotted against the effective scan vector length when scanning different aspect ratio triangles with vertical hatching

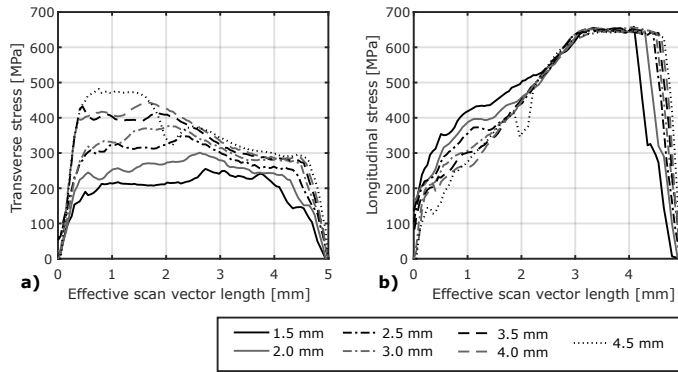


Figure 9.10: Graph showing a) the transverse and b) the longitudinal stresses plotted against the effective scan vector length when scanning different aspect ratio triangles with horizontal hatching

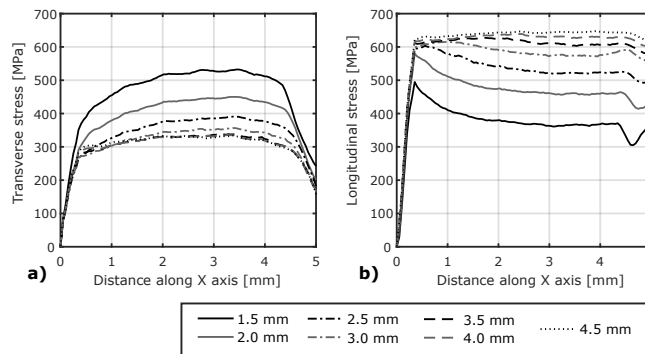


Figure 9.11: Graph showing a) the transverse and b) the longitudinal stresses with distance across the central X-axis when scanning different aspect ratio rectangles with vertical hatching

triangles, an absolute minimum between the stress components was observed at a critical scan vector length between 1.7 and 2.3 mm. Below this critical scan vector length, the greater contributions from the transverse stress dominate, and above this length the longitudinal stresses steadily increase the difference between stress components.

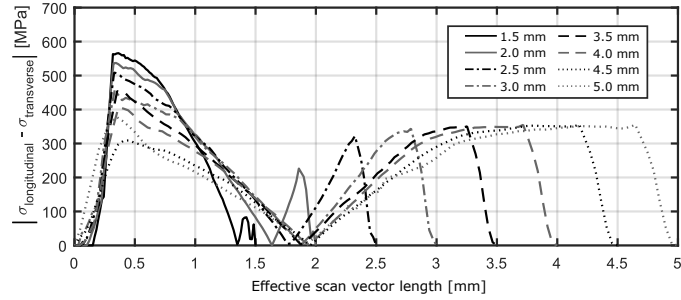


Figure 9.12: Graph of the absolute difference between the transverse and longitudinal stress components against the effective scan vector length, when scanning different aspect ratio triangles

When comparing the mean temperature of the rectangles (Figure 9.13(c)) with the transverse residual stress generated (Figure 9.11(a)) for the shortest scan vector lengths [1.5-2.5] mm, the transverse stress continued to increase until the mean temperature was approximately 750 °C. The transverse residual stress for greater scan vector lengths settles towards ~300 MPa, and it can be observed that the mean temperature for these sizes remain below ~750 °C.

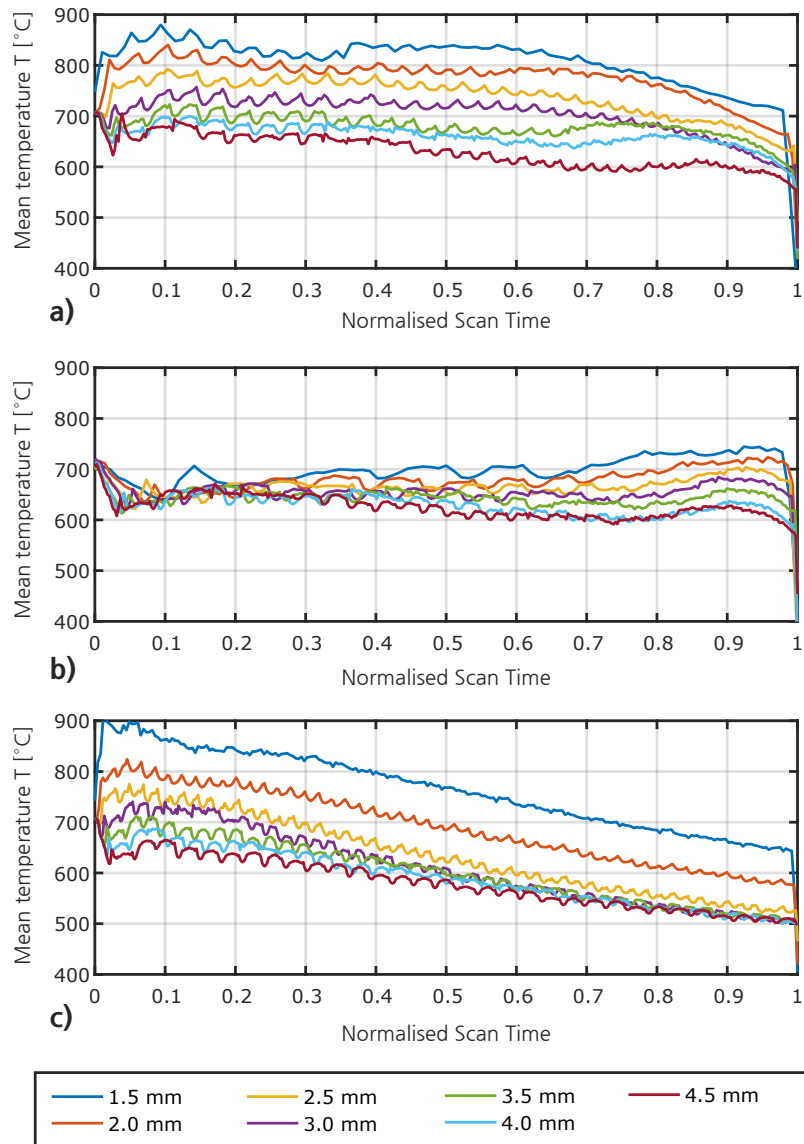


Figure 9.13: Graph of the mean temperature of consolidated elements normalised to the scan time for a) triangles hatched vertically b) triangles hatched horizontally, and c) rectangles hatched vertically

9.4 Discussion

Numerous simulations of geometric shapes were analysed by scanning different aspect-ratio triangle and rectangular primitives in order to determine the effect of geometry on the generation of residual stress, as shown in Figure 9.5. Previously discussed in Section 7.3, it was confirmed that scan vector length plays a significant role in the magnitude of stresses generated. A hypothesis formed was that reducing the mean effective length of the scan vectors, could reduce the residual stresses generated. This was achieved by rotating the hatch angle to be perpendicular to the triangle's hypotenuse. As a result of this optimisation, the overall magnitude of stress remained constant at approximately 430 MPa irrespective of the aspect ratio of triangle scanned.

For assessing any geometrical relationships with the residual stress generated, the profiles of the stress distributions taken through the triangle's centroid were analysed with respect to the effective scan vector length for different aspect ratio geometries. The transverse residual stresses generated perpendicular to the scan vectors varied considerably especially at short scan vector lengths irrespective of the aspect ratio, as shown in Figure 9.9(a) and Figure 9.10(a). There is a strong indication that the thermal history significantly affects the distribution transverse stress generated which doesn't correspond necessarily with the scan vector length.

It was seen in Figure 9.13, that the mean temperatures remained high (> 750 °C) for short scan vectors [1.5-2.5] mm when scanning the rectangular geometries and this resulted in higher transverse residual stresses. This over-heating effect is not experienced in lower aspect ratio geometries, because there is greater surface area for heat dissipation into the previously scanned region, which prevents excess heat-build. It is expected that changing the order of scanning by starting in the acute section of the triangle is expected to change the distribution of the transverse stress. This effect has not been reported in the literature and in practice short scan vectors are not often used for manufacturing parts using SLM.

Irrespective of geometry, the longitudinal stresses, as shown in both Figure 9.9(b), Figure 9.10(b) increased linearly with scan vector length and then plateaued at 650 MPa at a scan vector length of approximately 3 mm. Shorter scan vectors between 1.5-2.5 mm are susceptible initially to overheating effects at the start of scanning. Crucially, this is an important result, as this provides a predictable behaviour for the longitudinal stresses generated in the process.

Overall, diligence is recommended to reduce the use of short adjacent scan vectors since these exasperate the effects of previous thermal history within the scanned region. It is expected that choosing scan vector lengths beyond 5

mm will have negligible impact on the magnitude of the longitudinal stresses generated. Therefore, using island sizes beyond 5 mm are unlikely to yield any reduction in the magnitude of residual stresses generated, except changing the overall directionality of the stress throughout the entire scanned layer.

The rectangular aspect ratios correspond to a ‘stripe’ scan strategy, as shown in Figure 2.4(c). The results shown in Figure 9.11 indicate that the magnitude for both transverse and longitudinal stresses will remain constant along the length of the stripe, except for at the edges due to discontinuity of scanning. For shorter scan vector lengths, the thermal history had more of an effect on the stresses generated towards the start of scanning. Overall, the magnitudes of the longitudinal and to a lesser extent the transverse residual stresses in the stripes are determined by the scan vector length. Generally, both components of residual stress remain constant along the length of the stripe when scanning on a substrate.

The delta between the longitudinal and transverse stresses for all aspect ratio triangles, as shown in Figure 9.12 indicates that there is a critical scan vector length between 1.7-2.3 mm, which has the lowest level of anisotropy. The importance of this is that the level of anisotropy for the residuals stresses generated within the layer plane could potentially be controlled by varying the directionality and the length of the scan vectors chosen within a region. However, it is expected that observations for the generation of residual stresses using scan vectors that are adjacent to each other will behave differently to more complex scan strategies.

Ultimately, this study shows that the prediction of longitudinal stresses generated along the scan vectors is consistent and is determinable, whilst the generation of transverse stresses is more complex. In order to provide a predictive model for the generation of residual stresses within a layer, further analysis is needed to understand the effect of thermal history created by geometry and the scan order on the generation of transverse stresses. This investigation would need to find a relationship between the accumulation of heat in a scanned area over time, and the rate of change in scan vector length. Having a predictive model for the *meso*-scale generation of residual stress generation would enhance the proposed multi-scale method in this work.

9.5 Conclusions and summary

The study on the geometrical effect on the build-up of residual stress provided a chance to explore the relation between the static and dynamic changes in scan vector length on the generation of residual stress generation. Specific conclusions that can be drawn from the results are:

- Longitudinal stresses linearly increased with scan vector length before plateauing after a critical scan vector length of 3 mm, irrespective of geometry chosen
- Longitudinal stresses were largely independent of thermal history except at the start of scanning
- Transverse stresses were highly geometrically dependent owing to the different thermal histories.
- Transverse stresses were found to be significantly higher for short scan vectors (< 2.5 mm)
- Both the longitudinal and transverse stresses stabilise towards a constant value using a fixed scan vector length in the rectangular geometries - i.e. 'stripe' scan strategy
- Regions that are susceptible to localised overheating increase the magnitude of residual stresses generated

Laser scan strategy becomes less important for scan vector length beyond the typical 5 mm island sizes, in terms of the magnitude of residual stress generated. At the *macro*-scale, the distribution and orientation of scan vectors in relation to geometry becomes a more important consideration.

Chapter 10

Investigation of effect of support structures and overhang regions

10.1 Introduction

The thermo-mechanical behaviour will be affected by the composition of material underneath the scanned region, since this will affect the dissipation of heat. Generally, different scenarios exist and can be classified as

- Bulk solid regions
- Geometrical thin-wall structures e.g. lattices structures
- Unsupported over-hang regions (powder)
- Regions connected to support structures.

The choice of structure underneath a scanned region has been observed to influence the development of residual stress during SLM. A study by Hussein et al. reported that the type and unit-cell size of a lattice support structure affected the overall deflection of cantilever specimens, which provided an indicator for the level of residual stress [187]. From their results, it was observed that an increase in the unit cell size, and decrease in volume fraction tended to increase the total deflection of the cantilever. Their reasoning was that the development of residual stresses within the component can be controlled by preferential dissipation of heat into the support structures. Increasing the lattice density, it should effectively provide greater contact area for heat dissipation to occur, and

in turn reduce the level of residual stresses present. The mechanism for why this effect occurs is yet to be reported. It is also not known if this is a localised transient effect whilst the laser scans above the support geometry, or is instead the long-term dissipation of heat throughout the entire build-process.

A simulation study of the thermal conductivity of support structures was previously reported by Zeng et al. [178]. The steady-state thermal behaviour was determined by applying a fixed temperature difference to a support structure with symmetric boundary conditions. The support structure was a grid with a constant cross-section surrounded by powder. The effective thermal conductivity k_{eff} was calculated by measuring the average heat flux \bar{q} across the top surfaces using the 1D heat transfer equation,

$$\bar{q} = k_{eff} \frac{dT}{dz}. \quad (10.1)$$

It was reported that the effective conductivity was a linear combination of the temperature dependent thermal conductivity of the powder k_{powder} , and solid phase k_{solid} ,

$$k_{eff} = \phi k_{solid} + (1 - \phi) k_{powder}. \quad (10.2)$$

The non-linear effects of temperature dependent thermal conductivities were considered by broadening the temperature range between the upper and lower surface, but this resulted in a similar conclusion. However, their study only considered constant cross-section supports, and complex support geometries, such as lattices were not considered. Since the aim of their study was to create a representative volumetric element (RVE) for a subsequent analysis, the localised transient effects of the laser scanning above the support structure were ignored. Additionally, the effect on the generation of residual stress was not studied.

10.2 Methodology

To better understand the behaviour of supporting material underneath a scan region, a variety of test cases were performed in order to form a comparison when scanning over a solid substrate. Each test case, uses the laser and hatch parameters in Table 7.1 and Table 7.2, with a (5 x 5) mm square region and the alternating laser scan strategy. Test cases were undertaken for a single scan layer supported by a

1. powder region ($\phi = 0$)
2. pseudo-powder region ($\phi = 0.5$)

3. thin-wall support structure
4. double gyroid lattice structure

The thin-wall support structure, as shown in Figure 10.1(a), spans a volume of $(5 \times 5 \times 3)$ mm and was generated using Magics [167]. The shell structure was voxelised with a wall thickness of 0.08 mm, as described in Section 6.3.4. The double gyroid support structure, as shown in Figure 10.1(b), consists of three unit cells with a solid-void fractional density of 0.4 and spans the same volume of $(5 \times 5 \times 3)$ mm.

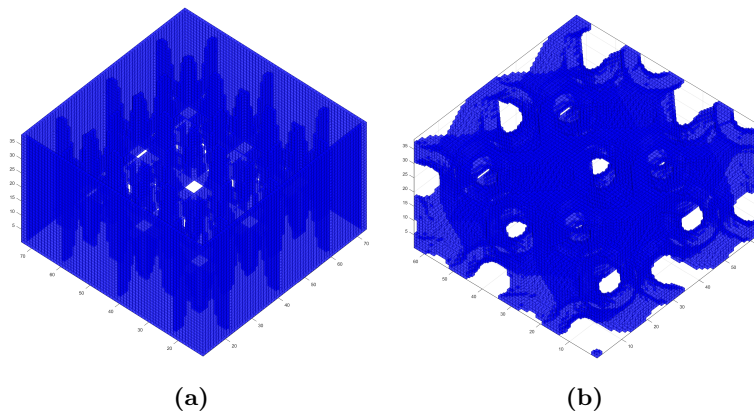


Figure 10.1: a) The voxelised thin-wall support structure generated using Magics, and b) the voxelised double gyroid lattice structure, both spanning a volume of $(5 \times 5 \times 3)$ mm

A comparison between the transient and steady-state heat transfer of the structures was conducted to determine the short and long term behaviour caused by the choice of underlying geometry. A steady-state thermal analysis with

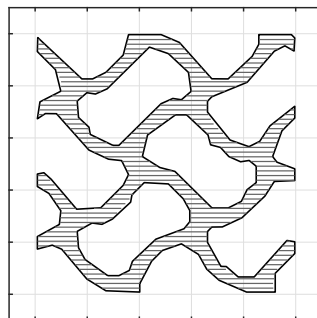


Figure 10.2: Scan pattern generated at the top of the lattice structure: hatch scan (grey), contour scan (black)

thin-walled support structure (Figure 10.1(a)) and the double gyroid structure (10.1 (b)) was performed to determine the effective thermal conductivity of these structures. The solid geometry was surrounded in a powder medium with the same temperature dependent thermal properties used in the transient analyses. For the analysis, a fixed mesh grid was used consisting of 8 noded hexahedral elements with element lengths of 0.08 mm. A fixed temperature differential was applied across the bottom and top surfaces in order to induce a heat flux through the structure. The remaining surfaces were adiabatic. The effective thermal conductivity k_{eff} was obtained using equation 10.2 by measuring the average heat flux across a cross-section of elements.

A final study was performed to observe the behaviour whilst scanning the cross-section of a double gyroid lattice. This test case should help to identify the thermo-mechanical behaviour when attempting to manufacture a more complex structure. The upper surface of the double gyroid structure was sliced and hatched, as described in Section 5.1, to produce the laser scan geometry shown in Figure 10.2. The scan consists of both a contour and hatch scan, which were performed over the voxelised double gyroid structure. All the structures were assumed to lack residual stresses, since the distribution is not known. The purpose of these test cases is to understand the effect of underlying geometry on the thermal dissipation and generation of residual stresses in the active layer.

10.3 Results

The effect of the support material underneath a scanned layer was investigated to understand the thermal dissipation characteristics and its effect on the generation of residual stress. The results are presented for each test-case followed by a steady-state thermal analysis of the two support structures.

10.3.1 Powder

The first test case was scanning a single (5 x 5) mm layer above a powder substrate to represent an overhang region.

Scanning upon a powder bed effectively insulated the scanned region and resulted in higher sustained temperature throughout the previously scanned regions, as shown in Figure 10.3(a). This is caused by the low thermal conductivity of powder medium, with preferential dissipation into the previously consolidated region, as shown in Figure 10.3(b). Typically, the solid substrate acts a thermal sink effectively allowing heat to dissipate away. Consequently, this had an immediate effect of changing the local behaviour of melt pool. The melt pool becomes elongated, and has a greater depth of penetration into the powder

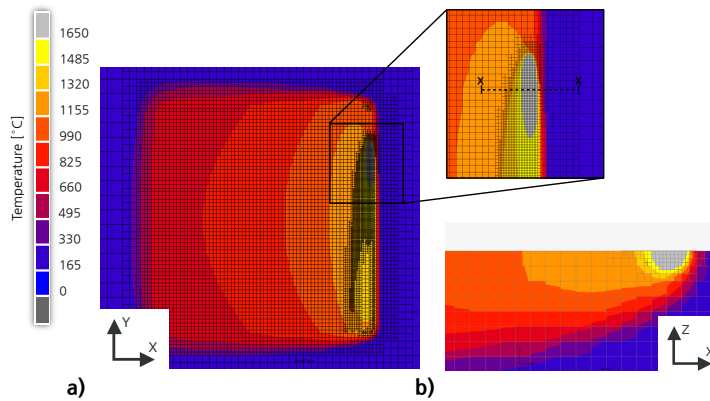


Figure 10.3: Surface profile view of the temperature distribution whilst scanning the (5 x 5) mm island directly upon the powder bed. b) A cross section taken through XX showing the temperature distribution of the powder bed

medium compared to when scanning the substrate. The lack of thermal dissipation in this case influenced the overall distribution of stresses, as shown in Figure 10.4. The transverse stresses shown in Figure 10.4(a) were significantly higher than when scanning on the solid substrate.

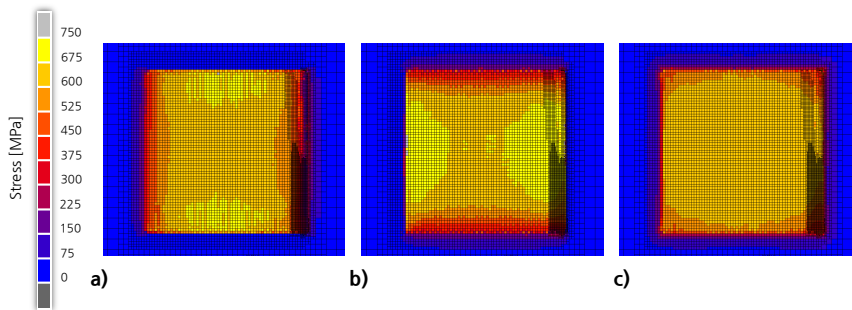


Figure 10.4: Profile views of the surface showing a) σ_{xx} , b) σ_{yy} , and c) the von Mises stress distribution of a (5 x 5) mm region scanned upon the powder bed. The stress values were taken when a uniform temperature of 200 °C was reached

The displacement profiles of the scanned region are shown in Figure 10.5, and were taken vertically and horizontally through the centre of the square region at a temperature of 200 °C. There is negligible mechanical restraint having powder as support material, therefore the layer is free to deform during processing. The total displacement towards the edges was, therefore, large relative to the layer thickness, at approximately 12-14 μm , and occurred equally in both X and Y directions, due to the similar magnitude of the longitudinal and transverse stresses.

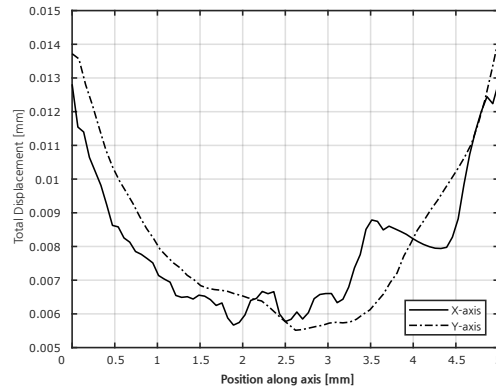


Figure 10.5: Graph of the total displacement along the central horizontal and vertical axes of the (5 x 5) mm island region when scanned directly upon the powder bed

10.3.2 Pseudo-powder

A fictitious pseudo-powder phase ($\phi = 0.5$) was used to determine the intermediate effect between scanning upon a powder bed and a substrate. It can be seen in Figure 10.6(b) that the thermal dissipation occurs more evenly into the material below the scanned layer, and the largest thermal gradients are situated close to the melt pool. The greater opportunity to dissipate heat increases the rate of cooling in the previously scanned areas, as shown in Figure 10.6(a).

The increased melt pool depth, and higher transverse stresses observed when scanning on a powder base are not evident when using this pseudo-powder phase, as shown in Figure 10.7. The increase in thermal dissipation also resulted in an increase in the anisotropy between the transverse and longitudinal stress components.

10.3.3 Thin-wall support structure

The thin-wall structure was calculated to have an average solid-powder volume fraction of 11.5%. The temperature profile along the surface is shown in Figure 10.8. The distribution is similar to when scanning on the powder bed, as shown previously in Figure 10.3(a).

The residual stresses in the layer produced above the support structure are shown in Figure 10.9. The general distribution and magnitude of the residuals stresses are similar to when scanning on powder, as shown in Figure 10.4. Small isolated regions that are supported by the thin-walled ribs, reduce the magnitude of the transverse stress generated along the scan vector, as illustrated in Figure 10.9(a). These regions have discontinuous geometry along the scan vector. The temperature distribution along sections X-X is shown in Figure 10.10(b), and

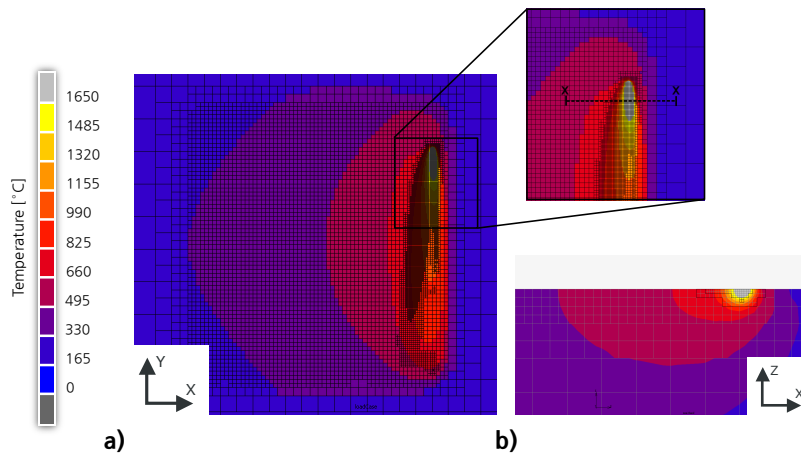


Figure 10.6: a) Surface profile view of the temperature distribution whilst scanning the (5 x 5) mm island directly upon a pseudo-powder phase ($\phi = 0.5$). b) Cross section taken through X-X showing the temperature distribution within the pseudo-powder bed

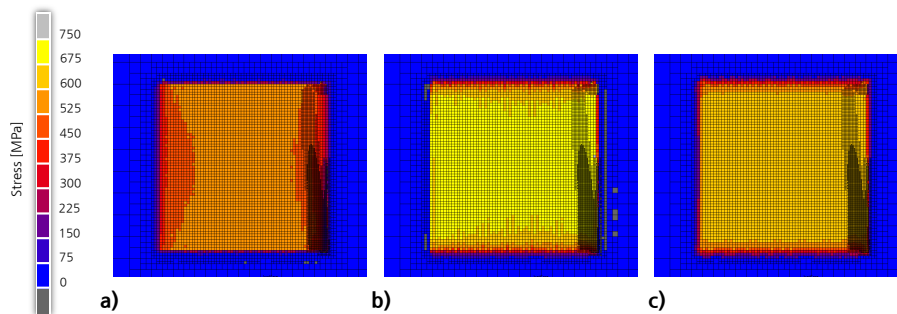


Figure 10.7: Profile views of the surface showing a) σ_{xx} , b) σ_{yy} , and the von Mises stress distribution of a (5 x 5) mm region scanned on the pseudo-powder bed. The stress values were taken when a uniform temperature on the scanned region reached 200 °C

Y-Y in Figure 10.11(b). The support structure provides an additional route for thermal dissipation, which preferentially cools more rapidly the intermediate region along the elongated melt pool. This has a result of creating discontinuity in the melt pool. The end of the melt-track sustains a longer molten period because it is supported by powder which provides greater resistance to thermal dissipation. The scan track along Y-Y showed similar behaviour to scanning on the powder bed, and consequently yielded a similar stress distribution for the transverse stress.

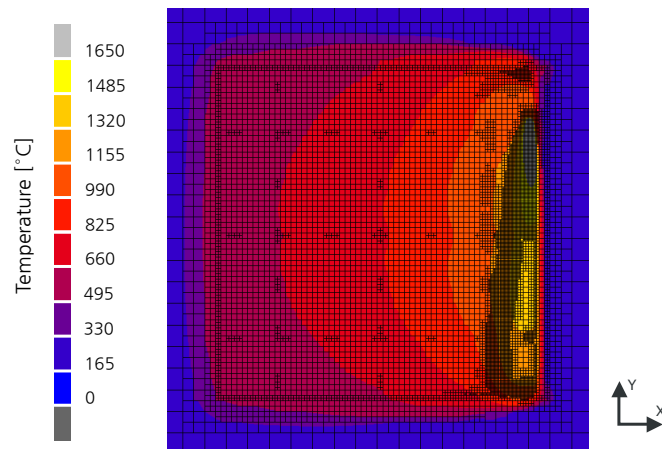


Figure 10.8: Surface profile view of the temperature distribution towards the end of scanning ($t = 0.499$ s) of the (5 x 5) mm single island above a thin-walled support structure

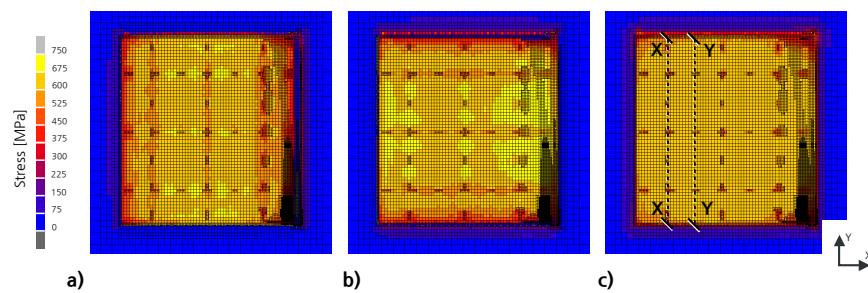


Figure 10.9: Profile views of the surface showing a) σ_{xx} , b) σ_{yy} and c) the von Mises stress distribution of a (5 x 5) mm region scanned upon a thin-wall support structure. The stress values were taken when a uniform temperature on the scanned region reached 200 °C.

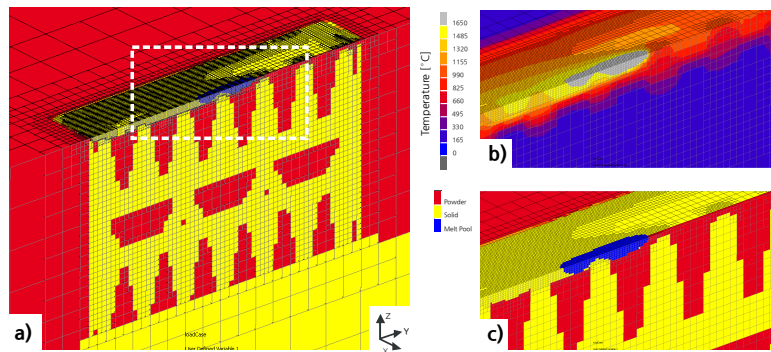


Figure 10.10: Cross-section through XX of the thin-wall support structure showing a) the extent of the support structure with close-ups of b) the temperature distribution and c) the state variable ϕ , whilst the laser scans along this section

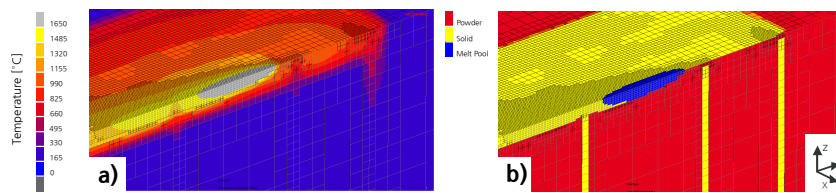


Figure 10.11: Cross-section through YY of the thin-wall support structure a) the temperature distribution and b) the state variable ϕ , whilst the laser scans along this section

10.3.4 Double gyroid support structure

The distributions of the residual stresses of the (5 x 5) mm region are shown in Figure 10.12 when scanning above a double gyroid structure. The transverse (Figure 10.12(a)) and longitudinal (Figure 10.12(b)) stress components were equal in magnitude and are approximately 600 MPa throughout the entire scanned region. The presence of lower magnitude residual stresses for both components were in regions where the upper surface of the double gyroid structure was exposed to the scanned layer. In this case, regions scanned above powder shared similar behaviour to the simulation when scanning upon only powder.

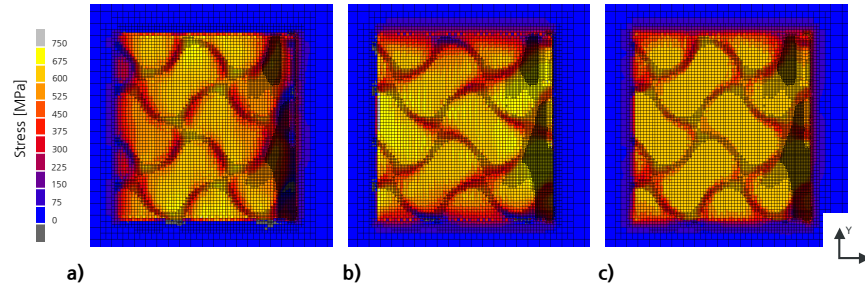


Figure 10.12: Profile views surface showing a) σ_{xx} , b) σ_{yy} and the von Mises stress distribution of a (5 x 5) mm region scanned on top a double gyroid structure. The stress values were taken when a uniform temperature on the scanned region reached 200 °C

10.3.5 Scanning the geometry of a double gyroid lattice

The overall time required to scan a single layer of double gyroid was 0.170 s for the hatched region, and an additional 0.206 s to scan the perimeter. During the scan of the hatched region, the position of the laser jumps between members within the lattice because a sort algorithm that minimises distance between adjacent scan vectors has not been implemented during the hatching process. The temperature distribution whilst scanning the hatched region midway (0.12 s) is shown in both Figure 10.13 and Figure 10.14. It is evident that there is preferential heat dissipation into previously consolidated regions and the lattice structure, with significant resistance in the interstitial sites containing powder. This suggests that the solid geometry of the double gyroid structure provides immediate routes for the dissipation of heat. The powder only influences the behaviour close to the melt pool and the HAZ, which experiences high temperatures. Due to the small volume of material melted in the active layer, previously scanned regions cool quickly through conduction into the gyroid structure.

The highest temperature gradients, as shown in Figure 10.15, were located near the scanned region and underneath the layer within the lattice structure. Within previously scanned regions, the temperature gradient is relatively small, compared to near the scanned region.

The high magnitudes of residual stresses in the scanned layer, as shown in Figure 10.16(a), are attributed to the hatching process creating short scan vector lengths leading to a concentration of heat in these areas. The overall response on the double gyroid structure due to the addition of residual stress is shown in Figure 10.16(b). The mechanical restraint of the lattice structure opposes the generated residual stresses within the top-layer, causing stresses to be generated at greater depths into the structure.

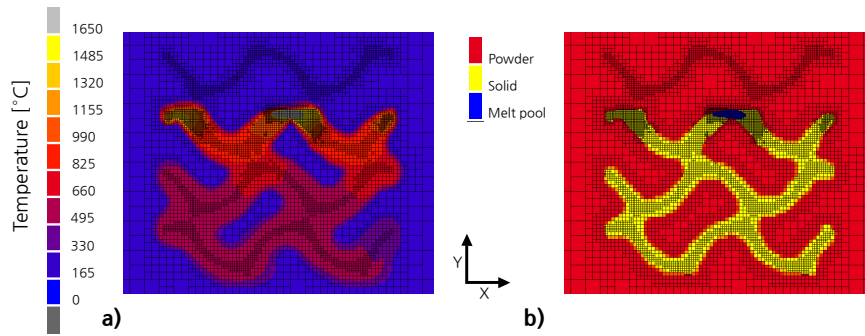


Figure 10.13: Surface profile view showing a) temperature and b) state variable ϕ , taken midway (0.12 s) when scanning the double gyroid structure

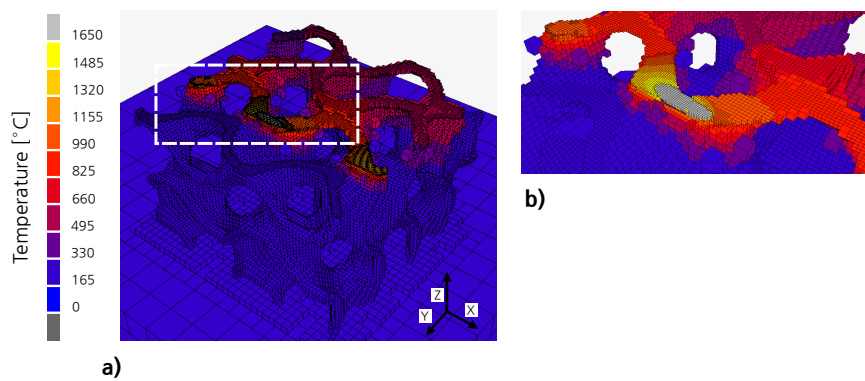


Figure 10.14: a) 3D view and b) close-up showing the temperature distribution taken midway (0.12 s) when scanning the double gyroid structure. Powder material is not shown.

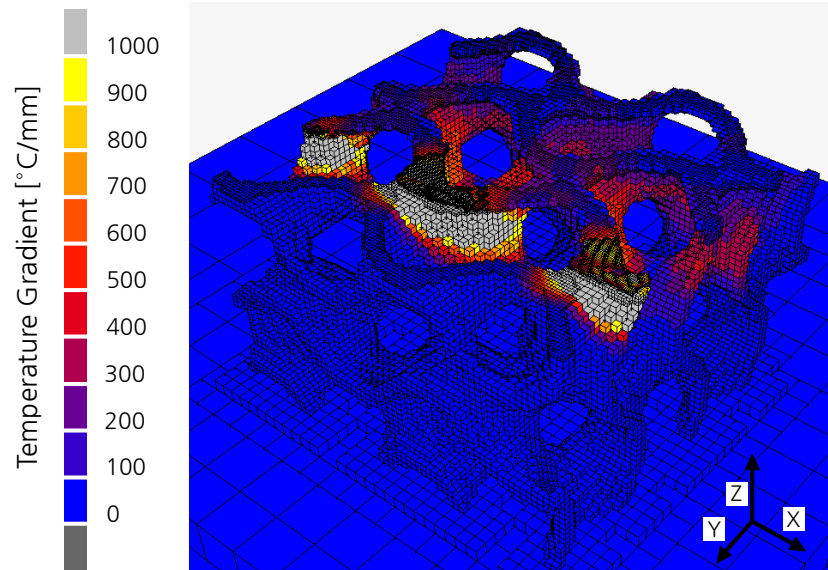


Figure 10.15: 3D view showing the temperature gradient taken midway (0.12 s) when scanning the geometry of a double gyroid structure. Powder material is not shown.

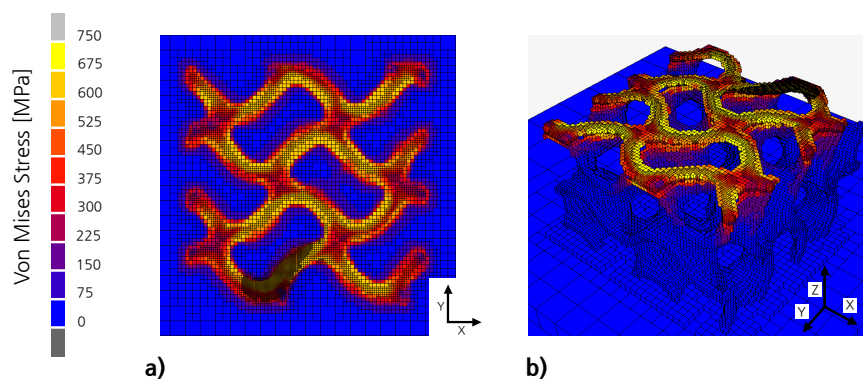


Figure 10.16: a) Surface profile view and b) 3D view showing the final von Mises stress for the scanned top layer of the double gyroid structure

10.3.6 Steady-state thermal analysis of support structure

The steady-state thermal analysis was performed on the thin-wall and double gyroid support structures. The heat fluxes within each support structure are shown in Figure 10.17. The calculated average heat flux in the Z direction and the effective thermal conductivity k_{eff} for the powder and the support structures are listed in Table 10.1. The low thermal conductivity of the powder provides a significant resistance to transferring heat, with preferential dissipation through the solid support structure. The heat flux in the thin-wall structure varied significantly throughout the cross-section, as shown in Figure 10.17(a), compared to the double gyroid structure shown in Figure 10.17(b). In the thin-wall support structure, the largest heat fluxes were in regions with the smallest cross-sections such as the teeth located at the top surface and the thin members vertically located along the centre. In the double gyroid structure, the heat flux was evenly distributed throughout the solid structure, with a small variation only occurring in curved regions of the structure.

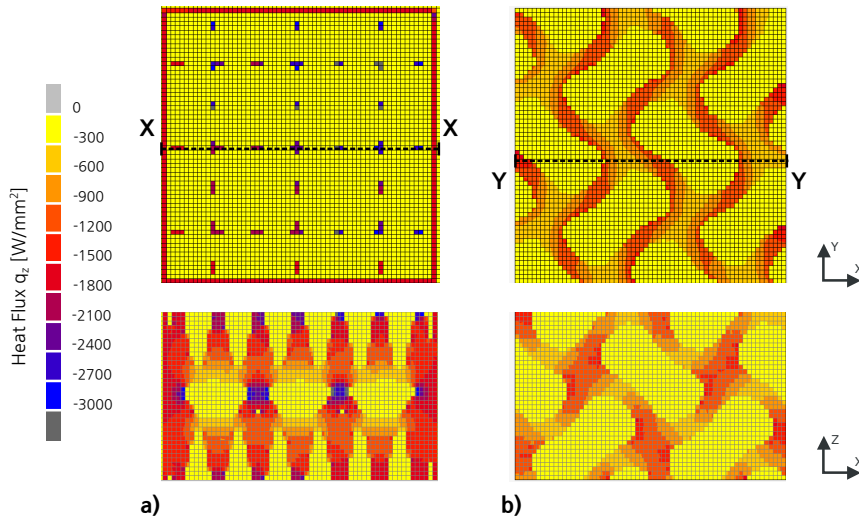


Figure 10.17: Profile views and cross-sections of the steady-state heat transfer showing the heat flux in Z-direction through a) the thin-wall and b) the double gyroid support structures

Taking into account the solid-void fraction of the thin-wall support (11.5%), the effective thermal conductivity shown in Table 10.1 corresponds to the empirical relationship proposed by Zeng et al. [178] in equation 10.2. However, the effective thermal conductivity of the double gyroid structure does not correspond with this relationship, and was approximately 12% off the expected prediction.

	Average heat flux in Z direction \bar{q}_z [W/mm ²]	Effective thermal conductivity k_{eff} [W/mK]
Powder ($\phi = 0.0$)	0.012	0.093
Pseudo-powder ($\phi = 0.5$)	0.779	5.9
Solid substrate ($\phi = 1.0$)	1.558	11.8
Thin-wall support	0.169	1.28 (10.8%)
Double gyroid support	0.442	3.36 (28.4%)

Table 10.1: Calculated average heat flux and effective thermal conductivity values through the support material. Percentages in brackets indicate the effective thermal conductivity relative to the solid material

10.4 Discussion

The effect of underlying support material and support structures was investigated to determine these boundary conditions on the generation of residual stress. When scanning directly upon a powder layer, the insulative properties of the powder provided a significant resistance for heat to dissipate away. This was evident in Figure 10.3, where a uniformly high temperature was sustained across the entire layer for the length of the scanning period. Whilst scanning above a powder region, the depth of the melt pool increased compared to when scanning upon a solid substrate.

Elongation and stability of the melt pool has been discussed by Gusarov [24] and Yadroitsev et al. [103], affecting the overall shape of a single melt-track. The previous parametric studies of single melt tracks by Gusarov and Yadroitsev [103] confirmed the capillary instability phenomena occurring within SLM, being dependent on the melt pool length L_m , the track diameter D_m , and the contact angle ϕ_t with the substrate. Melt track stability can be determined based on equation 2.30 (Section 2.3.4), which provides criterion for predicting the behaviour. The corresponding value of $\pi D_m/L_m$ from equation 2.30 was calculated using approximate sizes of the melt pool taken across the centre for each test case, using the assumed value for the contact angle $\phi_t = 1$. The melt pool dimensions and the calculated stability condition are presented in Table 10.2.

Although the thermo-mechanical model cannot fully account for melt-track stability because it neglects thermo-fluidic behaviour, it does provide an indication of the track stability based on the length. The calculation from equation 2.30 would suggest that scanning on a powder bed should have difficulty achieving stability due to the highly elongated melt pool. In practice, poor surface finishing is often observed in overhang regions.

When scanning above the powder layer, the layer is not constrained by a substrate or support material, and is therefore free to curl, as shown in the

	Powder ($\phi = 0$)	Pseudo-powder ($\phi = 0.5$)	Solid substrate ($\phi = 1$)
L_m [mm]	1.36	0.66	0.54
D_m [mm]	0.24	0.16	0.14
$\frac{\pi D_m}{L_m}$	0.55	0.76	0.81

Table 10.2: Dimensions of the melt pool and the stability condition when scanning above different medium

overall displacement plot in Figure 10.5. The level of distortion demonstrates the significant reason why parts in SLM require support structures connected to the base plate always. Unsupported regions scanned in over-hang regions are prone to greater distortion or curling which increases the susceptibility of colliding with the powder re-coating mechanism. In practical terms, support structures should attempt to mitigate excess heat, or reduce the total heat input into regions scanned above powder only.

The PDFs of stresses for the different mediums and support structures are shown in Figure 10.18. It can be seen in Figure 10.18(b), that the longitudinal stresses for each test case share similar asymmetric distribution, which peaked at approximately 700 MPa for both the pseudo –powder and powder test cases, and at 620 MPa when scanning on the solid substrate. This shows that the choice of underlying material has a marginal effect on the longitudinal stresses generated in the scanned layer above.

The transverse stresses, σ_{xx} , generated when using pseudo-powder phase, as shown in Figure 10.18, experiences a narrow distribution centred at approximately 500 MPa. This suggests that an increase in thermal conductivity reduces the magnitude of the transverse stresses generated. When scanning directly on the powder bed, the transverse stresses have a very broad distribution. This is also apparent when using either of the chosen support structures. This suggests that support structures have similar behaviour to scanning directly on powder bed. This could be explained by the non-uniform distribution of solid and powder material when using support structures. When using the support structures, the surface area exposed through the solid support is approximately 8.4%, and for the double gyroid is 43.6% distributed as shown in Figure 10.19.

The pre-sintering technique is a laser scan strategy employed to improve the processability of materials, as discussed in Section 2.6.2. The model assumed that the thermal and mechanical material properties could be interpolated when the state variable $\phi < 1$, but the model didn't account for any pre-sintering behaviour. More direct experimental work is needed to understand the effect of pre-sintering, and its effect on the thermal conductivity and laser absorption

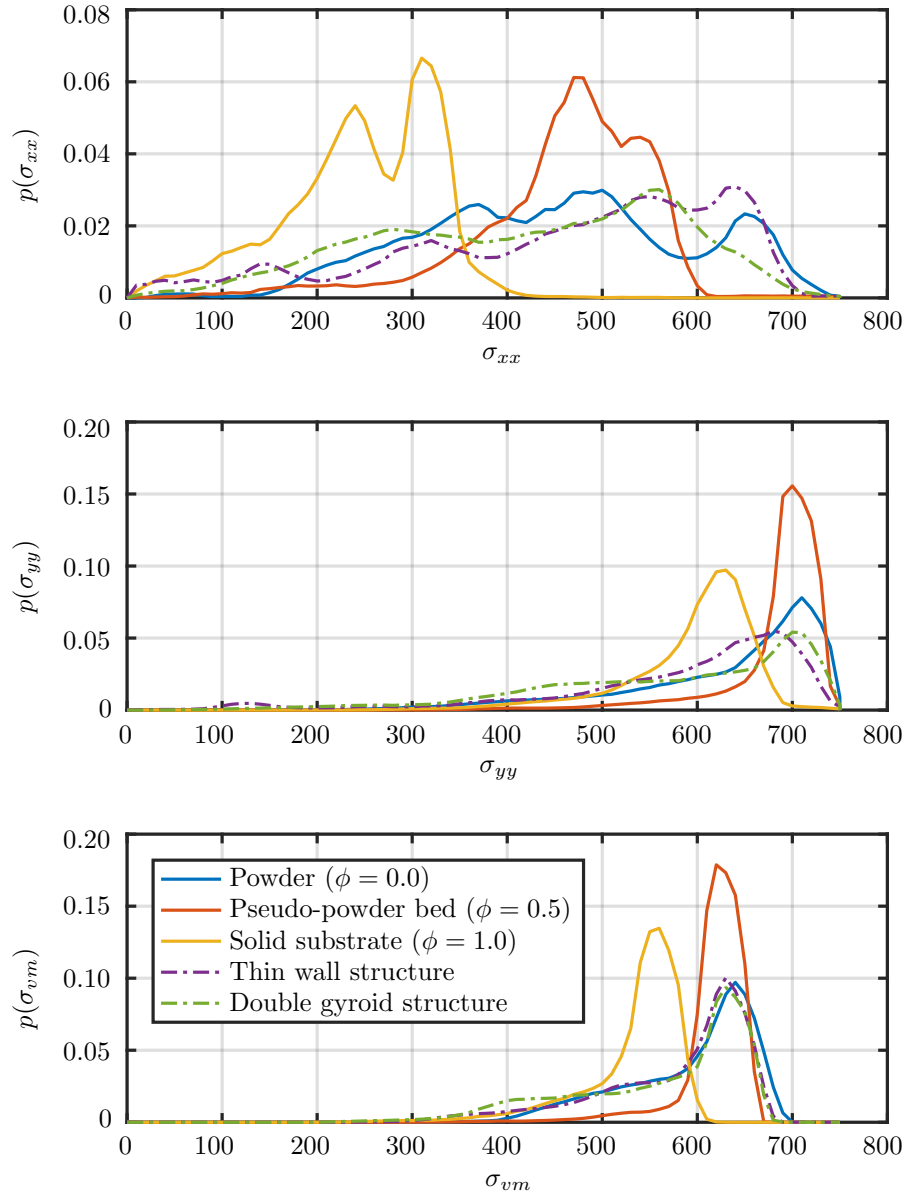


Figure 10.18: Graph of the PDFs for a) σ_{xx} , b) σ_{yy} and c) von Mises stress observed when scanning a (5 x 5) mm region above different support mediums and support structures. The stress were taken when the scanned area reached a uniform temperature of 200 °C

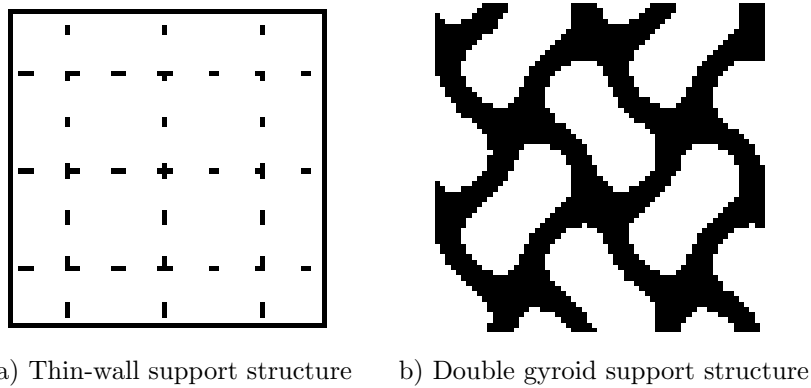


Figure 10.19: Material exposed underneath the scanned layer for a) thin-wall and b) double gyroid support structures

characteristics for metal powders. This relationship could be used as an input to the thermo-mechanical model and to investigate more variable phases in mediums effectively.

When scanning directly on the powder, the transverse stress was found to have an additional small peak at approximately 650 MPa, as shown in Figure 10.18(a). This coincides with the high stresses at the end of each scan vector, as shown in Figure 10.4. This suggests that the combination of low thermal dissipation in powder, has a pronounced effect in areas susceptible to overheating, i.e. regions of short scan vectors, or areas where heat becomes concentrated such as at the end of scan vectors. The double gyroid has a relatively similar effective thermal conductivity as the pseudo-powder, however, as shown in 10.18(a) the stress distribution for the pseudo-powder was much narrower than the double gyroid. This suggests that using an artificial pseudo-phase to represent the equivalent support structure underneath can only be considered if there is an even distribution of support material underneath the scanned layer.

These studies of the effect of support structures highlight the need to increase the thermal dissipation away from the layer in a controlled manner to prevent undesirable overheating. The thin-wall support structures do not provide sufficient thermal dissipation. Attempting to increase the distribution of smaller support structures, or increasing strut thickness is not practical. Rather it is recommended that the laser-power (or effective energy density) should be reduced in scanned regions that are only supported by powder.

Scanning the double gyroid structure, as shown in Figure 10.13 and Figure 10.14, revealed the localised thermal effect of scanning the narrow walls. The powder provides a strong resistance to heat dissipation, therefore heat is preferentially

dissipated through the structure. However, due to the low volume of material scanned, heat cannot accumulate, and previously scanned regions cool relatively quickly. Despite the use of short scan vectors, the un-optimised short scan vectors in combination with geometry result in the generation of high magnitude of residual stresses. Overall this suggests there is some localised overheating whilst scanning the thin walled features of the double gyroid lattice. Therefore, it is recommended that the laser parameters require optimising for these geometries, or the laser scan strategy be changed to avoid repeated and localised exposure in order to reduce the effects of overheating.

The proposed relationship in equation 10.2 by Zeng et al. [178] was acknowledged to be only suitable when assuming small temperature differentials between upper and lower surfaces, limiting the effect of non-linearity of the thermal conductivity properties used in the material. The maximum temperature difference that was used in their study was 100 °C, compared to 400 °C in this study. The thermal conductivity values of solid Ti-6Al-4V listed in Table 4.3, show a difference of 5.2 W/mK across the chosen temperature difference and this will contribute to the difference in the prediction of the effective thermal conductivity chosen. Due to linear interpolation of material properties within the simulation, the effective thermal conductivity of the pseudo-powder is approximately half of the solid.

The regions with the highest heat flux across the surface of the double gyroid (Figure 10.17(b)) correspond to the regions of lower magnitudes of transverse residual stresses, as shown in Figure 10.12(a). This follows a similar trend with the distribution of heat flux along the thin-wall support structure shown in Figure 10.17(a) and the observed stress in Figure 10.12(a), with regions of the scanned layer above the supporting geometry exhibiting lower transverse stresses.

This study is limited to the immediate transient effects across only a single layer rather than across multiple-layers. It is not known if extending the analysis across multiple-layers will show similar behaviour. Additionally, further work is needed to understand the long term accumulation of heat during a build. This could be achieved using far simpler layer based approaches such as those proposed in Section 3.4.1, and using the predicted temperature as initial conditions in the thermo-mechanical model. This is where the steady-state effective thermal conductivity used as an RVE would be an effective approach.

10.5 Conclusions and summary

The analysis of the effect of support structures and material underneath revealed some interesting findings on the generation of stress. When scanning directly

upon the powder-bed, the insulating properties of the powder provided a significant thermal resistance for the dissipation of heat, and caused uniform overheating across the scanned region. As a result, this increased the length and depth of the melt pool and most likely would create process instability. The most significant finding was that high transverse stresses of equal magnitude to the longitudinal stresses were generated uniformly across the scanned layer. The analysis of the pseudo-powder showed relatively high transverse stresses were generated and indicates that the transverse stresses are sensitive to the underlying support material.

The analysis for both the thin-wall and double gyroid support structures showed localised behaviour, with preferential heat dissipation along the upper surface of the geometry connected with the scanned layer. This had the effect of reducing the transverse and longitudinal residual stresses generated in these regions. This study indicates that although there is a localised effect of support structures on the melt pool, the control of residual stresses is largely determined by the ability to dissipate heat.

The steady-state analysis was proven to be a useful tool to predict the effective thermal conductivity, and therefore the heat dissipation of a structure without requiring a full transient analysis. However, despite similar effective thermal conductivity values shared between the pseudo-powder phase and the double gyroid support, there was a significant difference in the residual stresses generated. Therefore, the effective thermal conductivity method cannot faithfully provide a prediction of the residual stress in the immediate layer scanned.

Scanning the top layer of a double gyroid lattice structure showed that localised overheating occurs using short scan vectors repeatedly exposed, as only a small area of the gyroid structure is available to dissipate heat. This resulted in high values of residual stress being generated. It is therefore recommended that the laser parameters or the laser scan strategy be optimised for thin-walled structures in order to reduce the residual stresses generated.

Ultimately, support structures featuring low aerial connectivity with the scanned surface reduce the available area for heat to dissipate, and tend to share similar behaviour to when scanning directly on powder. It is therefore recommended that overhang regions have lower scan powers, or increase connectivity with some sacrificial support to improve the dissipation of heat.

Chapter 11

Multi-scale method for the prediction of residual stresses and distortion

Incorporating the stress field obtained in the *meso*-scale analysis into a larger domain is a potential methodology for reducing the computational resources required for simulating SLM at the scale required to gain insight into the effect of scan parameters larger parts. In selective laser melting, thermal history i.e. cooling-rates are highly localised towards *meso*-scale regions and are less dependent on the global state [148]. It has been suspected that when using the checkerboard island strategy, the islands have negligible influence on each other except when there is connectivity between islands [77, 186]. This factor is expected to contribute to the geometrical independence associated with this scanning strategy. Therefore, decomposing a large domain into discrete independent *meso*-scale regions as part of a multi-scale method is a feasible proposition. The multi-scale modelling methodology proposed provides an effective means for predicting the effect of scan strategy on residual stress in a larger SLM build envelope. This is achieved through tessellating island regions extracted from a detailed transient thermo-mechanical analysis performed at the *meso*-scale, such as the geometry in Chapter 9. A study examines the inter-dependency of the order of scanning islands and the formation of residual stresses in both a detailed transient analysis and with the proposed multi-scale approach in order to both verify the methodology proposed and to investigate the practical implications of using an island scanning strategy in selective laser melting.

The multi-scale method proposed has some similarity to previous work carried out by Li et al. [191]. However, in their method residual stresses were generated

along a single scan vector through the superposition of a thermal temperature profile surrounding the melt pool. An accurate representation of the thermo-mechanical behaviour cannot be obtained with this approach because the transient behaviour is ignored. The multi-scale method in this research uses the stress field captured across *meso*-scale region and therefore more accurately captures the stress generated in this process.

11.1 Details of the multi-scale methodology

In the proposed multi-scale methodology, two analysis scales are used to resolve the residual stress and distortion of a component. The *meso*-scale model accounts for the localised transient thermo-mechanical response within a hatched region consisting of a series of scan vectors that form ‘island’ regions, as shown in Figure 11.1(a). These are combined together and used in the *macro*-scale model to resolve the global mechanical response, as shown in Figure 11.1(b).

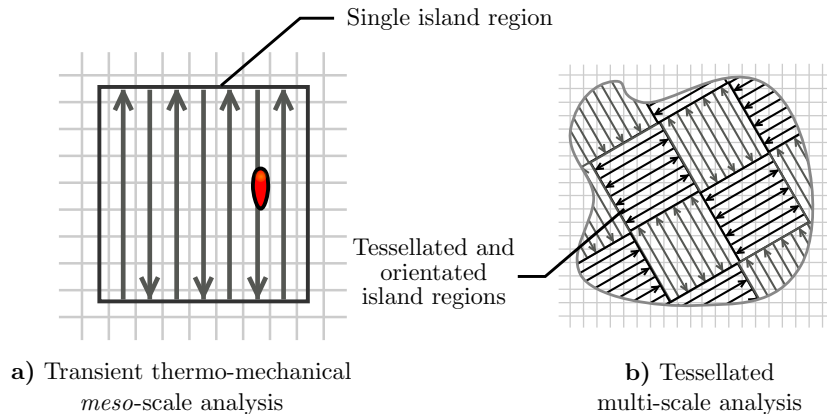


Figure 11.1: The *meso*-scale analysis consists of a transient thermo-mechanical analysis of a region scanned using a moving laser heat-source. b) The *macro*-scale analysis combines island regions obtained from the *meso*-scale to model the global mechanical response in a large region

The overall procedure for the multi-scale analysis is shown in Figure 11.2. The models at both analysis scales represented the material phases using a continuum, and were solved using the finite element method. For prediction of the distortion and the residual stresses in the multi-scale model, the Cauchy stress tensor σ was obtained from the transient thermo-mechanical analysis of the scanned geometries described in Chapter 9.

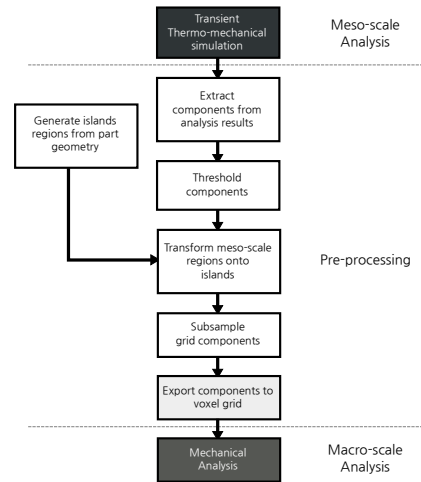


Figure 11.2: Diagram showing the breakdown of the steps in the methodology for performing the multi-scale analysis.

The stress fields were obtained from the transient thermo-mechanical simulation, which incorporates all the strain terms in equation 6.26 at temperature T . Compatibility between analysis scales requires the initial temperature in the *macro-scale* model to be the same as that in the *meso-scale* model when the stress tensor was obtained. This ensures the correct temperature dependent material properties are used at the *macro-scale*, and prevents any changes to the thermal strain.

The fields obtained from the *meso-scale* are pre-processed using standard image processing techniques to superimpose these regions onto a generated build model in a layer-wise fashion. The generated scan model represents each region of the checkerboard island scan strategy with full capability for manufacturing a component using SLM. A volumetric model of stresses and plastic strain components were generated and were directly mapped onto the *macro-scale* model, where a single pass mechanical analysis is performed.

An outline of the different features of the two analysis scales used in the multi-scale model described in this section are summarised in Table 11.1.

Accuracy of the multi-scale method requires comprehensively accounting for each sub-region within the macro-scale model. It becomes apparent that a combinatorial library of *meso-scale* simulations is required to represent the different scenarios present in a build. For example, the boundary conditions and the scan vectors used may change across the build. Different scan strategies, laser parameters could be used for each different geometric region, which will affect the thermo-mechanical response. The conditions affecting thermal dissipation

Thermo-mechanical analysis	Multi-scale analysis
<ul style="list-style-type: none"> • Transient thermo-mechanical analysis • A moving Gaussian laser heat source is applied across a series of scan vectors • Uses a multi-phase temperature dependent elasto-plastic material model tracked by a state variable • Local adaptive meshing used to improve performance and accuracy 	<ul style="list-style-type: none"> • Single-step mechanical analysis performed on a fixed mesh • Input generated from tessellating pre-generated stress-fields to match geometry • Effective single material, single temperature material model used

Table 11.1: Summary of the two models used at each scale in the multi-scale methodology

will also depend on the position of each region, because this may change the substrate (supported, overhang, solid), and the connectivity with other regions, along with scan order. To reduce these factors in the numerical investigation used to investigate and validate the proposed method in this paper, the boundary conditions were chosen to represent a bulk 'square' island region scanned upon a solid substrate.

The results required to be extracted from each element in the *meso*-scale model are the six unique components of the Cauchy stress tensor, σ . Two additional scalar fields are required from the *meso*-scale model: the element state variable, ϕ , and the total equivalent plastic strain, $\bar{\varepsilon}_p$. These components were taken after scanning a region at an average temperature of $T = 350$ °C, once a negligible change in temperature was observed during the manufacturing process, as shown in Figure 11.3.

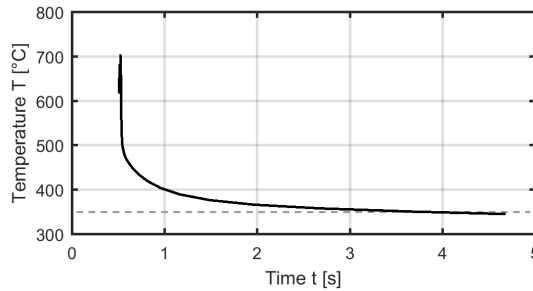


Figure 11.3: Graph showing average temperature of solid elements observed after scanning the single (5 x 5) mm island region in the *meso*-scale analysis

Quantities from the results were obtained using a *Python* script for all consolidated elements ($\phi > 0.9$) with a centroid position situated a layer thickness below the current layer to account for re-melting of the substrate. For each

component, the mean value was taken across all integration points per element and was then mapped from the centroid position onto individual grids for pre-processing.

11.1.1 Generation of input for macro-scale analysis

The element data obtained from the *meso*-scale model was further processed. The average value of each component was taken in the Z direction and redundant elements were removed. These island grids form units which were tessellated through a series of transformations onto the geometrical representation of checkerboards islands.

It is essential for a valid multi-scale representation that the sub-regions containing the scan vectors match directly with those generated for machine build files used during the manufacturing process. For the multi-scale analysis, the volumetric hatching method, as discussed in Section 5.1, generated island geometries, with each containing a geometrical description and attributes including position, size, and orientation. These attributes are used to define the transformation of the region types between analysis scales, and later could be extended to account for different scenarios encountered, such as islands located near overhangs, supports and edges, with supporting *meso*-scale analyses.

The quantities obtained from the *meso*-scale model must be transformed between reference frames from the local to the global coordinate system through affine transformations. The scalar quantities were rotated using Matlab's built-in function *imrotate*. The rotated stress tensor $\boldsymbol{\sigma}'$ requires each stress component to be transformed by a 2D rotation matrix R_Z about the Z axis using the following equation

$$\boldsymbol{\sigma}' = R_Z \boldsymbol{\sigma} R_Z^T. \quad (11.1)$$

This was applied to every element, for each unique rotation of the island throughout the model. The transformed stress tensor $\boldsymbol{\sigma}'$ for each island grid was then rotated using *imrotate*, as shown in Figure 11.4 to orientate the stress components for each island into the global coordinate system. Rotations are performed on the high-resolution grid to reduce aliasing effects that can be caused by a lower resolution. Depending on the size of the macro-scale analysis, the island grids could be scaled to match a different resolution, however, this should generally be avoided because the residual stress is highly dependent on the scan vector length.

For each component, the island grids were composed into a larger 2D grid to form a single layer. For intersecting elements between islands, the maximum value of the component is taken. A reduction in the resolution of the mesh is

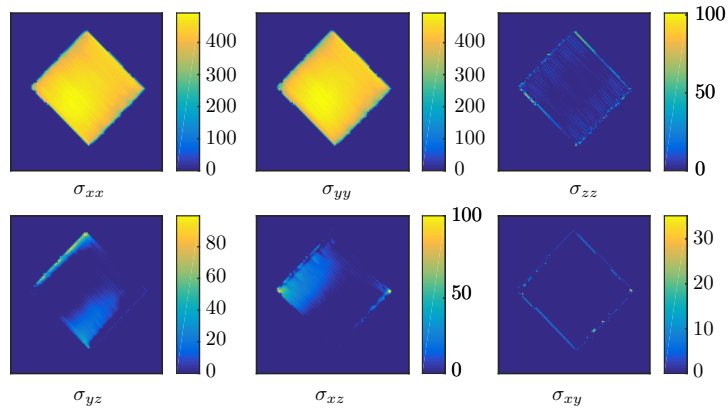


Figure 11.4: Rotation transformation of 45° applied to the stress tensor σ for a single (5 x 5) mm island region

required in the *macro*-scale analysis, and was achieved by subsampling using Matlab's *imresize* function. The grids were then exported into the openVDB grid format [182] to enable access to the simulation subroutines in the *macro*-scale analysis.

A significant benefit of using scalar grids along with a volumetric representation is that it enables the use of efficient image-processing techniques that intrinsically run parallel. The use of a structured grid makes mapping of quantities between analysis meshes and the part geometry by interpolation.

11.1.2 Macro-scale analysis procedure

Significant time savings are attainable in the proposed multi-scale method because the models used at each analysis scale are effectively decoupled. The non-linearity of the process is removed at the *macro*-scale because the final manufactured state of a *meso*-scale region is assumed to be time invariant i.e. the developed residual stresses and plastic strains will not vary significantly during and after the manufacturing process at the *meso*-scale. The transient temperature effects during the build process could be included to increase the accuracy between model scales, however, this would reduce the computational efficiency of this approach. Furthermore, the transient thermo-mechanical effects at this scale are ignored, reducing the *macro*-scale model to a linear static mechanical problem. An additional benefit is that complexity created by accounting for physical phenomena at the *meso*-scale is isolated and independent from the *macro*-scale. As a result, there is no performance penalty at this scale for including more detailed sub-models.

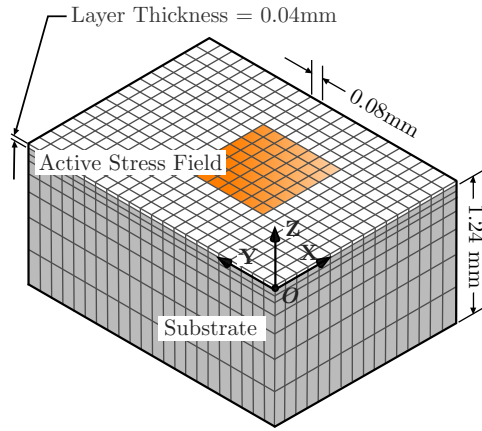


Figure 11.5: Illustration of the *macro*-scale model. A regular structured mesh is used, with the origin of the coordinate system positioned at the start powder-bed to enable one-one mapping

The *macro*-scale analysis requires at a minimum one mechanical pass, because each sub-region for each layer is activated instantaneously, reducing the number of iterations needed. The domain consists of eight noded hexahedral elements arranged in a regular structured mesh to enable one-to-one mapping directly from the voxel grid, as shown in Figure 11.5. This was achieved by calculating the element centroid within the model and assigning each component from individual voxel grids, with a scaling factor in the Z direction to account for the element aspect ratio. The mesh resolution in the XY plane was user defined to match the voxel grid input; however, the element height corresponds to the physical layer thickness.

The overall procedure for initialising the macro-scale analysis is shown in Figure 11.6. Elements are assigned the same material properties used in the *meso*-scale simulation with an initial uniform temperature $T_0 = 350\text{ }^\circ\text{C}$. The initial stress components and the equivalent plastic strain are assigned using the *UINSTR*, and *INITPL* Fortran subroutines. Elements are de-activated using the *UACTIVE* subroutine prior to the analysis for non-solid regions ($\phi \neq 1$), removing the need to generate a geometry dependent mesh.

During the mechanical analysis, the Newton-Raphson iterative method [173] was used to solve the set of non-linear equilibrium equations, as discussed in Section 6.1.1. The iterative procedure minimises the residual between external and interior forces within the structure until effectively the body is at an equilibrium state. The resolved displacement and stress field thus can be obtained.

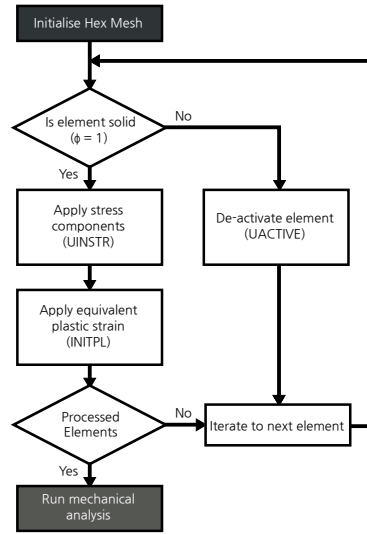


Figure 11.6: Diagram showing the steps for initialising the elements in the *macro-scale* model

11.1.3 Extension of the multi-scale method for complex geometries

The multi-scale method using the island regions described previously is limited by the geometry that it can represent because it can only account for bulk regions using square island regions. These island regions are often intersected by the part boundary, and in some cases become too large to represent a geometrical feature. Further development of the multi-scale method was considered to account for more complex geometry in the proposed multi-scale methodology.

The method involves decomposition of the 2D cross-sections into a finite number of repeatable geometries which can be mapped from a set of corresponding *meso-scale* scenarios modelled using the thermo-mechanical model. It requires prior knowledge of the scan vector geometry for the part, which in turn requires the use of the hatching script developed in Section 5.1.

The method takes the original voxelised geometry, for example as shown in Figure 11.7(a), and divides the cross-section into a series of hatched checkerboard islands, as shown in Figure 11.7(b), which can be intersected by the part boundary. In practice, large cross-sectional regions will contain full or partially intersected island regions. The partially intersected island can be excluded from this method, if their area remains largely unchanged in order to improve the throughput of the decomposition method.

Each clipped island region was hatched accordingly, as shown in Figure

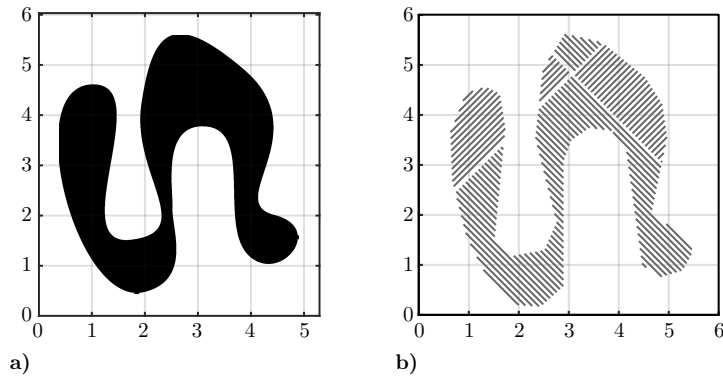


Figure 11.7: a) The original bitmap representing a layer for an arbitrary shape which is then subdivided and hatched into b) 5 mm checkerboard islands rotated at 45°

11.8(a), with the assumption that the scan vectors are always oriented parallel to the island edges, and have a constant hatch spacing throughout the island. The collection of scan vectors was then transformed into local coordinate system which have the vectors aligned in the y' direction, as shown in Figure 11.8(b). A 2D image of the scan vector length was created by a rastering technique using the length of each scan vector, as shown in Figure 11.8(c). By transferring to the local coordinate system and using an image with a resolution corresponding to the hatch spacing, all scan vectors can be accounted for. This removes any aliasing effects during rastering, since each row of the image exclusively contains only a single scan vector. A binning algorithm was used to decompose the image into regions of predefined intervals of scan vector length, as shown in Figure 11.8(d). The intervals are dependent on the number of scenarios simulating using the thermo-mechanical model, and this determines the fidelity for capturing the region. Image segmentation was used to isolate each sub-region in the image using Matlab's connected component labelling function, *bwconncomp*.

The sub-regions of the same scan lengths within the island geometry require mapping to a representative geometrical primitive available from previous simulations in the thermo-mechanical model, such as in Chapter 9. The bounding box for each sub-region was taken, and using the scan vector length, a representative rectangular region was identified, as shown in Figure 11.9.

Results obtained from a library of *meso*-scale simulations were then obtained to represent these regions and each stress component field was individually mapped onto each sub-region, as outlined in Section 11.1.1, and are then clipped using the original geometry. The multi-scale input generated with this method is shown for the von Mises stress in Figure 11.10(a) and the equivalent plastic strain, as presented in Figure 11.10(b).

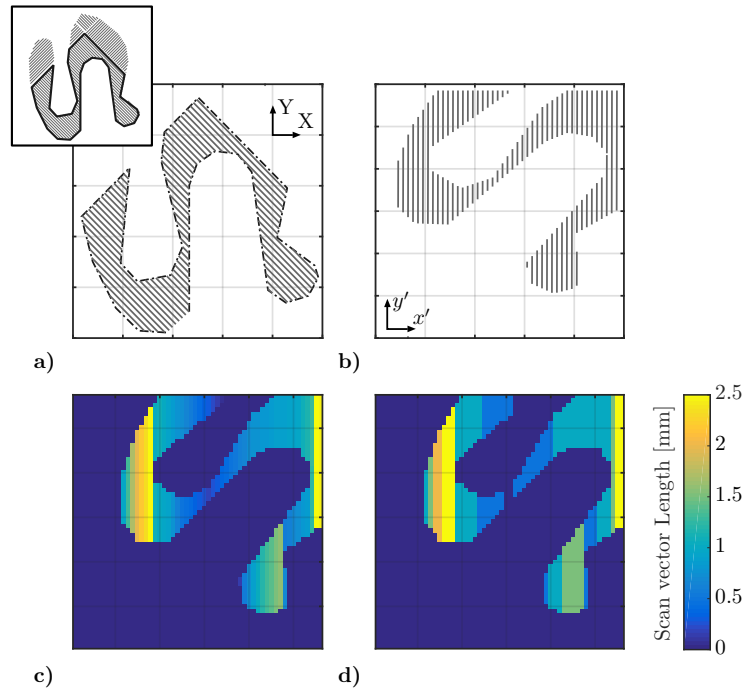


Figure 11.8: The method splits clipped island regions which are **a)** hatched in the global coordinate system and in **b)** are scaled and rotated into a local integer coordinate system corresponding to the hatch distance. Rasterising is performed on the scan vectors to determine **c)** the scan vector length, which are segmented in **d)** into regions of intervals of scan vector lengths.

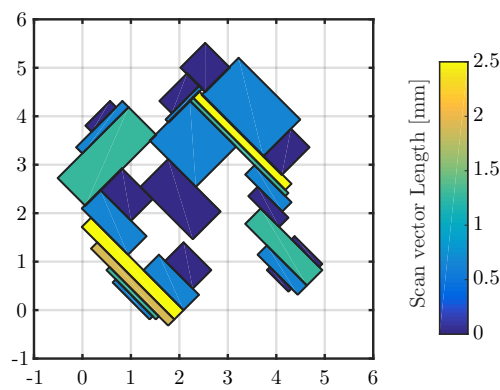


Figure 11.9: Generation of bounding boxes of scan vector lengths of an interval which are used for mapping previous results on the geometry

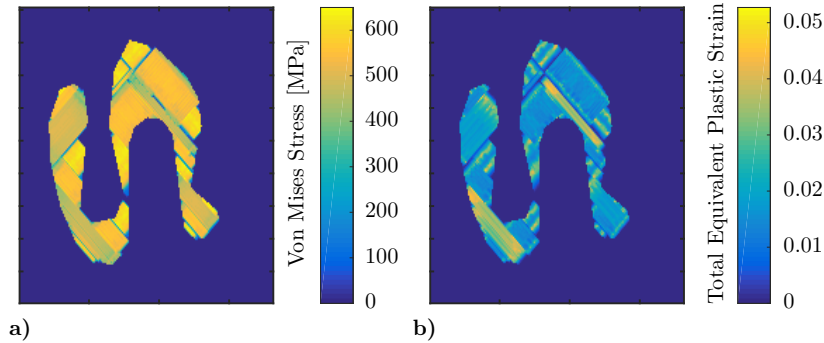


Figure 11.10: The result after mapping rectangular thermo-mechanical results onto the geometry showing a) the von Mises scalar field and b) the equivalent plastic strain field.

11.2 Test cases for the multi-scale methodology

Analysis of the multi-scale method is presented in Section 11.2.1, to determine the effect of the sensitivity of the image processing methods on the stress fields used as input in the *macro*-scale model. In order to determine the influence of transient effects when scanning between multiple islands, a direct comparison was performed between the multi-scale analysis and the detailed transient thermo mechanical model in Section 11.2.2. The multi-scale method is applied into 3D onto a set of 3D pillar geometries in Section 11.2.3. Finally, a test-case is performed on the extension to the thermo-mechanical model in Section 11.2.4, which compares the residual stress predicted in a more complex geometry between a detailed thermo-mechanical analysis and the multi-scale method.

11.2.1 Sensitivity analysis of the pre-processing method

Rotations of images with low resolutions tend to introduce aliasing and edge effects, and a high degree of subsampling can excessively numerically diffuse smooth values in areas of high contrast. A sensitivity analysis was first performed on the subsampling and image rotation methods, to determine their effect on the input and the final result for the macro scale analysis. The following variations were performed on a (5 x 5) mm island scan strategy to determine any effect:

1. Single island
2. Single island with a rotation of 45°
3. 2 x 2 islands
4. 2 x 2 islands with a rotation of 45°

Four levels of subsampling were performed using image scale factors of [0.2, 0.4, 0.6, 0.8] to observe any effects in the input grids used in the macro-scale model. A rotation of 45° was chosen to capture any aliasing effects caused by the combination of rotation and scaling when mapping regions onto the macro-scale model.

11.2.2 Direct comparison between the thermo-mechanical and multi-scale analyses

There is a need to determine the level of inter-dependency on the combination of multiple islands, and the effect the order of scanning has on the generation of residual stress. This will validate the method of superimposing residual stress fields generated with this multi-scale modelling approach. The addition of previously consolidated material in the area will affect the thermal dissipation during scanning, and the additional constraint along the shared edge will affect the distribution of residual stress created in the successively scanned islands. Therefore, it is expected that changing the order of scanning will affect the residual stress field generated. However, the overall magnitude is unlikely to change because the stress field is dominated by the stress generated parallel to the scan vector. Four test cases were performed to examine this:

1. Single Island - (5 x 5) mm region
2. 1 x 2 islands - (5 x 10) mm region
3. 2 x 2 islands - (10 x 10) mm region (sequential)
4. 2 x 2 islands - (10 x 10) mm region (staggered)

and are illustrated in Figure 11.11. The fourth case aims to examine the behaviour when islands are scanned initially unconnected, to represent using the LHI laser scan strategy. Results were obtained after all the islands had uniformly cooled to approximately 350°C .

Despite the scale of this simulation case, the low thermal conductivity of un-sintered metallic powders should significantly reduce any heat transport between islands. The transient thermo-mechanical model used the same laser

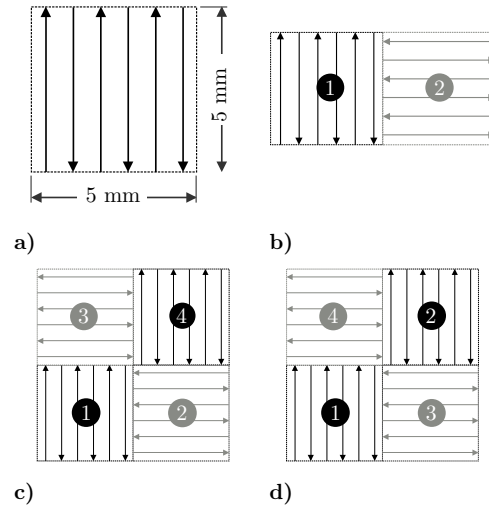


Figure 11.11: Laser scan paths used in the transient thermo-mechanical analysis for a) single island, b) 1 x 2 islands, c) 2 x 2 islands (sequential) and d) 2 x 2 islands (staggered) with unconstrained edges

scan and hatching parameters for processing Ti-6Al-4V using SLM as stated in Table 7.1 and 7.2. The results obtained from the transient thermo-mechanical analyses were then directly compared with the equivalent model created using the multi-scale method .

11.2.3 Analysis of 3D pillars using multi-scale method

The multi-scale method was extended into 3D, in order to understand the *macro*-scale response on a structure subjected to the in-built residual stresses created during the process. Previous studies in the literature were applied to relatively small, single layer regions, and the combined effects of stress building upon a large geometry needed to be investigated. This demonstrates an opportunity to predict the residual stress of a larger 3D structure, which are both feasible to manufacture and have the residual stress distribution experimentally measured.

A set of cuboid 3D pillars were created, as illustrated in Figure 11.12, with dimensions of (5 x 5 x 20) mm and (10 x 10 x 20) mm. These were created by tessellating the checkerboard island into the Z-direction, such the islands orientation rotated by 90° per physical layer. Using these relatively simple geometries would isolate any geometric effects from the study.

In order to keep the performance of the simulation to reasonable levels, in particular generating the mesh in the pre-processor, the element lengths in the

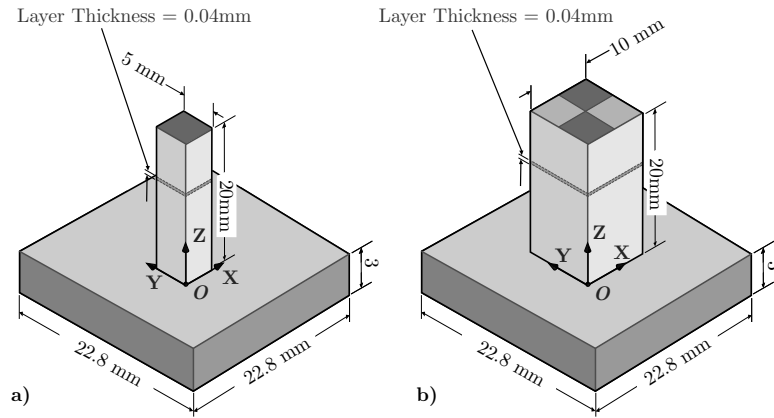


Figure 11.12: 3D pillar geometries used in the multi-scale analysis: a) single island (5 x 5 x 20) mm, and b) four islands (10 x 10 x 20) mm

macro-scale model were set to 0.2 mm in the XY plane (using a scale factor $f_s = 0.4$), whilst retaining the same physical layer thickness (0.04 mm).

11.2.4 Extension for modelling complex geometry

A test case was created to demonstrate the proposed extension of the multi-scale method in Section 11.1.3. A comparison was made between the multi-scale method and a full transient analysis using the thermo-mechanical model. This test cases used the previous geometry shown previously in Figure 11.7(a), with the corresponding checkerboard island scan vectors shown in Figure 11.7(b) required for both methods.

In the transient analysis, the final un-refinement level was chosen to have element lengths of 0.02 mm due to the thin features of the geometry. For the multi-scale method, an image upscale factor of 0.5 was used creating a macro-scale model with an element size of [0.08 x 0.08 x 0.04] mm.

11.3 Results

The results of the sensitivity analysis are presented in Section 11.2.1 showing the effect of image processing on the input and the corresponding results obtained in the macro-scale model. The results for the three variations of combining multiple islands together are shown in Section 11.2.2 and compared with the thermo-mechanical analysis. Then in Section 11.2.3, the multi-scale method is extended into 3D for predicting the mechanical behaviour of two 3D pillar geometries. Finally, the results for the proposed approach for extending the multi-scale method into complex geometry is presented in Section 11.2.4.

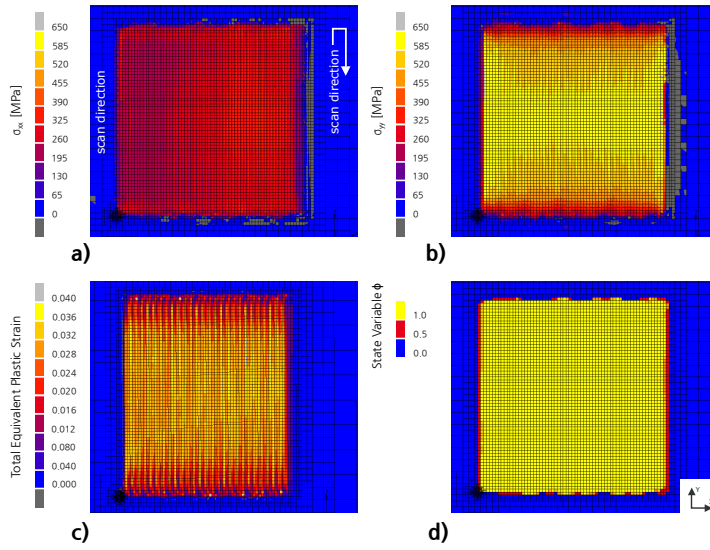


Figure 11.13: Profile views of the transient thermo-mechanical simulation of a (5 x 5) mm island showing a) σ_{xx} , b) σ_{yy} , c) the equivalent plastic strain $\bar{\epsilon}_p$ and d) the state variable ϕ

The thermo-mechanical analysis for the single island case (5 x 5) mm region was first conducted to obtain the stress fields, equivalent plastic strain and state variable, which are shown in Figure 11.13. These results were then used for the pre-processing step in Section 11.2.1.

11.3.1 Sensitivity analysis of the image processing

A sensitivity analysis was performed to determine the effect of combining the image-processing operations on the *meso*-scale grids prior to the tessellation and the effect of subsampling the grid at different resolutions after tessellation of the islands was completed. The input grids for a single stress component σ_{xx} and the probability density distribution $p(\sigma_{xx})$ for solid elements are shown in Figure 11.14.

The extent at which the stress field changes with the input resolutions is not discernible until choosing a small-scale factor ($f_S < 0.4$). Aliasing effects along the edges become more apparent choosing lower resolution, and to a greater extent choosing the 45° cases, as shown in Figure 11.14(b) and Figure 11.14(d). The PDFs for the single island cases more easily show a reduction in the peak stress value for this component at the low resolutions and a small broad distribution of lower stresses attributed to the aliasing. The effects of aliasing are most significant along the void-solid periphery due to interpolation.

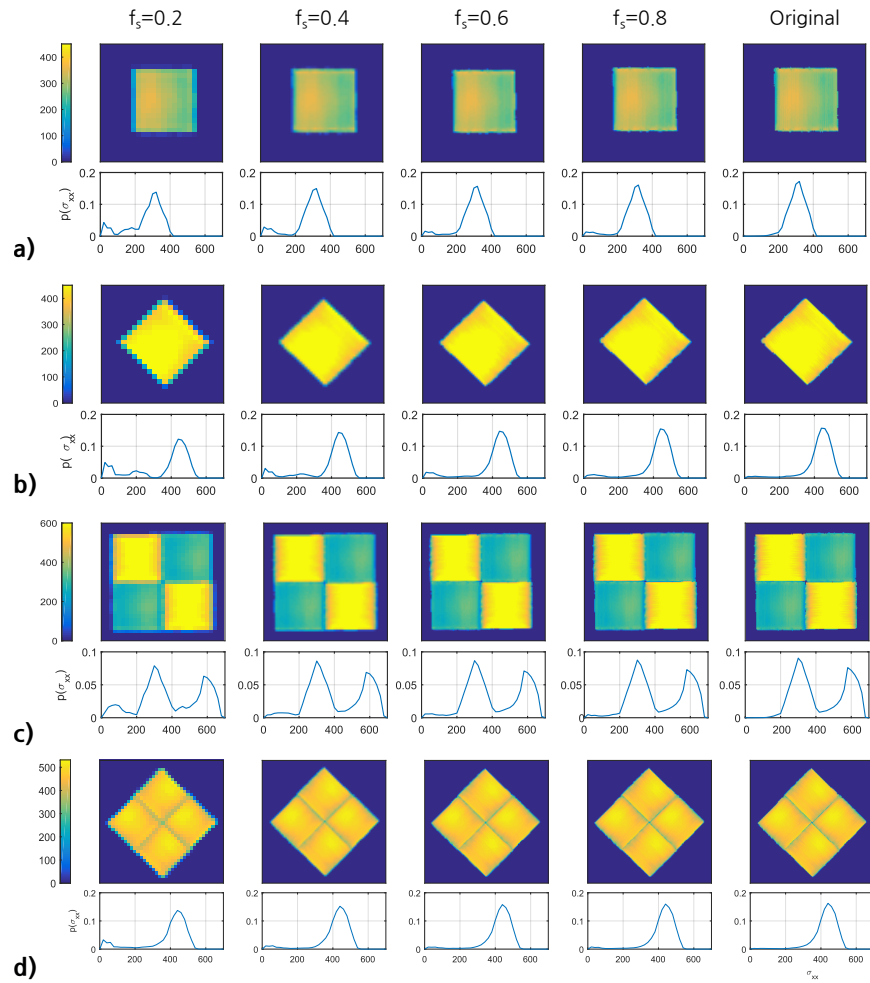


Figure 11.14: Image processing showing the image grid of the σ_{xx} components and the probability distribution $p(\sigma_{xx})$ for a) 1 x 1 island rotated at a) 0° , b) 45° and the 2 x 2 islands rotated at c) 0° and d) 45°

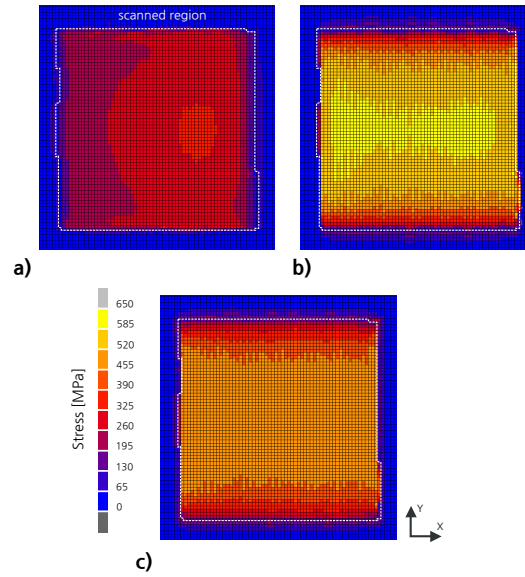


Figure 11.15: Profile views of the un-transformed single (5 x 5) mm island using the multi-scale method, showing a) σ_{xx} , b) σ_{yy} , and c) the von Mises stress

11.3.2 Comparison of the results obtained at the meso-scale between the multi-scale method and the thermo mechanical analysis

The first analysis using the multi-scale method was conducted on an un-transformed ($f_s = 1.0$) single island, which provides a reference between the two analysis methods. It was found there was negligible difference in the stress field, as shown in Figure 11.15, and also the stress distributions between analysis scales shown in Figure 11.16. Peaks in the distribution for both the transverse and longitudinal stresses have shifted lower by approximately 20 MPa.

In the transient thermo-mechanical analysis, a heterogeneous displacement field was distributed throughout the entire island, as shown in Figure 11.17(a). Whereas, the resolved displacement field in the model producing the multi-scale method shown in Figure 11.17(b) is smoothly distributed throughout the part. The greatest total displacements in the island are located along the edge, exhibiting the ‘curling’ phenomena observed in parts produced using SLM [77]. The greatest total distortion is present at the edges along the vertical axis (parallel to the scan vectors), as shown in Figure 11.18(b), caused by the dominating longitudinal stress. The curvature remains constant for the distortion along the vertical axis, whereas along the horizontal axis, as shown in Figure 11.18(a), it is asymmetric, with curvature only present ~ 1 mm from the edges. This shows the effect of the non-uniform transverse stresses present.

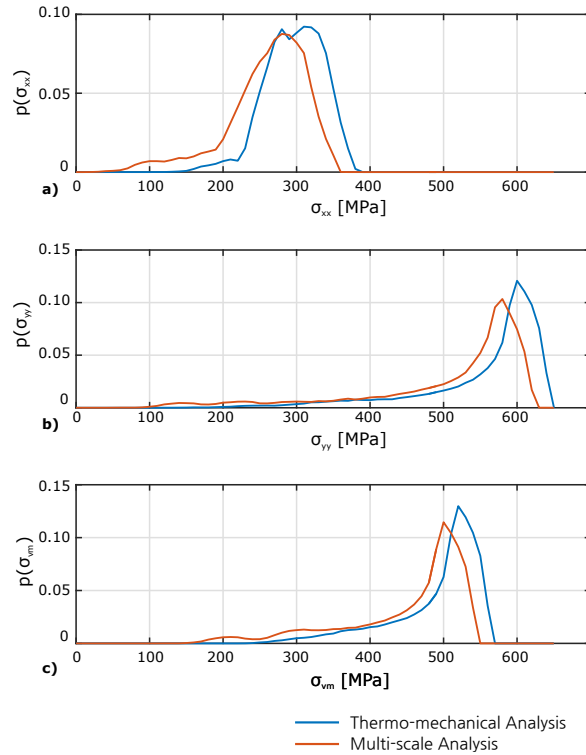


Figure 11.16: Graphs of the PDFs a) $p(\sigma_{xx})$, b) $p(\sigma_{yy})$, and c) $p(\sigma_{vm})$ for the thermo-mechanical and multi-scale analysis of single (5 x 5) mm island region

The final state of the residual stress after scanning two islands using the thermo-mechanical model is shown in Figure 11.19. Both probability distributions $p(\sigma_{xx})$ and $p(\sigma_{yy})$, show a bimodal distribution, created by the combination of two islands with orthogonal scanning directions. The components are not identical and indicate that transient behaviour has occurred, which has altered the generation of residual stress per island. The transverse stress (σ_{xx}) for the second island has a broader but larger magnitude (left peak in Figure 11.19(b)) than that observed in the island scanned first. It is evident that thermal dissipation was predominantly directed into the currently scanned island, as shown in Figure 11.21. Nevertheless, the temperature profile was skewed slightly towards the previous region, showing that transient thermal behaviour has some dependence on the scanning history and connectivity of the islands.

The stress distributions for both σ_{xx} and σ_{yy} in the multi-scale method were found to be nearly identical, as shown in Figure 11.20(a) and Figure 11.20(b). There was an increase in the stress magnitude indicated by the shift of right peak for both components, and these were more asymmetric compared to those found in the thermo-mechanical model. The von Mises stress distribution shown

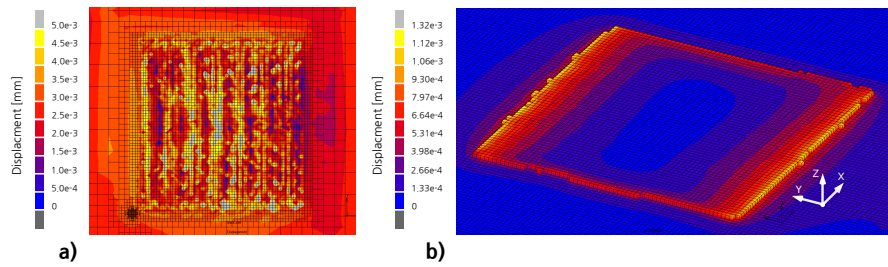


Figure 11.17: Total displacement [mm] of the untransformed single (5 x 5) mm island found in a) the thermo-mechanical analysis, and in b) the multi-scale analysis

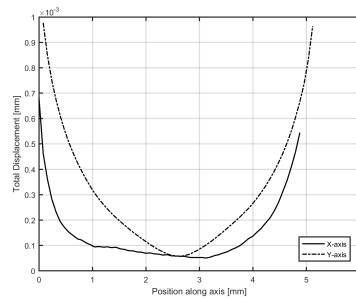


Figure 11.18: Graph of displacement profiles along the central horizontal axis and vertical axis from the single (5 x 5) mm island obtained in the multi-scale analysis

in Figure 11.20(b), becomes narrower with a sharper peak, indicating the stress magnitude was more concentrated at the upper end (500 MPa).

The thermo-mechanical analysis of the 2 x 2 island cases performed in different scan orders are compared with the multi-scale model in Figure 11.22, and the probability density distributions are shown in Figure 11.23. The longitudinal stresses generated parallel to the scan vector for both the thermo-mechanical and the multi-scale analyses correspond well with each other. For both the sequential (Figure 11.22(a)) and staggered strategies (Figure 11.22(b)) the distribution of longitudinal stresses do not significantly differ between islands. The transverse stresses vary between all the islands for both the thermo-mechanical and multi-scale analyses, and have a broad distribution of 200-400 MPa. A difference was observed for the transverse stress, as shown in Figure 11.23(a), between the sequential and staggered strategy. A greater shift in the transverse stress was found when using the staggered approach. The peak of transverse stresses shift to a greater value for connected islands, which is evident in Figure 11.23(a), with the sequential scanning having a higher magnitude peak for the transverse stress for islands(1,4) than the staggered strategy when islands(1,2) are isolated during scanning.

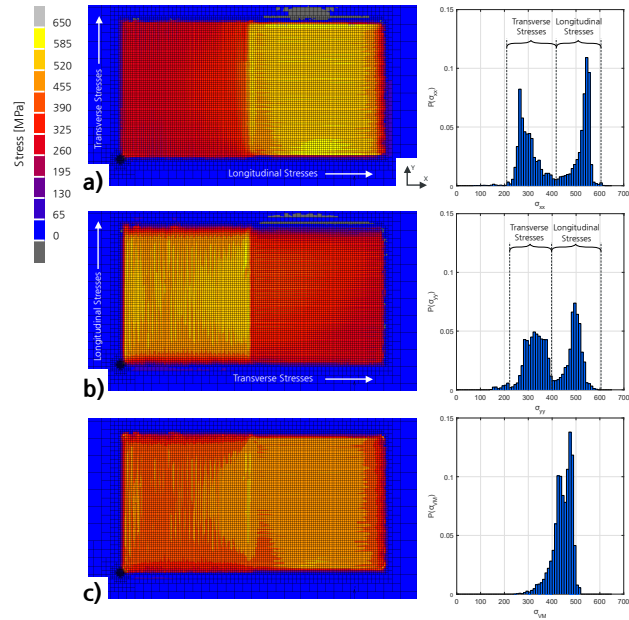


Figure 11.19: Thermo-mechanical analysis of the 1 x 2 island case, showing the profile view and PDFs for a) σ_{xx} , b) σ_{yy} and c) the von Mises stress

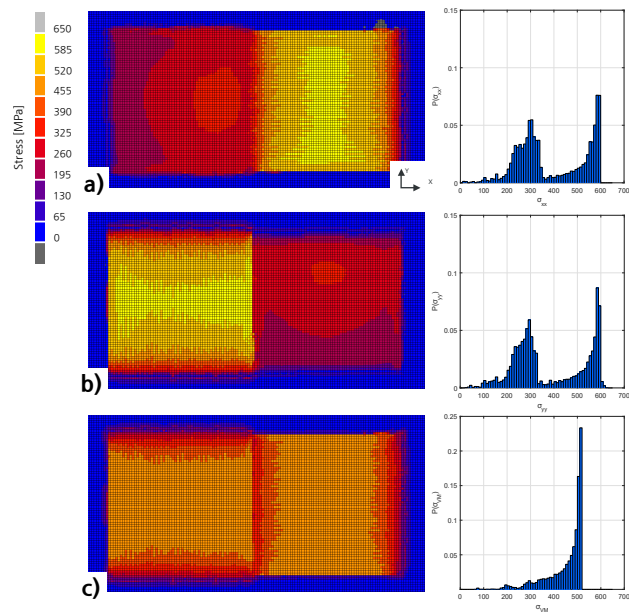


Figure 11.20: Multi-scale analysis of the 1 x 2 island case, showing the profile view and probability density function for a) σ_{xx} , b) σ_{yy} and c) the von Mises stress

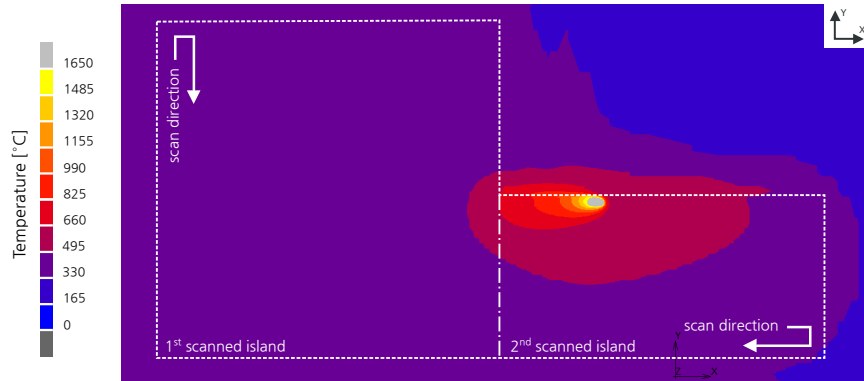


Figure 11.21: Profile view of the temperature taken at $t = 1.56$ s, midway through scanning the second island

The stress distribution for the longitudinal stress in the multi-scale analysis corresponds well for both the sequential and staggered scan orders found using the thermo-mechanical analysis. However, the transverse stress is significantly lower, by approximately 100-150 MPa, compared to both scan strategies simulated using the thermo-mechanical model.

For all 2×2 island analyses performed, the von Mises stress, as shown in Figure 11.23(c), was found to be a highly skewed asymmetric distribution between 300-550 MPa. This shows that the longitudinal stress significantly dominates the stress field at this analysis scale. The von Mises stress distribution for the multi-scale analysis has shifted lower, caused by the lower transverse stress within this analysis.

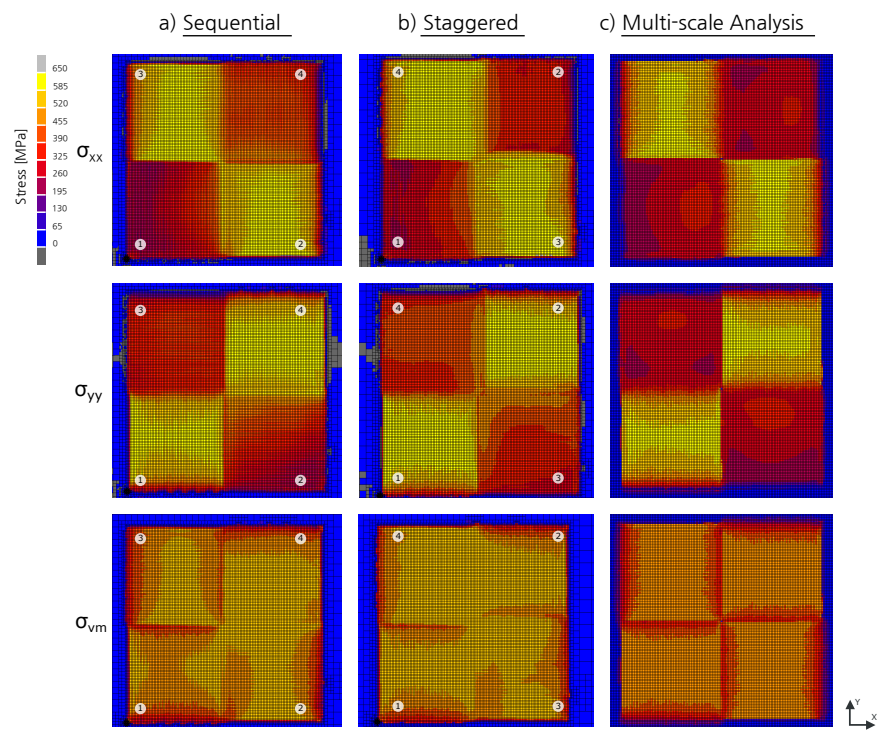


Figure 11.22: Comparison between all the 2 x 2 island cases, showing the profile view of stress components (σ_{xx} , σ_{yy} , σ_{vm}) for a) ordered and b) staggered island scanning and c) the multi-scale analysis

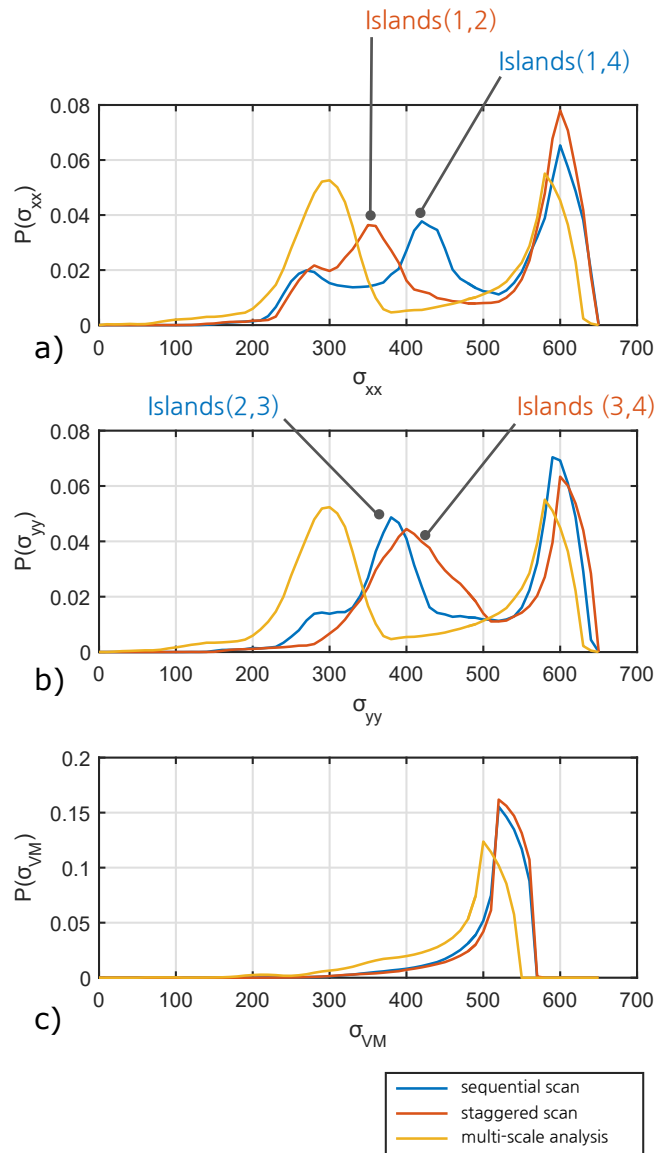


Figure 11.23: PDFs a) $p(\sigma_{xx})$, b) $p(\sigma_{yy})$ and c) $p(\sigma_{vm})$ of the 2×2 island cases for both the ordered and staggered scan orders obtained in the thermo-mechanical model, and those obtained from the multi-scale analysis

11.3.3 Analysis of 3D rectangular pillars

The multi-scale methodology was extended to incorporate multiple layers to determine the *macro*-scale stress distribution and predicted distortion in a 3D structure. Initially, this was tested on two 3D pillars previously described in Section 11.2.3 for a

1. (5 x 5 x 20) mm - single island pillar
2. (10 x 10 x 20) mm - 2 x 2 island pillar.

The stress distributions in the geometries were taken along a planar XZ cross-section 2.5 mm from the edge in both test cases. This is presented for the single island pillar in Figure 11.24, and the 2 x 2 island pillar in Figure 11.26. These results are presented without using nodal averaging, which when used obscures the inter-layer difference between stresses. This inter-layer difference results in the banded effect appearing in the structures for resolved σ_{xx} and σ_{yy} stresses between each layer. The total displacement in 3D for the single island is shown in Figure 11.25(a) and the 2 x 2 island case in Figure 11.27(a). Cross-sections were taken midway diagonally through the structure to try and capture the displacement and stress distributions throughout the entire cross-section of the structures.

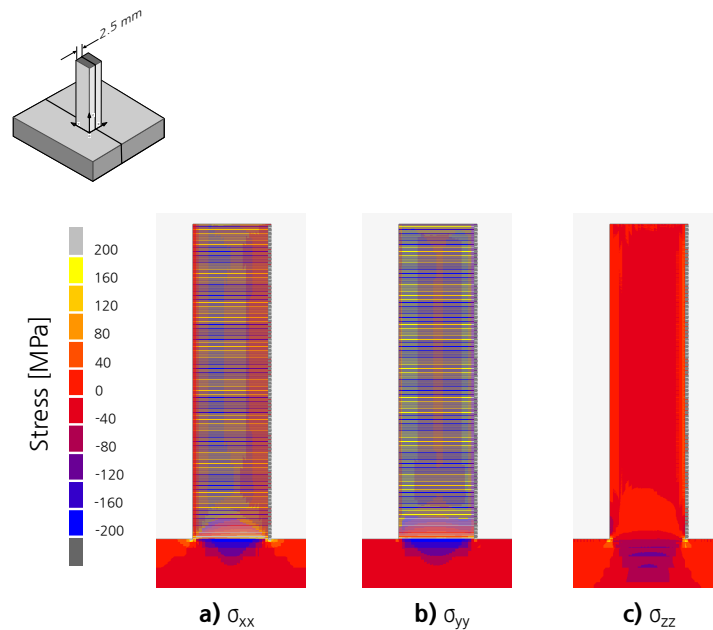


Figure 11.24: Planar cross-sections along the XZ plane taken 2.5mm from the edge for a (5 x 5 x 20) mm pillar analysed using the multi-scale method. The stress distributions: a) σ_{xx} , b) σ_{yy} and c) σ_{zz} are shown without using nodal averaging

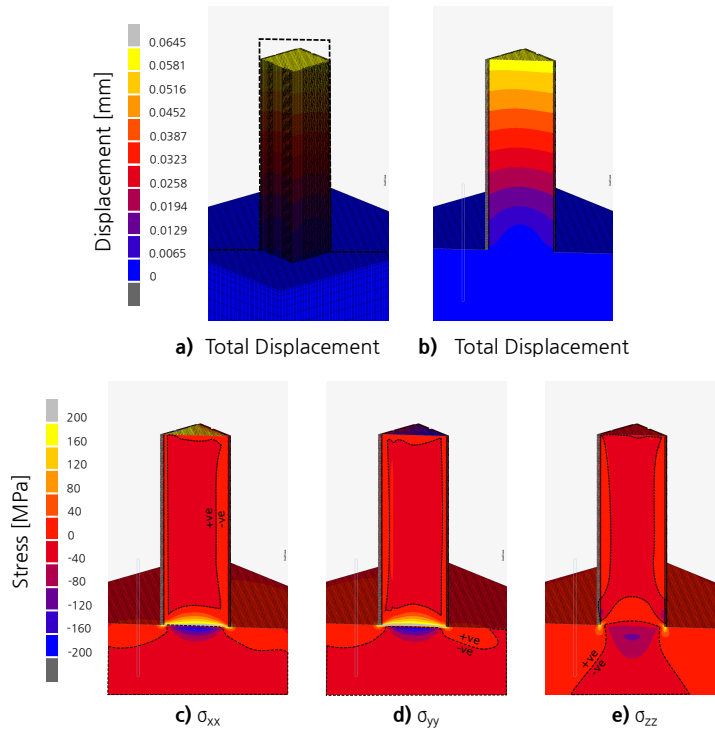


Figure 11.25: 3D View and cross-sections of a (5 x 5 x 20) mm pillar analysed using the multi-scale method showing a) total displacement, and cross-sections for b) the total displacement: c) σ_{xx} , d) σ_{yy} , and e) σ_{zz} . Results are shown using nodal averaging

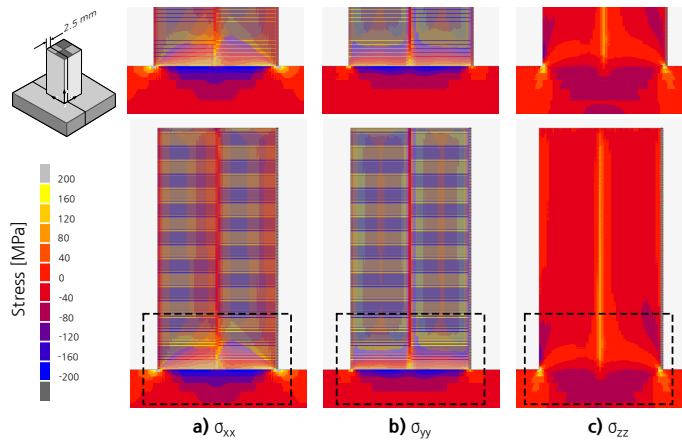


Figure 11.26: Planar cross-sections along the XZ plane taken 2.5mm from the edge for a (10 x 10 x 20) mm pillar analysed using the multi-scale method. The stress distributions: a) σ_{xx} , b) σ_{yy} and c) σ_{zz} are shown without using nodal averaging

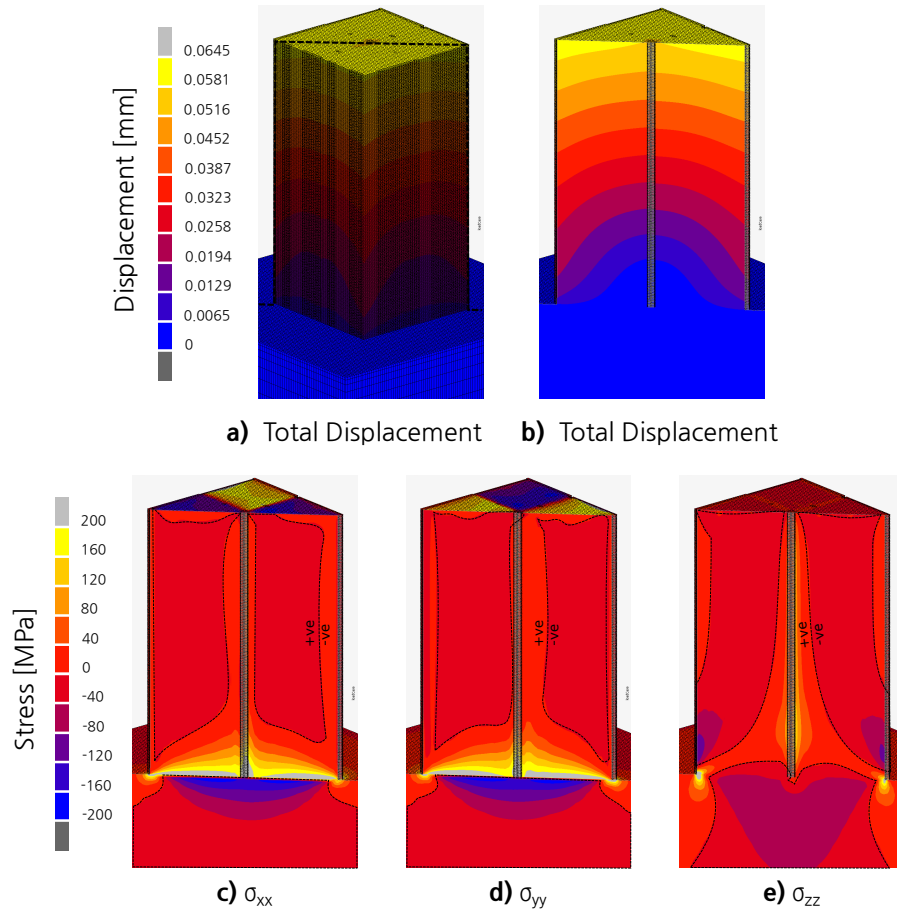


Figure 11.27: 3D View and cross-sections of a (10 x 10 x 20) mm pillar analysed using the multi-scale method showing a) total displacement and cross-sections for b) the total displacement: c) σ_{xx} , d) σ_{yy} , and e) σ_{zz} . Results are shown using nodal averaging

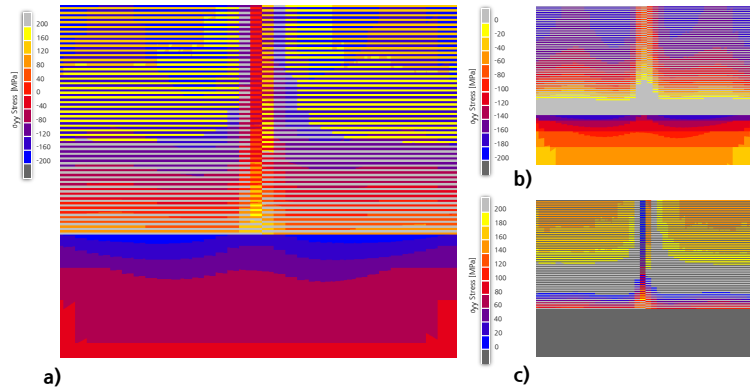


Figure 11.28: a) Close up of the cross-section showing σ_{yy} in the XZ plane, and the same but with b) compressive stresses removed and c) tensile stresses removed

It can be seen from the cross-sections for both test cases, as shown in Figure 11.24(a,b) and Figure 11.26(a,b), that the multi-scale method introduces banding between layers for the resolved σ_{xx} and σ_{yy} stresses, which is not apparent in σ_{zz} , as shown in Figure 11.24(c) and Figure 11.26(c). A closer inspection of the banding behaviour is shown in Figure 11.28. It can be seen that an alternating and abrupt change from compressive to tensile stress between layers is created as result of the perpendicular orientation of islands between adjacent layers.

For all test cases, the resolved stress distribution showed a large compressive region in the base plate, immediately followed by a large tensile region at the bottom of the part. For both test cases, throughout the centre of the part, a mildly compressive region was present for all stress distributions. As shown in Figure 11.27(c-e), the 2 x 2 island test case showed a small tensile region along the central axis where the tessellated islands connect. A stress concentration was observed along the corners of the part connected to base plate, for both test cases. This was most evident in σ_{zz} stress distribution, as shown for the single island pillar in Figure 11.25(e) and the 2 x 2 island pillar in Figure 11.27(e).

A cross-section of the vertical stress was taken along the XY plane at the boundary between the part and the base-plate and is shown in Figure 11.29. It can be seen that there is a compressive region in the centre of the part, with tensile stress concentrations at each of the corner.

The displacement plots for both test cases shown in Figure 11.25(a,b) and 11.27(a,b) were found to be uniform throughout the part. Distortion increased towards the edges of the part, owing to the ‘curling’ behaviour witnessed in parts produced using SLM.

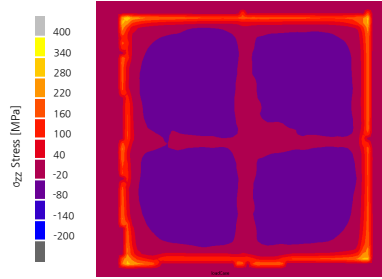


Figure 11.29: Cross-section showing σ_{zz} along the XY plane at the boundary between the 2 x 2 island pillar and the base-plate

11.3.4 Extension for modelling complex geometry

For evaluating the performance of the extension of multi-scale method to model more complex geometries, as described in Section 11.2.4, an analysis of the complex geometry case was performed using both the transient thermo-mechanical model and the multi-scale method.

The distribution the residual stresses when scanning the complex geometry obtained from the full transient thermo-mechanical analysis are shown in Figure 11.30. The predicted stress distribution obtained from the extension to the multi-scale method is shown in Figure 11.31. It can be observed that a large variation in the residual stress was present due to the complexity of the scanned geometry chosen. Generally, regions of high magnitude stresses, as shown in Figure 11.30(c), are located in regions with relatively long and short scan vectors.

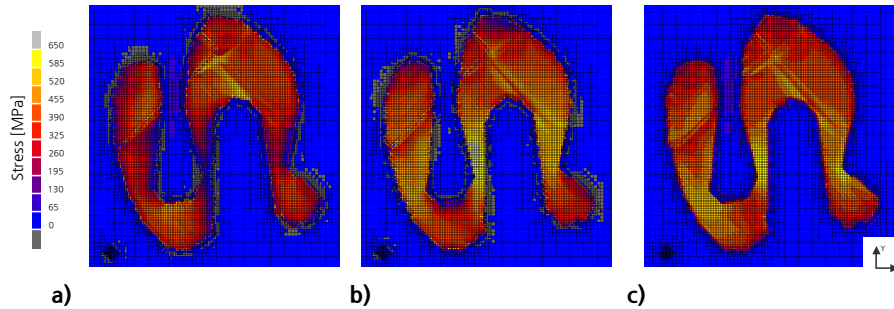


Figure 11.30: Surface profile views showing the a) σ_{xx} , b) σ_{yy} stress and c) the von Mises stress obtained from thermo-mechanical analysis of the complex geometry

The resolved stress field of the complex geometry obtained using the multi-scale method is shown in Figure 11.31(b) the extension to the multi-scale methods does appear to capture the variation in the distribution of stresses caused by the change in the scan vector length. Overall, the magnitude of stresses has been

reduced when comparing the input to the multi-scale analysis (Figure 11.31(a)) with the resolved stresses (Figure 11.31(b)).

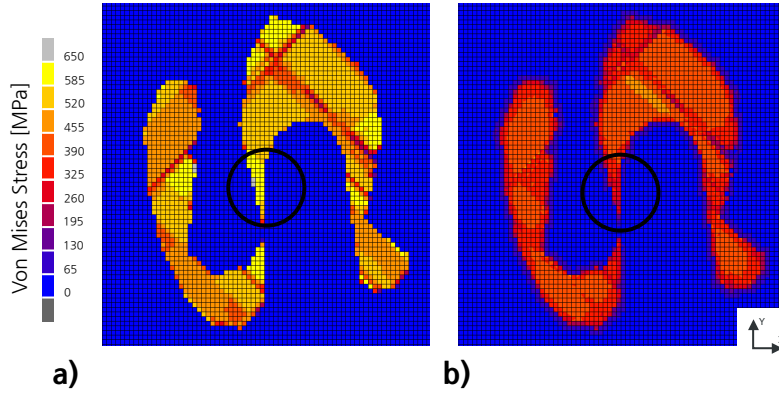


Figure 11.31: Surface profile view of the von Mises stress of the complex geometric cases from a) the input given to the multi-scale analysis, and b) the resolved stresses obtained from the multi-scale analysis method. Circles highlight large difference between the input and resolved stresses

11.4 Discussion

11.4.1 Sensitivity analysis of image processing

The sensitivity analysis in Section 11.3.1 showed that varying the pre-processing resolution does not significantly affect the distribution of the stress fields in the bulk regions until reaching small scale factors ($f_s = 0.2$). Aliasing effects become more significant when including rotation, however, these can be reduced by combining regions and reducing the void-solid perimeter regions. It is expected that for large regions these effects will not be significant, considering the relative scale between the resolution of the island and the part geometry defined for the multi-scale analysis.

For an indication of the domain size in a macro-scale model, a straightforward approximation for the number of active solid elements, n_{solid} , for a given area, A , can be calculated using,

$$n_{solid} \approx A \left(\left(\frac{f_s}{x_{el}} \right)^2 + c \right), \quad (11.2)$$

where f_s is the image scale factor, x_{el} is the original element size in the *macro*-scale model and c is the number of elements in the substrate per unit area. A regular mesh is assumed and this is approximate due the creation of elements along the edges caused by aliasing artefacts. Further performances could be gained in the

macro-scale model using octree based re-meshing, which can be defined at the pre-processing stage, or during the mechanical analysis.

11.4.2 Comparison between thermo-mechanical and multi-scale analyses

The multi-scale analysis of an un-transformed single island presented in Figure 11.17 showed ‘curling’ behaviour along the unconstrained edges for the overall response to the stress field input, as widely reported in literature. It also supports the theory of low normal stresses for isolated islands [77], where there is a reduction in the longitudinal stress towards the end of the scan vectors, as shown in Figure 11.15(b). However, the greatest difference was observed in the overall response of the total displacement, as shown in Figure 11.18. It is suspected that the small changes between the analysis scales are attributed to using the average stress component per element obtained at the *meso*-scale from the thermo-mechanical analysis, instead of directly mapping from the element’s integration points. Additionally, the element un-refinement procedure in the thermo-mechanical analysis further contributes towards this. The numerical averaging is suspected to smooth the stress fields and allowing the displacement field to resolve towards a global response. Furthermore, the resolution required to transfer between different analysis scales becomes less important provided the overall magnitude and directionality of the stress fields are captured, given the relative scales used in the macro-scale analysis. Potentially, individual elements in the macro-scale finite element model could be used for modelling sub-regions.

When scanning the 1 x 2 island case, the overall magnitudes of stresses observed in the thermo-mechanical analyses were less than the multi-scale counterparts. The von Mises stress for the multi-scale analysis, as shown in Figure 11.20(c), is heavily skewed towards the high end of the distribution, caused by the dominating longitudinal residual stresses created parallel to the scan vectors. Differences between the thermo-mechanical analysis and the multi-scale method were more significant in the transverse residual stresses. This is because the formation of the transverse residual stresses is more dependent on the transient behaviour or the overall scanning history preceding them, which is observable in the non-identical stress distributions shown in the Figure 11.19(a) and Figure 11.19(b). During the scanning of each island, the thermal dissipation at high temperatures was predominantly directed towards the currently scanned island, as shown in Figure 11.21. As each island becomes increasingly connected to its neighbours towards the end of the scan, there is an increased opportunity for preferential heat dissipation, into neighbouring regions. This has the effect of increasing the temperature gradient and consequently increases the generation

	Thermo-mechanical analysis time [s]	Thermo-mechanical analysis CPU time [s]	Multi-scale analysis time [s]	Multi-scale analysis CPU time [s]	Normalised Speedup (\times)
1 x 1 - island scan	58 687	938 992	463	1 852	507
1 x 2 - island scan	160 739	2 571 824	471	1 884	1 365
2 x 2 - island sequential scan	691 747	11 067 952	499	1 996	5 545
2 x 2 - island staggered scan	694 920	11 118 720	499	1 996	5 571

Table 11.2: Computational timings for performing the analyses using the thermo-mechanical and multi-scale analysis methods

of residual stresses in these regions.

Spatial distributions of the stresses for each island remain the same for the dominant longitudinal stresses parallel to the scan vector. However, the greatest source of error in the current implementation is that at the macro-scale, the multi-scale method cannot account for the change in the transverse stresses based on the scan order. This is because the superimposed sub-regions are modelled independently of the order of scanning. However, due to the relative anisotropy of the stress field, this results in the von Mises stress becoming dominated by contributions from the longitudinal residual stress, as shown in Figure 11.23, and the error accounting for the transient effects at the macro-scale becomes less important.

To account for the order of island scanning affecting the transverse stress component, a compensation method would be required during the pre-processing step. A naïve empirical approach is shifting the transverse stress distribution to match the distribution obtained at the *meso*-scale in the thermo-mechanical model, with the size of the shift dependent on the adjacency of islands created by the scanning order. Alternatively, a library of scenarios using different island combinations and scanning histories at the *meso*-scale could be obtained using the thermo-mechanical model for inclusion in the multi-scale method.

However, despite these differences, the power of the proposed method is demonstrated by the significant computational performance gains obtained, with 10^2 - 10^3 order of improvement using the multi-scale method, as shown in Table 11.2.

The detailed thermo-mechanical analyses were performed on a single 16 core CPU HPC node, with the multi-scale performed on a 4 core CPU workstation. The timings for each multi-scale analysis case used the full domain, without any reduction in resolution. Using a coarser mesh, with the minimum number of elements would reduce the analysis time required. Further performance gains will be experienced when simulating large volumes, since the complexity at the macro-scale is time independent by removing the need to account for the movement of the laser across each scan vector. Hence, the computational time depends only on the number of elements used within the volume.

11.4.3 Analysis of 3D Pillars

It was shown that the multi-scale method can easily be extended to a 3D structure, because of the use of a 3D volumetric grid for storing the stress and plastic strain fields. This was demonstrated with the analysis of 3D pillar structures, which were constructed by tessellating the islands in the Z direction across many layers and rotating these islands by 90° to investigate the inter-layer effect of accumulating residual stress. By simplifying the test cases to cuboid geometries, it isolated any effect caused by having clipped island geometry, and the need to account for different boundary conditions such as support and overhang material.

Despite the relatively small residual stress in the Z direction observed in all the single layer *meso*-scale analyses, there was a significant build-up of stress in the Z direction with multi-layers. This is the result of planar residual stresses accumulating across each layer but being constrained by the adjacent layer, which causes the creation of stress in the Z direction.

The stress distributions throughout both 3D pillar test cases showed a high compressive region in the base plate, followed by an abrupt change to tensile stresses at the bottom of the part, with a region of relatively small compressive stresses in the centre of the component. This behaviour follows similar trends observed in the experimental measurement of residual stress in SLM parts using the ‘slit’ method and XRD by Mercelis and Kruth [77]. It also agrees with the predicted distributions from analytical beam bending models as discussed in the review of the literature in Section 3.3.

The stress distributions observed in the multi-scale analysis follow a similar trend to the experimental work in a thesis by Vrancken who used the ‘contour’ and XRD methods to obtain in-plane measurements of residual stress [87]. Despite the difference in the size of the part, the stress distributions predicted using the multi-scale model for the (10 x 10 x 20) mm pillar (Figure 11.27 and Figure 11.29) are similar to those obtained by Vrancken’s study of a 15 mm cube (Figure 11.32). In their study, they noted a tensile region along the edges balanced by an inner region of compressive stresses. The top of the part also featured tensile regions, although in the *macro*-scale model these are relatively small. Their study identified stress concentrations occurring at the corners of the part, as shown in Figure 11.32(a) which were observed in the multi-scale model in Figure 11.29. These stress concentrations occur as a result of sharp geometric features and increase the susceptibility for failure during manufacture, both in the parts themselves and at the connections with support structures. This suggests that, as in common engineering practice, sharp edges should be avoided to reduce the potential for build-failure during manufacture.

The lower magnitude of stress predicted using the multi-scale method compared to those measured in Vrancken’s study, are attributed to not allowing the part to cool to room temperature, the difference in scan strategy and the size of part tested. However, Vrancken acknowledged that performing a secondary cut along the diagonal (Figure 11.32(b)) after removing the base-plate will cause a re-distribution of the macro-scale residual stress observed.

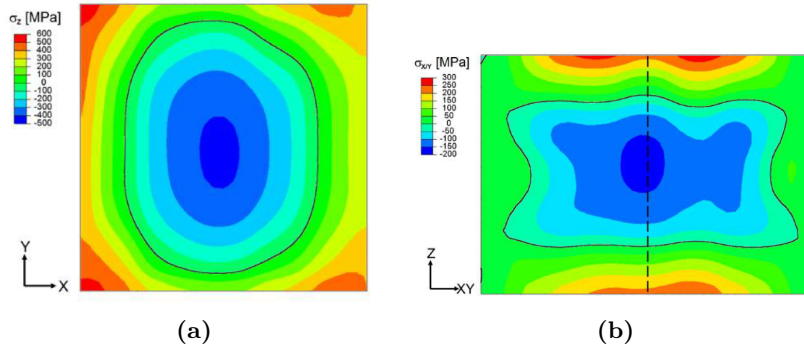


Figure 11.32: Residual stress measurements of a 15 mm cube of Ti-6Al-4V obtained using the contour method by Vrancken [87]: a) the σ_{zz} stresses located between the boundary of the sample and the base plate and b) the diagonal plane taken across the cross-section of the part.

In the multi-scale model, a banding effect was found between layer planes for the σ_{xx} and σ_{yy} distributions for both test cases, when nodal averaging was turned off in the pre-processor. The cause of this was attributed to the 90° change in the orientation of the stresses between layers. It is suspected that interpolating or sampling the stresses in the Z direction would eliminate this banding.

Even with the use of a scaling factor in the XY planes, the current methodology requires individual modelling of each layer. This results in a large number of elements being required for the analysis - over 1.3 million for the 2×2 island pillar. Hence, some method for homogenising the stress field over multiple layers is vitally important to further reduce the number of degrees of freedom in the *macro*-scale analysis sufficiently to enable ‘real’ parts to be modelled. Currently this method cannot reduce the complexity in the Z direction because each physical layer is included in the *macro*-scale model. To account for each layer, these could be gradually added in the multi-scale analysis, and then re-meshing could be performed to reduce the number elements during the analysis. Alternatively, layers could be bundled together, as done by Neugebauer et al. [134, 135], although this would force the assumption that the scan vector length does not vary largely between layers. However, in practice scan vectors are rotated between layers and their length and direction significantly change.

The current multi-scale approach activates elements instantly in a single mechanical analysis and does not include a series of thermal analyses to match the thermal history created during the entire build process. The part would experience the gradual accumulation of heat during the build, but also be subjected to the dissipation of heat into the part from the currently scanned layer. This itself will change the boundary conditions at the *meso*-scale model, but more importantly may introduce non-local temperature gradients generating thermal strain potentially leading to part level failure.

The 3D test cases used simple block geometries, and complex geometries will result in overhang and supported regions being present that require attention. Further work is needed to incorporate the findings from the thermo-mechanical studies on the effect of support material into a multi-scale modelling framework, and modelling of more complex geometries in 3D models.

11.4.4 Extension for modelling complex geometry

The extension to the multi-scale method, as described in Section 11.1.3, was the first attempt to model more complex geometry than the simple geometries composed of rectangles modelled previously. The input to the *macro*-scale model was generated by mapping stress fields, from a library of *meso*-scale regions, as detailed in Chapter 9. It was found that the multi-scale method, as shown in Figure 11.31, using the small library of *meso*-scale regions managed to satisfactorily capture the variation in residual stress in the detailed thermo-mechanical model shown in Figure 11.30. Generally, due to the variation in scan vector length in the geometry, a higher magnitude of residual stress was seen in regions composed of both short scan and long scan vectors. However, an overall decrease in the magnitude of stress between the input stress field and the resolved stresses was observed. This decrease is associated with modelling relatively small features on a ‘stress-free’ base plate. During the global solution stage, as stresses resolve due to equilibrium, stresses are generated in the base plate immediately below the scanned geometry, causing some stress relief in the built part.

An issue with the test-case for the detailed thermo-mechanical analysis is that the laser jumps alternates between regions for each individual scan vector, as shown in the highlighted pair of regions in Figure 11.33. This could potentially reduce the effect of overheating in narrow features compared to scanning these regions in a continuous manner. Currently no method for sorting scan vectors by distance is implemented in the hatching method (Section 5.1). In practice, the laser position can jump if the scan vectors have not been sorted by the pre-processing software.

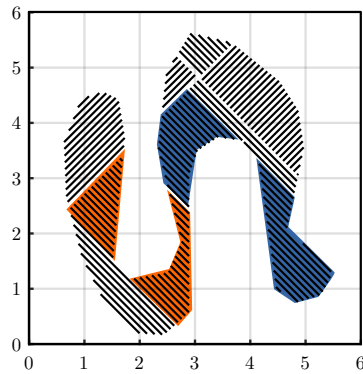


Figure 11.33: Illustration of the scan vectors in the thermo-mechanical model. The coloured regions highlight scan vectors that are jumped between during the simulation

Further work is needed to provide a satisfactory method for mapping between the laser scan geometry and the *meso*-scale regions. As shown in Figure 11.34, the use of a bounding box to map regions can under some situations be unsatisfactory. In particular, this is a problem in large diagonal regions of similar scan vector lengths i.e. the central section of the geometry in the test case. An improvement to the method would incorporate appropriately selected *meso*-scale scan geometries (triangles, trapezoids) depending on the shape of the scan vector geometries. This would be more effective at accurately mapping more features of complex geometries and lessen the need for clipping and scaling regions.

It is recommended that further investigations are undertaken to develop an empirical relationship between the laser scan vectors and the transverse and longitudinal residual stresses generated. Ideally, a relationship between both the scan vector length, and its incremental change in scan vector length with the residual stress components generated, would enable a method for generating inputs for any arbitrary geometry without requiring mapping from pre-generated *meso*-scale regions. This would significantly improve the flexibility and ease of generating the *macro*-scale models used in the multi-scale analysis.

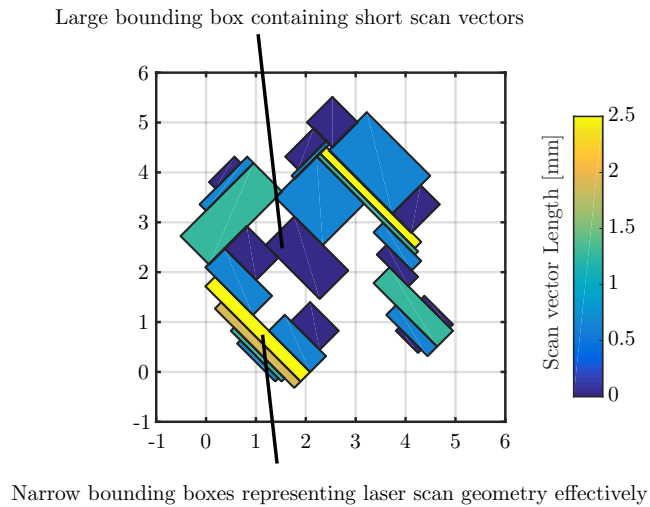


Figure 11.34: Illustration showing bounding box regions of scan vector lengths which incorrectly and satisfactory map between

11.5 Conclusions and summary

A multi-scale analysis method for predicting the residual stress generated in selective laser melting has been assessed by conducting a direct comparison between modelling scales. The *macro*-scale analysis used superposition of stress fields obtained from a detailed *meso*-scale region determined from a thermo-mechanical analysis, and can represent the overall stress field at multiple resolutions.

Conducting thermo-mechanical analyses over a series of islands showed that the generation of residual stress is dependent on the transient thermal history generated by the order of island scanning. The order of island scanning only had a significant effect on the distribution and magnitude of the transverse stress created perpendicular to the scan vectors. However, the more dominant longitudinal stress generated parallel to the scan vector did not vary significantly with the scan history. The use of staggered strategy (analogous to the LHI strategy) showed a reduction in the transverse stress for isolated islands, agreeing with the theory that minimising the heat conduction away from the island can reduce the magnitude of the residual stresses generated. The full thermo-mechanical simulations performed showed that fully scanned islands can effectively be treated independently within a bulk region.

The multi-scale method was extended into 3D simply by creating island pillars through tessellating the islands in the Z direction. The resolved stress distributions in both test cases for the base-plate and the part showed similar

behaviour to that observed in analytical beam-bending models and in experimental measurements of residual stress in literature. The stress distribution observed exhibited high compressive stresses in the base plate, with an abrupt change to tensile stresses at the bottom of the part, with a relatively small compressive region throughout the centre of the part. Further work is required to experimentally validate samples with the multi-scale method. Stress concentrations were also observed at sharp corners of the geometry connected to the baseplate. It is recommended that manufactured parts should avoid sharp geometrical features to avoid the creation of sites of stress raiser, which would lessen the risk of build-failure.

A current limitation with the multi-scale methodology is that each layer is explicitly modelled, which increases the number of elements required to model the part and severely limits the potential to predict behaviour across large regions. Modelling each layer was found to create bands of tensile and compressive stress created by adjacent layers and were associated with the abrupt change in directionality of stresses between adjacent layers. Further investigation is required to understand the development of residual stresses across multiple-layers and requires extending the thermo-mechanical model to account for this. Doing so would provide a better understanding of the effect of scanning across processed layers that have previously developed plastic deformation, and if the banding behaviour is solely an artefact of the multi-scale method. Based on this knowledge, a method for homogenising the stress input across multiple layers could be developed that would significantly improve the model's ability to predict stresses and distortion in large parts. Further work needs to consider coupling the multi-scale method with a thermal analysis to account for the dissipation of heat from the currently scanned layer during the entire build duration. This would provide a better insight into the thermal history acquired during the build and its effect globally across the part improving the prediction of the multi-scale model.

Currently, mapping and clipping a finite number of *meso*-scale results obtained from the thermo-mechanical model is a satisfactory method for generating the input to the *macro*-scale model. However, it is recommended that further work tries to identify an empirical relationship for the transverse and longitudinal residual stress components generated based on the scan vector length and incremental change in scan vector length across layer geometry. This would significantly improve the flexibility and ease of generating the input for complex geometries in the multi-scale method. Additionally, identifying relationships with key laser parameters could provide a further opportunity for optimising the laser scan geometry based on the geometry.

In summary, it is suggested that the multi-scale approach in which the

meso and *macro*-scale analyses are decoupled provides a significant increase in the ability to predict the residual stress and distortion generated in real parts produced by selective laser melting, enabling such factors as scan strategy optimisation for residual stress minimisation to be tackled in an effective and pragmatic manner

Chapter 12

Conclusions and recommendations for future work

In this work, a volumetric hatching method was created, alongside the ability to simulate and manufacture these on SLM machines. This was used in conjunction with a thermo-mechanical finite element model of the selective laser melting process. Using this model, a series of investigations were performed to understand the effect of scan strategy and scan area size on the generation of residual stress in SLM. Additionally, further studies were performed to investigate the role of laser parameters, geometry, and support structures on the SLM process and their effect on the generation of residual stress.

Controlling the thermal history plays a significant role in the generation of transverse residual stresses, and the layout and order of scan vectors has a significant role. Based on the findings in Chapter 7, the design of laser scan strategies should avoid long scan vector lengths and orientate the direction of scan vectors uniformly to produce an isotropic stress field in the component. The size of the hatch regions should be varied appropriately, to sustain a high elevated temperature without causing instability due to overheating in the process. By combining this knowledge, optimising the laser scan strategy could further mitigate the effects of the residual stress and reduce support structure requirements without requiring changes to the SLM machine or design of the part manufactured.

The use of adaptive meshing strategy, in conjunction with the use of HPC facilities, significantly increased the computational throughput for simulating SLM of a single layer. This enabled the simulation of large regions (upwards of 10 x 10 mm),

and the use of support structures in Chapter 10. It also enabled to simulate a large number of laser parameter combinations in Chapter 8 and geometrical test cases in Chapter 9. The parametric study of the laser parameters confirmed the following observations in the literature on the effect on melt-pool geometry:

- An increase in laser scan speed increased the melt pool aspect ratio
- An increase in laser power increased the melt pool width.

The parametric thermo-mechanical analysis revealed that the laser scan speed had the most influence on the magnitude and anisotropy of the residual stresses generated. Varying the hatch distance had little effect on the maximum magnitude of residual stresses generated, but decreasing the hatch distance significantly increased the level of yielding that occurred. The trends observed in the parametric study for the generation of residual stress are in close agreement with experimental measurements found in the literature. This provides further confidence in the thermo-mechanical model.

The study of the geometrical effect on scan strategy, as presented in Chapter 9, revealed the importance of the thermal history on the transverse stresses generated, influenced by the arrangement of scan vectors. The higher magnitude longitudinal stresses had consistent behaviour based on the scan vector length, irrespective of the choice of geometry and the thermal history. It was shown that the laser scan strategy becomes less important for scan vector length beyond the typical 5 mm island sizes, in terms of the magnitude of residual stress generated. Altogether, potentially, this provides a route towards optimising scan strategies at the *meso*-scale, and additionally, developing another heuristic for the multi-scale method.

From the study of the support structures in Chapter 10, it was found the insulating properties of the metal powder used in SLM provide a significant thermal resistance for the dissipation of heat, and caused uniform overheating across the scanned region. In particular, the analysis for both the thin-wall and double gyroid support structures showed localised behaviour, with preferential heat dissipation along the upper surface of the geometry connected with the scanned layer. This study indicated that although there is a localised effect of support structures on the melt pool, the control of residual stresses is largely determined by the ability to dissipate heat. Additionally, lattice structures such as the double gyroid showed localised overheating occurs using short scan vectors repeatedly exposed. Suitable scan strategies need to be developed to account for support structures.

It was identified in the literature, that multi-scale techniques could be used to improve the simulation performance for SLM. A multi-scale methodology was

developed, by combining information from the *meso*-scale obtained from the thermo-mechanical model, and using these to predict the mechanical response of a *macro*-scale part. This approach used the assumption that *meso*-scale regions in island scan strategies behave independently from each other. This assumption was verified by comparing with a thermo-mechanical analysis. This multi-scale method was applied to a 3D structure and also to a complex 2D geometrical shape. Performing the multi-scale analyses has verified that the proposed technique of superposition of *meso*-scale stress fields at the *macro*-scale is a valid technique. The main strengths of the proposed method is the decoupling of the *meso* and *macro* scale analyses. This has the benefits that:

1. The computational cost of the macro-scale analysis is independent of the complexity of the meso-scale analysis
2. A *meso*-scale analysis for a particular hatch scan needs only to be performed once, with the results then available to be used in any number of macro-scale analyses using that particular hatch scan.

These strengths translate into large computational time savings and also great flexibility, both in enabling added complexity to be included in the *meso*-scale analysis without affecting the *macro*-scale analysis and in utilising the results from a library of *meso*-scale analyses to investigate a wide range of *macro*-scale scenarios. Furthermore, the *multi*-scale approach is adaptable and can be further extended by adding a micro-scale analysis to inform the *meso*-scale analysis or further extending the macro-scale approach to enable large structure analysis.

12.1 Recommendation for future work

All studies performed using the thermo-mechanical model were limited to single layer, by the adaptive mesh refinement scheme chosen developed, as discussed in Section 6.3.3. This limits the ability to investigate the process across multiple-layers, including the intra-layer interactions of residual stress. In future, this could be achieved by storing the previous state variable, stress fields and plastic strain fields for a scanned layer, and then incorporating these into a subsequent analysis step using a scheme similar to that defined in Section 6.3.4.

Other methods for improving simulation throughput such as the use of GL analysis, super elements and background meshes could be explored, to extend the method across multiple-layers. However, for the aims of this research, the adaptive meshing scheme in-conjunction with the HPC facilities was found to be a satisfactory method for simulating large enough single layer regions.

Similarly, the multi-layer behaviour in the multi-scale method needs further investigation to determine the effect of combining multiple layers on the stress distribution, and examining if the thermal boundary conditions change according to the build position due to the accumulation of heat. If no substantial effect could be found, this potentially will lead to further performance gains, and improvements such as the use of unstructured meshes for the macro-scale analysis.

The multi-scale framework could potentially be extended downwards towards the micro-scale, which accounts for the interaction between the irradiation of the laser onto individual powder particles and the thermo-fluidic physics within the melt pool. Using a detailed micro-scale model would significantly improve the accuracy and information available from the multi-scale analysis without affecting the complexity of the model at the macro-scale. Accuracy in the thermo-mechanical model for modelling the *meso*-scale could be improved by factoring the effective heat transfer, and temperature distribution within the melt pool as a result of modelling the complex thermo-fluids within the melt pool, and more effective modelling of the laser irradiation within a powder-bed. Other information such as surface roughness could be inferred, and stochastic qualities such as the creation of defects (pores, voids) could enable the prediction of failure modes during manufacture and during part utilisation.

Applying the multi-scale methodology to more complex geometries, encountered in AM, remains a challenge. Further work is needed to provide a satisfactory method for mapping between the laser scan geometry and the *meso*-scale regions, which do not rely on the bounding box approach implement. This should account for a library of *meso*-scale cases, to better represent the overall layer geometry. Additionally, the 3D test cases used were simple geometries, and complex geometries will result in overhang and supported regions being present requiring attention. Further work is needed to incorporate the findings from thermo-mechanical studies on the effect of support material, and modelling more complex geometries in 3D models.

Bibliography

- [1] M. Baumers, C. Tuck, R. Wildman, I. Ashcroft, and R. Hague. “Shape Complexity and Process Energy Consumption in Electron Beam Melting: A Case of Something for Nothing in Additive Manufacturing?” In: *Journal of Industrial Ecology* 20.1 (Jan. 2016), n/a–n/a. DOI: 10.1111/jiec.12397.
- [2] N. Hopkinson, R. Hague, and P. Dickens. *Rapid manufacturing: an industrial revolution for the digital age*. John Wiley & Sons, 2006.
- [3] D. Brackett, I. Ashcroft, and R. Hague. “Topology optimization for additive manufacturing”. In: *Solid Freeform Fabrication Symposium*. 2011, pp. 348–362.
- [4] A. Aremu, I. Ashcroft, R. Wildman, R. Hague, C. Tuck, and D. Brackett. “The Effects of Bidirectional Evolutionary Structural Optimization Parameters on an Industrial Designed Component for Additive Manufacture”. In: *Proceedings of the Institution of Mechanical Engineers, Part B: Journal of Engineering Manufacture* 227.6 (2013), pp. 794–807. DOI: 10.1177/0954405412463857.
- [5] I. Maskery, A. O. Aremu, M. Simonelli, C. Tuck, R. D. Wildman, I. A. Ashcroft, and R. J. M. Hague. “Mechanical Properties of Ti-6Al-4V Selectively Laser Melted Parts with Body-Centred-Cubic Lattices of Varying cell size”. In: *Experimental Mechanics* (2015), pp. 1–12. DOI: 10.1007/s11340-015-0021-5.
- [6] R. Frykholm, Y. Takeda, B.-g. Andersson, and R. Carlström. “Solid State Sintered 3-D Printing Component by Using Inkjet (Binder) Method”. In: 63.7 (2016), pp. 421–426.
- [7] XJET. *XJET Nanoparticle Jetting*.
- [8] E. Saleh, J. Vaithilingam, C. Tuck, R. Wildman, I. Ashcroft, R. Hague, and P. Dickens. “3D inkjet printing of conductive structures using in-situ IR sintering”. In: *Proceedings of the 26th Solid Freeform Fabrication*

- Symposium*. 2015. DOI: 10.1017/CB09781107415324.004. arXiv: arXiv:1011.1669v3.
- [9] A. Gasper, S. Catchpole-Smith, and A. Clare. “In-situ synthesis of titanium aluminides by direct metal deposition”. In: *Journal of Materials Processing Technology* 239 (2017), pp. 230–239. DOI: 10.1016/j.jmatprotec.2016.08.031.
- [10] T. Amine, J. W. Newkirk, and F. Liou. “An investigation of the effect of direct metal deposition parameters on the characteristics of the deposited layers”. In: *Case Studies in Thermal Engineering* 3 (2014), pp. 21–34. DOI: 10.1016/j.csite.2014.02.002.
- [11] ASTM. “ASTM F2924-14, Standard Specification for Additive Manufacturing Titanium-6 Aluminum-4 Vanadium with Powder Bed Fusion”. In: *ASTM Standards* 10.04 (2014). DOI: 10.1520/F2924.
- [12] B. E. Stucker, T. L. Starr, and T. J. Gornet. *Powder Bed Fusion Systems, Apparatus, and Processes for Multi-Material Part Production*. Sept. 2014.
- [13] M. Van Elsen. *Complexity of Selective Laser Melting: a new optimisation approach*. 2007.
- [14] L. E. Murr, E. V. Esquivel, S. A. Quinones, S. M. Gaytan, M. I. Lopez, E. Y. Martinez, F. Medina, D. H. Hernandez, E. Martinez, J. L. Martinez, S. W. Stafford, D. K. Brown, T. Hoppe, W. Meyers, U. Lindhe, and R. B. Wicker. “Microstructures and mechanical properties of electron beam-rapid manufactured Ti-6Al-4V biomedical prototypes compared to wrought Ti-6Al-4V”. In: *Materials Characterization* 60.2 (2009), pp. 96–105. DOI: 10.1016/j.matchar.2008.07.006.
- [15] R. B. Eane. “Metal Powder Effects on Selective Laser Sintering”. PhD thesis. University of Leeds, 2002, p. 236.
- [16] M. Simonelli, C. Tuck, N. T. Aboulkhair, I. Maskery, I. Ashcroft, R. D. Wildman, and R. Hague. “A Study on the Laser Spatter and the Oxidation Reactions During Selective Laser Melting of 316L Stainless Steel, Al-Si10-Mg, and Ti-6Al-4V”. In: *Metallurgical and Materials Transactions A* (2015). DOI: 10.1007/s11661-015-2882-8.
- [17] N. K. Tolochko, Y. V. Khlopkov, S. E. Mozzharov, M. B. Ignatiev, T. Laoui, and V. I. Titov. “Absorptance of powder materials suitable for laser sintering”. In: *Rapid Prototyping Journal* 6.3 (2000), pp. 155–161. DOI: 10.1108/13552540010337029.

- [18] E. Uhlmann, A. Bergmann, and W. Gridin. “Investigation on Additive Manufacturing of Tungsten Carbide-cobalt by Selective Laser Melting”. In: *Procedia CIRP* 35 (2015), pp. 8–15. DOI: 10.1016/j.procir.2015.08.060.
- [19] B. Liu. “Further Process Understanding and Prediction on Selective Laser Melting of Stainless Steel 316L”. PhD thesis. University of Loughborough, 2013.
- [20] K. Kempen. “Expanding the materials palette for Selective Laser Melting of metals”. PhD thesis. KU Leuven, 2015.
- [21] A. S. Wu, D. W. Brown, M. Kumar, G. F. Gallegos, and W. E. King. “An Experimental Investigation into Additive Manufacturing-Induced Residual Stresses in 316L Stainless Steel”. In: *Metallurgical and Materials Transactions A: Physical Metallurgy and Materials Science* 45.13 (2014), pp. 6260–6270. DOI: 10.1007/s11661-014-2549-x.
- [22] I. Yadroitsev, L. Thivillon, P. Bertrand, and I. Smurov. “Strategy of manufacturing components with designed internal structure by selective laser melting of metallic powder”. In: *Applied Surface Science* 254.4 (Dec. 2007), pp. 980–983. DOI: 10.1016/j.apsusc.2007.08.046.
- [23] J. P. Kruth, G. Levy, F. Klocke, and T. H. C. Childs. “Consolidation phenomena in laser and powder-bed based layered manufacturing”. In: *CIRP Annals - Manufacturing Technology* 56.2 (2007), pp. 730–759. DOI: <http://dx.doi.org/10.1016/j.cirp.2007.10.004>.
- [24] A. V. Gusarov and I. Smurov. “Modeling the interaction of laser radiation with powder bed at selective laser melting”. In: *Physics Procedia* 5 (Jan. 2010), pp. 381–394. DOI: 10.1016/j.phpro.2010.08.065.
- [25] X. C. Wang, T. Laoui, J. Bonse, J. P. Kruth, B. Lauwers, and L. Froyen. “Direct Selective Laser Sintering of Hard Metal Powders: Experimental Study and Simulation”. In: *The International Journal of Advanced Manufacturing Technology* 19.5 (2002), pp. 351–357. DOI: 10.1007/s001700200024.
- [26] D. Rosenthal. “The theory of moving sources of heat and its application to metal treatments”. In: *Transaction of the American Society of Mechanical Engineers* 68 (1946), pp. 849–866.
- [27] J. F. Ready. *Effects of High Power Laser Radiation*. New York, London: Academic Press, 1971.
- [28] J. Goldak, A. Chakravarti, and M. Bibby. “A new finite element model for welding heat sources”. English. In: *Metallurgical Transactions B* 15.2 (1984), pp. 299–305. DOI: 10.1007/BF02667333.

- [29] S. Kolossov, E. Boillat, R. Glardon, P. Fischer, and M. Locher. “3D FE simulation for temperature evolution in the selective laser sintering process”. In: *International Journal of Machine Tools and Manufacture* 44.2-3 (Feb. 2004), pp. 117–123. DOI: 10.1016/j.ijmactools.2003.10.019.
- [30] K. Zeng, D. Pal, N. Patil, and B. Stucker. “A New Dynamic Mesh Method Applied to the Simulation of Selective Laser Melting”. In: *24th Proceedings of the Solid Freeform Fabrication Symposium*. Austin, Texas, 2013, pp. 549–559.
- [31] A. M. Prokhorov, V. I. Konov, I. Ursu, and I. N. Mihailescu. *Laser Heating of Metals*. Bristol, Philadelphia.: Hilger Bristol, 1990.
- [32] A. V. Gusarov and E. Kovalev. “Model of thermal conductivity in powder beds”. In: *Physical Review B* 80.2 (July 2009), p. 024202. DOI: 10.1103/PhysRevB.80.024202.
- [33] F. Verhaeghe, T. Craeghs, J. Heulens, and L. Pandelaers. “A pragmatic model for selective laser melting with evaporation”. In: *Acta Materialia* 57.20 (Dec. 2009), pp. 6006–6012. DOI: 10.1016/j.actamat.2009.08.027.
- [34] N. E. Hodge, R. M. Ferencz, and J. M. Solberg. “Implementation of a thermomechanical model for the simulation of selective laser melting”. In: *Computational Mechanics* 54.1 (Apr. 2014), pp. 33–51. DOI: 10.1007/s00466-014-1024-2.
- [35] T. Lee, M. Leok, and N. H. McClamroch. “Geometric numerical integration for complex dynamics of tethered spacecraft”. In: *Proceedings of the 2011 American Control Conference* March (2011), pp. 1885–1891. DOI: 10.1002/nme. arXiv: 1010.1724.
- [36] T. Laoui, X. Wang, and J.-P. Kruth. “Laser Penetration in a powder bed during selective laser sintering of metal powders: simulation versus experiments”. In: *Proceedings of the 11th Annual International Solid Freeform Fabrication Symposium* (2000).
- [37] C. D. Boley, S. A. Khairallah, and A. M. Rubenchik. “Calculation of laser absorption by metal powders in additive manufacturing.” In: *Applied optics* 54.9 (2015), pp. 2477–82. DOI: 10.1364/AO.54.002477.
- [38] R. Rai, J. W. Elmer, T. a. Palmer, and T. DebRoy. “Heat transfer and fluid flow during keyhole mode laser welding of tantalum, Ti-6Al-4V, 304L stainless steel and vanadium”. In: *Journal of Physics D: Applied Physics* 40.18 (2007), pp. 5753–5766. DOI: 10.1088/0022-3727/40/18/037.

- [39] D. A. G. Bruggeman. “Berechnung verschiedener physikalischer Konstanten von heterogenen Substanzen. I. Dielektrizitätskonstanten und Leitfähigkeiten der Mischkörper aus isotropen Substanzen”. In: *Annalen der Physik* 416.7 (Jan. 1935), pp. 636–664. DOI: 10.1002/andp.19354160705.
- [40] R. E. Meredith and C. W. Tobias. “Conductivities in emulsions”. In: *Journal of the Electrochemical Society* 108.3 (1961), pp. 286–290.
- [41] Y. C. Chiew and E. D. Glandt. “The effect of structure on the conductivity of a dispersion”. In: *Journal of Colloid and Interface Science* 94.1 (1983), pp. 90–104.
- [42] S. Yagi and D. Kunii. “Studies on effective thermal conductivities in packed beds”. In: *Journal of American Institute of Chemical Engineers* 3.3 (1957), pp. 373–381.
- [43] P. Zehner and E. U. Schlünder. “Die effektive Wärmeleitfähigkeit durchströmter Kugelschüttungen bei mäßigen und hohen Temperaturen”. In: *Chemie Ingenieur Technik* 45.5 (1973), pp. 272–276.
- [44] S. S. Sih and J. W. Barlow. “The Prediction of the Thermal Conductivity of Powders”. In: *Proceedings of the 6th Solid Freeform Fabrication Symposium*. Austin, Texas, 1995.
- [45] F. Klocke, C. Wagner, and F. Klocke. “Coalescence Behaviour of Two Metallic Particles as Base Mechanism of Selective Laser Sintering”. In: *CIRP Annals - Manufacturing Technology* 52.1 (2003), pp. 177–180. DOI: 10.1016/S0007-8506(07)60559-9.
- [46] E. Attar. “Simulation of Selective Electron Beam Melting Processes”. PhD thesis. University of Erlangen-Nurnberg, 2011.
- [47] M. Ashby. “A first report on sintering diagrams”. In: *Acta Metallurgica* 22.3 (Mar. 1974), pp. 275–289. DOI: 10.1016/0001-6160(74)90167-9.
- [48] N. K. Tolochko, M. K. Arshinov, A. V. Gusarov, V. I. Titov, T. Laoui, and L. Froyen. “Mechanisms of selective laser sintering and heat transfer in Ti powder”. In: *Rapid Prototyping Journal* 9.5 (2003), pp. 314–326. DOI: 10.1108/13552540310502211.
- [49] G. C. Kuczynski. “Self-Diffusion in Sintering of Metallic Particles”. In: *Sintering Key Papers*. Dordrecht: Springer Netherlands, 1990, pp. 509–527. DOI: 10.1007/978-94-009-0741-6_33.
- [50] O. Pokluda, C. T. Bellehumeur, and J. Vlachopoulos. “Modification of Frenkel’s model for sintering”. In: *AIChE Journal* 43.12 (Dec. 1997), pp. 3253–3256. DOI: 10.1002/aic.690431213.

- [51] I. Yadroitsev, A. Gusarov, I. Yadroitsava, and I. Smurov. "Single track formation in selective laser melting of metal powders". In: *Journal of Materials Processing Technology* 210.12 (Sept. 2010), pp. 1624–1631. DOI: 10.1016/j.jmatprotec.2010.05.010.
- [52] S. Chandrasekhar. *Hydrodynamic and Hydromagnetic Stability*. 1st. Dover Publications, 1962, p. 704.
- [53] I. Yadroitsev, N. K. Tolochko, S. E. Mozzharov, I. A. Yadroitsev, T. Laoui, L. Froyen, V. I. Titov, and M. B. Ignatiev. "Balling processes during selective laser treatment of powders Balling processes during selective laser treatment of powders". In: April (2004). DOI: 10.1108/13552540410526953.
- [54] M. Rombouts, J. P. Kruth, L. Froyen, and P. Mercelis. "Fundamentals of selective laser melting of alloyed steel powders". In: *CIRP Annals - Manufacturing Technology* 55.1 (2006), pp. 187–192. DOI: 10.1016/S0007-8506(07)60395-3.
- [55] Y. P. Lei, H. Murakawa, Y. W. Shi, and X. Y. Li. "Numerical analysis of the competitive influence of Marangoni flow and evaporation on heat surface temperature and molten pool shape in laser surface remelting". In: *Computational Materials Science* 21 (2001), pp. 276–290.
- [56] C. Zhao and I. M. Richardson. "Complex flow motions during laser welding". In: *40th American Institute of Aeronautics and Astronautics, Plasmadynamics and Lasers Conference*. San Antonio, Texas, 2009, pp. 1–7.
- [57] C. X. Zhao, C. Kwakernaak, Y. Pan, I. M. Richardson, Z. Saldi, S. Kenjeres, and C. R. Kleijn. "The effect of oxygen on transitional Marangoni flow in laser spot welding". In: *Acta Materialia* 58.19 (2010), pp. 6345–6357. DOI: 10.1016/j.actamat.2010.07.056.
- [58] N. T. Aboulkhair, N. M. Everitt, I. Ashcroft, and C. Tuck. "Reducing porosity in AlSi10Mg parts processed by selective laser melting". In: *Additive Manufacturing* 1-4 (2014), pp. 77–86. DOI: 10.1016/j.addma.2014.08.001.
- [59] D. R. Poirier and Geiger G. H. *Transport Phenomena in Materials Processing*. John Wiley & Sons, 2010, p. 670.
- [60] R. Choo and J. Szekely. "Vaporization kinetics and surface temperature in a mutually coupled spot gas tungsten arc weld and weld pool". In: *Welding Journal(USA)* (1992), pp. 77–93.
- [61] A. Block-Bolten and T. W. Eagar. "Metal vaporization from weld pools". In: *Metallurgical Transactions B* 15.3 (1984), pp. 461–469. DOI: 10.1007/BF02657376.

- [62] V. Juechter, T. Scharowsky, R. Singer, C. Körner, W.-S. Lee, C.-F. Lin, J. J. Z. Li, W. L. Johnson, W. K. Rhim, A. Crespo, P. Nie, O. a. Ojo, and Z. Li. “High-temperature deformation behaviour of Ti6Al4V alloy evaluated by high strain-rate compression tests”. In: *Acta Materialia* 77.11 (Sept. 2014), pp. 252–258. DOI: 10.1063/1.2349840.
- [63] C. Qiu, C. Panwisawas, M. Ward, H. C. Basoalto, J. W. Brooks, and M. M. Attallah. “On the role of melt flow into the surface structure and porosity development during selective laser melting”. In: *Acta Materialia* 96. August (2015), pp. 72–79. DOI: 10.1016/j.actamat.2015.06.004.
- [64] D. Bäuerle. *Laser Processing and Chemistry*. Berlin, Heidelberg: Springer Berlin Heidelberg, 2011. DOI: 10.1007/978-3-642-17613-5.
- [65] W. E. King, H. D. Barth, V. M. Castillo, G. F. Gallegos, J. W. Gibbs, D. E. Hahn, C. Kamath, and A. M. Rubenchik. “Observation of keyhole-mode laser melting in laser powder-bed fusion additive manufacturing”. In: *Journal of Materials Processing Technology* 214.12 (2014), pp. 2915–2925. DOI: 10.1016/j.jmatprotec.2014.06.005.
- [66] H. Zhao, W. Niu, B. Zhang, Y. Lei, M. Kodama, and T. Ishide. “Modelling of keyhole dynamics and porosity formation considering the adaptive keyhole shape and three-phase coupling during deep-penetration laser welding”. In: *Journal of Physics D: Applied Physics* 44 (2011), p. 485302. DOI: 10.1088/0022-3727/44/48/485302.
- [67] S. A. Khairallah, A. T. Anderson, A. Rubenchik, and W. E. King. “Laser powder-bed fusion additive manufacturing: Physics of complex melt flow and formation mechanisms of pores, spatter, and denudation zones”. In: *Acta Materialia* 108 (2016), pp. 36–45. DOI: 10.1016/j.actamat.2016.02.014. arXiv: arXiv:1011.1669v3.
- [68] H. Nakamura, Y. Kawahito, K. Nishimoto, and S. Katayama. “Elucidation of melt flows and spatter formation mechanisms during high power laser welding of pure titanium”. In: *Journal of Laser Applications* 27.3 (2015), p. 032012. DOI: 10.2351/1.4922383.
- [69] M. Megahed, H.-W. Mindt, N. N’Dri, H. Duan, and O. Desmaison. “Metal additive-manufacturing process and residual stress modeling”. In: *Integrating Materials and Manufacturing Innovation* 5.1 (Dec. 2016), p. 4. DOI: 10.1186/s40192-016-0047-2.
- [70] M. J. Matthews, G. Guss, S. A. Khairallah, A. M. Rubenchik, P. J. Depond, and W. E. King. “Denudation of metal powder layers in laser powder bed fusion processes”. In: *Acta Materialia* 114 (2016), pp. 33–42. DOI: 10.1016/j.actamat.2016.05.017.

- [71] L. Thijs, K. Kempen, J. P. Kruth, and J. Van Humbeeck. “Fine-structured aluminium products with controllable texture by selective laser melting of pre-alloyed AlSi10Mg powder”. In: *Acta Materialia* 61.5 (2013), pp. 1809–1819. DOI: 10.1016/j.actamat.2012.11.052.
- [72] X. Su and Y. Yang. “Research on track overlapping during Selective Laser Melting of powders”. In: *Journal of Materials Processing Technology* 212.10 (2012), pp. 2074–2079. DOI: 10.1016/j.jmatprotec.2012.05.012.
- [73] S. A. Khairallah and A. Anderson. “Mesoscopic simulation model of selective laser melting of stainless steel powder”. In: *Journal of Materials Processing Technology* 214.11 (Nov. 2014), pp. 2627–2636. DOI: 10.1016/j.jmatprotec.2014.06.001.
- [74] B. Vrancken, R. Wauthle, J. Kruth, and J. V. Humbeeck. “Study on the influence of material properties on residual stress in selective laser melting”. In: *Proceedings of the 24th Solid Freeform Fabrication Symposium*. Austin, Texas, 2013.
- [75] M. Torres. “An evaluation of shot peening, residual stress and stress relaxation on the fatigue life of AISI 4340 steel”. In: *International Journal of Fatigue* 24.8 (2002), pp. 877–886. DOI: 10.1016/S0142-1123(01)00205-5.
- [76] V. F. Terent’ev, M. S. Michugina, A. G. Kolmakov, V. Kvedaras, V. Čiuplys, A. Čiuplys, and J. Vilys. “The effect of nitriding on fatigue strength of structural alloys”. In: *Mechanika* 64.2 (2007), pp. 12–22.
- [77] P. Mercelis and J.-P. Kruth. “Residual stresses in selective laser sintering and selective laser melting”. In: *Rapid Prototyping Journal* 12.5 (Oct. 2006), pp. 254–265. DOI: 10.1108/13552540610707013.
- [78] J. Kruth, L. Froyen, J. Van Vaerenbergh, P. Mercelis, M. Rombouts, and B. Lauwers. “Selective laser melting of iron-based powder”. In: *Journal of Materials Processing Technology* 149.1-3 (June 2004), pp. 616–622. DOI: 10.1016/j.jmatprotec.2003.11.051.
- [79] G. S. Schajer. *Practical residual stress measurement methods*. English. Chichester, UK: John Wiley & Sons, 2013.
- [80] K. Mumtaz, P. Vora, and N. Hopkinson. “A Method to Eliminate Anchors/Supports from Directly Laser Melted Metal Powder Bed Processes”. In: *Proceedings of the 22nd Annual International Solid Freeform Fabrication Symposium*. Austin, Texas, 2011, pp. 55–64.

- [81] D. Tomus, T. Jarvis, X. Wu, J. Mei, P. Rometsch, E. Herny, J. F. Rideau, and S. Vaillant. “Controlling the microstructure of Hastelloy-X components manufactured by Selective Laser Melting”. In: *Physics Procedia* 41.0 (2013), pp. 823–827. DOI: 10.1016/j.phpro.2013.03.154.
- [82] M. Garibaldi, I. Ashcroft, M. Simonelli, and R. Hague. “Metallurgy of high-silicon steel parts produced using Selective Laser Melting”. In: *Acta Materialia* 110.May (May 2016), pp. 207–216. DOI: 10.1016/j.actamat.2016.03.037.
- [83] R. J. Moat, A. J. Pinkerton, L. Li, P. J. Withers, and M. Preuss. “Residual stresses in laser direct metal deposited Waspaloy”. In: *Materials Science and Engineering A* 528.6 (2011), pp. 2288–2298. DOI: 10.1016/j.msea.2010.12.010.
- [84] N. J. Harrison, I. Todd, and K. Mumtaz. “Reduction of micro-cracking in nickel superalloys processed by Selective Laser Melting: A fundamental alloy design approach”. In: *Acta Materialia* 94 (2015), pp. 59–68. DOI: 10.1016/j.actamat.2015.04.035.
- [85] A. Vasinonta, J. L. Beuth, and M. Griffith. “Process Maps for Predicting Residual Stress and Melt Pool Size in the Laser-Based Fabrication of Thin-Walled Structures”. In: *Journal of Manufacturing Science and Engineering* 129.1 (2007), pp. 101–109. DOI: 10.1115/1.2335852.
- [86] H. Pohl, A. Simchi, M. Issa, and H. Dias. “Thermal stresses in direct metal laser sintering”. In: *Proceedings of the 12th Solid Freeform Fabrication Symposium*. Austin, Texas, 2001, pp. 366–372.
- [87] B. Vrancken. “Study of Residual Stresses in Selective Laser Melting”. PhD thesis. KU Leuven, 2016.
- [88] M. Simonelli, Y. Tse, and C. Tuck. “Effect of the build orientation on the mechanical properties and fracture modes of SLM Ti-6Al-4V”. In: *Materials Science and Engineering: A* 616 (2014), pp. 1–11. DOI: 10.1016/j.msea.2014.07.086.
- [89] C. Hauser, T. Childs, C. Taylor, and M. Badrossamay. “Direct Selective Laser Sintering of Tool Steel Powders to High Density. Part A: Effects of Laser Beam Width and Scan Strategy”. In: *Proceedings of the 14th Solid Freeform Fabrication Symposium*. Austin, Texas, 2003, p. 12.
- [90] J.-P. Kruth, J. Deckers, E. Yasa, and R. Wauthle. “Assessing and comparing influencing factors of residual stresses in selective laser melting using a novel analysis method”. In: *Proceedings of the Institution of Mechanical Engineers, Part B: Journal of Engineering Manufacture* 226.6 (June 2012), pp. 980–991. DOI: 10.1177/0954405412437085.

- [91] A. H. Nickel, D. M. Barnett, and F. B. Prinz. “Thermal stresses and deposition patterns in layered manufacturing”. In: *Materials Science and Engineering: A* 317.1-2 (2001), pp. 59–64. DOI: 10.1016/S0921-5093(01)01179-0.
- [92] B. Qian, Y. S. Shi, Q. S. Wei, and H. B. Wang. “The helix scan strategy applied to the selective laser melting”. In: *International Journal of Advanced Manufacturing Technology* 63.5-8 (2012), pp. 631–640. DOI: 10.1007/s00170-012-3922-9.
- [93] J. Yang, H. Bin, X. Zhang, and Z. Liu. “Fractal scanning path generation and control system for selective laser sintering (SLS)”. In: *International Journal of Machine Tools and Manufacture* 43.3 (2003), pp. 293–300. DOI: 10.1016/S0890-6955(02)00212-2.
- [94] L. Ma and H. Bin. “Temperature and stress analysis and simulation in fractal scanning-based laser sintering”. In: *The International Journal of Advanced Manufacturing Technology* 34.9-10 (2006), pp. 898–903. DOI: 10.1007/s00170-006-0665-5.
- [95] S. Catchpole-Smith, N. Aboulkhair, L. Parry, C. Tuck, I. A. Ashcroft, and A. Clare. “Fractal scan strategies for selective laser melting of ‘unweldable’ nickel superalloys”. In: *Additive Manufacturing* 15 (2017), pp. 113–122. DOI: 10.1016/j.addma.2017.02.002.
- [96] M. Shiomi, K. Osakada, K. Nakamura, T. Yamashita, and F. Abe. “Residual Stress within Metallic Model Made by Selective Laser Melting Process”. In: *Annals of the CIRP* 53.1 (2004), pp. 195–198. DOI: 10.1016/S0007-8506(07)60677-5.
- [97] X. P. Li, C. W. Kang, H. Huang, and T. B. Sercombe. “The role of a low-energy-density re-scan in fabricating crack-free Al85Ni5Y6Co2Fe2 bulk metallic glass composites via selective laser melting”. In: *Materials and Design* 63 (2014), pp. 407–411. DOI: 10.1016/j.matdes.2014.06.022.
- [98] N. W. Klingbeil, J. L. Beuth, R. K. Chin, and C. H. Amon. “Measurement and Modeling of Residual Stress-Induced Warping in Direct Metal Deposition Processes”. In: *Proceedings of the 9th Solid Freeform Fabrication Symposium*. 1998. Austin, Texas, 1998, pp. 367–374.
- [99] D. Buchbinder, W. Meiners, N. Pirch, K. Wissenbach, and J. Schrage. “Investigation on reducing distortion by preheating during manufacture of aluminum components using selective laser melting”. In: *Journal of Laser Applications* 26.1 (2014), p. 012004. DOI: 10.2351/1.4828755.

- [100] A. Vasinonta and J. Beuth. “Process Maps for Controlling Residual Stress and Melt Pool Size in Laser-Based SFF Processes”. In: *Proceedings of the 11th Solid Freeform Fabrication Symposium*. Austin, Texas, 2000, pp. 200–208.
- [101] F. Abe, K. Osakada, M. Shiomi, K. Uematsu, and M. Matsumoto. “The manufacturing of hard tools from metallic powders by selective laser melting”. In: *Journal of Materials Processing Technology* 111.1-3 (2001), pp. 210–213. DOI: 10.1016/S0924-0136(01)00522-2.
- [102] P. Aggarangsi, J. L. Beuth, and D. D. Gill. “Transient Changes in Melt Pool Size in Laser Additive Manufacturing Processes”. In: *Proceedings of the 15th Solid Freeform Fabrication Symposium*. Austin, Texas, 2004, pp. 163–174.
- [103] I. Yadroitsev and I. Smurov. “Selective laser melting technology: From the single laser melted track stability to 3D parts of complex shape”. In: *Physics Procedia* 5.Part 2 (2010), pp. 551–560. DOI: 10.1016/j.phpro.2010.08.083.
- [104] P. Edwards and M. Ramulu. “Fatigue Performance Evaluation of Selective Laser Melted Ti-6Al-4V”. In: *Materials Science and Engineering: A* 598 (Jan. 2014), pp. 327–337. DOI: 10.1016/j.msea.2014.01.041.
- [105] D. Thomas. “The Development of Design Rules for Selective Laser Melting The Development of Design Rules for Selective Laser Melting”. PhD thesis. University of Wales, 2009.
- [106] T. M. Mower and M. J. Long. “Mechanical behavior of additive manufactured, powder-bed laser-fused materials”. In: *Materials Science and Engineering A* 651 (2016), pp. 198–213. DOI: 10.1016/j.msea.2015.10.068.
- [107] M. Simonelli, Y. Y. Tse, and C. Tuck. “On the texture formation of selective laser melted Ti-6Al-4V”. In: *Metallurgical and Materials Transactions A: Physical Metallurgy and Materials Science* 45.June (2014), pp. 2863–2872. DOI: 10.1007/s11661-014-2218-0.
- [108] I. Yadroitsev, P. Bertrand, and I. Smurov. “Parametric analysis of the selective laser melting process”. In: *Applied Surface Science* 253.19 (July 2007), pp. 8064–8069. DOI: 10.1016/j.apsusc.2007.02.088.
- [109] S. Dadbakhsh, L. Hao, and N. Sewell. “Effect of selective laser melting layout on the quality of stainless steel parts”. In: *Rapid Prototyping Journal* 18.3 (2012), pp. 241–249.

- [110] S. Tammas-Williams, P. Withers, I. Todd, and P. Prangnell. “Porosity regrowth during heat treatment of hot isostatically pressed additively manufactured titanium components”. In: *Scripta Materialia* 122 (2016), pp. 72–76. DOI: 10.1016/j.scriptamat.2016.05.002.
- [111] B. Song, S. Dong, B. Zhang, H. Liao, and C. Coddet. “Effects of processing parameters on microstructure and mechanical property of selective laser melted Ti6Al4V”. In: *Materials and Design* 35 (Mar. 2012), pp. 120–125. DOI: 10.1016/j.matdes.2011.09.051.
- [112] J. Kruth, J. Deckers, and E. Yasa. “Experimental Investigation of Laser Surface Remelting for the Improvement of Selective Laser Melting Process”. In: *Proceedings of the 19th Solid Freeform Fabrication Symposium*. Austin, Texas, 2008.
- [113] E. Yasa and J. Kruth. “Application of Laser Re-Melting on Selective Laser Melting Parts”. In: *Advances in Production Engineering & Management* 6.4 (2011), pp. 259–270.
- [114] R. H. Morgan, A. J. Papworth, C. Sutcliffe, P. Fox, and W. O’neill. “High density net shape components by direct laser re-melting of single-phase powders”. In: *Journal of Materials Science* 37.15 (2002), pp. 3093–3100. DOI: 10.1023/A:1016185606642.
- [115] A. Lamikiz, J. Sánchez, L. López de Lacalle, and J. Arana. “Laser polishing of parts built up by selective laser sintering”. In: *International Journal of Machine Tools and Manufacture* 47.12-13 (Oct. 2007), pp. 2040–2050. DOI: 10.1016/j.ijmactools.2007.01.013.
- [116] M. A. Pinto, N. Cheung, M. C. F. Ierardi, and A. Garcia. “Microstructural and hardness investigation of an aluminum–copper alloy processed by laser surface melting”. In: *Materials Characterization* 50.2-3 (Mar. 2003), pp. 249–253. DOI: 10.1016/S1044-5803(03)00091-3.
- [117] C. Körner, A. Bauereiß, and E. Attar. “Fundamental consolidation mechanisms during selective beam melting of powders”. In: *Modelling and Simulation in Materials Science and Engineering* 21.8 (2013), p. 085011. DOI: 10.1088/0965-0393/21/8/085011.
- [118] J. Nelson, S. Xue, and J. Barlow. “Model of the selective laser sintering of bisphenol-A polycarbonate”. In: *Journal of Industrial & Engineering Chemistry Research* (1993), pp. 2305–2317.
- [119] F.-J. Gürtler, M. Karg, K.-H. Leitz, and M. Schmidt. “Simulation of Laser Beam Melting of Steel Powders using the Three-Dimensional Volume of Fluid Method”. In: *Physics Procedia* 41 (2013), pp. 881–886. DOI: 10.1016/j.phpro.2013.03.162.

- [120] C. Körner, E. Attar, and P. Heigl. “Mesoscopic simulation of selective beam melting processes”. In: *Journal of Materials Processing Technology* 211.6 (2011), pp. 978–987. DOI: 10.1016/j.jmatprotec.2010.12.016.
- [121] A. Klassen, T. Scharowsky, and C. Körner. “Evaporation model for beam based additive manufacturing using free surface lattice Boltzmann methods”. In: *Journal of Physics D: Applied Physics* 47.27 (July 2014), p. 275303. DOI: 10.1088/0022-3727/47/27/275303.
- [122] C. Körner, A. Bauereiß, and E. Attar. “Fundamental consolidation mechanisms during selective beam melting of powders”. In: *Modelling and Simulation in Materials Science and Engineering* 21.8 (2013), p. 085011. DOI: 10.1088/0965-0393/21/8/085011.
- [123] M. Jamshidinia, F. Kong, and R. Kovacevic. “The Coupled CFD-FEM Model of Electron Beam Melting”. In: *ASME District F - Early Career Technical Conference Proceedings*. Birmingham, USA, 2013.
- [124] K. Dai and L. Shaw. “Thermal and mechanical finite element modeling of laser forming from metal and ceramic powders”. In: *Acta Materialia* 52.1 (Jan. 2004), pp. 69–80. DOI: 10.1016/j.actamat.2003.08.028.
- [125] T. Childs and C. Hauser. “Simulation and experimental verification of crystalline polymer and direct metal selective laser sintering”. In: *Proceedings of the 11th Solid Freeform Fabrication Symposium* (2000), pp. 100–109.
- [126] T. Chen and Y. Zhang. “Three-Dimensional Modeling of Selective Laser Sintering of Two-Component Metal Powder Layers”. In: *Journal of Manufacturing Science and Engineering* 128.1 (2006), p. 299. DOI: 10.1115/1.2122947.
- [127] I. Roberts, C. Wang, R. Esterlein, M. Stanford, and D. Mynors. “A three-dimensional finite element analysis of the temperature field during laser melting of metal powders in additive layer manufacturing”. In: *International Journal of Machine Tools and Manufacture* 49.12-13 (Oct. 2009), pp. 916–923. DOI: 10.1016/j.ijmachtools.2009.07.004.
- [128] M. F. Zaeh and G. Branner. “Investigations on residual stresses and deformations in selective laser melting”. In: *Production Engineering* 4.1 (Feb. 2010), pp. 35–45. DOI: 10.1007/s11740-009-0192-y.
- [129] D. Q. Zhang, Q. Z. Cai, J. H. Liu, L. Zhang, and R. D. Li. “Select laser melting of W–Ni–Fe powders: simulation and experimental study”. In: *The International Journal of Advanced Manufacturing Technology* 51.5-8 (Apr. 2010), pp. 649–658. DOI: 10.1007/s00170-010-2641-3.

- [130] N. Contuzzi, S. L. Campanelli, and A. D. Ludovico. “3D Finite Element Analysis in the selective laser melting process”. In: *International Journal of Simulation Modelling* 10.3 (Sept. 2011), pp. 113–121. DOI: 10.2507/IJSIMM10(3)1.169.
- [131] D. Riedlbauer, P. Steinmann, and J. Mergheim. “Thermomechanical finite element simulations of selective electron beam melting processes: performance considerations”. In: *Computational Mechanics* 54.1 (July 2014), pp. 109–122. DOI: 10.1007/s00466-014-1026-0.
- [132] F. Neugebauer, N. Keller, H. Xu, C. Kober, and V. Ploshikhin. “Simulation of Selective Laser Melting Using Process Specific Layer Based Meshing”. In: *Proceedings of the Fraunhofer Direct Digital Manufacturing Conference*. Bremen Center for Computational Materials Science. Bremen, 2014.
- [133] J. F. Li, L. Li, and F. H. Stott. “Thermal stresses and their implication on cracking during laser melting of ceramic materials”. In: *Acta Materialia* 52.14 (2004), pp. 4385–4398. DOI: 10.1016/j.actamat.2004.06.005.
- [134] F. Neugebauer, N. Keller, H. Xu, C. Kober, and V. Ploshikhin. “Simulation of Selective Laser Melting Using Process Specific Layer Based Meshing”. In: *Proceedings of the Fraunhofer Direct Digital Manufacturing Conference*. 2014.
- [135] N. Keller and V. Ploshikhin. “New Method for Fast Predictions of Residual Stress and Distortion of AM Parts”. In: *Proceedings of the 24th Solid Freeform Fabrication Symposium*. Austin, Texas, 2014, pp. 1229–1237.
- [136] C. Seidel, M. Zaeh, M. Wunderer, J. Weirather, T. Krol, and M. Ott. “Simulation of the Laser Beam Melting Process – Approaches for an Efficient Modelling of the Beam-material Interaction”. In: *Procedia CIRP* 25.C (2014), pp. 146–153. DOI: 10.1016/j.procir.2014.10.023.
- [137] C. Li, Liu J. F., Y. B. Guo, and Z. Y. Li. “A Temperature-Thread Multiscale Modeling Approach for Efficient Prediction of Part Distortion by Selective Laser Melting”. In: *Proceedings of the 26th Annual International Solid Freeform Fabrication Symposium*. Austin, Texas, USA, 2015.
- [138] A. Francois and E. Wyart. “Numerical model for thermal analysis of laser based additive manufacturing processes”. In: *ECCOMAS Congress 2016*. Hersonissos, Crete, 2016, p. 2016.
- [139] F. Wang, W. Liu, Y. Zhao, Y. Lai, and W. Han. “Subarea simulation and distributed computing of direct laser fabrication”. In: *The International Journal of Advanced Manufacturing Technology* (Dec. 2013). DOI: 10.1007/s00170-013-5488-6.

- [140] E. R. Denlinger, J. Irwin, and P. Michaleris. “Thermomechanical Modeling of Additive Manufacturing Large Parts”. In: *Journal of Manufacturing Science and Engineering* 136.6 (Oct. 2014), p. 061007. DOI: 10.1115/1.4028669.
- [141] C. D. Cantwell, D. Moxey, A. Comerford, A. Bolis, G. Rocco, G. Mengaldo, D. De Grazia, S. Yakovlev, J. E. Lombard, D. Ekelschot, B. Jordi, H. Xu, Y. Mohamied, C. Eskilsson, B. Nelson, P. Vos, C. Biotto, R. M. Kirby, and S. J. Sherwin. “Nektar++: An open-source spectral/hp element framework”. In: *Computer Physics Communications* 192 (2015), pp. 205–219. DOI: 10.1016/j.cpc.2015.02.008.
- [142] N. Zander, T. Bog, S. Kollmannsberger, D. Schillinger, and E. Rank. “Multi-level hp-adaptivity: high-order mesh adaptivity without the difficulties of constraining hanging nodes”. In: *Computational Mechanics* 55.3 (2015), pp. 499–517. DOI: 10.1007/s00466-014-1118-x.
- [143] S. Kollmannsberger, A. Özcan, M. Carraturo, N. Zander, and E. Rank. “A high-order accurate computational framework for the simulation of SLM processes”. In: *ECCOMAS Congress 2016*. 2015. Hersonissos, Crete, 2016, p. 2016.
- [144] J. Plews, C. A. Duarte, and T. Eason. “An improved nonintrusive global-local approach for sharp thermal gradients in a standard FEA platform”. In: *International Journal for Numerical Methods in Engineering* 91.4 (2012), pp. 426–449. DOI: 10.1002/nme.
- [145] D. Kim, C. . Duarte, and S. P. Proenca. “A generalized finite element method with global-local enrichment functions for confined plasticity problems”. In: *Computational Mechanics* 50.5 (Mar. 2012), pp. 563–578. DOI: 10.1007/s00466-012-0689-7.
- [146] H. Huang, H. Murakawa, H. Serizawa, and J. Wang. “Development of Thermal Elastic-plastic FEM for Line Heating with”. In: *Quarterly Journal of the Japan Welding Society* 31.4 (2013), pp. 134–137. DOI: <http://dx.doi.org/10.2207/qjws.31.134s>.
- [147] A. Lundbäck. “Modelling and Simulation of Welding and Metal Deposition”. PhD thesis. Luleå University of Technology, 2010, p. 110.
- [148] N. Patil, D. Pal, and B. Stucker. “A New Finite Element Solver using Numerical Eigen Modes for Fast Simulation of Additive Manufacturing Processes”. In: *Proceedings of the 24th Solid Freeform Fabrication Symposium*. Austin, Texas, 2013, pp. 535–548.

- [149] N. Patil. “A novel numerical framework for simulation of multiscale spatio-temporally non-linear systems in additive manufacturing processes .” In: (2014).
- [150] J. A. Turner and R. Dehoff. “Using Simulation to Locally Control Grain Structure in Additively Manufactured Parts”. In: *WCCM 2016*. Vol. 29. 17. Seoul, Korea, 2016, p. 6454. DOI: 10.1557/jmr.2014.140..
- [151] Y. Ueda, K. Fukuda, K. Nakacho, and S. Endo. “A New Measuring Method Finite Element Method”. In: *Transactions of Joining and Welding Research Institute* (1975).
- [152] L. Zhang, P. Michaleris, and P. Marugabandhu. “Evaluation of Applied Plastic Strain Methods for Welding Distortion Prediction”. In: *Journal of Manufacturing Science and Engineering* 129.6 (2007), p. 1000. DOI: 10.1115/1.2716740.
- [153] E. R. Denlinger, J. C. Heigel, and P. Michaleris. “Residual stress and distortion modeling of electron beam direct manufacturing Ti-6Al-4V”. In: *Proceedings of the Institution of Mechanical Engineers, Part B: Journal of Engineering Manufacture* 229.10 (Oct. 2015), pp. 1803–1813. DOI: 10.1177/0954405414539494.
- [154] I. A. Roberts. “Investigation of Residual Stresses in the Laser Melting of Metal Powders in Additive Layer”. PhD thesis. University of Wolverhampton, 2012.
- [155] I. Gibson, D. W. Rosen, and B. Stucker. *Additive Manufacturing Technologies*. Vol. 54. Boston, MA: Springer US, 2010, p. 462. DOI: 10.1007/978-1-4419-1120-9.
- [156] N. A. Alderson. “Thermal Modeling and Simulation of Electron Beam Melting for Rapid Prototyping on Ti6Al4V Alloys”. PhD thesis. North Carolina State University, 2012.
- [157] W. N. Dos Santos, P. Mummery, and A. Wallwork. “Thermal diffusivity of polymers by the laser flash technique”. In: *Polymer Testing* 24.5 (2005), pp. 628–634. DOI: 10.1016/j.polymeresting.2005.03.007.
- [158] M. Boivineau, C. Cagran, D. Doytier, V. Eyraud, M. .-.H. Nadal, B. Wilthan, and G. Pottlacher. “Thermophysical Properties of Solid and Liquid Ti-6Al-4V (TA6V) Alloy”. In: *International Journal of Thermophysics* 27.2 (Mar. 2006), pp. 507–529. DOI: 10.1007/s10765-005-0001-6.
- [159] R. A. Wood, R. J. Favor, and A. F. M. L. (U.S.) *Titanium alloys handbook*. English. Columbus, Ohio: Metals and Ceramics Information Center, 1972.
- [160] G. Rogers and Y. Mayhew. “Thermodynamic and Transport Properties of Fluids”. In: (1995), p. 28. DOI: 10.1038/cddis.2011.1.

- [161] P. Rangaswamy, H. Choo, M. B. Prime, M. A. M. Bourke, and J. M. Larsen. “High Temperature Stress Assessment in SCS-6/Ti-6Al-4V Composite using Neutron Diffraction and Finite Element Modeling”. In: *International Conference on Processing & Manufacturing of Advanced Material*. Los Alamos National Laboratory. Los Alamos, 2000.
- [162] MathWorks. *Matlab*. Natick, Massachusetts, United States., 2016.
- [163] S. F. F. Gibson. “Constrained Elastic SurfaceNets: Generating Smooth Models from Binary Segmented Data”. In: (1999).
- [164] G. Woods, E. Richard, S. L. Eddins, and C. Rafael. *Digital Image processing using MATLAB*. English. Upper Saddle River, N.J.: Pearson Prentice Hall, 2004.
- [165] D. H. Douglas and T. K. Peucker. “Algorithms for the Reduction of the Number of Points Required to Represent a Digitized Line or its Caricature”. In: *Classics in Cartography: Reflections on Influential Articles from Cartographica* 10.2 (2011), pp. 15–28. DOI: 10.1002/9780470669488.ch2.
- [166] A. Johnson. *LibClipper: An open source freeware library for clipping and offsetting lines and polygons*. 2014.
- [167] Materialise. *Magics*. Leuven, Belgium, 2016.
- [168] The Qt Company. *Qt c++ Library*. Espoo, Finland, 2016.
- [169] SLM Solutions. *Melt Pool Monitoring (MPM) System by SLM Solutions*. 2016.
- [170] K.-J. Bathe. *Finite Element Procedures*. Englewood Cliffs, N.J., USA: Prentice Hall, 1996.
- [171] P. Amestoy, I. Duff, and J.-Y. L’Excellent. “Multifrontal parallel distributed symmetric and unsymmetric solvers”. In: *Computer Methods in Applied Mechanics and Engineering* 184.2-4 (Apr. 2000), pp. 501–520. DOI: 10.1016/S0045-7825(99)00242-X.
- [172] O. Schenk and K. Gartner. “Parallel Sparse Direct Solver PARDISO — User Guide”. In: *PARDISO Project 0* (2014), pp. 0–65.
- [173] MSC Software Corporation. *MSC Marc Volume A*. Newport Beach, California, USA, 2015.
- [174] P. Fischer, V. Romano, H. P. Weber, N. P. Karapatis, E. Boillat, and R. Glandon. “Sintering of commercially pure titanium powder with a Nd:YAG laser source”. In: *Acta Materialia* 51 (2003), pp. 1651–1662. DOI: 10.1016/S1359-6454(02)00567-0.

- [175] D. Deng, H. Murakawa, and W. Liang. “Numerical and experimental investigations on welding residual stress in multi-pass butt-welded austenitic stainless steel pipe”. In: *Computational Materials Science* 42.2 (Apr. 2008), pp. 234–244. DOI: 10.1016/j.commatsci.2007.07.009.
- [176] E. Jones, T. Oliphant, and P. Peterson. *SciPy: Open source scientific tools for Python*. 2001.
- [177] D. Riedlbauer. “Thermomechanical Modelling and Simulation of Electron Beam Melting”. PhD thesis. University of Erlangen-Nürnberg, 2011.
- [178] K. Zeng, D. Pal, C. Teng, and B. E. Stucker. “Evaluations of effective thermal conductivity of support structures in selective laser melting”. In: *Additive Manufacturing* 6 (2015), pp. 67–73. DOI: 10.1016/j.addma.2015.03.004.
- [179] M. Nikoukar, N. Patil, D. Pal, and B. Stucker. “Methods for Enhancing the Speed of Numerical Calculations for the Prediction of the Mechanical Behavior of Parts Made Using Additive Manufacturing”. In: *Proceedings of the 24th Solid Freeform Fabrication Symposium*. 2013. Austin, Texas, 2013, pp. 525–534.
- [180] A. H. Aitkenhead. *Polygon Mesh Voxelisation Matlab Script*. 2013.
- [181] D.-J. Kroon. *Polygon2Voxel Matlab Script*. 2012.
- [182] K. Museth. “VDB”. In: *ACM Transactions on Graphics* 32.3 (June 2013), pp. 1–22. DOI: 10.1145/2487228.2487235.
- [183] Kitware Inc. *CMake*. New York, NY, USA, 2016.
- [184] J. Liu, M.-J. Tan, Y. Aue-u-lan, M. Guo, S. Castagne, and B.-W. Chua. “Superplastic-like forming of Ti-6Al-4V alloy”. In: *The International Journal of Advanced Manufacturing Technology* 69.5-8 (2013), pp. 1097–1104. DOI: 10.1007/s00170-013-5101-z.
- [185] C. H. Fu and Y. B. Guo. “Three-Dimensional Temperature Gradient Mechanism in Selective Laser Melting of Ti-6Al-4V”. In: *Journal of Manufacturing Science and Engineering* 136.6 (Oct. 2014), p. 061004. DOI: 10.1115/1.4028539.
- [186] M. Simonelli. “Microstructure Evolution and Mechanical Properties of Selective Laser Melted Ti-6Al-4V”. PhD thesis. University of Loughborough, 2014.
- [187] A. Y. Hussein. “The Development of Lightweight Cellular Structures for Metal Additive Manufacturing”. PhD thesis. 2013.

- [188] L. Parry, I. Ashcroft, and R. Wildman. “Understanding the effect of laser scan strategy on residual stress in selective laser melting through thermo-mechanical simulation”. In: *Additive Manufacturing* 12 (2016), pp. 1–15. DOI: 10.1016/j.addma.2016.05.014.
- [189] F. Calignano. “Design optimization of supports for overhanging structures in aluminum and titanium alloys by selective laser melting”. In: *Materials and Design* 64 (Dec. 2014), pp. 203–213. DOI: 10.1016/j.matdes.2014.07.043.
- [190] S. Kou. *Welding Metallurgy*. 2nd. Hoboken, New Jersey, USA: John Wiley & Sons, Inc., 2003, p. 466.
- [191] C. Li, C. Fu, Y. Guo, and F. Fang. “A multiscale modeling approach for fast prediction of part distortion in selective laser melting”. In: *Journal of Materials Processing Technology* 229 (2016), pp. 703–712. DOI: 10.1016/j.jmatprotec.2015.10.022.